

2019

# The Design and Manufacture of a Glass Fibre Reinforced Polymer (GFRP) Bolted Flange Joint for Oil and Gas Applications

Aljuboury, Muhsin Ali Marie

<http://hdl.handle.net/10026.1/13659>

---

<http://dx.doi.org/10.24382/680>

University of Plymouth

---

*All content in PEARL is protected by copyright law. Author manuscripts are made available in accordance with publisher policies. Please cite only the published version using the details provided on the item record or document. In the absence of an open licence (e.g. Creative Commons), permissions for further reuse of content should be sought from the publisher or author.*



**UNIVERSITY OF  
PLYMOUTH**

**THE DESIGN AND MANUFACTURE OF A GLASS  
FIBRE REINFORCED POLYMER (GFRP) BOLTED  
FLANGE JOINT FOR OIL AND GAS  
APPLICATIONS**

by

**MUHSIN ALI MARIE ALJUBOURY**

A thesis submitted to the University of Plymouth in partial  
fulfilment for the degree of

**DOCTOR OF PHILOSOPHY**

School of Engineering

University of Plymouth

April 2019

Copyright@2019 Muhsin Ali Marie Aljuboury

*This copy of the thesis has been supplied on condition that anyone who consults it is understood to recognize that its copyright rests with its author and that no quotation from the thesis and no information derived from it may be published without the author's prior consent.*

## **Abstract**

Metallic bolted flange and pipes both have been increasingly replaced by fibre reinforced polymer (FRP) materials in many applications which deal with extreme harsh environments such as oil, gas, marine, chemical etc. However, only a handful of research works have been conducted regarding the bolted flange joint (BFJ) made of FRP materials. Also, the availabilities of standards and codes are very limited for the composite BFJ. Hence, the design guidelines for fabrication methods and dimensional considerations of bolted FRP flange are yet to be optimised fully. For instance, the ASME Boiler and Pressure Vessel Code, Section X, does not include specific rules for the design of bolted FRP flange joints. As a result, it is difficult to understand the consequences of the reliability of FRP flanges made with parametric variations and dimensional alterations.

Therefore, the current research aims to produce a bolted GFRP flange joint with high performance through a series of experimentations and numerical simulations. A mould has been designed and manufactured using aluminium, glass, O-ring gasket and bolts. The bolted GFRP flanges have been fabricated using vacuum infusion process, polyester and fibreglass braid sleeves. Various experiments were conducted to solve the faced issues during the manufacturing process. Several experiments were carried out with different strain gauges to measure the bolt load. The GFRP flange has been assembled with other required components to produce the pressure vessel and tested under various bolt and internal pressure loads using different gaskets (Nitrile and Viton), which are suitable for the oil and the gas applications.

Numerically, finite element analysis (FEA) of the BFJ comprised of composite flange and pipe, flange-pipe adhesive bonding, gasket and fastener has been conducted using ANSYS Mechanical. The FEA has been performed considering the orthotropic properties of the composite materials and the non-linearity behaviour of the rubber gasket. The FEA also includes the simulation of the fluid pressure penetration (FPP) between the flange and the gasket using the contact element real constant criterion (PPNC). Furthermore, another FEA model has been developed for a metal flange using the same boundary conditions as the GFRP flange. This flange has been investigated experimentally and numerically in published work [1]. The agreements between the obtained results and the previous results are excellent. This confirms the validity of the FEA performed in this project.

The BFJ has been tested under various bolt and internal pressure loads experimentally and numerically and the strains in three directions (axial, hoop and radial) have been measured and calculated. The obtained results show that the influence of the bolt load is higher than the pressure load and the leakage pressure increases with increasing the bolt load. The effects of the flange dimensions on the maximum axial, hoop and radial strains, axial displacement, flange rotation and leakage pressure have been investigated using the FEA. The dimensions considered are the flange outer diameter and thickness, hub length and thickness. Most of the flange joint dimensions (within the selected range) have a small effect on the results and that confirms that the flange dimensions should be reduced to save the materials cost. The current flange is very strong and this is due to the good selection of the materials, fabric structure and the fabrication process, which gives high fibre content. In addition, the results show that the gasket materials and thickness has very small influences on the flange strains, axial displacement and rotation. The leakage pressure is affected by the gasket materials more than the thickness.

## Acknowledgements

First of all, I would like to express my sincere gratitude to my supervisors, **Md Jahir Rizvi, Stephen Grove** and **Richard Cullen**, School of Engineering at Plymouth University, for their assistance, encouragement, guidance, criticism and support throughout the present research project. I am also grateful to them for allowing me to develop my own ideas.

I dedicate this PhD work to my lovely wife **Marwa Aljuboury** for her unceasing encouragement, support and attention, my mother the most important person in my life and my kids **Adam** and **Mawa** for providing a balance in my life, which made this PhD work easier.

I take this opportunity to express gratitude to all of the members of staff at University of Plymouth, who directly or indirectly, have lent their hands in this PhD study, especially the technicians team, **Terry Richards, Zoltan Gombos, Mike Sloman, Neil Fewings, Rick Preston, Julian Seipp** and **Sam Thorpe** who provided the technical supports.

Special thanks must be given to **Casper Kruger** of Pipex px® for supplying some of the materials and technical advices. Also, I would like to thank **Keith Lawrence** at Vishay Measurements Group UK Ltd and **Andrew Ramage** at Techni Measure for their technical supports.

I have to express my gratitude to the Higher Committee for Education Development (**HCED**) in Iraq, who provided all the financial supports for my stays in Plymouth and study expenses.

I am also grateful to the anonymous referees for their respective comments on the manuscripts of journal and conference papers.

Finally, I want to express now my most sincere thanks to all who contributed to the development of this thesis during the last four years.

## Author's declaration

At no time during the registration for the degree of Doctor of Philosophy has the author been registered for any other University award without prior agreement of the Doctoral College Quality Sub-Committee.

Work submitted for this research degree at the University of Plymouth has not formed part of any other degree either at the University of Plymouth or at another establishment.

This PhD study was financed with the aid of a scholarship from the Higher Committee for Education Development (HCED) in Iraq.

Paper presentations were given at relevant conferences and several papers have been published.

Word count of the thesis: **55,931** words

Figure count of the thesis: **165** figures

Table count of the thesis: **11** tables

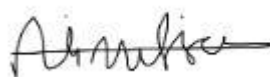
External Contacts:

Email: [muhsin.aljuboury@yahoo.com](mailto:muhsin.aljuboury@yahoo.com) or [muhsin.meng@gmail.com](mailto:muhsin.meng@gmail.com)

Researchgate: [https://www.researchgate.net/profile/Muhsin\\_Aljuboury](https://www.researchgate.net/profile/Muhsin_Aljuboury)

Linkedin: <https://www.linkedin.com/in/muhsin-aljuboury-730458111/>

ORCID: <https://orcid.org/0000-0002-7300-3056>



Signed.....

Date..... 1<sup>st</sup> April 2019 .....

## **List of contents:**

|                            |       |
|----------------------------|-------|
| Abstract .....             | iii   |
| Acknowledgements .....     | v     |
| Author's declaration ..... | vi    |
| List of contents:.....     | vii   |
| List of figures: .....     | xiv   |
| List of tables:.....       | xxiii |
| Nomenclature: .....        | xxiv  |

## **CHAPTER ONE**

## **INTRODUCTION**

|  |    |
|--|----|
| 1.1 Introduction .....                         | 1  |
| 1.2 Motivation of the research.....            | 3  |
| 1.3 Methodology .....                          | 4  |
| 1.4 Structure of the thesis .....              | 6  |
| 1.5 Outline of the research .....              | 7  |
| 1.6 Skills development training attended ..... | 8  |
| 1.7 Publications work from this PhD work ..... | 9  |
| 1.7.1 Submitted journal articles .....         | 10 |

## **CHAPTER TWO**

## **LITERATURE REVIEW**

|   |    |
|---|----|
| 2.1 Introduction .....                                    | 11 |
| 2.2 Overview of metallic bolted flange joints .....       | 12 |
| 2.3 Overview of composite bolted flange joints.....       | 16 |
| 2.3.1 Materials system.....                               | 16 |
| 2.3.2 Fibres reinforcement .....                          | 18 |
| 2.3.3 Manufacturing techniques of bolted GFRP flange..... | 19 |
| 2.3.4 Use of Braided fabric .....                         | 21 |
| 2.4 Performance of metallic bolted flange joints.....     | 23 |
| 2.4.1 Effects of nominal flange diameter .....            | 24 |



|                      |  |                              |
|----------------------|--|------------------------------|
| 2.4.2                | Effects of flange thickness .....                                    | 24                           |
| 2.4.3                | Effects of hub thickness .....                                       | 25                           |
| 2.4.4                | Effects of hub length .....  | 25                           |
| 2.4.5                | Effects of flange rotation .....                                     | 25                           |
| 2.4.6                | Effects of thermal loading .....                                     | 26                           |
| 2.4.7                | Effects of material's stiffness .....                                | 27                           |
| 2.4.8                | Effects of bolt preload .....  | 27                           |
| 2.4.9                | Effects of bolt spacing .....  | 28                           |
| 2.4.10               | 2D Axisymmetric and 3D FE modelling of the flange .....              | 28                           |
| 2.4.11               | Considerations for FRP flanges .....                                 | 29                           |
| 2.5                  | Published research on Composite flange joints .....                  | 29                           |
| 2.6                  | Research gap and justification of the project .....                  | 31                           |
| 2.7                  | History of standards development .....                               | 33                           |
| 2.8                  | Compressed gaskets .....   | 34                           |
| 2.8.1                | Metallic gaskets .....   | 34                           |
| 2.8.2                | Semi-metallic gaskets .....  | 36                           |
| 2.8.3                | Non-metallic gaskets .....   | 39                           |
| 2.9                  | The characteristics composite pipes commonly used with flanges ..... | 40                           |
| 2.10                 | Co-bonding of composite flange with composite pipe .....             | 42                           |
| 2.11                 | Fasteners of flange joint .....                                      | 45                           |
| 2.12                 | Issues with drilling of composite materials .....                    | 47                           |
| 2.13                 | Summary .....  | 52                           |
| <b>CHAPTER THREE</b> |  | <b>DESIGN &amp; ANALYSIS</b> |
| 3.1                  | Introduction .....   | 53                           |
| 3.2                  | Design variables .....   | 54                           |
| 3.2.1                | Flange dimensions .....  | 55                           |
| 3.2.2                | Hub dimensions .....   | 55                           |

|       |  |    |
|-------|--|----|
| 3.2.3 | Gasket material and thickness .....                      | 55 |
| 3.2.4 | Bolt load .....  | 55 |
| 3.2.5 | Internal fluid pressure .....                            | 56 |
| 3.3   | Design constants .....                                   | 56 |
| 3.4   | Analytical design analysis (based on the ASME code)..... | 57 |
| 3.4.1 | Full face flange geometry.....                           | 57 |
| 3.4.2 | Gasket loads .....                                       | 58 |
| 3.4.3 | Flange loads .....                                       | 59 |
| 3.4.4 | Gasket seating (Bolt up) conditions .....                | 60 |
| 3.4.5 | Operating conditions .....                               | 62 |
| 3.4.6 | Flange stresses calculations.....                        | 65 |
| 3.5   | Design loads .....                                       | 66 |
| 3.6   | Summary .....  | 66 |

## **CHAPTER FOUR**

## **GFRP FLANGE FABRICATION**

|       |   |    |
|-------|---|----|
| 4.1   | Introduction .....                          | 67 |
| 4.2   | Mould design .....                          | 68 |
| 4.2.1 | Mandrel .....                               | 68 |
| 4.2.2 | Plate.....                                  | 69 |
| 4.2.3 | The mould assembly .....                    | 70 |
| 4.3   | GFRP Flange fabrication.....                | 70 |
| 4.4   | Issues with the manufacturing process ..... | 75 |
| 4.4.1 | Resin flow problem.....                     | 75 |
| 4.4.2 | Voids and cracks problem.....               | 76 |
| 4.5   | Solving the issues .....                    | 77 |
| 4.5.1 | Inlet and outlet positions .....            | 77 |
| 4.5.2 | Resin Viscosity .....                       | 81 |
| 4.6   | Composite flange drilling.....              | 83 |

|   |  |     |
|---|--|-----|
| 4.7                                     | Flange-pipe adhesive bonding.....          | 86  |
| 4.8                                     | Other end of the pipe.....                 | 88  |
| 4.9                                     | Blind flanges .....                        | 88  |
| 4.10                                    | Assembly of the joint components .....     | 89  |
| 4.11                                    | Summary.....                               | 90  |
| <b>CHAPTER FIVE</b>                     |  |     |
| <b>EXPERIMENTAL METHODOLOGY</b>         |  |     |
| 5.1                                     | Introduction .....                         | 91  |
| 5.2                                     | Materials characterisations.....           | 92  |
| 5.2.1                                   | Fibre volume fraction ( $V_f$ ) .....      | 92  |
| 5.2.2                                   | Fibre orientation (Braiding angle) .....   | 93  |
| 5.2.3                                   | Fibre orientation (Crimp angle) .....      | 95  |
| 5.3                                     | Autodesk Heliux composite validation.....  | 96  |
| 5.4                                     | Flange-Gasket friction.....                | 98  |
| 5.5                                     | Data measuring equipment.....              | 100 |
| 5.5.1                                   | Strain indicators and recorders.....       | 100 |
| 5.5.2                                   | Composite flange strain gauges .....       | 101 |
| 5.5.3                                   | Bolt strain gauges.....                    | 101 |
| 5.6                                     | Construction of the test rig .....         | 110 |
| 5.6.1                                   | Digital torque wrench .....                | 110 |
| 5.6.2                                   | Fittings .....                             | 110 |
| 5.6.3                                   | Pump test.....                             | 110 |
| 5.6.4                                   | Pressure Gauges .....                      | 110 |
| 5.7                                     | Testing procedure.....                     | 111 |
| 5.8                                     | Summary .....                              | 112 |
| <b>CHAPTER SIX</b>                      |  |     |
| <b>NUMERICAL SIMULATION METHODOLOGY</b> |  |     |
| 6.1                                     | Introduction .....                         | 113 |
| 6.2                                     | FEA model of bolted GFRP flange joint..... | 114 |

|                      |  |                                  |
|----------------------|--|----------------------------------|
| 6.2.1                | Geometry and the dimensions of the flange joint .....        | 114                              |
| 6.2.2                | GFRP flange simulation.....                                  | 116                              |
| 6.2.3                | Filament winding pipe modelling .....                        | 118                              |
| 6.2.4                | Bonded flange-pipe modelling.....                            | 118                              |
| 6.2.5                | Fasteners modelling .....                                    | 118                              |
| 6.2.6                | Modelling the rubber gasket.....                             | 119                              |
| 6.2.7                | Elements selection and contact interfaces.....               | 122                              |
| 6.2.8                | Boundary and loading conditions.....                         | 123                              |
| 6.3                  | Summary .....  | 126                              |
| <b>CHAPTER SEVEN</b> |  | <b>VALIDATION</b>                |
| 7.1                  | Introduction .....   | 127                              |
| 7.2                  | Experimental validation .....                                | 128                              |
| 7.2.1                | Bolt up condition.....                                       | 129                              |
| 7.2.2                | Operating conditions .....                                   | 133                              |
| 7.3                  | Numerical validation .....                                   | 151                              |
| 7.3.1                | Metallic flange joint geometry and material properties ..... | 151                              |
| 7.3.2                | 3D CAD model .....   | 152                              |
| 7.3.3                | 2D FEA axisymmetric models .....                             | 154                              |
| 7.3.4                | Simulation results.....                                      | 155                              |
| 7.4                  | Summary .....  | 158                              |
| <b>CHAPTER EIGHT</b> |  | <b>RESULTS &amp; DISCUSSIONS</b> |
| 8.1                  | Introduction .....   | 159                              |
| 8.2                  | ASME code predictions.....                                   | 160                              |
| 8.3                  | Bolted flange joint deformation .....                        | 162                              |
| 8.4                  | Flange diameter effect .....                                 | 162                              |
| 8.5                  | Flange thickness effect .....                                | 172                              |
| 8.6                  | Hub length effect .....                                      | 177                              |

|  |  |            |
|--|--|------------|
| 8.7  | Hub thickness effect .....                         | 182        |
| 8.8  | Comparison of design variables effect .....        | 187        |
| 8.9  | Flange axial displacement .....                    | 188        |
| 8.9.1  | <i>Axial displacement vs hoop angle</i> .....      | 189        |
| 8.9.2  | <i>Axial displacement vs radial distance</i> ..... | 191        |
| 8.10   | Flange rotation .....                              | 194        |
| 8.11   | Leakage pressure .....                             | 197        |
| 8.11.1   | Leakage pressure vs flange diameter .....          | 197        |
| 8.11.2   | Leakage pressure vs flange thickness .....         | 199        |
| 8.11.3   | Leakage pressure vs hub length .....               | 201        |
| 8.11.4   | Leakage pressure vs hub thickness .....            | 203        |
| 8.12   | Results contribution .....                         | 204        |
| 8.13   | Summary .....                                      | 206        |
| <br><b>CHAPTER NINE                      CONCLUSIONS &amp; RECOMMENDATIONS</b>         |  |            |
| 9.1  | Conclusions .....                                  | 207        |
| 9.1.1  | Composite flange standards or design codes .....   | 207        |
| 9.1.2  | Manufacturing of the GFRP flange .....             | 208        |
| 9.1.3  | Bolted GFRP flange testing .....                   | 208        |
| 9.1.4  | FEA model of GFRP flange joint .....               | 209        |
| 9.1.5  | Validation of results .....                        | 209        |
| 9.1.6  | Effect of the applied loads .....                  | 210        |
| 9.1.7  | Effect of the flange dimensions .....              | 210        |
| 9.1.8  | Effect of the gasket materials and thickness ..... | 210        |
| 9.2  | Recommendations for future work .....              | 211        |
| <b>APPENDICES .....</b>  |  | <b>213</b> |
| Appendix (A): Helius composite validation properties of the composite properties ..... |  | 213        |

|   |            |
|---|------------|
| Appendix (B): Calibration of the strain indicators and recorder (P3's)..... | 215        |
| Appendix (C): Calibration of the digital torque adaptor.....                | 217        |
| Appendix (D): Calibration of the pressure gauge .....                       | 218        |
| <b>REFERENCES.....</b>  | <b>219</b> |

## List of figures:

|  |    |
|--|----|
| Fig. 1.1: The flow chart of the project .....  | 7  |
| Fig. 2.1: Bolted flange (a) Full face gasket flange (b) Ring type joint<br>(c) Flat ring gasket flange .....     | 13 |
| Fig. 2.2: Metallic flange (a) Raised face flange (b) Tongue and groove flange .....                              | 15 |
| Fig. 2.3: Vacuum bagging process.....  | 21 |
| Fig. 2.4: Mandrel over-braiding.....   | 21 |
| Fig. 2.5: Circular braiding around a complex shape.....  | 22 |
| Fig. 2.6: Flange failure at the flange neck .....  | 22 |
| Fig. 2.7: Loading analysis of the flange.....  | 23 |
| Fig. 2.8: Metallic gaskets (a) Ring joint gasket (b) Lens ring gasket (c) Corrugated<br>gasket .....             | 35 |
| Fig. 2.9: Semi-metallic gaskets (a) Spiral wound gasket (b) Metal jacketed gasket (c)<br>Kammprofile gasket..... | 38 |
| Fig. 2.10: Three different types of flange-pipe adhesive bonded joint.....                                       | 43 |
| Fig. 2.11: Delamination (a) Peel-up delamination (b) Push-out delamination .....                                 | 47 |
| Fig. 2.12: (a) Helical flute ‘‘Stub Length’’ K10 drill; (b) ‘‘Brad & Spur’’ K10 drill                            | 50 |
| Fig. 2.13: Drills used in the experimental work: (a) EDP27199, (b) A1141, (c)<br>A1163 and (d) A1167A .....      | 50 |
| Fig. 2.14: Photographs for various step-core drills.....   | 51 |
| Fig. 3.1: Schematic diagram of the flange joint.....   | 54 |
| Fig. 3.2: FFG Flange geometry.....   | 57 |
| Fig. 3.3: Flange under gasket seating conditions .....   | 61 |
| Fig. 3.4: Flange under operating conditions .....  | 63 |

|  |    |
|--|----|
| Fig. 4.1: The mandrel .....  | 69 |
| Fig. 4.2: The glass plate .....  | 69 |
| Fig. 4.3: The Mould of the composite flange.....   | 70 |
| Fig. 4.4: Schematic diagram of the vacuum infusion process.....  | 71 |
| Fig. 4.5: Common failure on the GFRP flanges [34] .....  | 72 |
| Fig. 4.6: Laid braided fiberglass fabric on the mandrel and the plate.....   | 73 |
| Fig. 4.7: Diffusion mesh distribution .....  | 74 |
| Fig. 4.8: Bagging and resin infusion .....   | 74 |
| Fig. 4.9: Machining of the composite flange .....  | 75 |
| Fig. 4.10: Flange with dry regions on the face.....  | 76 |
| Fig. 4.11: Microscopy image for the flange-hub intersection.....   | 77 |
| Fig. 4.12: Glass mould of the experiments .....  | 78 |
| Fig. 4.13: The vacuum infusion process of the experiments.....   | 78 |
| Fig. 4.14: Inlet & outlet positions of the conducted experiments .....   | 79 |
| Fig. 4.15: Flange without dry fabric on the face .....   | 79 |
| Fig. 4.16: Microscope images at the flange-hub intersection (a) model A, (b) model B, (c) model C.....             | 80 |
| Fig. 4.17: Thermocouple position in the flange-hub intersection .....  | 81 |
| Fig. 4.18: The temperature variation during the infusion and curing process at the flange-hub intersection.....    | 81 |
| Fig. 4.19: The variation of the polyester viscosity with the time at different temperature (without catalyst)..... | 82 |
| Fig. 4.20: The variation of the polyester viscosity with the time at different temperature (1% catalyst) .....     | 83 |
| Fig. 4.21: Drilling tools of the composite .....   | 84 |



|   |     |
|---|-----|
| Fig. 4.22: 22 mm drilled holes of used tools in the experimental work .....   | 85  |
| Fig. 4.23: Drilled holes with different speeds.....   | 86  |
| Fig. 4.24: During the drilled and the final GFRP flange .....   | 86  |
| Fig. 4.25: Chamfering the composite pipe.....   | 87  |
| Fig. 4.26: Flange-pipe bonding.....   | 87  |
| Fig. 4.27: HD and blind flanges: (a) Acrylic blind flange attached to the fabricated flange and (b) HD and steel blind flange attached to the HD flange. .... | 89  |
| Fig. 4.28: Schematic diagram of the pressure vessel .....   | 89  |
| Fig. 5.1: Composite samples for calculating the $V_f$ .....   | 93  |
| Fig. 5.2: Braiding angle of the flange disc and the hub .....   | 94  |
| Fig. 5.3: Filament-winding angle of the composite pipe .....  | 94  |
| Fig. 5.4: Microscope picture of the crimp angle.....  | 95  |
| Fig. 5.5: Calculated orientation distribution factor for a plain weave tow with varying crimp angle .....   | 96  |
| Fig. 5.6: Composite laminate (a) under the vacuum (b) samples of the test.....  | 97  |
| Fig. 5.7: Illustration of the 3-points bending test.....  | 97  |
| Fig. 5.8: Inclined plane friction tester.....   | 99  |
| Fig. 5.9: Relationships of ramp weight components.....  | 99  |
| Fig. 5.10: Strain indicator and recorder .....  | 100 |
| Fig. 5.11: The strain gauges set up on the composite flange body .....  | 101 |
| Fig. 5.12: Bolts with two strain gauges bonded on the shank.....  | 102 |
| Fig. 5.13: Quarter Bridge with two gauges connected in series method [106].....   | 103 |
| Fig. 5.14: Bolts with embedded strain gauges .....  | 104 |
| Fig. 5.15: Holding attachment for the bolt testing .....  | 105 |
| Fig. 5.16: Tensile test data of the bolt SSG1 .....   | 106 |

|   |     |
|---|-----|
| Fig. 5.17: Tensile test data of the bolt SSG2 .....                                 | 107 |
| Fig. 5.18: Tensile test data of the bolt CSG1 .....                                 | 107 |
| Fig. 5.19: Tensile test data of the bolt CSG2 .....                                 | 108 |
| Fig. 5.20: Comparison of the tensile test data of all the bolts.....                | 109 |
| Fig. 5.21: Comparison of the tensile test data of the CSG bolts .....               | 109 |
| Fig. 5.22: Bolt tightening diagram [108] .....                                      | 111 |
| Fig. 6.1: Symmetric of the bolted flange joint .....                                | 115 |
| Fig. 6.2: 3D FEA model of the bolted flange joint .....                             | 115 |
| Fig. 6.3: Dimensions of the bolted flange joint (mm).....                           | 116 |
| Fig. 6.4: Fastener modelling .....  | 119 |
| Fig. 6.5: Characteristics of the Nitrile gasket obtained experimentally .....       | 120 |
| Fig. 6.6: Characteristics of the Viton gasket obtained experimentally .....         | 120 |
| Fig. 6.7: Boundary conditions during the bolt-up and the operating conditions ..... | 124 |
| Fig. 6.8: Schematic diagram of the fluid pressure penetration modelling .....       | 125 |
| Fig. 7.1: FEA model.....  | 129 |
| Fig. 7.2: Pressure vessel during the test .....                                     | 129 |
| Fig. 7.3: Hub axial strain, $\mu\epsilon$ .....                                     | 131 |
| Fig. 7.4: Hub hoop strain, $\mu\epsilon$ .....                                      | 132 |
| Fig. 7.5: Flange hoop strain, $\mu\epsilon$ .....                                   | 133 |
| Fig. 7.6: Axial strain, $\mu\epsilon$ (top-left) .....                              | 135 |
| Fig. 7.7: Axial strain, $\mu\epsilon$ (top-right).....                              | 135 |
| Fig. 7.8: Axial strain, $\mu\epsilon$ (bottom-left).....                            | 136 |
| Fig. 7.9: Axial strain, $\mu\epsilon$ (bottom-right).....                           | 137 |
| Fig. 7.10: Hoop strain, $\mu\epsilon$ (top-left) .....                              | 138 |
| Fig. 7.11: Hoop strain, $\mu\epsilon$ (top-right).....                              | 139 |

|  |     |
|--|-----|
| Fig. 7.12: Hoop strain, $\mu\epsilon$ (bottom-left).....   | 140 |
| Fig. 7.13: Hoop strain, $\mu\epsilon$ (bottom-right) .....   | 140 |
| Fig. 7.14: Flange hoop strain, $\mu\epsilon$ .....   | 141 |
| Fig. 7.15: Flange radial strain, $\mu\epsilon$ , (bolt centre).....  | 143 |
| Fig. 7.16: Flange radial strain, $\mu\epsilon$ , (mid-point).....  | 144 |
| Fig. 7.17: Bolt axial strain, $\mu\epsilon$ .....  | 145 |
| Fig. 7.18: Bolt axial stress, MPa.....   | 145 |
| Fig. 7.19: Distribution of contact pressure on gasket .....  | 147 |
| Fig. 7.20: Leakage propagation with the internal pressure up to leakage pressure .   | 148 |
| Fig. 7.21: Leakage pressure variation of Flange-Nitrile gasket with the bolt load..  | 149 |
| Fig. 7.22: Leakage pressure variation of Flange-Viton gasket with the bolt load ...  | 150 |
| Fig. 7.23: Bolted flange joint (All dimensions in mm).....   | 151 |
| Fig. 7.24: (a) 3D model flange joint with mesh (b) Boundary conditions.....  | 153 |
| Fig. 7.25: (a) 2D FEA model flange joint with mesh (b) Boundary conditions .....   | 154 |
| Fig. 7.26: Flange hub stress variation with the internal pressure up to leakage point<br>.....   | 155 |
| Fig. 7.27: Fluid pressure penetration of the 3D FEA (a) Internal pressure 2 MPa (b)<br>Internal pressure 8 MPa (c) Internal pressure 14.05 MPa (Leakage point) ..... | 156 |
| Fig. 7.28: Fluid pressure penetration of the 2D FEA (a) Internal pressure 2 MPa (b)<br>Internal pressure 8 MPa (c) Internal pressure 13.87 MPa (Leakage point) ..... | 157 |
| Fig. 7.29: Variation of the leakage pressure with the bolt load for the 2D and 3D<br>FEA .....   | 157 |
| Fig. 8.1: Total deformation of the bolted flange joint.....  | 162 |
| Fig. 8.2: Axial strain (mm/mm) .....   | 164 |

|   |     |
|---|-----|
| Fig. 8.3: Maximum axial tensile strain ( $\mu\epsilon$ ) variation with the flange diameter for range of gasket types and thickness .....                   | 164 |
| Fig. 8.4: Maximum axial tensile strain ( $\mu\epsilon$ ) variation with the bolt load and internal pressure for range of the flange diameter.....           | 165 |
| Fig. 8.5: Maximum axial compression strain ( $\mu\epsilon$ ) variation with the flange diameter for range of gasket types and thickness .....               | 167 |
| Fig. 8.6: Hoop strain (mm/mm) .....   | 168 |
| Fig. 8.7: Maximum hoop strain ( $\mu\epsilon$ ) variation with the flange diameter for range of gasket types and thickness .....                            | 168 |
| Fig. 8.8: Radial strain (mm/mm).....  | 170 |
| Fig. 8.9: Maximum radial strain ( $\mu\epsilon$ ) variation with the flange diameter for range of gasket types and thickness .....                          | 170 |
| Fig. 8.10: Bolt axial strain ( $\mu\epsilon$ ).....   | 171 |
| Fig. 8.11: Bolt axial strain ( $\mu\epsilon$ ) variation with the flange diameter for range of gasket types and thickness.....                              | 171 |
| Fig. 8.12: Maximum axial tensile strain ( $\mu\epsilon$ ) variation with the flange thickness for range of gasket types and thickness .....                 | 172 |
| Fig. 8.13: Maximum axial compression strain ( $\mu\epsilon$ ) variation with the flange thickness for range of gasket types and thickness.....              | 173 |
| Fig. 8.14: Maximum axial compression strain ( $\mu\epsilon$ ) variation with the bolt load and the internal pressure for range of the flange thickness..... | 174 |
| Fig. 8.15: Maximum hoop strain ( $\mu\epsilon$ ) variation with the flange thickness for range of gasket types and thickness .....                          | 175 |
| Fig. 8.16: Maximum radial strain ( $\mu\epsilon$ ) variation with the flange thickness for range of gasket types and thickness .....                        | 176 |

|  |     |
|--|-----|
| Fig. 8.17: Bolt axial strain ( $\mu\epsilon$ ) variation with the flange thickness for range of gasket types and thickness .....             | 177 |
| Fig. 8.18: Maximum axial tensile strain ( $\mu\epsilon$ ) variation with the hub length for range of gasket types and thickness .....        | 178 |
| Fig. 8.19: Maximum axial compression strain ( $\mu\epsilon$ ) variation with the hub length for range of gasket types and thickness .....    | 179 |
| Fig. 8.20: Maximum hoop strain ( $\mu\epsilon$ ) variation with the hub length for range of gasket types and thickness .....                 | 179 |
| Fig. 8.21: Maximum hoop strain ( $\mu\epsilon$ ) variation with bolt load and internal pressure for range of the hub length.....             | 180 |
| Fig. 8.22: Maximum radial strain ( $\mu\epsilon$ ) variation with the hub length for range of gasket types and thickness .....               | 181 |
| Fig. 8.23: Bolt axial strain ( $\mu\epsilon$ ) variation with the hub length for range of gasket types and thickness .....                   | 182 |
| Fig. 8.24: Maximum axial tensile strain ( $\mu\epsilon$ ) variation with the hub thickness for range of gasket types and thickness .....     | 183 |
| Fig. 8.25: Maximum axial compression strain ( $\mu\epsilon$ ) variation with the hub thickness for range of gasket types and thickness ..... | 184 |
| Fig. 8.26: Maximum hoop strain ( $\mu\epsilon$ ) variation with the hub thickness for range of gasket types and thickness .....              | 185 |
| Fig. 8.27: Maximum radial strain ( $\mu\epsilon$ ) variation with the hub thickness for range of gasket types and thickness .....            | 186 |
| Fig. 8.28: Maximum radial strain ( $\mu\epsilon$ ) variation with the bolt load and internal pressure for range of the hub thickness.....    | 186 |

|  |     |
|--|-----|
| Fig. 8.29: Bolt axial strain ( $\mu\epsilon$ ) variation with the hub thickness for range of gasket types and thickness.....       | 187 |
| Fig. 8.30: Flange axial displacement variation with the hoop angle at the inner and outer diameters .....                          | 189 |
| Fig. 8.31: Flange axial displacement variation with the hoop angle for range of the bolt load, P 0 bar .....                       | 190 |
| Fig. 8.32: Flange axial displacement variation with the hoop angle for range of the internal pressure, BL7.4 kN .....              | 191 |
| Fig. 8.33: Flange axial displacement variation with the radial distance at the right and left edges.....                           | 192 |
| Fig. 8.34: Flange axial displacement variation with the radial distance at the right edge for range of the bolt load .....         | 192 |
| Fig. 8.35: Flange axial displacement variation with the radial distance at the right edge for range of the internal pressure ..... | 193 |
| Fig. 8.36: Schematic diagram of the flange bending .....   | 194 |
| Fig. 8.37: Flange rotation variation with the hoop distance for range of the bolt load .....                                       | 195 |
| Fig. 8.38: Flange rotation variation with the internal pressure for range of the bolt load.....                                    | 196 |
| Fig. 8.39: Flange rotation variation with the hoop a for range of the internal pressure .....                                      | 196 |
| Fig. 8.40: Leakage pressure variation with the flange diameter for different gasket materials and thickness .....                  | 197 |
| Fig. 8.41: Contact pressure between the flange and the gasket .....  | 198 |

|   |     |
|---|-----|
| Fig. 8.42: Leakage pressure variation with the bolt load for different flange diameter .....                          | 199 |
| Fig. 8.43: Leakage pressure variation with the flange thickness for range of the gasket materials and thickness ..... | 200 |
| Fig. 8.44: Leakage pressure point .....   | 200 |
| Fig. 8.45: Leakage pressure variation with the bolt load for different flange thickness .....                         | 201 |
| Fig. 8.46: Leakage pressure variation with the hub length for range of gasket materials and thickness .....           | 202 |
| Fig. 8.47: Leakage pressure variation with bolt load for different hub length .....                                   | 202 |
| Fig. 8.48: Leakage pressure variation with the hub thickness for various gasket materials and thickness .....         | 203 |
| Fig. 8.49: Leakage pressure variation with the bolt load for different hub thickness .....                            | 204 |
| Fig. A.1: Design of GFRP lamina.....  | 213 |
| Fig. A.2: GFRP lamina properties .....  | 213 |
| Fig. A.3: Design of GFRP laminate.....  | 214 |
| Fig. A.4: 2D and 3D mechanical properties of the GFRP laminate .....  | 214 |
| Fig. B.1: Calibration data of P3, SN 0161615 .....  | 215 |
| Fig. B.2: Calibration data of P3, SN 0169299 .....  | 215 |
| Fig. B.3: Calibration data of P3, SN 0170024 .....  | 216 |
| Fig. B.4: Calibration data of P3, SN 0170060 .....  | 216 |
| Fig. C.1: Calibration data of digital torque adaptor .....  | 217 |
| Fig. D.1: Calibration data of pressure gauge .....  | 218 |

## List of tables:

|  |     |
|--|-----|
| Table 2.1: The difference between composites materials and steel materials for 1 m pipe in the marine environment..... | 32  |
| Table 3.1: Gasket parameters for elastomers without fabric or high percent of asbestos fibre .....                     | 58  |
| Table 5.1: Fibre volume fraction experimental data .....   | 93  |
| Table 5.2: Comparison of the Young's modulus for a composite laminate.....   | 98  |
| Table 6.1: Mechanical properties of the glass fibre, polyester resin and the adhesive .....                            | 117 |
| Table 6.2: Typical orthotropic mechanical properties of the flange and the pipe....                                    | 117 |
| Table 6.3: Compressive response of the Nitrile rubber gasket .....   | 121 |
| Table 6.4: Compressive response of the Viton rubber gasket.....  | 121 |
| Table 6.5: Shear modulus and transfer shear stiffness of the rubber gaskets .....                                      | 122 |
| Table 8.1: Stress values comparison for ASME code and FEA .....  | 161 |
| Table 8.2: Summary of design variables and their effect on the maximum strains .                                       | 188 |



## Nomenclature:

|                              |   |
|------------------------------|---|
| <b><i>BFJ</i></b>            | Bolted flange joint   |
| <b><i>PRP</i></b>            | Fibre reinforced polymers   |
| <b><i>GFRP</i></b>           | Glass fibre reinforced polymers   |
| <b><i>FEA</i></b>            | Finite element analysis   |
| <b><i>V<sub>f</sub></i></b>  | Fibre volume fraction   |
| <b><i>PPNC</i></b>           | The contact element real constant criterion   |
| <b><i>G</i></b>              | Diameter of gasket load reaction  |
| <b><i>B</i></b>              | Inside diameter of flange   |
| <b><i>C</i></b>              | Diameter of bolt circle   |
| <b><i>h<sub>G</sub></i></b>  | Radial distance from bolt circle to circle on which <i>H<sub>G</sub></i> acts                         |
| <b><i>B</i></b>              | Inside diameter of flange   |
| <b><i>y</i></b>              | Seating stress of the gasket  |
| <b><i>m</i></b>              | Gasket factor   |
| <b><i>H<sub>G</sub></i></b>  | Difference between bolt load and hydrostatic end force  |
| <b><i>W</i></b>              | Flange design bolt load   |
| <b><i>H</i></b>              | Total hydrostatic end force   |
| <b><i>H<sub>D</sub></i></b>  | Hydrostatic end force on area inside of the flange  |
| <b><i>P</i></b>              | Design internal pressure  |
| <b><i>h<sub>D</sub></i></b>  | Radial distance from bolt circle to circle on which <i>H<sub>D</sub></i> acts                         |
| <b><i>R</i></b>              | Radial distance from outer edge of the hub to the bolt circle   |
| <b><i>g<sub>1</sub></i></b>  | Thickness of hub at back of flange  |
| <b><i>H<sub>T</sub></i></b>  | Difference between total hydrostatic end force and the hydrostatic end force<br>area inside of flange |
| <b><i>h<sub>T</sub></i></b>  | Radial distance from bolt circle to circle on which <i>H<sub>T</sub></i> acts                         |
| <b><i>W<sub>m2</sub></i></b> | Minimum bolt loading for bolt-up conditions   |
| <b><i>W<sub>m1</sub></i></b> | Minimum bolt loading for design conditions  |
| <b><i>H<sub>Gy</sub></i></b> | Bolt load for gasket yielding   |

|           |  |
|-----------|--|
| $H'_{Gy}$ | Compression load required to seat gasket outside $G$ diameter  |
| $b$       | Effective gasket width or joint-contact-surface seating width  |
| $h'_G$    | Radial distance from bolt circle to gasket load reaction   |
| $A$       | Outside diameter of flange   |
| $A_1$     | Minimum bolting area required for the operating conditions   |
| $A_2$     | Minimum bolting area required for the bolt-up conditions   |
| $A_m$     | Total required cross-sectional area of bolts   |
| $A_B$     | Total cross-sectional area of bolts at root diameter of thread or section of least diameter under stress |
| $S_a$     | Allowable bolt stress at ambient temperature   |
| $S_b$     | Allowable bolt stress at design temperature  |
| $SFa$     | Allowable flange stress at ambient temperature   |
| $SFo$     | Allowable flange stress at design temperature  |
| $M_G$     | Component of moment due to $H_G$   |
| $M_T$     | Component of moment due to $H_T$   |
| $M_D$     | Component of moment due to $H_D$   |
| $M_o$     | Total moment   |
| $h''_G$   | Flange lever arm   |
| $H_p$     | Total joint-contact-surface compression load   |
| $H'_p$    | Total adjusted joint-contact-surface compression for full-face gasketed flange                           |
| $N$       | Number of bolts  |
| $SH$      | Longitudinal or axial hub stress   |
| $SR$      | Radial flange stress   |
| $SRAD$    | Radial stress at bolt circle   |
| $ST$      | Tangential or hoop flange stress   |
| $T$       | Shape factor (Fig. RD-1176.5 in the standard)  |
| $t$       | Flange thickness   |
| $U$       | Shape factor (Fig. RD-1176.5 in the standard)  |
| $V$       | Shape factor (Fig. RD-1176.2 in the standard)  |

|                             |  |
|-----------------------------|--|
| <b><i>Y</i></b>             | Shape factor (Fig. RD-1176.5 in the standard)          |
| <b><i>Z</i></b>             | Shape factor (Fig. RD-1176.5 in the standard)          |
| <b><i>A<sub>i</sub></i></b> | Internal cross section area of the pipe                |
| <b><i>A<sub>k</sub></i></b> | Cutting section area of the pipe                       |
| <b><i>P<sub>k</sub></i></b> | Equivalent pressure of the hydrostatic end force $H_D$ |
| <b><i>FN3</i></b>           | Flange with 3 mm Nitrile gasket                        |
| <b><i>FN5</i></b>           | Flange with 5 mm Nitrile gasket                        |
| <b><i>FV3</i></b>           | Flange with 3 mm Viton gasket                          |
| <b><i>FV5</i></b>           | Flange with 5 mm Viton gasket                          |
| <b><i>LP</i></b>            | Leakage pressure                                       |

# CHAPTER ONE

## INTRODUCTION

### 1.1 Introduction

Bolted flange joints are increasingly used in pressure containing equipment, such as pressure vessels and pipes due to the convenience in forming reliable joints between two pieces of equipment. Most of these flanges are made of traditional materials (mostly metallic materials). However, in many applications such as in oil, gas, and offshore applications or in chemical industries, the corrosion resistance of these materials are low compared with their non-metallic counterparts such as composite materials. A study in the USA indicated that during 1980's, the corrosion cost was approximately \$8 billion a year and this was the 60% of the U.S steel output that went into replacement products [2]. A further study [3] in the USA also has claimed that the annual direct cost of corrosion for drinking water and sewer systems was \$36 billion /year and for the gas-distribution network it was \$5 billion/year [3]. Hence, the high costs of installation and/or maintenance of the equipment and products made of conventional materials have led the designers and engineers to find sustainable solutions of corrosion problems. One of the best solutions that can be utilized to overcome the corrosion related problems, which are linked with the

metallic materials, is to use a material with good corrosion resistance, such as composite materials (fibre reinforced polymers) instead of metallic materials.

Continuous fibre reinforced composites are preferred in pressure vessels, pipelines, marine, automotive, aerospace, sporting goods and infrastructure, oil and gas industries due to their unique combination of properties which include high strength and modulus to weight ratio and high corrosion resistance [4, 5]. For instance, the weight of a 12 inch diameter pressurized fuel line for carrying liquid hydrogen in a space shuttle has been reduced by 20% when it has been manufactured from composite materials [6]. In addition, fibre reinforced polymer (FRP) has long life expectancy, less environmental concerns and low installation and maintenance costs [7]. Another important advantage of FRP is that the designers have the ability to vary the material properties for a specific application. For example, high resin content provides maximum corrosion resistance; high fibre content provides maximum physical strength. Therefore, the designers can combine these two elements to produce a satisfactorily reliable design. Similarly, they can also vary the mechanical properties by changing the directions of the fibres to resist a specific loads in a specific directions.

In spite of good performance of FRP materials in the applications of pressure vessels and piping systems over the last four decades, only a few research works [7, 8] can be found regarding the bolted FRP flange joints. In addition, standardization and the relevant design codes, which could be used as design guidelines for fabrication methods and dimensional considerations of bolted FRP flange joints, are inadequate. Currently, all design methods are modified from their counterpart of metallic design methods neglecting the composite flange behaviours, which are different from those of the metal flanges. Therefore, the use of currently available standards leads to additional challenges when applied to composite flange manufacturing process.

Therefore, the current research is aiming to develop a good manufacturing process of bolted glass fibre reinforced polymers (GFRP) flange joints using 2D fibreglass braid and vacuum infusion process (VIP). This included the design and manufacture of the required mould for the composite flange, which has a complex geometry. Experimental work has been carried out to identify the strength and the reliability of the manufactured flange joint. Two failure mechanisms have been examined; (1) the

standpoint of strength or stiffness (mechanical failure) and (2) failure from joint leakage. In order to maximize the performance and to understand the physics of failure, finite element analysis has also been developed for a detailed 3D model of the flange joint. The simulation has taken into account the orthotropy of the composite materials and the nonlinear behaviour of the rubber gaskets as well as fluid pressure penetration (FPP), which leads to the leakage pressure.

This chapter presents an introduction about this PhD project on the bolted GFRP flange joint for oil and gas applications.

## **1.2 Motivation of the research**

The main motivation of this research is to maximize the performance of the bolted FRP flange joints, which currently face many problems, and to reduce the materials cost of manufacturing the FRP flange. The main objectives of this research are:

- To design and manufacture a mould with high quality and performance
- To propose a new technique for manufacturing FRP flange, connecting it to the composite pipe and testing the joint's reliability through experiments.
- To develop a 3D model of the composite pipe joint that includes flange, pipe, gasket and fasteners and to perform FEA using ANSYS software.
- To validate the simulation results (strains and leakage pressure) with the experiments. This reduces both the costs and the time required for experimental investigations.
- To investigate the effect of the applied loads and the flange dimensions on the strain distributions, flange axial displacement, flange rotation and leakage pressure in the bolted GFRP flange joints and find the possibility of reducing some of these dimensions.

### 1.3 Methodology

This research is conducted by the methodology shown below:

- Designing and manufacturing the required mould for the composite flanges.
- Fabricating the composite flanges using glass fibre braid, polyester and vacuum infusion process and carrying out experiments to find out the fibre volume fraction and fibre direction in many places over the flange body.
- Assembling the pressure vessel components, which are composite flanges, pipe blind flanges and other, and conducting tests under various bolt and internal pressure loads.
- Manufacturing composite laminates using the same materials and the manufacturing process as used for the composite flange to conduct experiments such as bending, drilling and measuring the coefficient of friction between composite and rubber gaskets.
- Conducting compression test for the rubber gaskets to find out their non-linear behaviour during the loading and unloading conditions.
- Carrying out tensile tests for the used stainless steel bolts to find out the Young's modulus and comparing the strain readings of the fixed strain gauges with the Instron data as well as the theoretical results.
- Based on the experimental results, Helius composite software is used to calculate all the mechanical properties of the composite flange and the pipe.
- Finite element analysis (FEA) is used to simulate the GFRP joint system, which includes flange, pipe, adhesive bonding, fastener (bolt and washer) and rubber gasket.
- The fluid pressure penetration (leakage propagation) between the flange and the rubber gasket has been simulated using the contact element real constant (PPNC) criterion.

- Developing another FEA model and use the same boundary conditions and PPNC criterion for a metal flange, which has been studied experimentally and numerically by somebody else.
- Comparing the experimental results with the FEA result for the validation purposes.
- Numerically, studying the effects of the flange dimensions, the gasket thickness and the gasket material on the flange joint performance and investigate the possibility of reducing the manufacturing cost of the flange.



## **1.4 Structure of the thesis**

Chapter 1 presents general introduction about the PhD work.

Chapter 2 provides overview of metallic and composite flanges and related literature. Also, it includes the details about gaskets types, composite pipes, adhesive bonding, fasteners and composite drilling.

Chapter 3 reports the design parameters (variables and constants) and the comprehensive analytical approach of the ASME code, Section X, for the FRP bolted flange joint.

Chapter 4 provides the details about the manufacturing process of the composite flange including design and manufacture the mould, solving the manufacturing issues identified and assembly of all components to make the pressure vessel.

Chapter 5 describes tests that are needed to calculate all the mechanical properties of the composite flange in Helius composite (Autodesk) software. It also contains explanation about the data measurement equipment and the test rig.

Chapter 6 provides all details of the finite elements analysis models of the composite and the metal flange joints including the simulation of the fluid pressure penetration.

Chapter 7 compares the experimental and the numerical results to validate the FEA for using it in further investigations. In addition, it discusses details of the other FEA model for the metal flange and compares results with previous work.

Chapter 8 reports the effect of the flange dimensions and gasket thickness and material on the maximum flange axial, hoop and radial strains, flange axial displacement, flange rotation and the leakage pressure.

Chapter 9 summarizes the findings of this study and provides recommendations for the future work.

## 1.5 Outline of the research

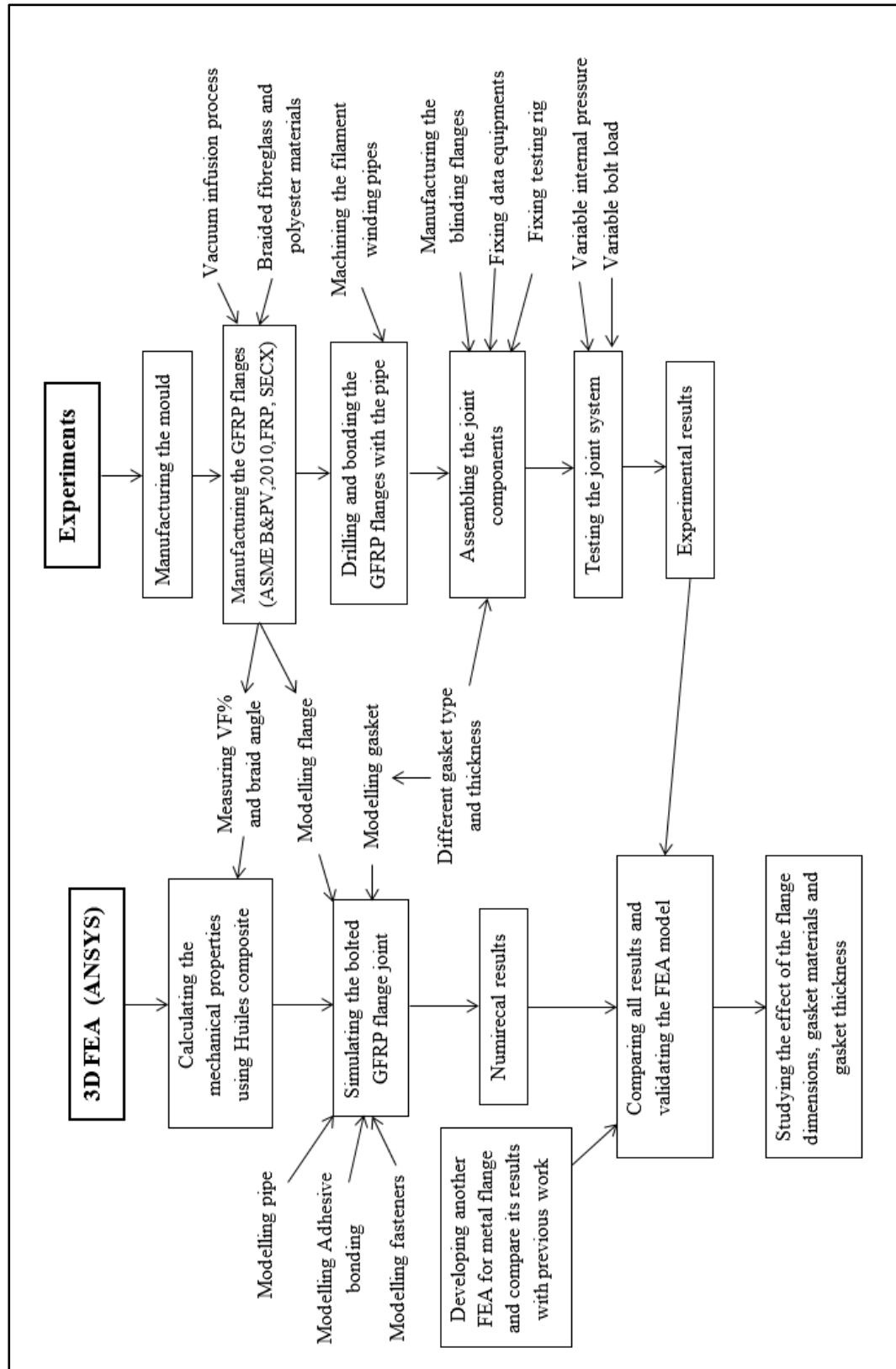


Fig. 1.1: The flow chart of the project

## 1.6 Skills development training attended

- Laser Safety Awareness Training, Plymouth University, 13 July 2018, UK.
- Introduction to teaching and learning (PGCAP711), Plymouth University, 7 Feb.-11 June 2018, UK
- Ph.D. course: “Fracture Mechanics for Laminated Composite Structures”, 13-17 Nov. 2017, Aalborg University, Denmark.
- GRAD school: Residential Development Programme for Postgraduate Researcher, 04-07 July 2017, Universities of the West of England, Plymouth and Bath Spa.
- ANSYS Fluent Turbulence Modelling, 15 - 18 May 2017, ANSYS Training Centre.
- ANSYS Fluent Combustion Modelling, 18 - 21 April 2017, ANSYS Training Centre.
- Introduction to ANSYS Fluent Meshing, 27 - 31 March 2017, ANSYS Training Centre.
- ANSYS Mechanical Rotordynamics, 20 - 23 March 2017, ANSYS Training Centre.
- Introduction to ANSYS Meshing, 16 - 19 Jan. 2017, ANSYS Training Centre.
- Introduction to ANSYS DesignModeler, 09 - 12 Jan. 2017, ANSYS Training Centre.
- ANSYS Mechanical User Programmable Features (UPFs), 12 - 14 Dec. 2016, ANSYS Training Centre.
- Introduction to ANSYS nCode DesignLife, 28 Nov. - 02 Dec. 2016, ANSYS Training Centre.
- Introduction to ANSYS LS-DYNA, 28 Nov. - 09 Dec. 2016, ANSYS Training Centre.
- Introductory to ANSYS Fluent, 17 - 27 Oct. 2016, ANSYS Training Centre.
- ANSYS CFX Multiphase, 17 - 26 Oct. 2016, ANSYS Training Centre.
- Introduction to ANSYS Explicit Dynamics, 30 Aug - 6 Sept. 2016, ANSYS Training Centre.
- ANSYS Mechanical Rigid Body Dynamics, 22 - 25 Aug. 2016, ANSYS Training Centre.

- ANSYS Mechanical Linear and Nonlinear Dynamics, 25 July-3 Aug. 2016, ANSYS Training Centre.
- Introduction ANSYS Mechanical, 11-22 July 2016, ANSYS Training Centre.
- Introduction to ANSYS CFX, 20 - 30 June 2016, ANSYS Training Centre.
- ANSYS Mechanical Heat Transfer, 06 –09 June 2016, ANSYS Training Centre.
- ANSYS Mechanical Material Nonlinearities, 06 –13 June 2016, ANSYS Training Centre.
- Introduction to ANSYS Composite PrepPost (ACP), 10-18 May 2016, ANSYS Training Centre.
- ANSYS Mechanical Advanced Connections, 21 April - 4 May 2016, ANSYS Training Centre.
- Introduction to ANSYS, 16 – 17 November, 2015, ANSYS Training Centre.
- Course MAT347 Composites Design and Manufacture at the Plymouth University by John Summerscales, 2015.
- Academic English for research student, Sep. 2014-March, 2015, Plymouth University, UK.

### 1.7 Publications work from this PhD work

- Aljuboury, M., Rizvi. Md, Grove S., Cullen, R., '' *Bolted flange joint made of glass fibre reinforced polymer (GFRP) for pipelines*'', The ASME 2018 Pressure Vessels and Piping Conference (PVP2018), 15-20 July 2018, Prague, Czech Republic. Available at: <http://proceedings.asmedigitalcollection.asme.org/proceeding.aspx?articleid=2711945>
- Aljuboury, M., Rizvi. Md, Grove S., Cullen, R., '' *Development of manufacturing a bolted flange joint from glass fibre braid reinforced polymer using a vacuum infusion process (VIP)*'', International Conference on Manufacturing of Advanced Composites (ICMAC 2018), 10-12 July 2018, Nottingham university, UK.
- Aljuboury, M., Rizvi. Md, Grove S., Cullen, R., '' *Stress analysis of bolted FRP flange connections under internal pressure*'', 5<sup>th</sup> PRIMaRE Conference, Bristol University 5-6 July 2018, UK.

- Aljuboury, M., Rizvi. Md, Grove S., Cullen, R., '' *Bolted flange joint made of glass fibre reinforced polymer (GFRP) for oil and gas applications*'', Postgraduate Society Research Showcase, Plymouth University, June 2018.
- Aljuboury, M., Rizvi. Md, Grove S., Cullen, R., '' *Bolted FRP flange joints for pipelines: A review of current practice and future challenges*'', IMechE, Part L: Journal of Materials: Design and Applications, April 2018. Available at: <http://journals.sagepub.com/doi/abs/10.1177/1464420718766563>
- Aljuboury, M., Rizvi. Md, Grove S., Cullen, R., '' *A numerical investigation of the sealing performance of a bolted GFRP flange joint with rubber gasket*'', Eleventh International Conference on Composite Science and Technology /ICCST/11 April 4–6, 2017, UAE.
- Aljuboury, M., Rizvi. Md, Grove S., Cullen, R., ''*Manufacturing glass fibre reinforced polymer (GFRP) bolted flange connections by using a vacuum infusion process*'', Eleventh International Conference on Composite Science and Technology /ICCST/11 April 4–6, 2017, UAE.
- Aljuboury, M., Rizvi. Md, Grove S., Cullen, R., ''*Manufacturing glass fibre reinforced polymer (GFRP) bolted flange connections by using a vacuum infusion process*'', Postgraduate Society Research Showcase, Plymouth University, March 2017.

### 1.7.1 Submitted journal articles

- Aljuboury, M., Rizvi. Md, Grove S., Cullen, R., '' *A numerical investigation of the sealing performance of a raised face metallic bolted flange joint* '', International Journal of Pressure Vessel and Piping, June 2017. Status: Under revision.
- Aljuboury, M., Rizvi. Md, Grove S., Cullen, R., '' *Bolted GFRP flange joints for pipelines: A design and manufacture*'', IMechE, Part B: Journal of Engineering and manufacture: Design and Applications, Nov. 2018. Status: Under revision.

# CHAPTER TWO

## LITERATURE REVIEW<sup>1</sup>

### 2.1 Introduction

Bolted flange joint (BFJ) refers to a structure that includes flange disc, hub, pipe, gasket and fasteners. Based on the geometry, flanges can be categorized into many types, which will be described in detail in the next section. Regardless of the type, flanges are fabricated using traditional materials, however, some of those can be manufactured from non-metallic materials such as FRP composites. The flanges that can be manufactured from both metallic and composite materials are full faced gasket flange and raised face flange. On the other hand, ring type gasket or O-ring gasket flange, ring gasket flange, tongue and groove flange, male and female flange so far cannot be manufactured using composite materials due to the complex shapes of these flanges near the contact faces. However, more studies are required to achieve these big challenges. Regarding the gaskets, which seal the matched flanges, they are divided into three types (metallic, semi-metallic and non-metallic gaskets) based on the materials. In addition, each one of these has different geometries and used for certain applications.

The chapter includes an overview of the BFJ, which are made of metallic and composite materials as well as the previous relevant research works.

---

<sup>1</sup> This chapter has been published as an article in IMechE Part L: Journal of Materials: Design and Applications [9].

## 2.2 Overview of metallic bolted flange joints

Based on the contact faces, bolted flanges are categorized into several types. The main purpose of these categorizations is to seat the sealing gaskets to meet the requirements of the design conditions, such as internal pressure and design temperature specified by ASME B16.5 [10] and B16.47 [11]. Among others, most common flanges are the full face gasket, ring gasket or O-ring gasket, raised face, male-female and tongue-groove flanges. All these flanges, will be discussed in this chapter.

**Full faced gasket flanges (FFG)**, are also known as full faced gasket (FFG) flanges as the entire contact faces are covered by a gasket (Fig. 2.1.a). Therefore, the gasket will sit on the same plane as the bolting circle. The FFG flange provides a good resistance against the bending moment produced by the bolt-up force. However, this type of flange with full face gasket requires a high bolting force to maintain the seal. This is due to the large area of contact, which needs more pressure to deform the gasket into the irregularities within the contact areas of the mating flange faces. Thus, the FFG flange is preferred for low-pressure applications with a soft gasket. In addition, it is most common to use FRP materials or brittle materials such as cast iron to produce this type of flange. These materials provide resistance to bending moments produced by the flange rotation [5].

**Ring Type Joints (RTJ)**, as shown in Fig. 2.1.b, are also called O-ring gasket flange have two identical grooves cut into flanges faces. A soft metal (self-energizing) octagonal or oval gaskets is placed between these identical grooves. By applying compressive stress through bolt force, the “soft” metal gasket deforms into the grooves of the flanges, which are made of materials harder than the gasket, and creates a very tight and efficient seal. In addition, the metal-to-metal contact takes place outside of the bolt circle so that the rotation and the bending moment of the flange are very limited. However, high fabrication accuracy is required for maintaining the dimensions of the gasket grooves in order to achieve the required tightness. Ring type joints are used for high pressure and/or high-temperature applications such as power plant, petroleum, petrochemical and refineries [12]. Therefore, this type of flange is rarely manufactured with FRP materials [13].

**Flat ring gasket flanges** have physical geometry similar to the FFG flange, but both the gasket shape and the applications are different. This type of flange uses a flat ring gasket that sits at the inside area of the bolt circle. Therefore, no contact occurs between the flanges outside the bolt circle and this leads to rotation of the flange when the connection is tightened. This rotation also produces high bending stresses at the hub-flange intersections. These bending (axial) stresses with hubless flanges (Fig. 2.1.c1) are higher than those with the hubbed flanges (Fig. 2.1.c2) [8]. This difference is due to the additional materials that resist rotation in the hubbed flange. However, these flanges are simple in shape and easy to manufacture. Both metallic and the non-metallic gaskets are used with this type of flange. The main use of the ring gasket flange can be found in low and medium pressure applications.

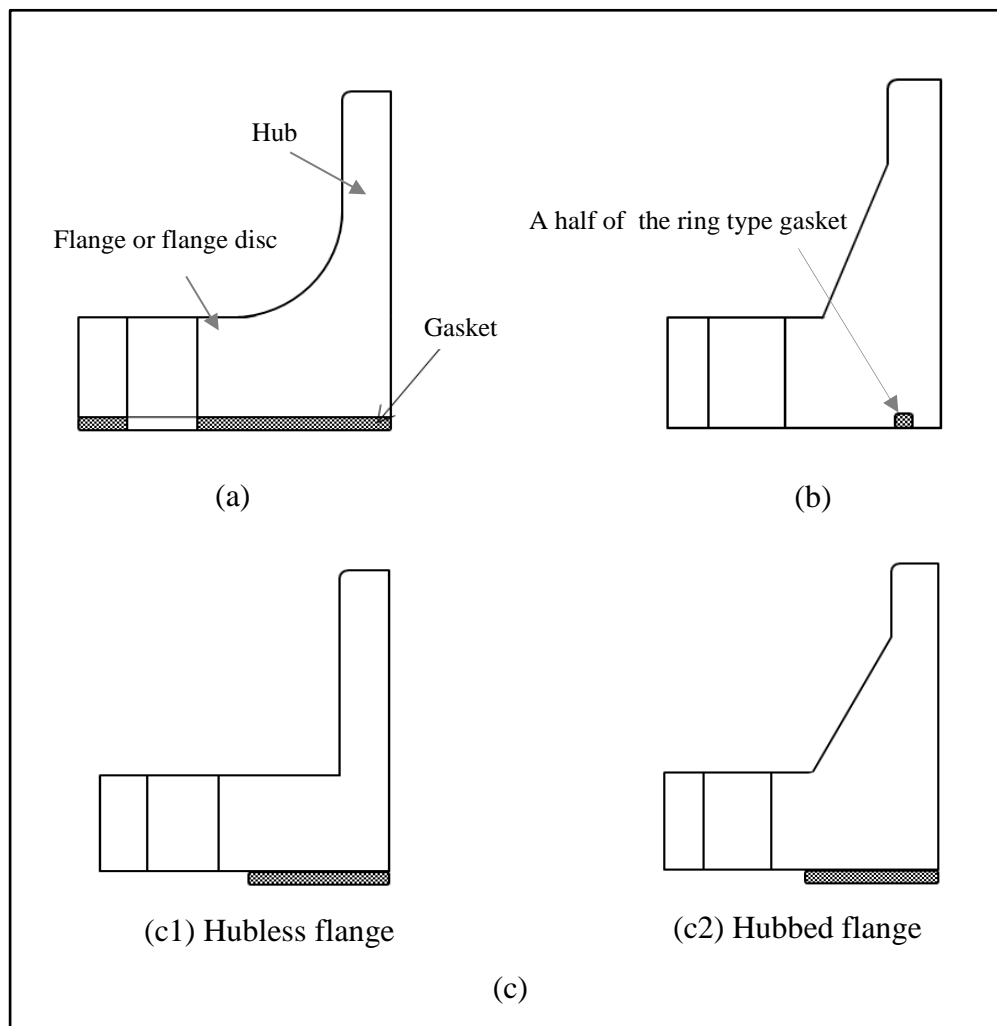


Fig. 2.1: Bolted flange (a) Full face gasket flange (b) Ring type joint  
(c) Flat ring gasket flange



***Raised face flanges*** (Fig. 2.2.a) have the area inside the bolt circle higher than the bolting surface area. This is to reduce the contact area between the flange and the gasket and to achieve high pressures on a small gasket area. Consequently, the pressure containment capability of the joint increases but a high flange rotation, which is considered one of the disadvantages of this flange, is produced in the hub region due to the moment of the bolt force, and hence no flange contact outside the bolt circle is established [13]. Nevertheless, many types of gaskets are used with this type of flange such as flat ring, spiral wound and double-jacketed. Raised face flanges are very popular for applications that have medium and low-pressure service.

***Tongue and groove flanges*** have matched faces. One of the flange faces has a rib (tongue) machined on its face, while the mating flange face has a groove (Fig. 2.2.b). The gasket is placed onto the groove and it cannot be pushed to the outside due to the hydrostatic force produced by the internal pressure [13]. The main difference between this flange and the O-ring gasket flange is that it has a raised ring on one flange face and a groove on the other face of the mating flange, whereas the O-ring gasket flange has two identical grooves on each matching flange face [13]. Advantages include self-alignment, evenly distributed compressive forces on the gasket, less erosive or corrosive contacts of the gasket with the fluid in the pipe and better sealing performance. However, the replacement of the gasket is very difficult for some applications and this leads to damage to the flange especially for high-temperature applications. Also, this type of flange incurs high manufacturing costs [12]. The main applications are pump covers, valve bonnets, toxic fluids and explosives.

***Male and female flanges***, the male and female flanges have two matched faces. One of the mating flanges named as male flange has a ring area that is extruded from its contact face whereas the other mating flange names as female flange has a groove machined into its face. For this type of flange, the gasket is squeezed into a narrow place and is prevented from moving to outside by the outer surfaces of the female flange as shown in Fig. 2.2.c. This flange differs from the tongue and groove flange as well as the raised face flange. This is because both the inside diameter of the extruded area of the extruded ring and the depression matched extend into the flange base. This retains the gasket on its outer diameter for this type of flange and makes it

distinct from the tongue and groove flange as well as the raised face flange [13]. This type of flange is easy to assemble and it can be used in any position. Its sealing is very good and better than the raised face flange. Thus it is used for the service pressures that is higher than those used with the raised face flange but lower than those used with the tongue and groove flange. This type of flange is also used with the heat exchanger shell to channel and cover flanges.

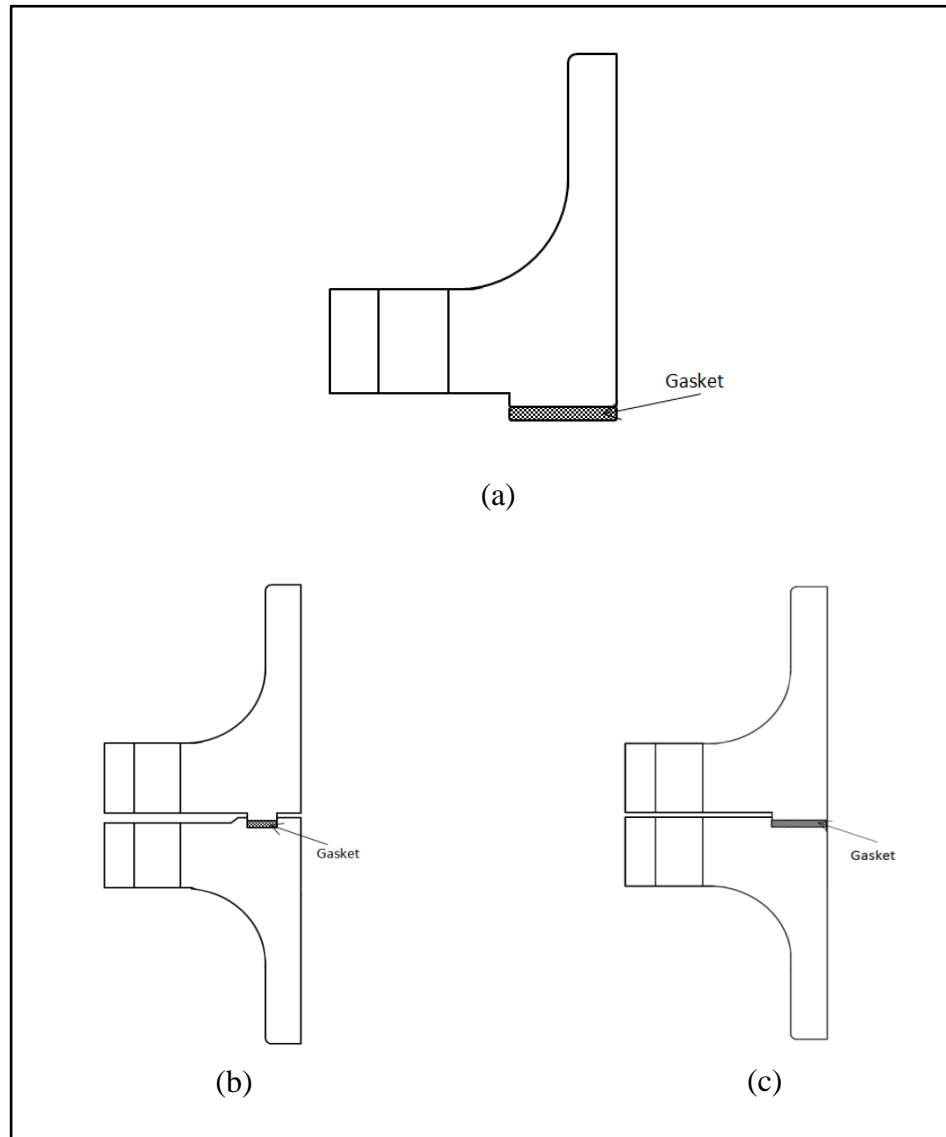


Fig. 2.2: Metallic flange (a) Raised face flange (b) Tongue and groove flange  
(c) Male and Female flange

## 2.3 Overview of composite bolted flange joints

Bolted flange joints made of fibre reinforced plastic (FRP) are widely used in many industries such as chemical, power plants, petrochemical and offshore oil and gas industries. This is because the systems in these industries usually include pumps, valves and other fittings that require periodic removal for maintenance. The FRP bolted flanges were developed in response to significant corrosion problems with either metallic and non-metallic pipes [14]. In addition, the use of composite flanges to connect composite pipe helps to avoid the mismatches during thermal expansion of metal connecting pieces and composite pipes [15].

In this study, full face gasket (FFG) flange has been chosen for study. As the gasket covers all its face, the FFG flange has a good ability to reduce or minimize the applied bending moment. It has therefore become attractive to designers, especially for use with brittle materials such as cast iron, glass, porcelain and other ceramic materials [16].

### 2.3.1 Materials system

#### 2.3.1.1 Matrix Materials

The main purpose of the matrix in a composite material is to support the fibres and to transfer the load between them. In the through-thickness direction of composites (at right angles to the plane of the reinforcement), mechanical properties are very much matrix dominated, and designers must pay particular attention to transverse interlaminar shear stresses. These matrix-dependent properties are also affected by the operating temperatures. Moreover, the matrix protects the fibres from the environment such as water absorption, chemical or acidic attack as well as mechanical abrasion. Generally, matrix materials can be polymer, metals or ceramic. Due to the low costs and the ease of manufacturing, thermosetting polymer matrices (such as polyester, epoxy and vinylester) are commonly used in composites structures [17].

**Polyester resins**, polyester resins are widely used in many applications that require good resistance against water or chemical attack as well as good weather ability characteristics such as tanks, pipes, liners, automobiles and aircrafts [7, 17-20].

Polyester resins are; low in cost, fast in cure, have relatively high shrinkage [18] and good capability of releasing the mould after curing. In this present study, these features of polyester helped to remove the GRP flanges from the mould after curing. In addition, they have high insulation, high UV resistance and moderate strength. Moreover, polyester resins are very versatile material. At room temperature, the liquid polymer that is available at varying viscosity is stable for months or even years. In spite of this great stability, it can be triggered to cure within few minutes by adding a peroxide catalyst [17, 21, 22]. Considering the above advantages, polyester resin has been chosen as a matrix to fabricate the GRP flange in the present study.

*Epoxy resins* provide higher mechanical performance, good resistance against corrosion and chemical attack and lower water absorption compared to other commonly-available resins [7, 17, 18]. They are used with various fibres reinforcement for many composite structures such as aircraft, missiles, boats and automotive. In addition, epoxy resins are used as adhesives, caulking compounds, casting compounds, sealants, vanishes and paints. Epoxies are cured quickly and easily at temperatures between 5°C and 150°C (depending on the curing agent) without releasing any volatiles. This results in low shrinkage (1.2% - 4% by volume), and hence helps to achieve accurate dimensions of fabricated structures. However, epoxy resins are more expensive and care is required with regard to mould release. [19, 21].

*Vinyl ester resins* are widely used in chemical-resistant FRP equipment such as pipe, ducts, scrubbers, flue stocks and storage tanks, which represent their largest commercial usage of Vinylester [19]. This type of resin has excellent resistance to acid, base, solvents, hypochlorites and peroxides and can be used in a neat form (e.g. no diluent). Moreover, Vinylester resins are superior to the polyester resins due to low viscosity and fast curing as well as are superior to the epoxy resins due to better chemical resistance and tensile strength. Vinylester resins have less volumetric shrinkage upon curing compared to polyester resins but the shrinkage is greater than epoxy resins. The cost of Vinylester resin lies between the costs of epoxy and polyester resins. However, Vinylester resins exhibit only moderate adhesive strength because of high volumetric shrinkage values [7, 17, 18].

### 2.3.2 Fibres reinforcement

**Glass Fibres**, glass fibres are produced by melting glass at/around a temperature of 1200°C and extruding it through a large number of holes that exist in a spinneret. The diameter of those holes is usually 1 or 2 mm and between 5 to 15 µm is the diameter of the glass filaments that are drowned around a mandrel. Glass fibres are widely used to reinforcement for general composites due to better hardness, corrosion resistance and inertness properties. Furthermore, they are flexible, light weight and cheaper than most other relatively high modulus fibres. These characteristics have made glass fibres the most common type of fibre reinforced used in low cost industrial applications. Glass fibres are divided into five types. E-glass fibres are preferred where high tensile strength, good corrosion or chemical resistance and low costs are required. S and R glass fibres are used where enhanced mechanical properties are required but the cost is three to four times higher than that of E-glass fibres. C-glass fibres are used for corrosion resistance in an acid environment. D-glass fibres are used for dielectric properties in electrical applications [17, 23]. In this study, E - glass fibres have been used due to the advantages discussed earlier.

**Carbon fibres**, carbon fibres are generally fabricated using two types of procedures: textile procedures which is named polyacrylonitrile (PAN) and pitch precursors. Generally, carbon fibres are lightweight, strong and have high tensile strength-weight ratio as well as high tensile modulus-weight ratio. Unlike glass fibres, these are available with various tensile modulus and strength values. Therefore, carbon fibres are dominant in the aerospace applications where the high performance and the weight saving are considered as more critical than the costs. In addition, carbon fibres have good fatigue strength, high thermal conductivity which is even higher than that of copper and have very low coefficient of linear thermal expansions (CTE) All together, those properties provide dimensional stability in applications that have a large range of variations in temperature such as aerospace applications. In contrast, carbon fibres have low impact resistance, low strain-to-failure and high electrical conductivity which may cause electric shock or short-circuiting in unprotected electrical machinery [17, 21].

**Aramid fibres**, aramid fibres are man-made organic polymer (an aromatic polyamide) manufactured by extruding an acidic solution of a proprietary precursor (a polycondensation product of terephthaloyl chloride and p-phenylene diamine) from a spinneret. Aramid fibres, which are also known as Kevlar, absorb energy during failure. As a result, these fibres have good resistances to impact and ballistic. In addition, these fibres have low density and high strength which contribute to achieve high strength to weight and high modulus to weight ratios. Hence, these fibres are ideal for the aircraft and for body armor [17, 18, 21]. Furthermore, Aramid fibres have very low thermal conductivity and very high coefficient of vibration damping. There are several disadvantages of Aramid fibres. For example: lower resistance to compression, temperature dependent mechanical properties and the fibre loses about 75-80% of its tensile strength when the environmental temperature is increased from a room temperature to 177°C. Therefore, these fibres are not preferred for high temperature applications. Moreover, Aramid fibres are very sensitive to ultraviolet lights and a significant percentage of tensile strength is lost during prolonged direct exposures to the sun. The most common commercially available Aramid fibres are known as Kevlar 29, Kevlar 49 and Kevlar 149.

### 2.3.3 Manufacturing techniques of bolted GFRP flange

There are various fabrication processes to combine fibre reinforcements and resins for producing composite components or structures. The American Society of Mechanical Engineers (ASME) [24] has recommended four methods for producing GRP flanges: contact moulding, filament-winding, resin transfer moulding and vacuum infusion process.

**Contact moulding** or hand lay-up is a simple, low cost process and suitable for large structures. This is an open moulding process and only one male or female mould is used. The layers of fibres (in the form of mat, woven roving and cloth) impregnated with resin are placed inside the mould and compacted using a roller to eliminate air bubbles and to facilitate uniform resin distribution. This process is repeated many times until the required thickness is reached. Usually, curing of hand lay-up is done at ambient temperature but heating could be applied to accelerate the process. It is a slow process (up to 500 units per year per mould) [7, 17, 23, 25].

**Filament winding** is primarily used for hollow products such as pipes, pillars, storage tank and containers. This is done by impregnating continuous fibre reinforcement with resin, then winding onto a rotating mandrel using a delivery eye. The delivery eye moves back and forth along the axis of the mandrel, so the angle of the fibre orientation and the thickness of the composite laminate are both dependent on the mandrel's rotational speed and the linear speed of the delivery eye. Various physical strengths can be obtained by varying the winding angle of the fibre. Most commercial companies prefer to use this process to fabricate GRP flange due to its high production rate (up to 500 kg of composites per day) [17, 18, 25].

**Resin transfer moulding (RTM)** injects pre-catalysed resin (at relatively low pressure) into a matched mould cavity containing fibre reinforcement. The dimensions of the product are directly controlled by the tool cavity thus a moulding of consistent shape and weight can be obtained. The advantages of this technique are: (1) the fibre volume fraction can be controlled very well; (2) usually very consistent mechanical properties; (3) a wide variety of resin systems and fibre reinforcements can be applied; and (4) very complex components can be produced. However, matched moulds with high dimensional accuracy as well as higher capital costs of equipment and moulds are required [26-28].

**Vacuum infusion moulding (VIP)**, this process is similar to the contact moulding process. The only difference is that a uniform pressure is applied in this method on the parts before curing to improve the consolidation of fibre, to remove the trapped air and volatiles. As shown in Fig. 2.3, this pressure is generated by drawing a vacuum in the space between the parts once a sheet of soft plastic is placed over it and sealed at the edges. Before applying the vacuum, release film or release agent is used to avoid the sticking between the parts and the mould. Also, the layers of fibre are laid up onto the tool (mould) with peel ply and the resin distribution medium. The porous of the peel ply helps to prevent sticking between the laminate and the resin distribution medium and also leaves an imprint or pattern of the surface to improve adhesive bonding. The resin distribution medium works as channels of air and volatiles and helps distributing the resin injected through inlet port. The main advantage of this method is to achieve high fibre content with low void numbers. This method is also suitable for production of large, high quality, lower cost

composite parts. However, this method creates health and safety issues as the volatiles are emitted during curing. [25, 26, 29]. As the advantages of the vacuum moulding method supersedes the disadvantages, this method has been chosen to fabricate the GFRP flange in the present study. In addition, this method can be used for commercial production of the composite flange but it requires braiding machine, which expedites the lay-up of the fabric. In this study, the fabric is laid-up manually due to the machine is not exist in the lab.

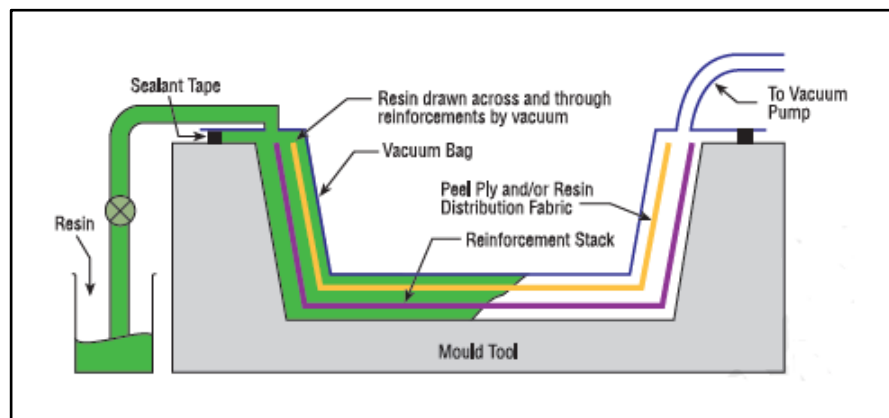


Fig. 2.3: Vacuum bagging process [18]

### 2.3.4 Use of Braided fabric

Two-dimensional braids are available in two types: (1) biaxial and (2) triaxial. Biaxial braid is the most commonly used and is produced using two sets of yarn carriers that rotate around the braiding axis. One of these two sets rotates in clockwise direction whereas the other set moves to the opposite direction creating a single layer of braided fabric [30]. Triaxial braid is involves a third yarn carrier which adds longitudinal yarns to the biaxial interlacing yarns (Fig. 2.4) [31].

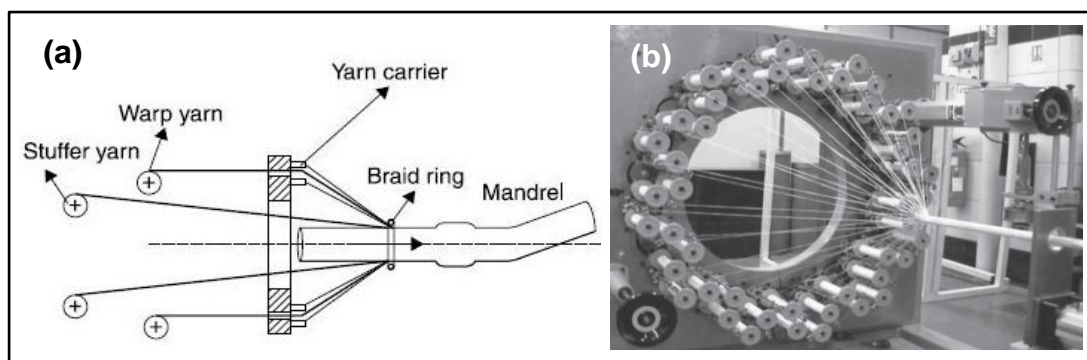


Fig. 2.4: Mandrel over-braiding [31]



Biaxial yarn angles can be varied from  $25^\circ$  to  $75^\circ$  [18] so the braid can be dropped over the top of mandrels that vary in cross-sectional shapes and/or dimensions along their length without needing to cut the yarn (Fig. 2.5). The attachment points or holes can be preformed into the fabric to reduce the steps in component finishing and to improve the mechanical performance of the components. This is because biaxial braid helps to avoid cutting the fibre reinforcements at the attachment site [31]. In contrast, triaxial braid cannot be used with a mandrel which has varying cross-sectional areas as the axial/warp yarn locks the diameter of the braid and prevents the internal expansion and contraction.

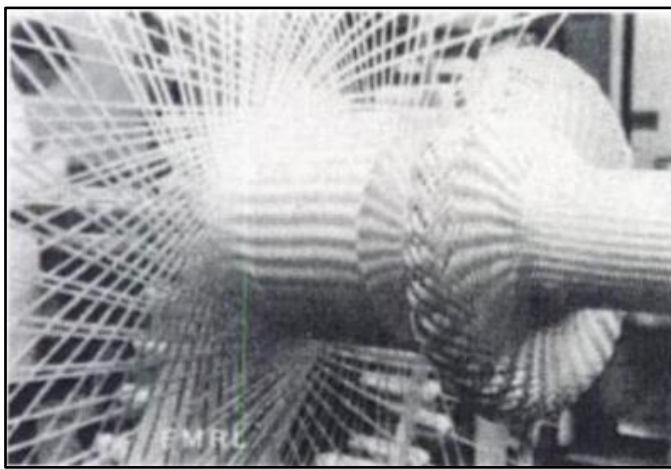


Fig. 2.5: Circular braiding around a complex shape [32]

A previous study [33] has indicated that the most common types of failures in commercially available GRP flanges manufactured by hand lay-up or filament winding processes occur at the flange-hub intersections, due to the discontinuity of fibres in this region (Fig. 2.6). Therefore, in this study, biaxial braid has been chosen to manufacture the GFRP flange joint.



Fig. 2.6: Flange failure at the flange neck [33]

## 2.4 Performance of metallic bolted flange joints

The flat face flange has been widely used in the early years of the process industries. At that time, cast iron was commonly used to manufacture the flange. Without having any existing standards, full face (FF) flanges were manufactured and widely used because the gasket covers a large area of its face and this reduces the undue stress on the flange. The FF flanges were usually used to connect pipe-to-pipe, pipe to pump or any other equipment such as pressure vessels at various levels of the pressure and temperature.

When the use of flanges started to grow, wrought-iron rolled plate replaced cast iron. The new method used a rolled angle section which was then riveted to the vessel's shell. When the welding technique was introduced to join pipes, tanks and pressure vessels at high-pressure levels, manufacturers preferred to use forged-steel materials to produce FF flanges.

To date, many theories, methods, and standards such as ASME, JIS, BS, CODA and DIN have been developed to make the design of the flange viable and reliable. Most of these standards has been built up based on the structural geometry and applied loads. Fig. 2.7 shows analysing of the applied loads on the flange. The following sections will discuss in detail the factors that affect the performance of metallic flange joints.

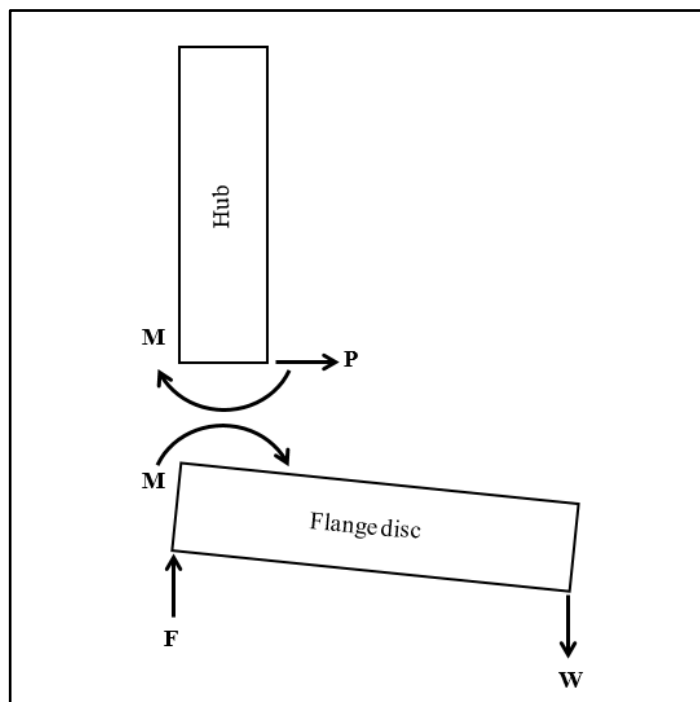


Fig. 2.7: Loading analysis of the flange

### **2.4.1 Effects of nominal flange diameter**

The variation of the nominal diameter of bolted flange connection has an effect on the flange performance and is considered as a key to optimise the design. Omiya et al. [34] has studied stress analysis of flange joint using Elasto-Plastic (EP) FEA and ASME method. They have found that the hub stress with larger diameter is smaller than that with a smaller diameter. However, they have found opposite trends when the ASME design method has been used. Also, a variation in the axial bolt force (load factor) was observed as positive with the smaller nominal diameter and as negative with the larger nominal diameter. According to the EP-FEA analysis based on the JIS B 2490 standards, leakage of gas was predicted. It has been seen that the sealing performance of smaller nominal diameter with a non-asbestos gasket was better than that of larger nominal diameter with an asbestos gasket. Naser [35] has studied the influence of the nominal diameter of the bolted flange. The study has shown that all the stresses in tangential flange, hoop and longitudinal hub have decreased with the increase in the nominal flange diameter.

### **2.4.2 Effects of flange thickness**

The most important factors that have significant effects on the performance of the flange and its optimum design are the flange geometry and the dimensions. The variation of flange thickness has been studied by many researchers. Nash et al [36] has developed a finite element model of a full face metal-to-metal tapered-hub flange. They found that the flange thickness had a large effect on the radial flange stress, but had no significant effect on either the longitudinal or the tangential hub stresses. In addition, they have compared the results with ASME and PD5500 codes and found that the flange radial stress of these codes was conservative (i.e. safe, since they predict high stress) whereas the flange tangential stress was not conservative (i.e. unsafe) when compared to the FEA results. Naser [35] performed analytical, FE modelling and experimental investigations for the bolted flange connection and it has been observed that the thickness has a positive effect on the flange stress (hoop and radial), which is decreased with the decrease in the flange thickness. The study also proposed a new design method for bolted flanges.

### **2.4.3 Effects of hub thickness**

Stress concentration at the hub/flange intersection due to flange bending is one of the important problems that probably lead to failure of the flanges. A number of studies have focused on this problem and tried to solve it by varying the hub thickness. Naser [35] studied the relationship between hub thickness and flange stress (hoop and radial). It has been claimed that the flange hoop stress is increased but the flange radial stress is decreased with the increase in the hub thickness.

### **2.4.4 Effects of hub length**

Hub length plays an important role for maximizing the bolted flange design because of its influence on the stresses of the joint system, especially, for the hub stress and for the strength of the pipe-flange adhesive bonded connection. Nash et al [36] stated that the hub longitudinal stress is reduced significantly as the hub length is increased but the flange radial stress is almost independent of the hub length. It has also been observed that the flange tangential stress is reduced slightly as the hub length is increased.

### **2.4.5 Effects of flange rotation**

Applying bolt load and internal pressure together tend to bend the flange and cause rotation. This generates a deformation of the gasket accompanied by uneven compression which has a significant effect on the sealing performance. Shoji and Nagata [37] conducted a comparison study of raised face bolted flange joint with nonlinear gasket using a 2D axisymmetric and 3D FE (finite element) models. The results of the numerical simulations indicate that the flange rotation is larger in pressurized condition for both 2D and 3D models. Furthermore, they have noted that the modelling of bolt holes in 3D has no significant effect on the results.

The influence of variation in taper angle (different flange's surface profiles), flange thickness and bolt preload were studied by Abid and Nash [38] using two-dimensional axisymmetric model. They found that the highest values of longitudinal, radial and tangential stresses are at the hub/flange intersection, at bolt circle diameter and at inside diameter, respectively. The maximum longitudinal stress was recorded for the positive taper angle. The highest value of radial stress

was observed for the negative taper angle. In addition, the tangential stress is increased with an increase in the flange thickness for positive angles, but it is decreased for negative and no taper angles. It has been observed that the longitudinal stress is decreased with an increase in the flange thickness up to 20 mm and then becomes constant above 20 mm in all three flange profiles. In contrast, the flange rotation is reduced as flange thickness is increased. Other researchers [39, 40] have observed that the flange rotation is decreased by increasing the temperature of the joint system.

#### **2.4.6 Effects of thermal loading**

In high temperature applications, the effects of thermal loading (internal fluid operating temperature) should be taken into account in the analysis of the structural integrity and sealing ability for the bolted flange joint. Unfortunately, many the current codes and standards for flange joints do not account for the influence of temperature [39, 41]. Abid [39] and Abid and Ullah [40] developed a 3D nonlinear FE model to investigate bolted flange joint strength and sealing capacity under combined internal pressure and different steady-state thermal loadings. The results indicated that both the sealing and the strength are greatly influenced by the thermal load. The radial variation of the temperature distribution through the flange and the gasket is greater in the hub because the flange ring works as a cooling fin. Apart from bolt axial stress, the stresses of the flange, bolt and gasket decreased by applying the internal pressure and all the stresses decrease further with additional thermal loads. However, the internal pressure does not affect the axial bolt stress when the thermal load is decreased. Guruchannabasavaiah et. al [42] carried out a non-linear finite element analysis to study the effect of internal fluid temperature and bolt load on the gasket sealing between a flange and blind flange in a pressure vessel. The results showed that the vertical deformation in the blind flange increased with both the bolt load and thermal load and the maximum stress intensity was affected significantly as bolt load increased. In addition, the contact stress between the gasket and the flange interfaces was greatly increased by increasing the bolt load but reduced rapidly as thermal load is applied. Therefore, a gap occurs at the lower values of the applied bolt force.

### 2.4.7 Effects of material's stiffness

Sawa et al [1] have studied the influence of the material stiffness of the hub, flange and gasket ( $E_1$ ,  $E_2$  and  $E_3$ , respectively) as well as gasket thickness. A 3D theory of elasticity was used to analyse the distribution of the contact stress which dictates the sealing performance. The results revealed that the distribution of the contact stress tends to be uniform as the ratio of  $E_1/E_3$  and the thickness both are increased. Also, the gasket seating width and the moment arm were both increased by increasing both the ratio of  $E_1/E_3$  and the thickness of the gasket, whereas it has been considered constant in JIS and ASME standards. On the other hand, the hub stress is increased as the internal pressure and the thickness of the gasket both are increased and the stress for aluminium gasket was larger than that of the mild steel gasket.

### 2.4.8 Effects of bolt preload

To avoid bolt failure during the operating condition, it is necessary to understand the relationship between the axial bolt force and the internal pressure. The bolt load has been calculated during bolt up or the operating conditions in many standards or codes such as EN1591-1 [43], ASME PCC-1-2013 Appendix O [44] and the ASME Boiler and Pressure Vessel Code, section X [24]. Nash et al. [36] found that the hub longitudinal stress was largely affected by the bolt preload, but the flange radial stress was slightly influenced and the maximum flange tangential bending stress was almost independent of the bolt loads. On the other hand, increasing the pre-stress bolts has a positive effect on the longitudinal displacement to prevent the leakage. Omiya et al. [34] proposed a new method of calculating the preload bolt by taking into account the allowable leak rate and the scattered bolt preloads. In addition, previous studies [41,42] have clarified that the internal pressure has insignificant influence on the pre-bolt load, in contrast, the maximum allowable internal pressure largely depends on the axial bolt force [1, 45]. Furthermore, other researchers have commented that the bolt load is affected by the temperature of the internal fluid due to different thermal expansion values of the bolt flange and gasket [39, 40]. Zahavi [46] has conducted nonlinear FEA analysis for bolted flange connections by taking into account the changes in the geometry and the friction between flange-gasket faces subjected to the loads to increase the accuracy of the results obtained for bolt force and to accurately predict the leakage point. Moreover, Rotscher diagram has

been used and the results have been compared with the experimental results from other published papers. In the study, it was noted that the incremental bolt force was almost independent on the internal pressure and a good agreement could be found between of the compared results.

#### **2.4.9 Effects of bolt spacing**

Do et al [47] have investigated the impact of bolt spacing on the circumferential distribution of gasket contact stress in bolted flange joints. This study [48] has applied an analytical approach which was developed based on the theory of circular beam on elastic foundation as well as a finite element based numerical method together with an analytical models developed by Koves. Two bolted heat exchanger (HE) flange joints with various bolt dimension and bolt numbers were studied. One of the flanges was 24 inch HE flange and the other was 52 inch HE flange. Also, they have studied the influence of the gasket modulus. The results have indicated that the bolt spacing has a great effect on the circumferential gasket contact stress. It has also been found that both the flange thickness and the stiffness of the gasket have a significant influence on the stress distribution.

#### **2.4.10 2D Axisymmetric and 3D FE modelling of the flange**

In order to save time and data volume, many studies have carried out the comparisons between 2D axisymmetric and 3D FE analyses. Hwang and Stallings [49] have performed a comparison study between 2D axisymmetric finite element model and a 3D solid finite element model for the bolted flange connections. This study has applied axisymmetric and non-axisymmetric loadings for both 2D and 3D models and non-axisymmetric bolt pretensions for 3D model only. Both the bending and the shear forces were unevenly distributed and both the torque and the axial forces were evenly applied on the top boundary surfaces of the pipe section. The results have indicated that the 2D axisymmetric model provides accurate results with axisymmetric loading. When non-axisymmetric bolt pretension is applied, the differences in results between the 2D and the 3D models were found between -1 and + 1 % in the pipe sections and between -3 and + 21% in the joint sections. Approximately 35% variation in results between 2D and 3D models was observed in



the pipe sections for the non-axisymmetric loading representing the operating conditions.

#### **2.4.11 Considerations for FRP flanges**

Most of the above parameters are still valid for the FRP bolted flange but the natural behaviour of the composite materials should be taken into account by the designers. These parameter are the orthotropy of the FRP material, which can be used to reinforce the composite in the direction that is subjected to high loads, the orthotropic thermal conductivity, the range of the working temperature and others, which some of them will be mentioned in next section. Therefore, in this study, some of the above parameters will be selected to investigate their effect on the performance of the GRP flange joints.

### **2.5 Published research on Composite flange joints**

A review of literature reveals that only a few studies have focused on composite flange joints. Tao et al. [15] investigated the development of connection between carbon fibre poles and advanced composite material flanges rather than the traditional flanges manufactured by aviation aluminium alloy in stratosphere truss structure. A Toray T700S–12K carbon fibre in three-dimensional full five directional braiding technology and tri-functioned epoxy resin TDE - 85# were used to manufacture the flange through RTM (resin transfer moulding) process. FEA has been applied for the numerical analysis. The results reveal that the joint of carbon fibre poles with the carbon-fibre composite flange performed better than the aviation aluminium alloy flange under the same operating conditions.

Sanjay et al. [50] have conducted analytical stress analyses of a non-gasket composite flange and a metallic flange. They have also conducted finite element analysis for carbon-epoxy composite flange to calculate the radial and the axial stresses. Both flanges were subjected to internal pressure of 15.32 MPa. The results show that the composite flange has better performance compared to the metallic flange, and the fibre orientations should be [0/45] and [0/60] to ensure the best performances.



Whitfield et al. [51] carried out both numerical and experimental studies for creep and unsymmetrical shrinkage during the post-cure of GFRP pipe flange manufactured by hand lay-up method. Chopped strand mat fibre and Derakane Momentum 411-350 vinylester resin and a steel mould have been used for manufacturing the flange. The steel mould represented the inside dimensions of the flange. A number of strain gauges were embedded during lamination between the layers and on the outer surfaces. From the investigations, they have noted that the correlations between spring back results are poor but for strain, results are good. The authors listed two possible reasons, firstly, due to the thermal stress related creep in the resin at the elevated temperature during post-cure and secondly, various cure profiles have been applied at various stages of lamination process. Sun [7] has studied the FRP bolted flange connections. Analytical approach using classical and shear deformable laminated plate and shell theory as well as finite element analysis have been carried out for identical flanges. An experimental investigation has been carried out for non-identical flanges (e.g. blind flange). E glass woven roving and mat, and Vinylester resin were used to manufacture the flanges along with two types of gaskets (rubber and asbestos). A good agreement has been found between the analytical and the numerical results.

Estrada and Parsons [8, 52] have investigated the strength and the leakage of a modified glass fibre reinforced plastic (GFRP) stub flange joint by using three-dimensional analysis and axisymmetric finite element models. It has been found that over three-quarters of the contact between the gasket and the flange are lost, however, the pressure in the remaining contact portion is greater than the internal pressure. Most of the contact between the hub and the stub has been lost due to the stub rotation whereas the pressure remains almost uniform in the circumferential direction except at the ends where the contact pressure is higher on the sides of the bolts.

Kurz [53] performed analytical, experimental and numerical investigations on the design of floating type bolted flange connections (better known as Loose Flange) made of GRP materials capable of working at temperatures up to 80 °C in chemical industries. Various types of gaskets made of rubber (EPDM) and polytetrafluoroethylene (PTFE) were used to check the performances of the gaskets with GRP bolted flange at that elevated temperature. It has been found that both the PTFE-gasket and PTEF-gasket with diffusion barrier perform better than EBDM-

gaskets with sufficient tightness to achieve the leak rate criterion of the TA Luft and are capable of tolerating the creep relaxation. In terms of the design analysis of other parts of the components, the bolt-force has been decreased with heating up to 80 °C but bending occurred at the top surface of loose flange between bolts in the circumferential direction. It has also been noted that the loose flange rotates due to the moment. The results of analytical, experimental and FEA simulations all have shown good agreements with each other.

Kittel [54] have studied the optimisation of GRP-Loose flange joints. Two models including PTFE gaskets have been used to simulate the optimisation of material properties and geometric shapes. An evolutionary algorithm has been used for the optimisation. They have observed that a number of parameters such as thickness of flat washer, height of collar and number of materials in lower layer have no influence on the characteristics of the flange connection. In contrast, other parameters such as type of screw, width of flat washer, materials of upper layer and the thickness of the loose flange have a large effects on the performance of the flange connection.

Fangueiro [55] has performed experimental investigations on the development of fibrous preforms of FRP T-pipe connections. 3D weft-knitted fleecy fabrics with different structures such as fleece yarn linear, average ground yarn and average fleece yarn have been tested to optimize the mechanical properties. Glass fibre and polyester resin were used with RTM to manufacture the T-tube connection. The results obtained from the tests indicate that the sample PA Glass 544 Tex exhibit the best performance to manufacture the T-connection with 43% fibre mass fraction and this is close to the desired value of 40%.

## **2.6 Research gap and justification of the project**

As shown earlier and during the recent decades, a few studies have focused on the fibre reinforced polymer bolted flange joint. In 1997, Estrada [8] studied the design and analysis of a fibre reinforced plastic joint for filament winding pipes using finite element analysis. Later in 1999, Estrada and Parsons [52] investigated the strength and leakage of a GFRP flange joint using FEA. In 2004, the creep and unsymmetrical shrinkage during the post curing of GFRP pipe flanges have studied

by Whitfield et al. [51]. In 2007, Kittel [54] conducted an optimisation of GRP-Loose flange joints. In 2011, Tao et al. [15] carried out an investigation to manufacture a composite flange for poles joining of the stratosphere truss structure instead of the metal materials. In 2012, Kurz [53] studied the design of floating type bolted flange connection with composite flange at range of temperatures. In 2014, Sanjay et al. [50] carried out an analytical stress analyses of a non-gasket composite flange and a metallic flange.

So far, the found research works indicated there is a shortage in the research of this field and also there were gaps during the recent years. This was one of the reasons for choosing this project as the replacing of metallic pipes and flanges by composite pipe and flange has widely increased recently. This is not only due to the ability of the FRP materials' resistance to chemical reaction but also due to their inherent mechanical properties of high strength and larger modulus to weight ratio. Table 2.1 shows a comparison of composites materials and steel materials (traditional materials) for 1 m pipe and 6-inch diameter in the offshore environment.

Table 2.1: The difference between composites materials and steel materials for 1 m pipe in the marine environment

| <b>Composites materials</b>     | <b>Steel materials</b>            |
|---------------------------------|-----------------------------------|
| Weighs 36 Kg/m                  | Weighs 6 Kg/m                     |
| The estimated life cycle 7 year | The estimated life cycle 20 years |
| Less corrosion resistant        | High corrosion resistant          |
| High life cost                  | Low life cost                     |
| Low strength to weight ratio    | High strength to weight ratio     |

The commercial available composites flanges are suffering from a weakness at the neck as shown in Fig. 2.6 due to the distribution of the used fabric. So that the chosen structure of the fabric can contribute significantly to tackle the problem and reduce flange bending.

Furthermore, a technical report [56], which was titled a technology gap review of composites in the UK oil and gas industry, has been prepared by Martin for The UK National Composite Network in 2007. This report indicated that there is a gap in the research of joints of the composite pipes, which are used for the oil and gas in the UK. This another reason for selecting this study.

Finally, the other reason that encouraged us for developing this project is the good support from a local company (Pipex). This company has a wide range of the experiences in the joints of the composite pipes. Also, they accepted to provide us some of the required materials and use their machines.

## **2.7 History of standards development**

Over the last few decades, many theories and methods have been proposed about the design of a flange based on an elastic analysis of the interaction of flange bending and gasket compression mechanisms. The first method is called Taylor-Forge method. This method has been developed during 1920s and 1930s by D. B. Westrom and E.O. Waters [57] and published as an Engineering Department Bulletin by Taylor-Forge in 1951 [58]. Later, it was included in a booklet, Modern Flange Design, by the same company.

This method is based on using two separate ring gaskets instead of a full face gasket, one lies outside and the other is in the inside of the bolt circle [16]. Based on Taylor-Forge method, a number of design codes and standards have been published such as ASME, CODAP, DIN, JIS and BS [57, 59]. In 1961, Schwaigerer published the second method using the basic design rules of the full face gasket flange connection [60]. A third method has been published by Blach et al. in 1986 [61]. These two methods were based on uneven gasket compression to resist the applied bending of the flange under the operating condition. For composite flange, section X has been added in 1968 to the ASME Boiler and Pressure Vessel Code with the following title “Fibre-Reinforced Plastic Pressure Vessels” [24]. This section, Fibre-Reinforced Plastic Pressure Vessels, is adopted in this study to design the FRP full face flange.

## 2.8 Compressed gaskets

When placed between two objects (e.g. flanges) gasket create a static seal, preventing leakage under various operating conditions such as high pressure and/or temperatures. Once axial load is applied through bolts, gaskets deform and fill the microscopic spaces and surface irregularities between the mating flange faces. Gaskets also compensate for any dimensional changes in the flange geometry caused by pressure or temperature variations during operation [12]. Depending on the nature of the applications, gaskets are required to have a number of characteristics such as good recovery, limited relaxation, good compressibility, face adaptability, high strength and chemical and temperature resistance. Based on the materials used, gaskets can be as: metallic, semi-metallic and non-metallic [62, 63] which are discussed in details in the following sections.

### 2.8.1 Metallic gaskets

Metallic gaskets are manufactured from one or a combination of more than one metal with various geometries and sizes. These gaskets are often used for high pressure and/or high temperature applications thus require bolt loads higher than those applied for semi-metallic and non-metallic gaskets to ensure high quality sealing. Ring joint, lens joint and corrugated metal gaskets (Fig. 2.8) are considered as the dominant types in the current market.

Ring gasket joints are usually fabricated as oval or octagonal cross sections (Fig. 2.8.a) depending upon the geometry of the flange grooves [13, 64]. Various metals and alloys are used to make the ring gaskets. These materials should be softer than the materials used for the flange so that the gasket plastically deforms (rather than the groove) and flows into groove's irregularities. This deformation occurs due to high axial bolt load which is applied upon a small bearing area of the ring gasket. Ring gaskets are mainly used in the petroleum industries for high pressure and temperature applications that require high integrity sealing and with valves and pipework assemblies [13, 63].

Lens ring gaskets have spherical sealing faces especially designed to suit mating flange recesses (Fig. 2.8.b). These gaskets provide high integrity and are used for high pressure/temperature applications [63]. As for all the metallic gaskets the

materials must be softer than the flange materials. Therefore, the deformation will occur on the gaskets rather than on the flanges when compressive load is applied. Both the compressive load and some of the hydrostatic pressure force increase the contact pressure between the flange and the gasket to insure the sealing

Corrugated metal gaskets are divided mainly into two categories, which are corrugated gasket without layers or corrugated solid metal and corrugated gaskets with soft layers. The corrugated gaskets without layers can be made like flat, tongue, groove and sectional ones. They are preferred in the applications that require mechanical strength, good thermal conductivity as well high corrosion resistance and high pressure [13]. The corrugated gaskets with soft layers are usually covered with soft layers on both sides. However, based on the sealed medium, additional layers can be used with uneven or distorted sealing surface. These layers are made of graphite, ceramic or PTFE materials. These type of gaskets are suitable with low pressure and higher temperature applications with acids, oils and chemical mediums. Fig. 2.8.c illustrates the corrugated gaskets with soft layers.

Finally, most of the metallic gaskets are not common gasket with the FRP bolted flanged joints, which require a soft gaskets such as rubber gaskets.

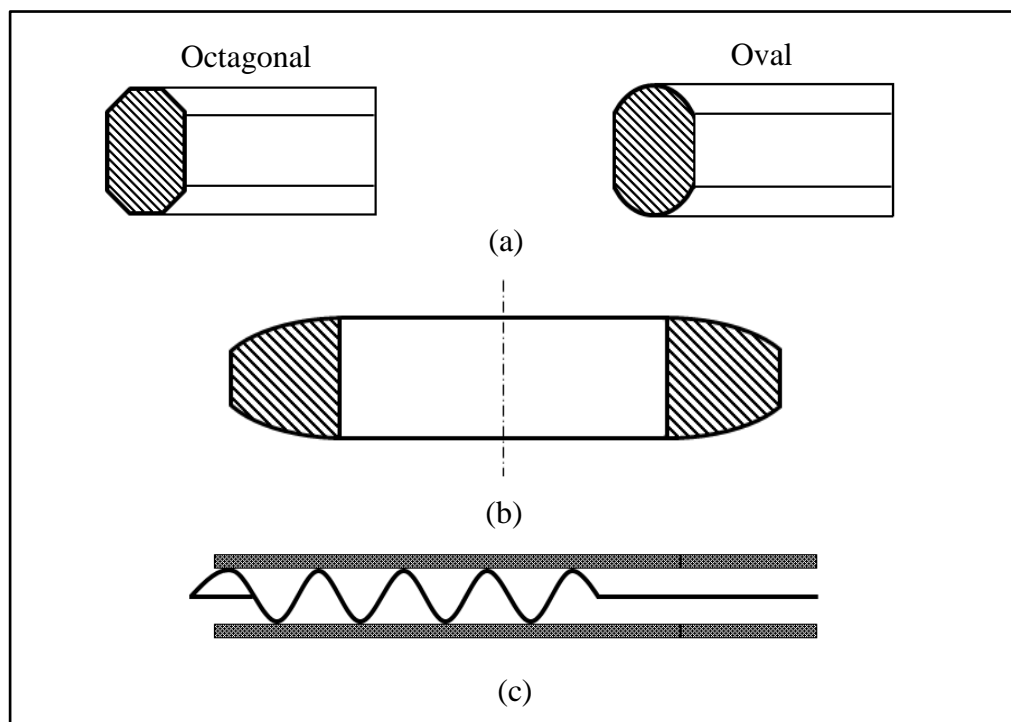


Fig. 2.8: Metallic gaskets (a) Ring joint gasket (b) Lens ring gasket  
(c) Corrugated gasket

Żyliński [45] performed a numerical analysis of bolted flange connection using an aluminium gasket. FEA has been developed to model the bolted joint with special elements, hexahedral 21-node and 28-node isoparametric, for the contact zone. Due to the cyclic symmetry of the joint, a  $1/16^{\text{th}}$  portion of the bolt joint has been modelled. The effect of internal pressure in the gap between the gasket and the arising flange was taken into account during the progression of joint opening. Experimental results were used for comparison. The results reveal that the contact pressure is increased along the gasket radius direction but it is decreased as the internal pressure is increased. Apparently, there is no clear difference between the results for 21-node and 28-node elements. In addition, the working load (internal pressure) has insignificant influence on the pre-bolt load, but the pre-bolt load has a decisive effect on the maximum permissible internal pressure. On the other hand, the maximum permissible internal pressure was independent of the gasket thickness. Furthermore, the maximum von-Mises stress is observed at contact surfaces between the bolt head and the flange.

### 2.8.2 Semi-metallic gaskets

Semi-metallic gaskets consist of both metallic and non-metallic materials. The metallic portion provides the strength to the gaskets while the non-metallic part is intended to offer resiliency, conformability and sealability. These types of gaskets are used for various operating conditions and can generally be used at higher pressures and temperatures than the non-metallic gaskets [62]. Mainly, semi-metallic gaskets are used with most types of the flange such as raised face, tongue and groove and male and female flange.

The spiral wound gasket (SWG) is one of the important semi-metallic types. This gasket is a composite structure of metal strip, sealing strip of fillers and outer/inner steel rings as shown in Fig. 2.9.a. The mechanical properties of the SWG are dominated by the metal spiral strips which are usually stainless steel. Therefore, the SWG has a good resilience and recovery due to V-shape of the metallic spiral strip. Also, it meets the most accurate conditions for both loads; temperature and pressure in the flange joint and has a good resistance in corrosive and toxic mediums. However, complete parallel flange faces are required to install it [63, 65, 66]. Krishna et al [59] had carried out a comparison of the gasket's influence on the

sealing performance of a bolted flange. A three-dimensional FE model of bolted flange connections with gaskets has been developed and analysed using ANSYS. Spiral wound gaskets with various filling such as; asbestos (AF), graphite (GF) and PTFE (TF) filled have been used with their nonlinearity characteristics obtained from experiments. The results show that the distribution of the contact stress is non-uniform in the radial direction across the gasket width and depends on both the gasket type and the flexibility of the flange. These factors are not accounted by the ASME code, so the leakage may occur even at the flange rotation of less than  $3^\circ$  that is specified by ASME. The highest and the lowest axial bolt force have been observed with TF and GF gaskets respectively when the internal pressure is increased. This is due to low and high stiffness of TF and GF gaskets respectively. It is also apparent from the results that the TF spiral wound gasket has the least variations in the contact stress distributions whereas the GF spiral wound gasket has an opposite trend.

Omiya et al. [34] have studied the influence of non-linear characteristics of non-asbestos and asbestos spiral wound gaskets (SWG) on the sealing performance. Contact stress distribution has been calculated and the leak rate has been examined. It has been found that the radial variations of gasket stress distributions with a smaller nominal diameter of the flange joint (around 3 inch) are smaller than those with a larger nominal diameter (around 20 inch). In addition, the sealing performance with smaller nominal diameter and non-asbestos gasket is better than those with larger nominal diameters and asbestos gaskets.

The metal jacketed gasket consists of a metallic shell that surrounds either metallic or non-metallic compressed filler (Fig. 2.9.b) The metal jacket provides blow out resistance and resists the pressure, temperature and corrosion, whereas the filler provides the gasket resilience and compressibility. Generally, this type of gasket is used with heat exchangers, pumps and valves. However, it requires flatness of flange with smooth surface finishes and high bolt loads.

Another type of semi-metallic gasket is named as Kammprofile (grooved) gasket. This gasket consists of a metal ring (outer) made of steel. Kammprofile ring with concentric grooves made of steel, sealing and sealing layers made of either graphite or PTFE or even metals (e.g. aluminium and silver) as shown in Fig. 2.9.c.



Kammprofile gaskets are used for high pressure and temperature applications such as power plant, nuclear industries, heat exchanger and pipelines. However, it is very expensive and could be damaging to the flange faces if it is used without soft covering layers and/or subjected to a high bolt load. The Kammprofile gaskets have the same concept of the metal reinforced gasket which consists of core material and two soft layers covering the faces.

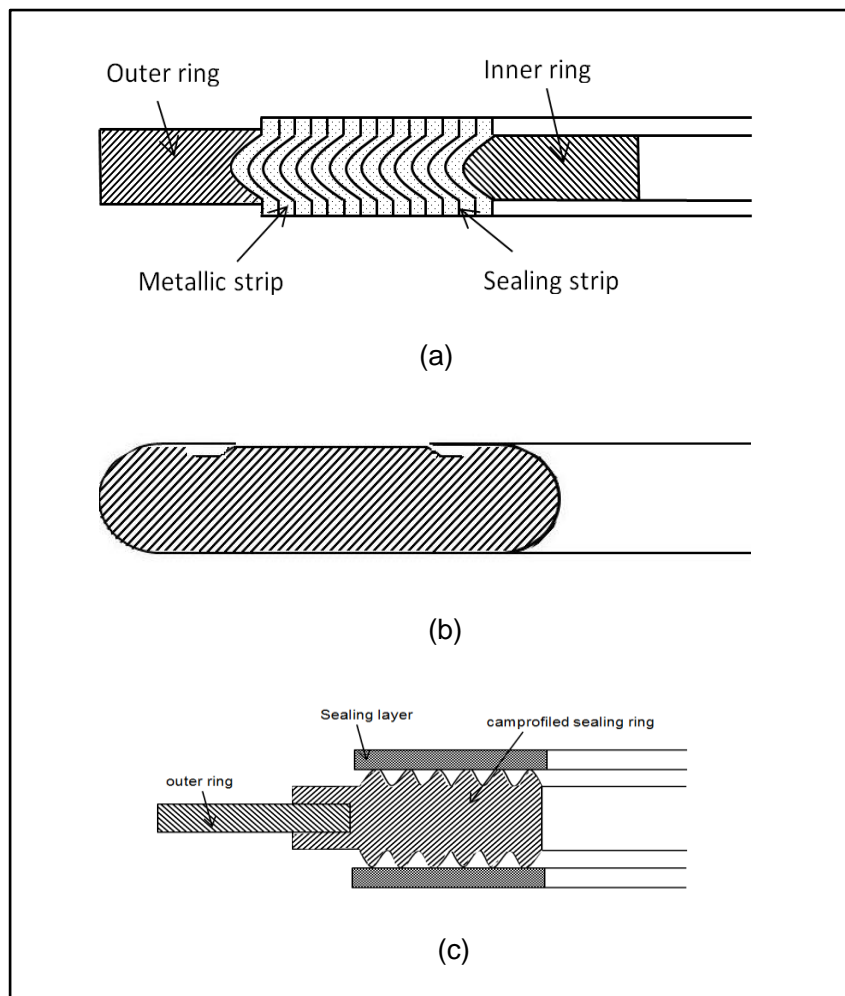


Fig. 2.9: Semi-metallic gaskets (a) Spiral wound gasket (b) Metal jacketed gasket  
(c) Kammprofile gasket

### 2.8.3 Non-metallic gaskets

Non-metallic gaskets are usually fabricated as composite sheets and then punched according to the required geometry. Often, these gaskets are used in low to medium pressure applications. However, these gaskets could be used for extreme chemical environment and temperature if chosen correctly. Non-metallic gaskets are suitable for the use with flat face flange and raised face flange. The advantages of these gaskets are: good chemical resistance, low bolted load is required, they can be deformed easily and fill the irregularities of flange faces to keep the seal and do not require the flange surfaces to be perfectly finished. However, the blowout resistance for these gaskets is low. Depending on the types of materials used, non-metallic gaskets are classified into the following types: PTFE, rubber, graphite and fibre reinforced gaskets.

PTFE gaskets have good chemical resistance. These types of gaskets are easy to adapt perfectly to the flanges and have good ability to maintain the sealing. Furthermore, these gaskets have excellent isolation properties. However, there are a few drawbacks, for example, poor mechanical properties, creep and limited temperature resistance. Moreover, PTFE gaskets are not suitable to use with fluorine gas and Melton alkali metals.

One of the most common non-metallic gaskets is rubber such as EPDM, Neoprene, Nitrile, Viton and Silicone. EPDM and Neoprene gaskets are widely used throughout the water industry due to excellent resistance to water, steam, heat, weathering, chemical, mechanical and wear. Nitrile gaskets are mainly used in the oil industries and have high resistance to aliphatic hydrocarbon oil.

Viton gaskets have excellent resistance to chemical attack by oxidation and are widely used in the chemical industries. Also, these gaskets have good resistance to oil at low temperature and hot air. These gaskets are not influenced by sunlight and ozone. However, the resistance is weaker against steam, aliphatic and aromatic hydrocarbons. Therefore, the Nitrile and Viton rubber gaskets have been chosen in this study.

Graphite gaskets are usually reinforced with a stainless steel insert. These gaskets have good corrosion resistance is excellent against a wide variety of acids, alkalis, salt solution, organic components and heat transfer fluids even at high temperatures.

Furthermore, graphite gaskets are used in oxidizing conditions at temperatures from -200°C to +500°C. However, these gaskets are affected by sulphuric and phosphoric acids, and it is recommended to avoid using this type of gasket in such cases.

Fibre reinforced gaskets are usually manufactured as sheets and then cut or punched depending on the required shape and size. These sheets consist of three components, fibres, fillers and binders. The quality and the properties of the gaskets are dependent on the properties of these components as well as production processes. The fibres aramid, carbon, cellulose, glass and mineral fibres are often used as reinforcement fibres and NBR (Nitrile Butadiene Rubber) is most commonly used as a binder. Generally, fibre reinforced gaskets are cheap and easy to cut or punch to obtain the required size but the temperature resistance is low because of the rubber binder.

Shoji and Nagata [37] presented FE analysis of a raised flange with nonlinear gasket using a 2D axisymmetric and 3D solid element FE models. Based on the load condition, the analysis has been carried out in two steps- pre-load and pressurized. Due to the nonlinearity of the gasket, they have used two values of modulus of elasticity (compression and decompression) depending on the states of the gasket whether in compression or decompression. Results of the numerical simulations indicate that the gasket stress increased from the inner radius toward the outer radius of the gasket for both the 2D and the 3D models, and the stresses are higher in pre-load condition than in pressurized condition.

## **2.9 The characteristics composite pipes commonly used with flanges**

Filament winding technology is the most favourable process for the manufacture of FRP pipe because of its high rate of productivity. Therefore, the use of these pipes has been increased in various applications alongside the further development of this technology [67, 68]. Xia [69] developed an analytical procedure to assess the influence of stacking sequence for the multi-layers filament wound structures using three-dimensional (3D) anisotropic elasticity theory. Three specific carbon fibre/epoxy angle-ply pipe designs, A [+55/-55/+55/-55], B [+55/-55/+30/-30] and C [+55/-30/+30/-55], were analysed. All these pipes were tested under internal pressure and the stress, strain and displacement distributions calculated. The pipe of type A has almost constant hoop and axial stresses through the thickness and its hoop to

axial stress ratio is 2. However, types B and C show discontinuous variations of the hoop and axial stresses at the interface laminas and their hoop to axial stress ratio is no longer constant. In terms of shear stress, all three types show discontinuities, but the smallest range was with type A. Moreover, all three types exhibit continuous variations of hoop strain and the smallest values are observed with type A. Furthermore, only types B and C show discontinuous radial strain and the variation is higher with  $\pm 55^\circ$  lay-up angle than that of  $\pm 30^\circ$  lay-up angle. The radial displacement is not affected significantly by the stacking sequence whereas the hoop rotation depends largely on the stacking sequence, especially for type C.

Merting et al. [70] carried out an experimental investigation for tubular filament-wound structures which were made using a state of the art production method. Three winding angles  $\pm 30^\circ$ ,  $\pm 45^\circ$  and  $\pm 60^\circ$  were utilized for winding eight tows of Owens-Corning E-glass fibre. The specimens were tested under internal pressure and axial force. The results indicate that the multi-angle wound pipe exhibits overall better performance in resisting damage compared to the  $\pm 60^\circ$  angle-ply lay-up.

Meijer and Ellyin [71] conducted a study of the strength of  $[\pm 60^\circ]_T$  glass fibre reinforced epoxy tubes to produce a baseline failure envelope when they subjected to multiaxial stress. These pipes are manufactured by filament winding and tested under 14 different ratios of hoop to axial stress. These stresses are the consequences of applying internal pressure together with tensile and compressive axial loads. According to the results, they observed five distinct modes of axial tensile structure failure such as weepage, local leakage, burst and axial compressive failures. They also developed the maximum strain failure criterion that was fitted to the failure strain data but was observed to be unsatisfactory for two regions of the data. Moreover, it is found that when the local leakage failure occurred under an axial compressive stress, the maximum strain failure criterion over-predicted the strength at the stress ratios.

Onder et al. [72] studied the influence of winding angle and temperature on the burst pressure of the filament wound composite pressure vessel. They utilized FEM, experimental approaches and an elastic solution procedure developed based on Lekhnitskii's theory to verify the optimum winding angle. In addition, the Tsai-Wu failure criterion, maximum stress and strain theories were used to predict the burst

pressure of tubes, which were tested under the closed-ended condition. The glass fibre reinforced (GRP) pipes were manufactured with four layers, which were oriented symmetrically and anti-symmetrically at  $[+45^{\circ}/-45^{\circ}]_s$ ,  $[+55^{\circ}/-55^{\circ}]_s$ ,  $[+60^{\circ}/-60^{\circ}]_s$ ,  $[+75^{\circ}/-75^{\circ}]_s$  and  $[+85^{\circ}/-85^{\circ}]_s$ . They concluded that the optimum winding angle of the composite pressure vessel under internal pressure loading should be  $\pm 55^{\circ}$ . Hygrothermal loading has insignificant influence on the burst pressure, whereas it is affected significantly by temperature, especially at high temperatures. Arikan [73] conducted a failure analysis of filament wound composite pipes with an inclined surface crack under static internal pressure. The pipes were made from glass/ epoxy with antisymmetric layers at  $(\pm 55^{\circ})_3$  winding angles with different angles of the cracks. According to the results, the burst pressure increases with the increase in the crack angles. The delamination area also increases with an increase in both the burst strengths and the crack's angles.

Based on the above findings and the others, the optimum winding angle of filament wound composite pipes subjected to internal pressure is  $\pm 55^{\circ}$  which leads to produce equal circumferential and axial stresses [8]. Therefore, a filament winding pipe with  $\pm 55^{\circ}$  winding angle will be used to test the flange in this study.

## **2.10 Co-bonding of composite flange with composite pipe**

The use of adhesive bonding methods with very large and complex composite structures [74] made of similar or dissimilar materials is continuously increasing. The parts of such complex structures are usually manufactured separately and bonded using adhesives to reduce labour and fabricating costs [75, 76]. Both the adhesive properties and the joining methods significantly affect the performance and the behaviour of adhesively bonded composite structures [77]. In many applications, traditional mechanical joints with fasteners have been replaced by adhesively bonded joints because of its advantages; these include fast and unexpansive joining techniques, uniform stress distribution over large area without holes (holes cause stress concentration) and high dynamic strength [78-81].

For the FRP flange-pipe joint, industry prefers the convenience of adhesive bonding. The bonding technique is generally divided into three categories: Taper-taper,

straight-taper and straight-straight joint [82]. There are a few other types which can also be used, however, these are the most common (Fig. 2.10).

**1. Taper-Taper joint:** the inner diameter of fitting or flange bell or socket is tapered and the outer diameter of the end of the pipe is also tapered (shaved). Then, they are matched and joined by a thin glue line and no integral pipe stop is required. Due to the largest contact area between the matching components, taper-taper joint is considered the strongest option. However, this type of joint requires more manufacturing time compared to the others.

**2. Straight- Tapered joint:** the flange bell, fitting, or socket is tapered internally and the end of the pipe is shaved with uniform outer diameter (i.e. straight pipe end). A thin glue line is not often achieved and this results in lower joint strength. However, the required installation time is less than the taper-taper joint.

**3. Straight –Straight joint:** the end of the pipe is prepared with straight shave or standing, and the flange bell or fitting or socket has no tapered surfaces. The main advantages of this type of joint are shortest fit up time requiring fewer tools. However, this type of adhesive joining technique offers medium strength and it requires an integral pipe stop.

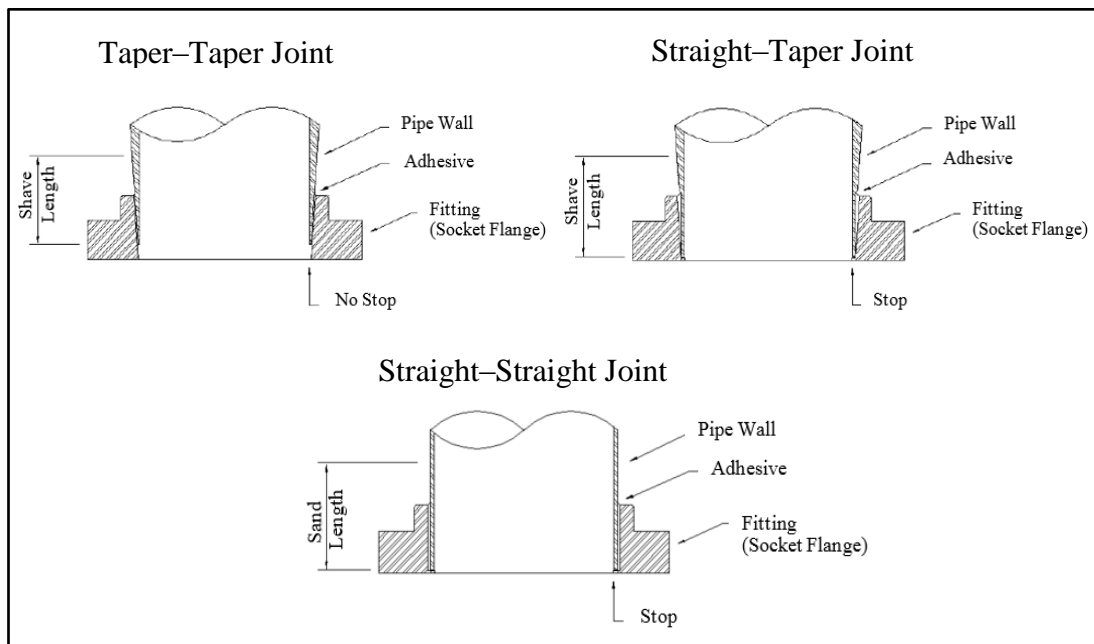


Fig. 2.10: Three different types of flange-pipe adhesive bonded joint [82]

Nemes [83] examined the adhesive bonded joints for pipes made from different materials (hybrid materials) like titanium, aluminium and carbon/epoxy. They discovered that the maximum values of orthoradial stress ( $\sigma_{\theta\theta}$ ) exist on the free edges of adhesive and the shear stress has two peaks that are located at equal distances from the free ends. Moreover, the shear stress ( $\tau_{rz}$ ) decreases with the length of overlap which has an optimum dimension of 80 mm. Furthermore, increasing the thickness of the adhesive has a positive effect on the orthoradial stress but reduces shear stress values.

Yang [14] studied the design of adhesive joint for composite pipes which is subjected to tensile loads. It has been found that the maximum peel and shear stresses occur at the free edges of adhesive length but both stresses are nearly zero in elsewhere. The optimal lengths of the joints are 65 mm and 90 mm for 54° wound pipe and 20° coupling respectively.

Cheng [84] presented a study about adhesive bonding for smart composite pipes by using piezoelectric layers within composite layers of coupler under tensile loading. The piezoelectric layers work as a sensor for the deformation produced by the applied mechanical load and provide signals which are used to calculate the peel and the shear stresses. According to the results, maximum peel and shear stresses are located at the edges of adhesive layer. The optimal design conditions could be achieved by choosing suitable piezoelectric materials.

Oh [85] investigated the tubular adhesive joint for the steel-composite adherents piping under thermal expansion and mechanical torsion. A finite element was utilized to calculate the thermal residual stresses generated by the cooling of the joint from 80 °C to 20 °C. It has been discovered that the torque transmission capability increases with the increase of stacking angles up to  $\pm 25$  degrees and then decreases. Thermal stress has a significant effect on the adhesive joints. Oh [86] in a separate article discussed the torque capacity of tubular adhesive joints with different composite adherent. It has been illustrated that the steel-carbon/epoxy joint is much affected by the thermal stress compared with the steel-glass/epoxy joint, so at a stacking angle  $\phi = 45^\circ$  the failure might occur due to thermal stress only even without any external loads. The strength of steel-carbon/epoxy is lower at high

values of  $\phi$ . However, the strength of steel-glass/epoxy joint increases with  $\phi$ . However, the effect of residual stress reduces when  $\phi$  is increased.

Kumar [87] has presented a study of tubular adhesive bonds with functionally modules graded bond line (FMGB) and mono-modules line (MMB) under tensile loads. Based on the findings, it can be said that the peel and shear stress peaks of FMGB are much smaller than those in state of mono-modules adhesive joint under the same load conditions. Spaggiari and Dragoni [88] have carried out an analytical investigation on the tubular lap bonded joint under torsion to regularize the torsional stresses by using functionally graded modulus adhesive (FGA). The aim of that is to change theoretically the elastic properties of the adhesive as a function of the reinforcement inside the bond line. This will allow to minimize the stresses considerations which are usually high at the edges.

EDO [82] performed comparative studies of butt and strap joints with adhesively bonded joints (taper-taper joint, straight-taper joint and straight- straight joint). All the joints were experimentally tested under various loads such as tensile, bending, allowable wind loads and thermal load. The results have shown that the butt and the strap joints are stronger than all other types of adhesively bonded joints when subjected to environmental loads. Results from bending and tensile tests have shown that taper-taper joint has a superior strength over other types of adhesively bonded joints. However, taper- taper joint is slightly weaker under thermal and wind loads.

### **2.11 Fasteners of flange joint**

In most flange and gasket joints, fasteners apply the compressive pressure on the gasket through flanges. The main function of these fasteners is to clamp the connection sufficiently for maintaining the seal and preventing the slip of the gaskets. Therefore, the fasteners must be made of strong materials to keep the tension that is induced on the initial preload as well as the additional loads that are induced during the operating condition due to the internal pressure, temperature and corrosion. To achieve a successful installation, all components of the flange assembly should be taken into account by the designers. However, one of the most neglected components in the joining process is the fasteners and this negligence results in frequent joint leakage. Hence, the principal fastener components such as bolts or studs, nut and



washers should be chosen carefully depending on the application requirements. On the other hand, the bolt load should be applied correctly as one of the major weaknesses in the FRP flange industry at the moment is that most FRP manufacturers publish torque values but with no bolt load or lubricant on which they are based. This creates confusion/ignorance at installation resulting in cracking of flanges at one end or leakage of gaskets at the other.

The bolt is a threaded fastener with a nut at each end. Since the performance of the seal is dependent upon the level of the tension in the fasteners, ASME recommends applying a preload of 40% to 70% of a bolt's yield stress. Therefore, the materials should be chosen with a good safety factor based on the application conditions. The standards also recommend that the number of fasteners should be chosen in such a way that the distribution of pressure across the gasket remains as uniform as possible. Due to the flange bowing, the compression stress of the gasket is greater near the fasteners's holes.

Nuts are always associated with fasteners of flanged joints in which finished hex nuts and heavy hex nuts are most commonly used. Heavy hex nuts are slightly thicker and larger than finished hex nuts and used with high temperature and high pressure applications which require high axial forces. This load is generated by tightening nuts along the threads of the fasteners, so the threads play a major role in clamping operation. To avoid stripping these threads, it is necessary to choose fasteners and nuts with sufficient size, materials strength and length of engagement. The other problem between fastener components that should be avoided is galling, which is a cold welding (partial or full) and occurs between the mating faces that are under high loads due to the molecular bonds between them. To avoid this problem, it is recommended to use correct lubricant, coarse thread surfaces rather than fine and appropriate fastener components materials that are resistant to galling.

Washers are very important in bolted flange joints. They are recommended with FRP joints to distribute the applied loads of the bolts around the bolt holes. Consequently, a more even gasket load will be achieved, reducing potential leak paths of contained media. In addition, the use of washers is to protect the nut seating area and improve translation of torque inputs into bolt preload during the tightening process by reducing the friction between the turning nut and joint components resulting more

accurate torque readings when using a torque wrench. Moreover, washers prevent embedding the nuts against the flange faces or inside the fasteners holes, thus the damage at joint surfaces.

## 2.12 Issues with drilling of composite materials

As the field of composite applications expands, the need for various types of machining such as drilling, milling, turning and cutting have increased. For example, it has been reported that over 100,000 holes [89] are made for a small single engine aircraft so in a large transporter aircraft, millions of holes are made. Consequently, drilling account for as much as 40% for all machining processes [90]. It has been found that the FRP flange with drilled bolt holes performs better in terms of strength than those with moulded holes [91]. However, drilling is a complex process and requires better understanding of drilling composites because of the inhomogeneous and anisotropic properties [92]. Typical damage in composites after drilling include peel-up and push out delaminations [93-95] as shown in Fig. 2.11, intralaminar cracking, fibre/matrix debonding and thermal damage by the heat produced during drilling. The most serious defect is delamination as it leads to decrease the load carrying capacity of composite laminates [96]. Delamination generally occurs between adjacent laminas. Therefore, the properties of resin and the fibre as well as its configuration play important roles in its occurrence.

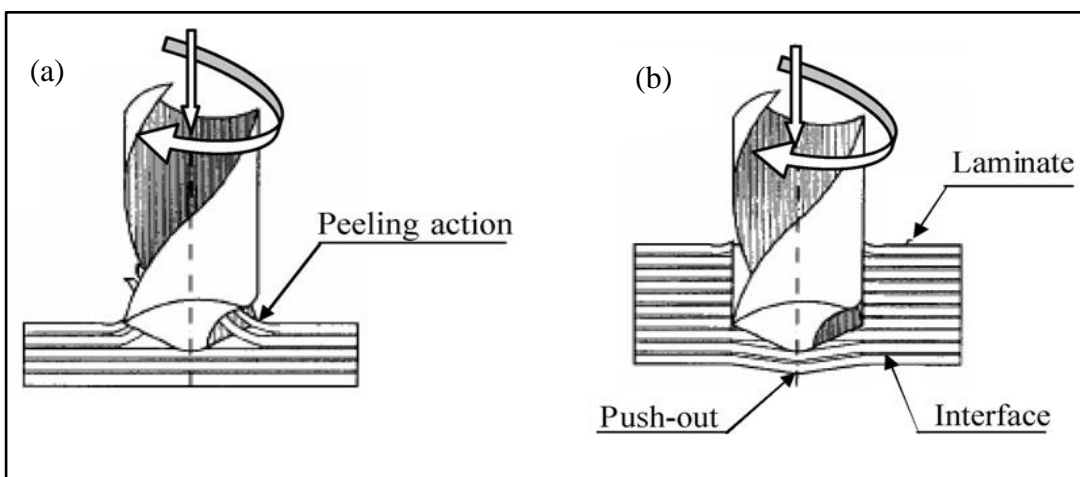


Fig. 2.11: Delamination (a) Peel-up delamination (b) Push-out delamination [92]

It is worth mentioning that peel-up delamination occurs due to the cutting force when the drill starts to abrade the laminate. This is because an upward peeling force is created with the forward movement of the drill. This force tends to separate the upper laminae from the uncut portion held by the downward thrust force. The value of this force depends on the friction between drill and composite and drill tool geometry [96, 97]. On the other, the push-out delamination is caused by the compression, which is applied on the workpiece by the drilling tool. This force pushes and breaks the interlaminar bond between adjacent laminae in the regions around the hole. At some point, the push-out delamination will occur when the uncut portion becomes smaller and its resistance of the deformation is decreased and the thrust force exceeds the bond strength between the composite layers. Thereby, the adjacent layers at the bottom surface of the laminate are deboned before completing the drilling process. In order to avoid delamination, it is recommended to reduce the thrust force by changing the geometry of the drill tools [96, 97].

Tagliaferri et al. [98] conducted an experimental investigation about drilling of composite panels, which were made of six layers of glass fabric VR 181/ epoxy prepreg with autoclave curing. High speed steel (HSS) tool of 8 mm in diameter has been used with cutting fluid but without backing. The experimental results show that the damage extent is significantly affected by the cutting parameters. Increasing the cutting speed shows less damage extent whereas higher feed speed leads to poorer cut quality. They also observed that the damage extent does not influence the tensile strength of GFRP laminate that contains the holes. They have recommended that the optimal cutting speed/feed speed ratio can be obtained for maximum bearing strength by lowering the drilling speeds.

Khashaba [99] has carried out a study for randomly oriented GFRP laminates to evaluate the influence of the varying fibre volume fraction ( $V_f$ ) and drill size on the notched tensile strength and pin bearing strength. The results indicate that the fibre volume fraction plays a significant role on the notched tensile strength, pin bearing strength and stress intensity factor. Due to the important effect of the ratio of randomly oriented GFRP laminate to drill diameter, it is recommended that this ratio must be greater than 5 for the development of full bearing strength.

In a separate work, Khashaba [94] carried out an experimental study to determine the influence of the drilling variables and material variables on the thrust force, torque and delamination of GFRP (thermoset) composites. The drilling variables considered are cutting speed and feed rate whereas material variable involved fibre shape, filler and matrix type such as cross-winding/polyester, continuous-winding with filler/polyester, chopped/polyester, woven/polyester and woven/epoxy composites. In this study, a more accurate but inexpensive technique for measuring the delamination size within  $10^{-3}$  mm has been demonstrated. The results have revealed that the sand filler in the continuous-winding composite raises the values of cutting forces and push-out delamination and increases further with increasing cutting speeds. In contrast, the push-out delamination decreases with an increase in cutting speeds for drilling cross-winding, woven and chopped composites. This happens due to a decrease in the thrust force. It is worth noting that the woven fabric composites have higher push-out delamination than that made of chopped fibres. For the same fibre shape (woven), the matrix has significant influence on the delamination and the torque. Both the peel-up and the push-out delamination as well as the torque of woven/polyester composite are higher than that for woven/epoxy composites. The thrust forces in drilling continuous-winding composite are more than three orders of magnitude higher than those in the cross-winding composites. During drilling both the chopped and the continuous-winding composites; delamination, chipping and spalling damage mechanisms were observed, however, the delamination was observed at different edge position angles with drilling woven composites.

Davim et al. [100] have studied the effect of cutting parameters (cutting speed and feed rate) and drill geometry on the thrust force, damage, surface roughness and cutting pressure. Two different types of 5 mm diameter drills (helical flute “Stub Length” and brad & spur) as illustrated in Fig. 2.12 have been used to drill a disc made of GFRP material using a hand lay-up process. They have also utilized analysis of variance (ANOVA) and Taguchi technique for identifying the impacts of drilling conditions. Based on their experimental findings, they have concluded that both the specific cutting pressure and the thrust force have been significantly affected by the cutting parameters. Damage increases with cutting speed and the feed rate. On the other hand, the cutting speed has the highest influence on the surface roughness. It

has also been observed that better cutting performance could be achieved with the Bard & Spuer tool than the Helical flute “Stub Length”.

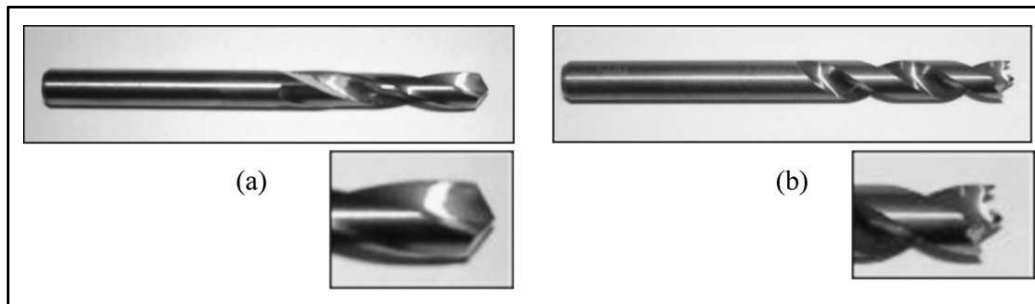


Fig. 2.12: (a) Helical flute “Stub Length” K10 drill; (b) “Brad & Spur” K10 drill[100]

Abrao et al. [101] carried out comprehensive investigations to identify the influence of drill geometries on the drilling performances of GFRP composites. A number of drills (EDP27199, A1141, A1163 and A1167A as can be seen in Fig. 2.13) have been used and the effect of the cutting parameters has been investigated. Results from this work indicate that the lowest and the highest thrust forces could be obtained from EDP27199 and A1167A drills respectively. The thrust force increases as the feed is increased and this happens due to the elevation in the shear area. The effect of cutting speed on the thrust force can be considered as negligible. The least damage on the laminate has been observed with tool drill EDP27199 which provides lowest thrust force. The second smallest delamination area has been found with drill tool A1167A with the highest thrust force. The damaged area increases considerably with feed rate and moderately with cutting speed.

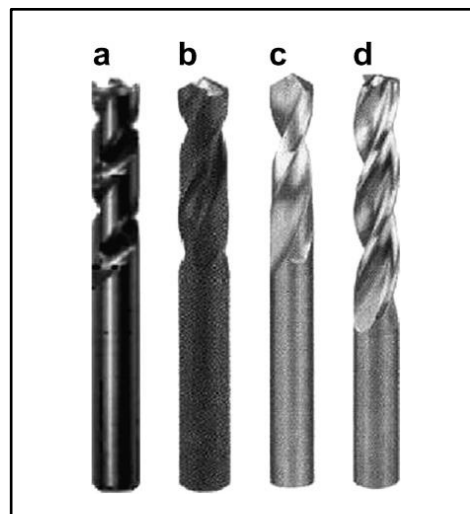


Fig. 2.13: Drills used in the experimental work: (a) EDP27199, (b) A1141, (c) A1163 and (d) A1167A [101]

Tsao [90] investigated the drilling of carbon fibre reinforced plastic (CFRP) laminates using three types of step-core drills (step-core twist drill, step-core saw drill and step-core candle stick drill) as shown in Fig. 2.14. The study examined the effects of drilling parameters such as diameter ratio, feed rate and spindle speed on the thrust force. By analysing the variation of these types of drills and their drilling parameters, it has been concluded that the step-core saw drill offers the highest drilling thrust force compared to the other step-core drills and the thrust force is influenced significantly by the selected cutting parameters. The thrust force has inverse relations with both the diameter ratio and the spindle speed but has a proportional relation with the feed rate. It has been concluded that a combination of low feed rate (e.g. 8 mm/min), high spindle speed (e.g. 1200) rpm and the high diameter ratio (e.g. 0.74 mm/mm) could be the best experimental condition of drilling CFRP with various step-core drills.

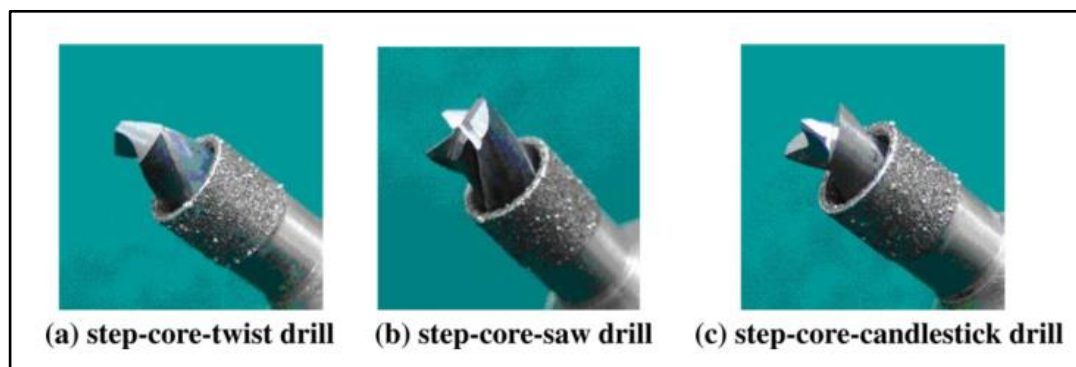


Fig. 2.14: Photographs for various step-core drills [90]

Finally, the GFRP laminate of the flange will be drilled to create the holes of the bolts with high cutting speed/feed rate ratio to minimize the damage of the composite flange. In addition, Brad & Spur'' K10 drill or EDP27199 drill tool has been recommended for the drilling holes. It will be compared with other drill tools to choose the best for this project.

### 2.13 Summary

Metallic bolted flange joints (BFJ) are heavy and susceptible to corrosion in the presence of water and other liquids. Fibre reinforced polymers (FRP) are an alternative material, but relatively little published work on their design and manufacture has been found. In addition, agreed standards and relevant design codes for bolted FRP flange joints appear to be inadequate. Currently, used design procedures are modified forms of metallic design methods, which neglect the unique characteristics of composite laminates. The manufacturing process, together with the reinforcement and laminate specification, are not defined adequately, although they affect the strength of the flange. This has resulted in the failure of some of the current BFJ designs, which are available in the market. Furthermore, the mismatch between the mechanical properties of metallic flange and composite pipe can result in weak points in the structure of pipelines – differential thermal expansion can be avoided by using a composite flange, and this is especially important in high temperature applications.

Other areas that need more investigation include the composite pipe-flange adhesive bond, which is subjected to an unsymmetrical load around the axis of the pipe, due to the bolt loads as well as the internal pressure. Optimizing the composite drilling parameters could produce bolt holes with less damage. The rubber sealing gasket plays an important role in the joint performance, and an understanding of its nonlinear behaviour and its influence on leakage propagation is required so that material selection can be optimised.

Next chapter includes design parameters of the bolted flange joint and the comprehensive analytical approach of the ASME code, which is used in this project.

## CHAPTER THREE

# DESIGN & ANALYSIS

### 3.1 Introduction

During analysis of the bolted flange connection, there are several design parameters affect the performance of the flange joint and they should be taken into account. These parameters can be divided into three groups: (1) flange dimensions and materials, (2) gasket type and thickness and (3) applied loads. Selecting the parameters that have significant effects is very important for the current project. Therefore, among the above groups, several important parameters have been chosen in this study to obtain a bolted flange joint with high quality and performance for the oil and gas applications. Most of these parameters have been determined by the ASME Boiler and Pressure Vessel Code, Section X, but they will be varying to investigate their effects and the possibility of reducing the flange dimensions and the materials, which lead to reduce the flange cost. The ASME approach was modified from its counterpart of the metallic flange codes, which neglect the composite material behaviour. In addition, the analytical approach of ASME code, which is explained in this chapter, does not take into account of the mechanical properties of the composite material and the type of manufacturing process. However, it has been used as a benchmark to develop further investigations.



The present chapter includes the explanations of the selected design variables, constants and the parameters, which have been neglected. In addition, it contains comprehensive analytical approach of the ASME code for the bolted flange joint made of composite materials.

### 3.2 Design variables

In this study, various variables are considered for improving the design of the bolted flange connection. These variables include flange dimensions (flange and hub), gasket materials and thickness and applied loads (bolt load and internal pressure). See Fig. 3.1. These parameters are used as design factors and the other, which will be discussed in section 3.3, are applied as fixed parameters. The variable parameters are selected due to the expectation of their significant influences in obtaining a high performance GFRP bolted flange joint system in terms of; durability, cost, lifetime and good corrosion and chemical resistances, which represent a big problem for the metallic flanges, during the operating conditions. These factors are discussed in the following sections.

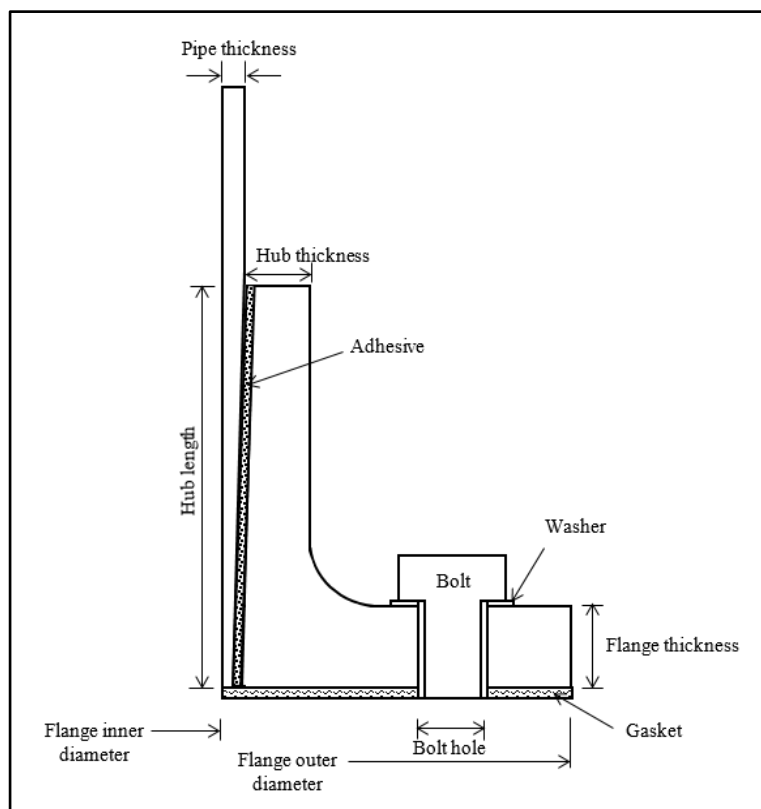


Fig. 3.1: Schematic diagram of the flange joint

### **3.2.1 Flange dimensions**

Flange dimensions mean the dimensions of the flange disc; thickness and the outer diameter as shown in Fig. 3.1. These dimensions have significant effects on the flange deformation, flange bending, strain distribution, flange rotation and the leakage pressure. Minimizing these dimensions can lead to reduce the required materials, thereby the material cost of the flange joint.

### **3.2.2 Hub dimensions**

Similarly, hub dimensions include two parameters; hub thickness and hub length, which are illustrated in the Fig. 3.1. The flange bending is affected significantly by the hub thickness, especially at the flange-hub intersection when the bolt load is applied. High strain concentration usually occurs at this area and it represents the weakest points for the current commercial flanges. For the hub length, it affects mostly on the axial and hoop strains as well as the required materials and the pipe machining. Therefore, the effect of the hub dimensions will be investigated in this study to find out the possibility of reducing them while keeping sufficient required strength and thickness of the flange joint.

### **3.2.3 Gasket material and thickness**

As mentioned earlier, Nitrile and Viton rubber gaskets have been chosen for this study with two thicknesses (3 and 5 mm) to investigate their impacts on the joint performance. These types of the rubber gaskets are usually used for the oil and gas industries. Furthermore, their non-linear behaviours during the loading and the unloading conditions have been taken into account in the FE analysis of this study. Therefore, the relationships between the flange strains in three directions (axial, hoop and radial) and the leakage pressure with the gasket material and thickness have been investigated in this project.

### **3.2.4 Bolt load**

Initial clamping of the flange pairs is done by the axial bolt force, which is the main load in the bolt up conditions. The impact of this force on the flange performance, strains distribution, axial displacement, flange rotation and leakage pressure

development, have been studied during the seating conditions and operating conditions.

### **3.2.5 Internal fluid pressure**

The internal pressure of the fluid is the main load that applies to the joint system during the operating conditions. During the test or in the FEA, the internal pressure has been changed up to the point that the leakage occurs. At the same time, the variations of the flange strains in three directions, flange axial displacement and flange rotation with the internal pressure up to the leakage point have been recorded to study the interaction between them.

### **3.3 Design constants**

Many parameters have been considered as fixed in this study, these parameters are flange inside diameter, flange materials, bolt number and external loads. For the inside diameter of the flange, it has been chosen to be 6 inch and all the analytical calculations and manufacturing processes have been built based on this value. The value of the inside diameter represents a medium between small and big pipe diameters and gives a good indications about wide range of the inside diameter effect. Also, it helps to reduce the cost of the fabricated flange as the big diameters costs more.

In terms of the flange materials, glass fibre and polyester polymer have been used as reinforcement and matrix respectively. Regarding the fabric structure, a sleeve braid with 8-inch diameter has been chosen. This type of fabric structure provides continuity of the fibre from the hub to the flange disc and in the hoop direction as well. Therefore, this increases the strength and reduces the bending of the flange, especially at the hub-flange intersection, which represents the weakest point in the current commercial flanges.

Other parameters have been neglected in this study such as external loads and the number of bolts. The external loads, which can be external pressure, axial force and bending force, have been ignored in this project so far because they represent an advance step in the design of the bolted flange joint, which will be investigated later. Regarding the bolt number, it has been fixed to 8 bolts as recommended by the ASME code[24].

### 3.4 Analytical design analysis (based on the ASME code)

The first ASME Boiler and Pressure Vessel Code was issued in 1915. This code was published as one volume and was later divided into many sections. Other sections were added or deleted as well as some of these sections were divided into many divisions.

In 1968, section X was added to the ASME Boiler and Pressure Vessel Code with the following title “Fibre-Reinforced Plastic Pressure Vessels”. This section included the design method calculations of the FFG flange made of fibre reinforced plastic materials that allowed for the design engineers to obtain a safe flange design. Therefore, it is necessary to review briefly the theoretical calculations of this code. This design method has been developed based on the following conditions: in the operating conditions, it should resist the hydrostatic force, and also the gasket must be placed under adequate compression stress to keep the tightness of the joint. In the gasket seating (Bolt-up) conditions, the compression required to seat the gasket is completely governed by the gasket material’s properties, bolt cross section area and contact area [35]. The following sections will describe the theoretical approaches of the flange design.

#### 3.4.1 Full face flange geometry

Due to the axisymmetric nature of the flange around the axial axis, half of the full face flange geometry is drawn as can be seen in Fig. 3.2. The nomenclatures of the flange dimensions are the same as the nomenclatures of the ASME code [24].

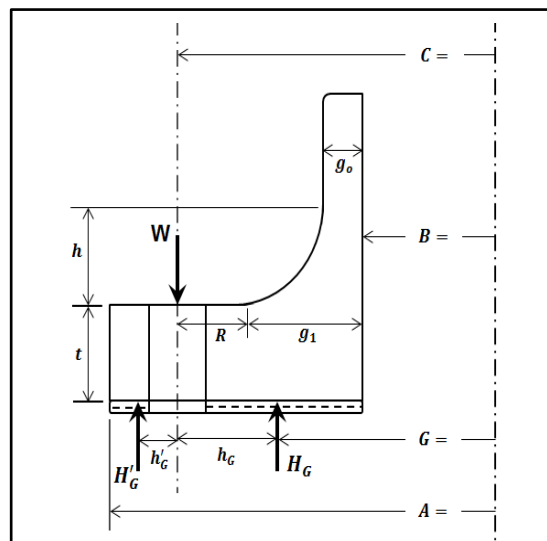


Fig. 3.2: FFG Flange geometry

### 3.4.1.1 Effective gasket diameter

The effective gasket diameter ( $G$ ) represents the diameter of the circle on which  $H_G$ , the difference between bolt load and hydrostatic end force, acts.

$$G = C - 2h_G \quad \dots (3.1)$$

Where  $h_G$  is the radial distance from bolt circle to circle on which  $H_G$  acts

$$h_G = \frac{(C - B)(2B + C)}{6(B + C)} \quad \dots (3.2)$$

### 3.4.2 Gasket loads

The design of the flange must create adequate compression load on the gasket to achieve a good sealing during the operating conditions. Gasket and their behaviour play an important role in the sealing performance, so the gasket must be sufficiently compressed by the flange to compensate internal voids or space, which might lead to leakage. To design a bolted flange joint, the designer needs to know the gasket constants. As shown in Table 3.1, these constants are  $y$  (seating stress) and  $m$  (gasket factor), which are used in the calculations of the bolted flange design. The seating stress ( $y$ ) is defined as the minimum gasket stress required for achieving the initial sealing.

To find the required compressive load on the gasket to keep the tightening, the gasket factor ( $m$ ) is used when the joint system is pressurized. This factor is employed to ensure that the flange has sufficient strength and bolt load to maintain the joint tightness when withstanding the force effect due to the internal pressure. The hardness (Shore A) of the rubber gaskets used in the study is 75. Due to the compression load on the gasket, the gasket will produce reaction forces and these forces are discussed below.

Table 3.1: Gasket parameters for elastomers without fabric or high percent of asbestos fibre

| Gasket material               | Gasket factor<br>$m$ | Min. Design Seating Stress $y$<br>Pis (MPa) |
|-------------------------------|----------------------|---|
| Below 75A Shore Durometer     | 0.5                  | 0 (0)                                       |
| 75A or Higher Shore Durometer | 1                    | 200 (1.4)                                   |

### 3.4.2.1 Total gasket load ( $H_G$ ) in seating conditions

When a flange is bolted up and the flange rotation is neglected, the compressive stress applied on the gasket will be uniform. The amount of this stress depends on the physical properties of the gasket materials and the effective gasket area as well as the bolt cross section area. Since no internal pressure is applied and the gasket compression force is the only force reacting to the bolt load, the bolt load is balanced by the gasket compression force [102]

### 3.4.2.2 Total gasket load ( $H_G$ ) in operating conditions

In the operating conditions, as the internal pressure is applied, the hydrostatic force will be produced on the face of the flange. The bolt load is balanced by the sum of gasket compression force and the total hydrostatic force which acts on the flange face and can be expressed as:

$$H_G = W - H \quad . . . (3.3)$$

Where, H is the total hydrostatic force.

## 3.4.3 Flange loads

### 3.4.3.1 Hydrostatic end force ( $H_D$ )

When the pipe connection system is pressurized by a fluid, forces develop on the internal surfaces of the joint system as well as in the area of the inside diameter of the flange. Therefore, the hydrostatic end force is the normal force exerted on the area inside the flange due to the hydrostatic pressure of the internal fluid, and it reaches the flange through the hub. Hydrostatic pressure is defined as the force per unit area. Therefore, the hydrostatic end force is equal to:

$$H_D = \frac{\pi}{4} B^2 P \quad . . . (3.4)$$

And the lever arm of the hydrostatic end force is equal to the radial distance from bolt circle to circle on which  $H_D$  acts:

$$H_D = R + g_1 = C - B \quad . . . (3.5)$$

### 3.4.3.2 Hydrostatic force under the gasket ( $H_T$ )

According to the ASME code for designing flat face flanges with gaskets, a partial leakage has been assumed to take place between the flange and the gasket. This leakage causes an additional hydrostatic force on somewhere in the area between the inner diameter of the flange and the diameter of the bolt hole circle.

$$H_T = H - H_D \quad \dots (3.6)$$

The lever arm can be expressed as:

$$h_T = 0.5(R + g_1 + h_G) \quad \dots (3.7)$$

### 3.4.3.3 Total hydrostatic force (H)

It represents the total hydrostatic end forces, which act in the area of the effective gasket diameter.

$$H = \frac{\pi}{4} G^2 P \quad \dots (3.8)$$

## 3.4.4 Gasket seating (Bolt up) conditions

### 3.4.4.1 Bolted load during seating conditions

Gasket seating is a first stage when no internal pressure is applied. To prevent a leakage and to achieve a seal, all facing surface irregularities of the flange must be filled with gasket material. This is done with direct force by bolting the flanges as illustrated in Fig. 3.3. The minimum required bolted load, which is calculated by ASME code, is equal to:

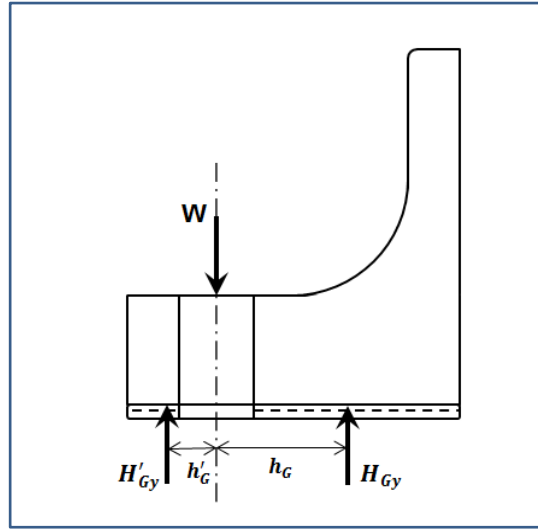


Fig. 3.3: Flange under gasket seating conditions

$$W_{m2} = H_{Gy} + H'_{Gy} \quad \dots (3.9)$$

Where,  $H_{Gy}$  is the bolt load for gasket yielding and  $H'_{Gy}$  is a compression load required for seating gasket outside G diameter.

$$H_{Gy} = b\pi Gy \quad \dots (3.10)$$

$$H'_{Gy} = \left( \frac{h_G}{h'_G} \right) H_{Gy} \quad \dots (3.11)$$

$h'_G$  is the radial distance from the bolt circle to the circle of the gasket load reaction.

$$h'_G = \frac{(A - C)(2A + C)}{6(C + A)} \quad \dots (3.12)$$

The bolting area required for the seating conditions ( $A_2$ ) is:

$$A_2 = \frac{W_{m2}}{S_a} \quad \dots (3.13)$$



### 3.4.4.2 Flange moment during seating conditions

As mentioned earlier, the gasket compression force is the only force that resists the bolt force during the bolt-up conditions, so the total moment produced as a result of this force is:

$$M_G = H_G h_G'' \quad . . . (3.14)$$

And the flange lever arm ( $h_G''$ ) is:

$$h_G'' = \frac{h_G h_G'}{h_G + h_G'} \quad . . . (3.15)$$

### 3.4.5 Operating conditions

When the joint system is pressurized, the two forces will be applied on the flange. The first one, as mentioned earlier, is named as hydrostatic end force ( $H_D$ ), which comes from the applied pressure on the inside area of the flange. The second one is the Hydrostatic Force under the Gasket which acts on the face of the flange. The sum of these forces produces the total hydrostatic force ( $H$ ). In addition, there are three loads, bolt load ( $W$ ), the total gasket load required to maintain the seal ( $H_P$ ) and total adjusted joint-contact surface compression for the gasket flange ( $H_P'$ ), which already existed from the bolt-up stage, but the values and the names are changed. These loads are illustrated in Fig. 3.4 and calculated as shown in the following equations.

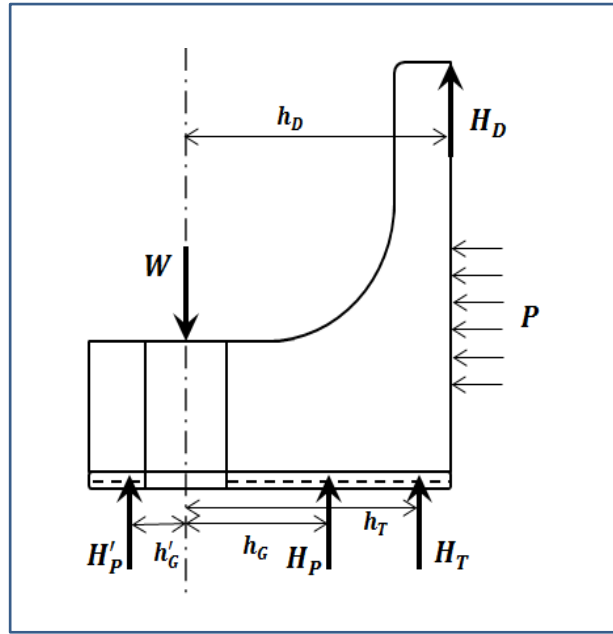


Fig. 3.4: Flange under operating conditions

The minimum gasket load required ( $H_P$ ) is equal to:

$$H_P = 2b\pi GmP \quad \dots (3.16)$$

$$b = (C - B)/4 \quad \dots (3.17)$$

And the total adjusted joint-contact surface compression for the gasket flange ( $H'_P$ ) is:

$$H'_P = \left( \frac{h_G}{h'_G} \right) H_G \quad \dots (3.18)$$

#### 3.4.5.1 Bolted load during operating conditions

When designing the bolted flange connection, it is necessary to calculate the minimum required bolt load for the operating conditions ( $W_{m1}$ ) based on the requirement for a particular situation. Therefore, the minimum bolt load required for the design conditions is:

$$W_{m1} = H_P + H + H'_P \quad \dots (3.19)$$

The bolting area required for the operating condition ( $A_1$ ) is:

$$A_1 = \frac{W_{m1}}{S_b} \quad \dots (3.20)$$

So, the total cross-section area required for the bolt is:

$$A_m = \text{Greater ( } A_1 \text{ or } A_2 \text{)} \quad \dots (3.21)$$

Based on the value of  $A_m$ ,  $A_B$  will be calculated by summing up the areas of the selected bolts at the root diameter of a thread or section of least diameter under stress.

The flange design bolt load ( $W_a$ ) can be determined from the following equation:

$$W_a = 0.5 (A_m + A_B) S_a \quad \dots (3.22)$$

### 3.4.5.2 Flange moment during operating conditions

The moment acts on the flange during the operating conditions is produced by the hydrostatic force, so the component of the moment due to the  $H_D$  is:

$$M_D = H_D h_D \quad \dots (3.23)$$

And the component of the moment due to the hydrostatic force under the gasket ( $H_T$ ) is

$$M_T = H_T h_T \quad \dots (3.24)$$

The total moment during the operating conditions is

$$M_o = M_D + M_T \quad \dots (3.25)$$

### 3.4.6 Flange stresses calculations

The flange stresses in three directions (axial, radial and tangential or hoop) have been calculated using the following equations:

The radial stress at the bolt hole ( $S_{RAD}$ ):

$$S_{RAD} = \frac{6M_G}{t^2(\pi C - Nd_1)} < allowable \quad \dots (3.26)$$

The radial flange stress ( $S_R$ ):

$$S_R = \frac{\beta M}{\lambda t^2} < allowable \quad \dots (3.27)$$

$$M = \frac{M_{max}}{B} \quad \dots (3.28)$$

The hub stress ( $S_H$ ):

$$S_H = \frac{M}{\lambda g_1^2} < allowable \quad \dots (3.29)$$

And the tangential or hoop stress ( $S_T$ ):

$$S_T = \left( \frac{MY}{t^2} \right) - ZS_R < allowable \quad \dots (3.30)$$

Where,

$t$ : The flange thickness

$N$ : Number of bolts

$d_1$ : Bolt hole diameter

$\beta$ ,  $\lambda$ ,  $Y$ , and  $Z$ : Shape factors that are obtained from the chart figures in the code.

### 3.5 Design loads

The design internal pressure for bolted flange joint for this study has been chosen to be 3.4 bar and it will be varied to investigate its effect. Based on the selected design pressure, inside flange diameter, gasket materials and the comprehensive analytical approach of the ASME code, the flange dimensions and the bolt load have been found. As the outside diameter is variable in this study, the bolt load has been calculated at outside diameter of 300 mm and 320 mm as 9.69 kN and 7.4 kN respectively. However, the bolt load is variable in this study but the above is the design bolt load.

### 3.6 Summary

The current chapter includes the design parameters and the comprehensive analytical approach of the ASME code for the glass fibre reinforced polymer bolted flange joint. The design parameters have been divided into groups, which are design variables and design constants. The design includes flange and hub dimensions, gasket materials and thickness and the applied load, which are bolt and internal pressure loads. The design constants involve the fixed parameters in this study, which are the flange inside diameter and the flange materials (i.e. glass fibre braid and polyester). In addition, other parameters have been neglected such as the external loads as well as the number of bolts. The analytical approach includes all the required equations for calculating all the flange loads, moments and stresses during the gasket seating (bolt up) conditions and the operating conditions.

The next chapter will describe all the details of the manufacturing process for the bolted GFRP flange joint including the designing and the manufacturing the required mould and all the required components for making the pressure vessel.

## CHAPTER FOUR

# GFRP FLANGE FABRICATION

### 4.1 Introduction

Producing any product with high quality and performance requires many steps. These steps are understanding the conditions of the intended application, choosing suitable materials, identifying the tools required for design and manufacture and selecting the suitable fabrication process. In terms of the conditions, the product should have sufficient resistances against the internal and the external conditions. For instance, choosing the composite materials instead of metal for oil and gas industries due to their high strength to weight ratio, corrosion resistance etc. Also, the structure of the fabric should be selected carefully to optimize the mechanical properties of the composites. The required tool such as the mould for the GFRP flange should be designed and manufactured with high quality to achieve the requirements of the flange. For the manufacturing process, it should also achieve the design requirements and be quicker as well as cheapest.

In the present chapter, an experimental investigation is conducted to manufacture a GFRP bolted flange by using glass fibre braid, polyester resin, vacuum infusion process and the designed and manufactured mould. This particular type of fabric has

been chosen in this study because of its continuity over the entire flange body. Therefore, it is anticipated that the failure that usually occurs at the flange-hub intersections due to the discontinuity of fibres in this region will be minimised. In addition, a number of experiments have been conducted to improve the method of flange fabrication thus to obtain a composite flange with high quality and performance.

## **4.2 Mould design**

Designing the mould is one of the important factors that has significant effects on the manufacturing of composite flange using vacuum infusion process. Therefore, designing and manufacturing the mould with high quality not only determines the inherent quality of the composite material, but also controls the surface grade of the composite. Furthermore, appropriate mould plays a significant role in maximising the properties of the composite material that are greatly affected by fabricating process. In this study, the mould has been designed and manufactured with mainly two parts to facilitate the flange removal from the mould after the curing. These parts are the mandrel and the plate, as well as the O-ring gasket and the bolts.

### **4.2.1 Mandrel**

The mandrel has been made of aluminium bar with 7" diameter. Aluminium alloy material (6082 T6) has been chosen due to its sufficient strength and dimensional stability to withstand the bag pressure loads and compressive load during the forming and curing cycles. To achieve the required dimensions, the rod is machined and tapered from one edge as shown in the Fig. 4.1. The purpose of this taper, which is equal to  $1.75^\circ$ , is to achieve the requirements of the taper-taper joint between the flange and the pipe and also to facilitate the removal of the flange from the mould and to avoid the stacking problem or damage to the flange. The external surface of the mandrel that is in contact with composite is subjected to surface finishing process to remove all asperities that increase the chance of the flange mould bonding and also to obtain a flange with good internal surface. This will improve the bond strength between the flange and the pipe. In addition, the tapered end face of the mandrel has been machined to create a groove for a O-ring gasket (3.53 mm of cross

sectional diameter) and four holes with threads have been created for inserting the bolts during assembly.

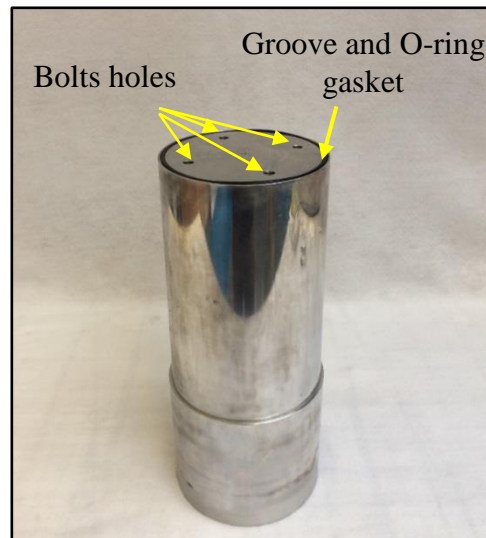


Fig. 4.1: The mandrel

#### 4.2.2 Plate

The second main part of the mould is the plate, which is placed at the bottom and in direct contact with the lower flange face. Therefore, it requires a good surface finish to avoid sticking over this area. Initially, the plate has been made of aluminium alloy (6082 T6) with dimensions 650 mm x 650 mm x 10 mm and 4 holes have been drilled around the centre of the plate for the assembly purposes. During the infusion process, the resin flow has been found as problematic and this will be discussed in details later. This led to change the aluminium plate by another one that has been made of glass. See Fig. 4.2. The reason of choosing glass material is to observe the resin flow during the infusion process and find the best inlet and outlet positions for the resin.

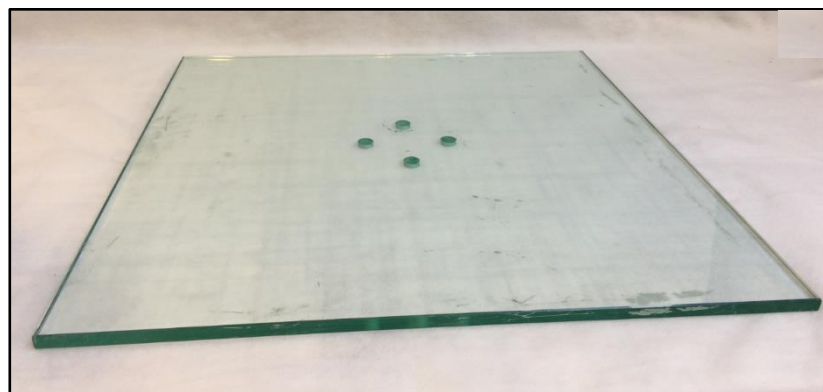


Fig. 4.2: The glass plate



### 4.2.3 The mould assembly

As showing in the Fig. 4.3, the parts of the mould have been assembled by using four bolts of size M10 as well as O-ring rubber gasket. These bolts pass through the plate holes and are fastened to the identical holes that have been drilled in the taper end face of the mandrel by using a thread tool. Before the assembly, the gasket has been fitted in the groove. The purpose of using this gasket is to prohibit the leakage through holes of the bolts during the vacuum and to prevent the resin from reaching the contact area between the mandrel and the plate during the infusion.

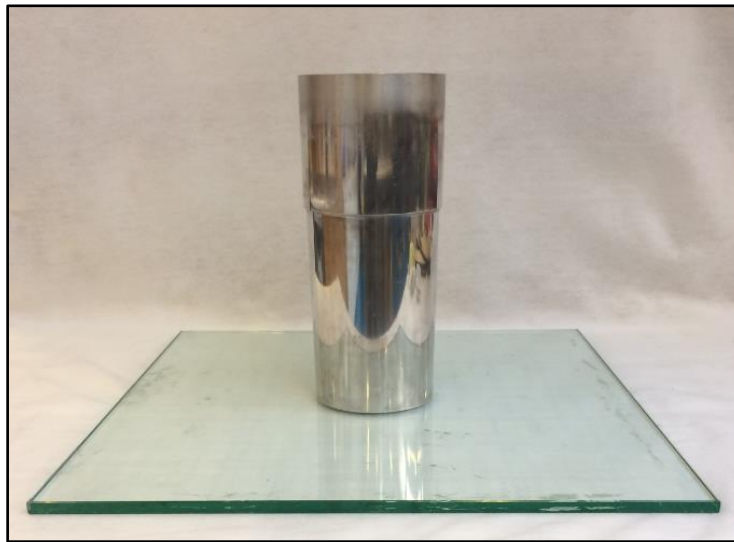


Fig. 4.3: The Mould of the composite flange

### 4.3 GFRP Flange fabrication

As mentioned earlier, the vacuum infusion process (bag moulding) has been chosen to manufacture the composite flange of 6-inch nominal diameter. This manufacturing method has been selected due to its flexibility for manufacturing composite with complex geometry. It is unexpansive and it provides good strength compare with other methods such as hand layup or RTM, which also require close system mould. Fig. 4.4 illustrates a schematic of manufacturing GFRP flange by using a vacuum infusion process. This manufacturing process has included a number of steps which are described briefly as follows:

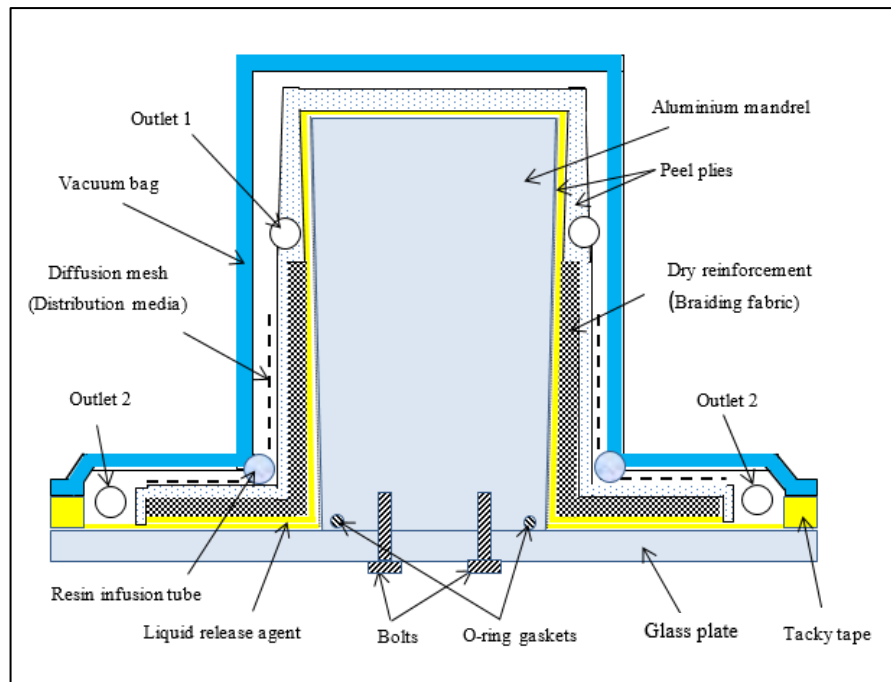


Fig. 4.4: Schematic diagram of the vacuum infusion process

1. **Release agent:** after assembling the mould parts, all its surfaces that are in contact with the composite flange are coated with a released agent (FREKOTE 770-NC PT CN) to avoid composite sticking and to facilitate the removal of flange from the mould. In addition, to stop any reaction between the resin and the mould materials, which might affect on the composite mechanical properties.
2. **Peel ply:** the peel ply is used in two instances. At the first instance, it is used to cover the surface of the mould, which is in contact with the flange before putting the fabric. This helps the trapped air bubbles between the fabric and the mould to leave during the vacuum and the resin infusion, thereby, reducing the voids or porosities and improving the mechanical properties of the composite flange. The other purpose of using the first peel ply is to leave an imprint or pattern on the flange surface to enhance adhesive bonding between the flange and the pipe. In addition, to increase the coefficient of friction between the rubber gasket and the flange face and preventing the pushing out of the gasket during the operating condition.

For the second instance, it is used between the fabric and the diffusion mesh as well as the bag to prevent them from sticking to the composite flange after the curing action and to improve the outer surface finish of the flange.

3. **Fabric layup:** braid fibreglass has been chosen to fabricate the composite flange in this study. This type of the fabric has been chosen due to its continuity from the hub to the flange around the entire flange (flange neck) and the continuity in the radial and hoop directions, which minimize the flange rotation under the uneven distribution of the bolt loads. In addition, this will reduce the bending moment, thereby reducing the flange rotation that encourages the leakage propagation. A number of previous studies [33] [9] have indicated that the most common types of failures in commercially available GRP flanges manufactured by hand lay-up or filament winding processes occur at the flange-hub intersections, due to the discontinuity of fibres in this region. See Fig. 4.5. The layers of the braid fibreglass sleeves are laid up over the mandrel and expanded out over the plate more than the required diameter of the flange as shown in Fig. 4.6. This process is repeated many times until the required thickness is achieved.

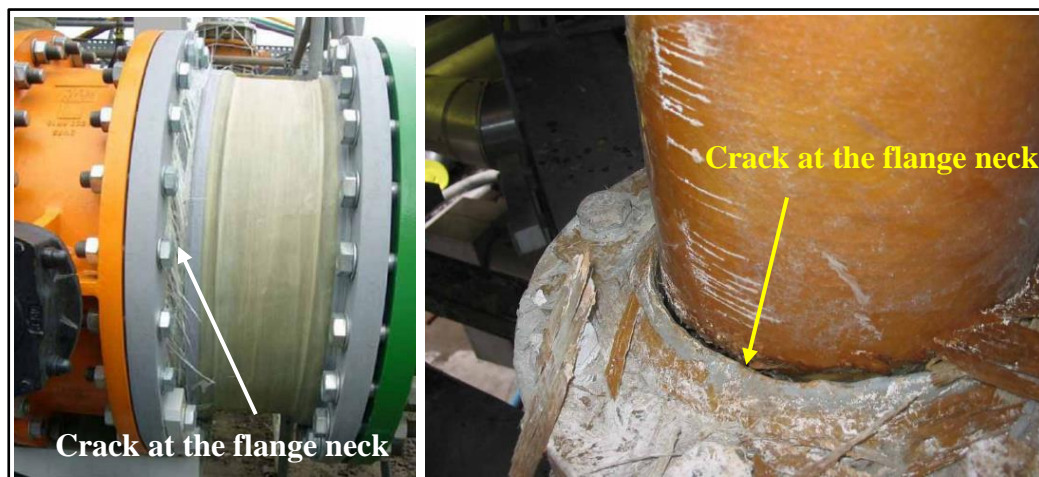


Fig. 4.5: Common failure on the GFRP flanges [33]

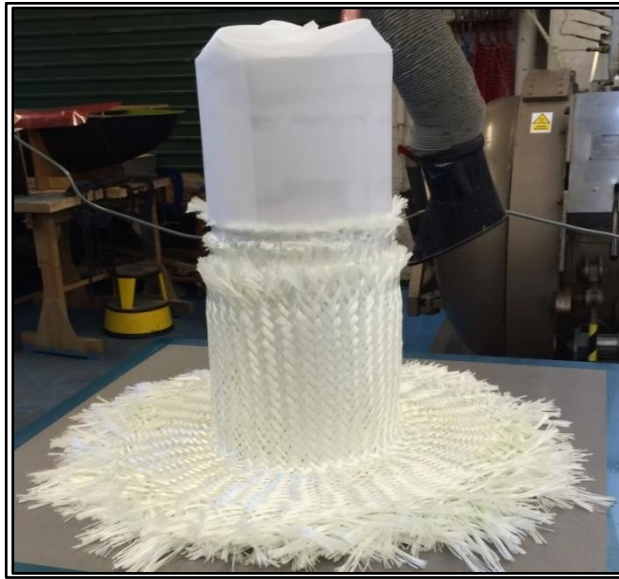


Fig. 4.6: Laid braided fiberglass fabric on the mandrel and the plate

4. **Diffusion mesh:** after covering the fabric by a peel ply as explained earlier, a diffusion mesh (breather) is placed to ensure that all air pockets are eliminated and to facilitate the flow of the resin from the inlet tube, which is placed near the neck of the flange during the infusion process, to the outlets. See Fig. 4.7.
5. **Vacuum infusion process:** a flexible bag is used to cover all the components. The edges of the bag are stacked on the edges of the plate to close the system as shown in the Fig. 4.8. Meanwhile, the outlets of the infusion process have been kept fixed at the top and along the outer diameter of the flange. After that, a vacuum is applied and the polyester resin, which is mixed with 1% of a catalyst, is infused through the inlet of the system. In addition, the vacuum process is continued until the flange is completely cured at the room temperature. After the curing, the vacuum process is stopped, vacuum bag, diffusion mesh, and peel ply all are stripped off and the flange is removed from the mould.

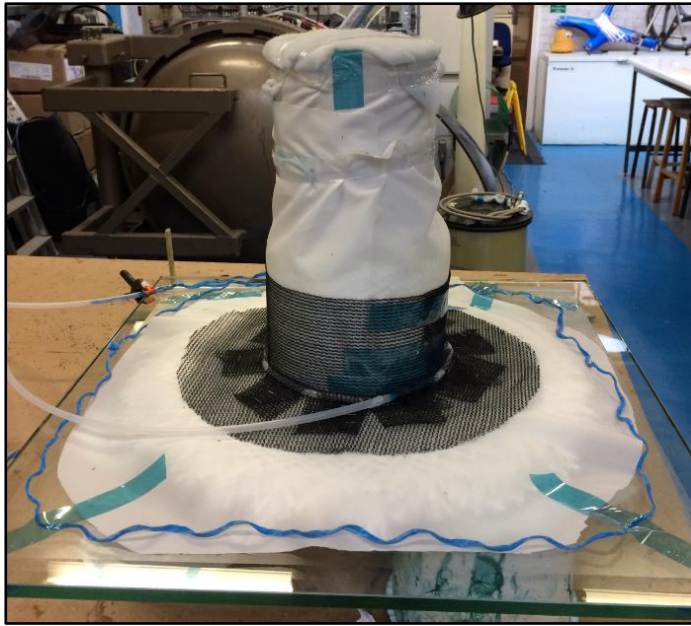


Fig. 4.7: Diffusion mesh distribution



Fig. 4.8: Bagging and resin infusion

6. **Flange machining:** as the wastage of the braiding at the edges cannot be avoided, initially the braiding fabric has been kept larger than the required physical dimensions of the flange and finally has been shortened by cutting off the unwanted regions of the manufactured flange as can be seen in Fig. 4.9.



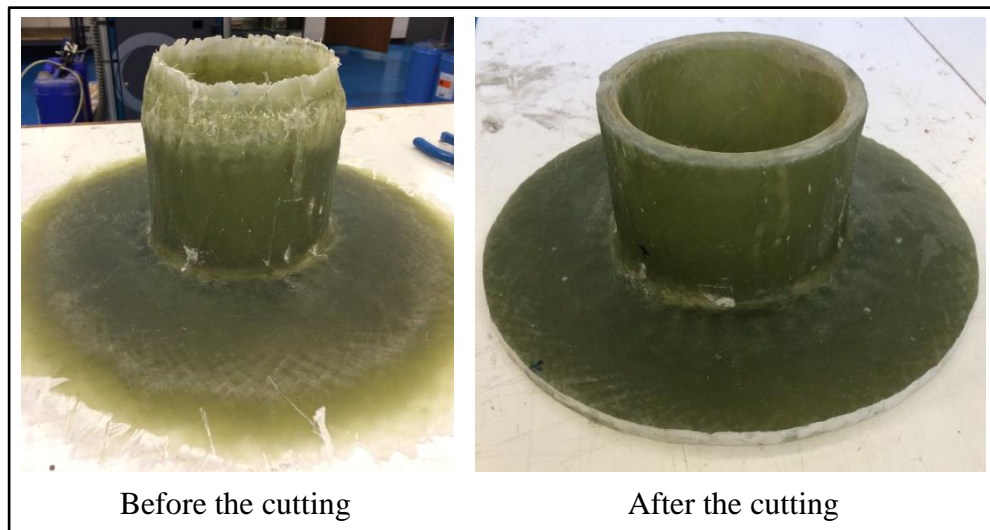


Fig. 4.9: Machining of the composite flange

#### 4.4 Issues with the manufacturing process

During the manufacturing of the GFRP flange, two issues have been identified: (1) dry region and (2) voids and cracks at the flange neck. Details of these issues are discussed below.

##### 4.4.1 Resin flow problem

The main issue that has been faced during the GFRP flange fabrication process is the dry region (inadequate resin flow). This has led to have dry regions around the diameter of the bolts holes circle and at the lower face as illustrated in Fig. 4.10. Initially, the inlet of the resin has been placed at the outer diameter or edge of the flange disc while the outlet has been fixed on the top. The first flow flows from the flange edge (outer diameter) toward the centre through the diffusion mesh and the other, reverse flow, flows from the internal diameter of the flange toward the outer diameter of the flange and at the bottom face of the flange. The arrangement forces the resin to flow in the opposite directions and produces trapped air at the meeting regions. Thus, the resin doesn't fill the meeting regions properly and leads to have dry regions.

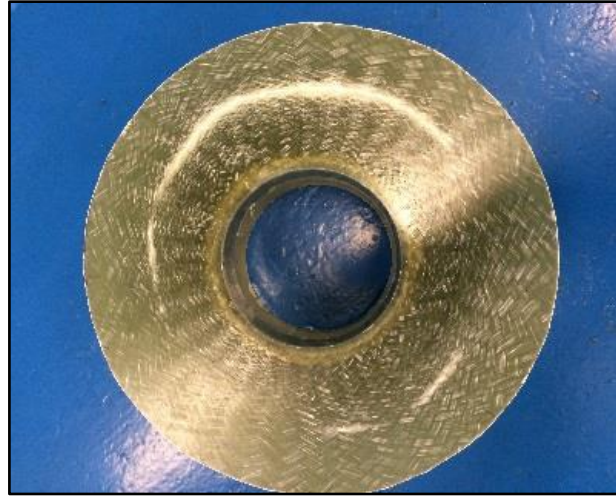


Fig. 4.10: Flange with dry regions on the face

#### 4.4.2 Voids and cracks problem

After curing the composite flange, it has been cut into many pieces for a number of purposes such as performing mechanical tests, measuring the fibre volume fraction ( $V_f$ ) and capturing optical microscopy images. In order to investigate the voids and the cracks, many samples have been taken from the flange-hub region (flange neck), which represents the critical point in the flange. Fig. 4.11 shows an image of the flange neck region. It can be seen that many voids and cracks occur at this region when the inlet of the infusion was in the flange edge and the outlet was in the top of the flange. This case is named as Model A, which will be discussed elaborately later. In addition, most of the voids and cracks were found close to the upper face of the flange. This occurs due to the resin shrinkage and exothermal behaviours at the flange neck. As this region connects the flange and the hub, it experiences the most effects of the flange shrinkage. Also, it is the thickest part in the flange, thus high temperature is produced due to exothermal reaction.

The reason of concentrating the voids and the cracks at the upper half of the flange is that the lower surface and the internal faces of the flange are bigger than the upper face and they have direct contacts with the mould, which is made of aluminium and glass. The mould helps to cool the composite by transferring the heat through it to

the environment. In contrast, the upper face of the flange-hub intersection area is less and covered by peel ply and the vacuum bag, which are inhibiting the heat transfer. Therefore, the amount of the transferred heat from the lower and the internal faces of the flange is more than that from the upper face. As a result, most of the voids and the cracks have been formed at the upper half of the composite instead of the lower half.

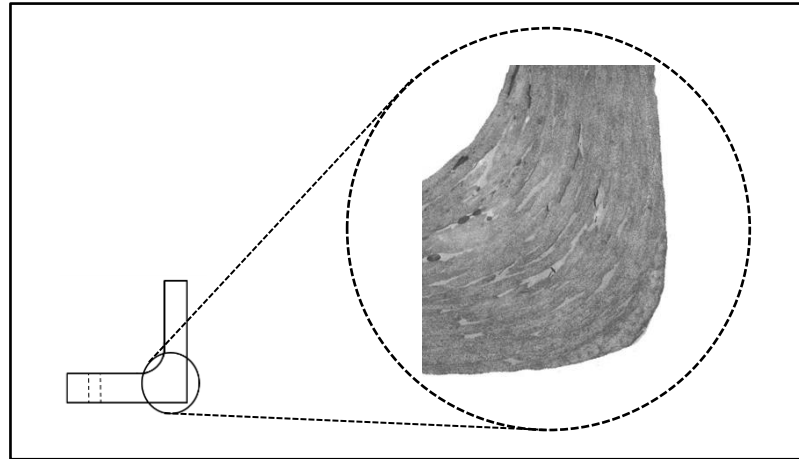


Fig. 4.11: Microscopy image for the flange-hub intersection

## 4.5 Solving the issues

To solve or minimize the issues faced during manufacturing the GFRP flange, two investigations have been carried out. The first investigation, which involves substantial number of experiments studies the effect of the inlet and the outlet positions on the formation of the dry areas, voids and cracks. The other investigation is conducted by changing the infusion temperature to study its influence on the viscosity of the resin.

### 4.5.1 Inlet and outlet positions

Changing the inlet and the outlet positions is one of the important parameter that has significant effect on flange strength and especially on the faced issues, i.e. dry region, voids and cracks. To do this investigation, another mould has been manufactured using just glass material as shown in the Fig. 4.12. This mould has allowed to see all the resin flow in the regions.

In addition, in each experiment, a portion of the flange has been fabricated as illustrated in the Fig. 4.13 using the same fabric, resin and manufacturing process.



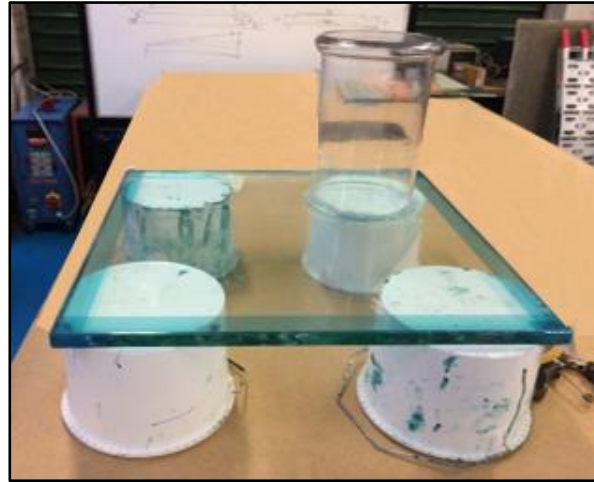


Fig. 4.12: Glass mould of the experiments

Three experiments (Model A, Model B and Model C) with different inlet and outlet positions, which are shown in the Fig. 4.14, have been carried out. Model A has the inlet at the flange edge and the outlet in the top of the flange as shown earlier in the above sections. Model B has the inlet at the top of the flange and the outlet at the flange disc edge. The third one is model C that includes the inlet at the flange neck and two outlets- one at the flange disc edge and the other at the top of the flange hub. The results showed that the model C has achieved the best resin flow and also quicker than the other models. This helps to distribute the resin over all the flange body within a short time and avoid any dry fabric which occurred with the model A. (See Fig. 4.15).



Fig. 4.13: The vacuum infusion process of the experiments

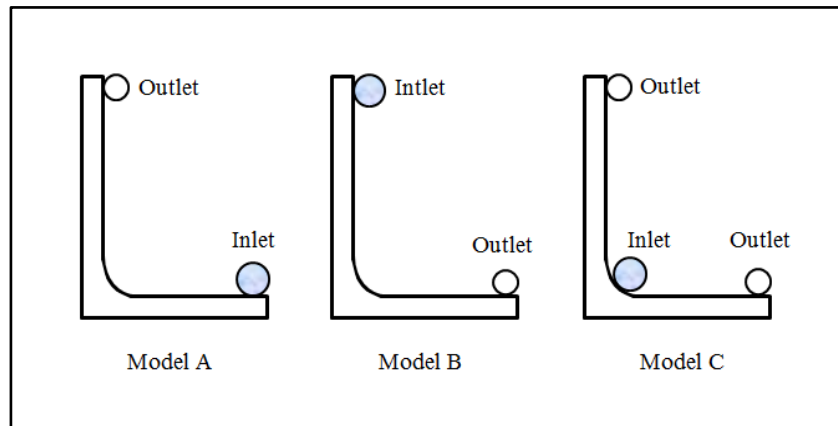


Fig. 4.14: Inlet & outlet positions of the conducted experiments

In addition, the voids and the cracks percentages have been calculated by using Image J software for the samples that have been cut from the the neck of the flange (flange-hub intersection) for each experiment as shown in the Fig. 4.16. The obtained results showed that the voids and the crack precentages have been reduced significantly with the Model C (4.3% for Model A, 4.24% for Model B and 1.58% for Model C). This has been taken into account to choose Model C for manufacturing the final form of the composite flange.

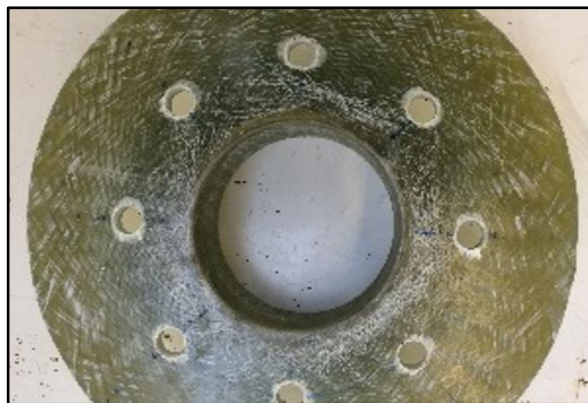


Fig. 4.15: Flange without dry fabric on the face

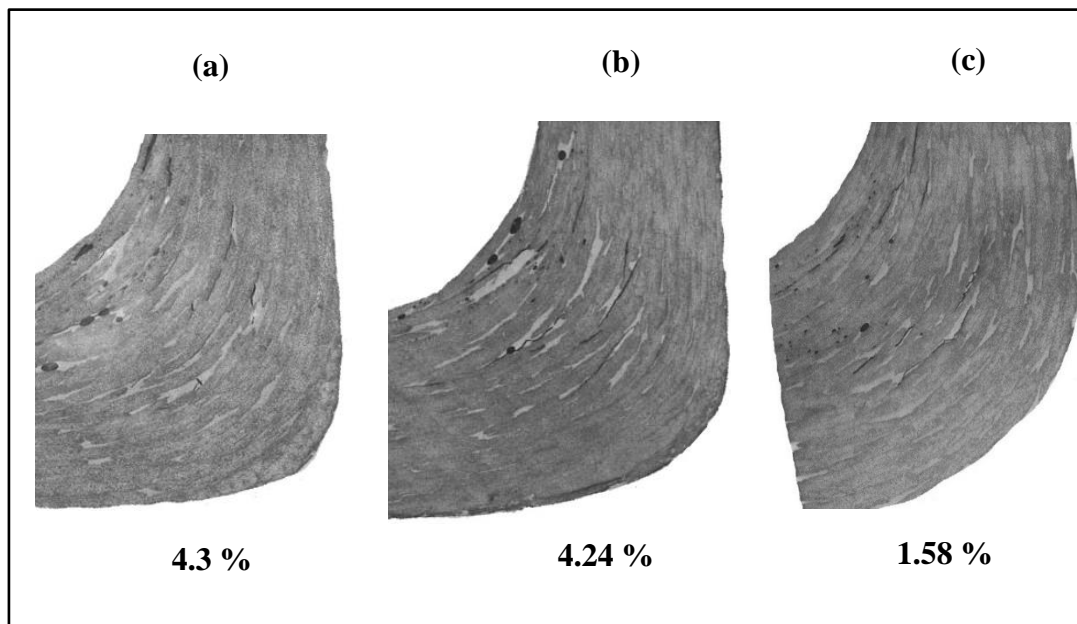


Fig. 4.16: Microscope images at the flange-hub intersection (a) model A, (b) model B, (c) model C.

Furthermore, the temperatures at the flange–hub intersection and through the thickness have been monitored for the Model C during the infusion and throughout the curing. This is done by embedding a thermocouple through the composite layers at the aforementioned position, which is illustrated in the Fig. 4.17. This region has been chosen because it is the thickest and expected hottest part in the flange body due to small surface area, which limits the heat transfer. The variation of the temperature with time has been shown in the Fig. 4.18. The results showed that the temperature has increased during the first three hours but decreased later. The room temperature was  $18.3^{\circ}\text{C}$ . The maximum temperature was  $31.2^{\circ}\text{C}$  after three hours from the starting time. This is because of the exothermal reaction during the curing of the resin. However, the variation range was not high enough in this model (C) and that was because of the position of the inlet resin infusion. This helps to cool this part by transferring the heat from this part to the others through the resin, which flow through this region. This in turn helped to reduce the voids and crack in this part for the model C.

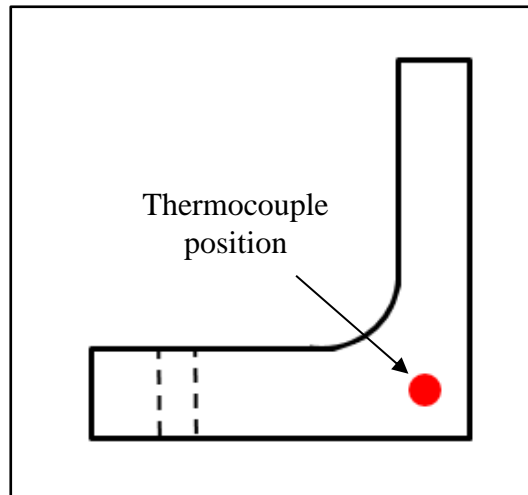


Fig. 4.17: Thermocouple position in the flange-hub intersection

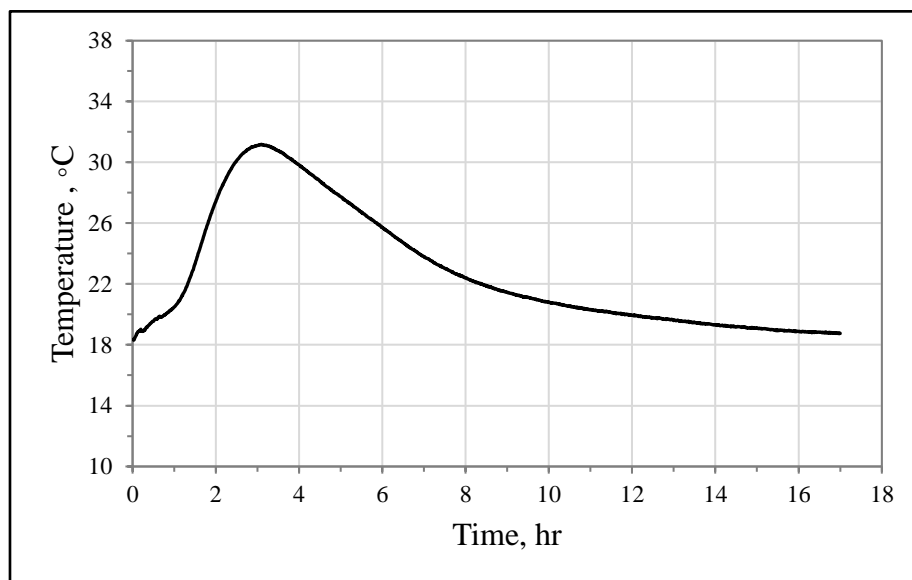


Fig. 4.18: The temperature variation during the infusion and curing process at the flange-hub intersection

#### 4.5.2 Resin Viscosity

The viscosity of the resin has also significant impact on the resin flow and on the curing time. The resin viscosity can be changed by varying the temperature. Therefore, series of experiments have been conducted to find out the best infusion temperature that reduces the viscosity and facilitates the flow of the resin through the layers of the fabric. The experiments have been carried out using the Brookfield rheometer machine for the polyester resin with zero% and 1% catalysts at various

ranges of temperature. The resin without catalyst has been tested to see the effect of the evaporation on the resin viscosity. The 1 % catalyst has been chosen because the manufacturer has recommended the ideal range of the catalyst as 1-2%. Therefore, it has been fixed to 1% to increase the curing time thereby ensuring good distribution of the resin.

Fig. 4.19 explains the viscosity variation of the resin with the time for various ranges of temperature. The results show that the viscosity increases from 0.25 Pas to almost 2.2 Pas during the first 30 minutes of the time regardless the temperature. After that, the recorded viscosity has decreased. In reality, it should not decrease but it has been happened as the resin film has been separated into two layers. One of them has stucked onto the upper plate and the other stucked onto the lower plate of the device. The recorded viscosity after the peak is affected by the friction between the two layers. The temperature has insignificant effect on the viscosity when the resin is used without catalyst.

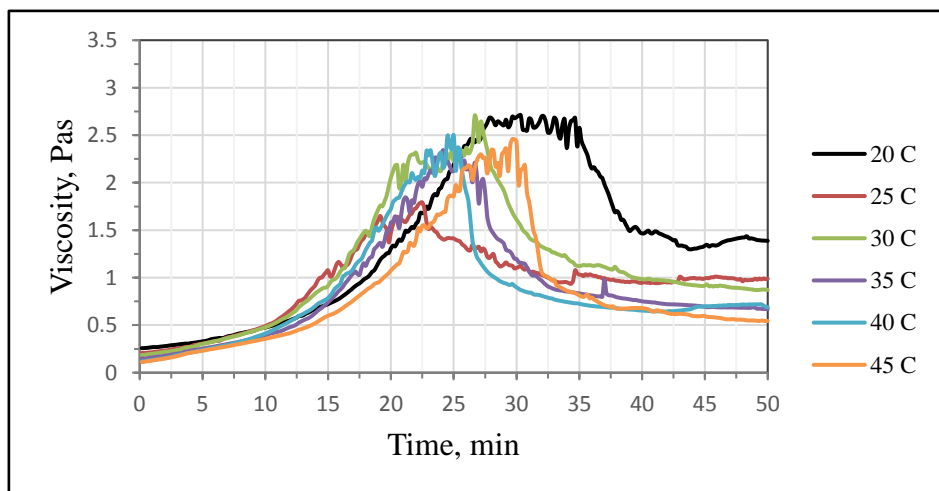


Fig. 4.19: The variation of the polyester viscosity with the time at different temperature (without catalyst).

Fig. 4.20 illustrates the variation of the resin viscosity with time for different temperatures (20 to 50° C) for the resin mixed with 1% of the catalyst. It seems that the temperature has significant effect on the resin viscosity. At the high temperatures, 35 to 50° C, the resin viscosity is increased rapidly and the resin is cured quickly. In addition, the torque has reached the maximum allowable torque of the device and the break has occurred. The time of the break decreases with the increase in the

temperature. At the temperatures 25 and 30° C, the viscosity has increased up to 2.5 Pas during the first 30 minutes but dropped after that. This means the resin film has splitted into two layers. At the room temperature (20° C), the viscosity has also increased up to 2.5 Pas during the first 35 minutes and reduced gradually after that. The longest period with less viscosity has been achieved at the temperature 20° C. Therefore, this temperature has been chosen to infuse the composite flange. This temperature allows the resin to distribute gradually over all regions of the fabric before curing. Furthermore, it lets the trapped air to move and leave the resin. Finally, at the room temperature, it does not require any heating system thus makes the manufacturing process efficient and reduces the costs.

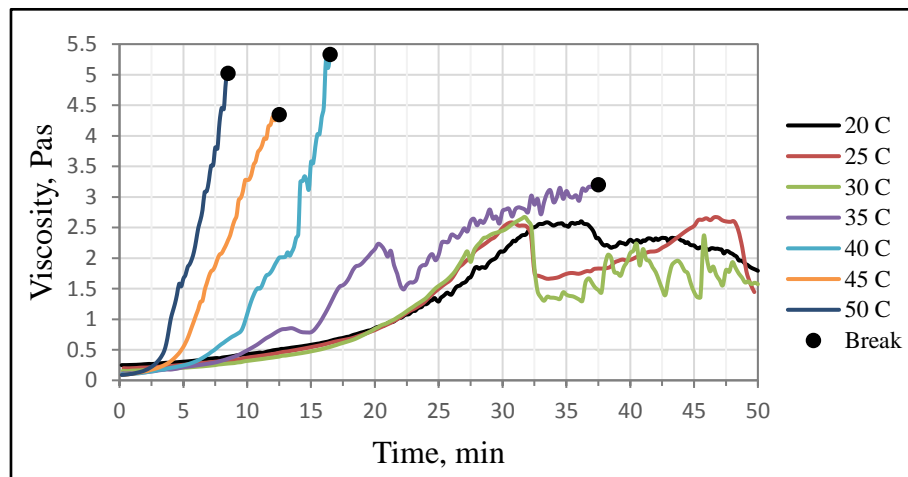


Fig. 4.20: The variation of the polyester viscosity with the time at different temperature (1% catalyst)

#### 4.6 Composite flange drilling

Drilling the composite flange is one of the main fabrication steps after the curing. The bolts holes are also critical regions in the GFRP flange due to the applied bolt force. So that the holes performance have significant effect on the flange performance as most of the maximum strains concentrate at the bolts holes. In addition, it was found that the flange with drilled bolts holes performed better, in terms of strength, than those with moulded holes [91]. A number of researchers [9, 100] have carried out comparative studies on the drilling of the glass fibre reinforced plastics (GFRP), which are manufactured by hand lay-up, using Stub Length drill

and Brad & Spur K10 drill. They found that the Brad & Spur K10 drill produced less damage on the GFRP composite than the Stub Length.

In this study, a comparative study has been conducted using two types of drilling tools with the same cutting conditions for a GFRP plate made of the same fabric and the resin which have been used to manufacture the flange. These tools are Erbauer diamond tile drill bit and Brad & Spur K10 drill, which are illustrated in the Fig. 4.21. The Brad & Spur K10 drill has been recommended by Davim et al [100]. During the drilling, a wood plate has been used under the composite flange. The purpose of this plate is to support the composite flange laminate and minimize the push-out delamination. The results have been evaluated in both sides (Inlet and Outlet). As shown in the Fig. 4.22, the Erbauer diamond tile drill bit has produced a hole with less damage and better than the Brad & Spur K10 drill in the both sides i.e. the inlet and the outlet of the hole. Therefore, Erbauer diamond tile drill has been chosen to drill the holes of the bolts for the composite flange used in this study.

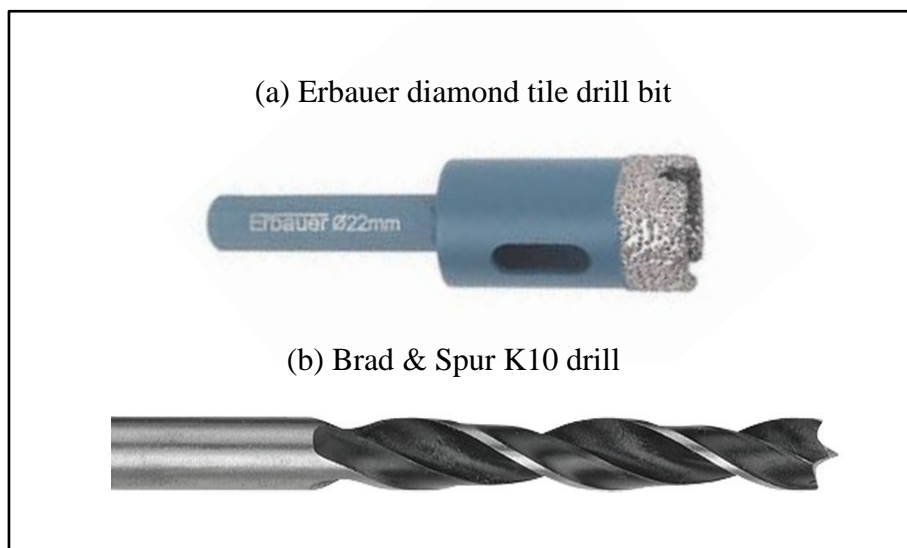


Fig. 4.21: Drilling tools of the composite



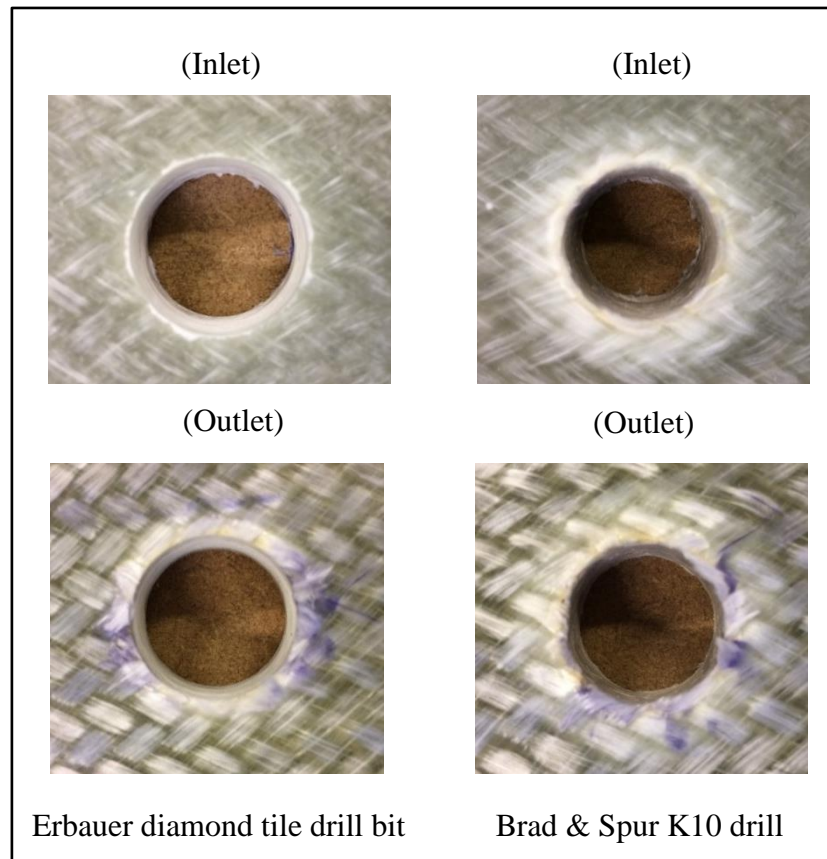


Fig. 4.22: 22 mm drilled holes of used tools in the experimental work

In addition, other experiments have been conducted to find out the best rotation speed for the Erbauer diamond tile drill bit. Various speeds, e.g. 600, 800, 1200 and 2200 rpm have been used to drill the same composite laminate as shown in the Fig. 4.23. The findings show that the best hole in both sides has been achieved at the rotation speed of 800 rpm as illustrated in the Fig. 4.24. During drilling, water has been used to reduce the heat and to avoid the burning of the composite around the holes.



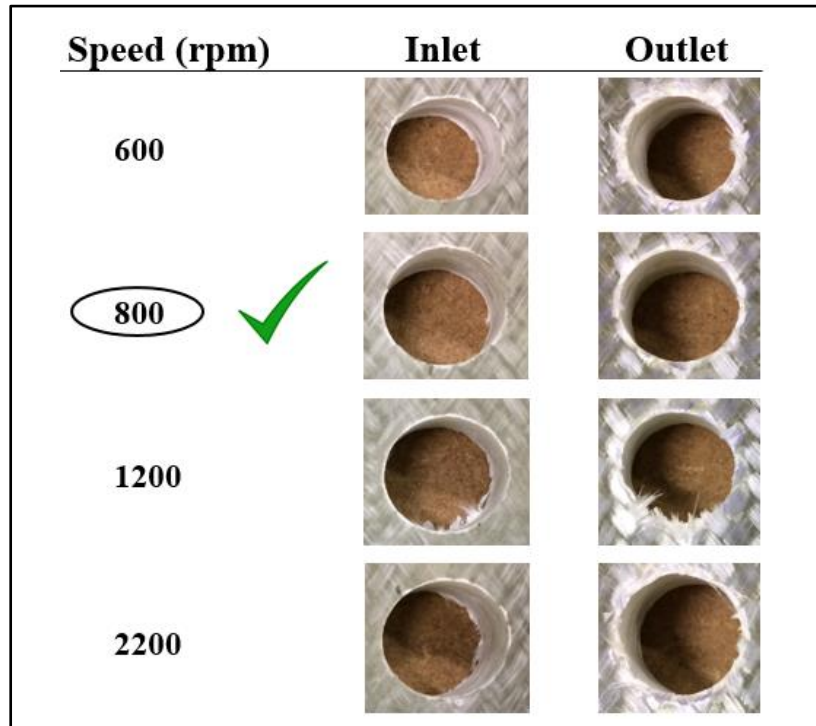


Fig. 4.23: Drilled holes with different speeds

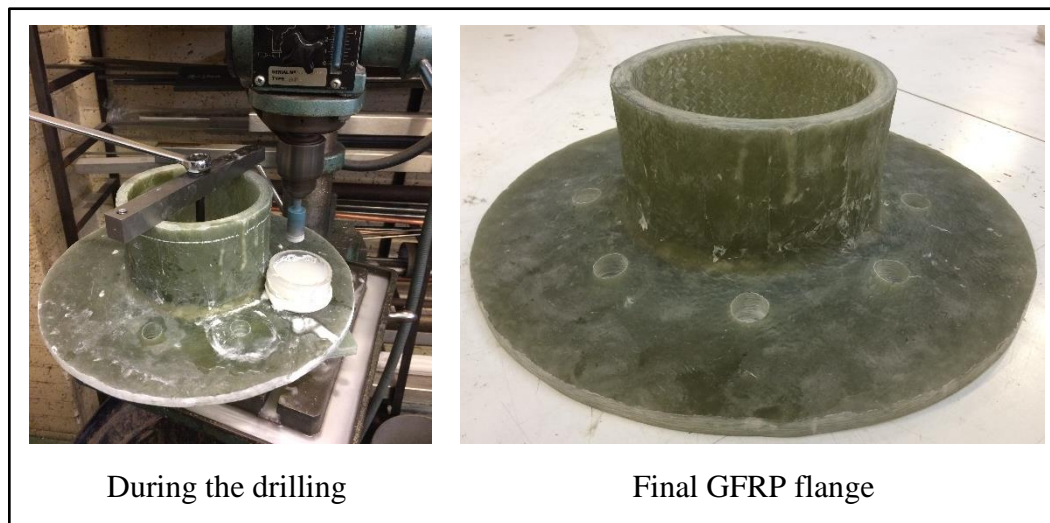


Fig. 4.24: During the drilled and the final GFRP flange

#### 4.7 Flange-pipe adhesive bonding

Flange-pipe bonding is important and it has been done through many steps. Firstly, the filament winding pipe shown in Fig. 4.25 has been chamfered at its ends to achieve the requirements of the taper-taper joint between the flange and the pipe. The internal face of the flange has been sanded to improve the bonding strength.

Epoxy adhesive (PSX<sup>®</sup>-60), which is provided by a commercial company Pipex, has been used. The adhesive bonding was reinforced by steel particles and other. Secondly, an axial force has been applied using hand puller winch to combine the flange and the pipe. The purpose of using this tool is to apply axial force on the flange-pipe joint during the bonding process. This force leads to increase the contact surface area between the flange, the pipe and the adhesive, subsequently maximizes the strength of the adhesively bonded joint. A heating blanket has been placed at the inside of the joint. The purpose of the electric heating blanket is to heat up the joint and keep the temperature constant at 130°C, (as recommended by the supplier) during the curing process. Fig. 4.26 shows the flange-pipe joint after the bonding.



Fig. 4.25: Chamfering the composite pipe



Fig. 4.26: Flange-pipe bonding

#### 4.8 Other end of the pipe

The other end of the pipe has been closed by using a Heavy Duty (HD) flange supplied and bonded by Pipex in addition to the adhesive bonding. This end of the pipe has been chamfered by the same method as is used for the other end of the pipe. The applied chamfering method has been described in earlier sections. See Fig. 4.27 (b).

#### 4.9 Blind flanges

Two blind flanges have been used to close the ends of the pipe, which have been bonded with the fabricated flange in one end and the HD flange in other end of the pipe. The blind flange, which is used for closing the fabricated flange, has been made of Acrylic material of thickness 50 mm as shown in the Fig. 4.27 (a). The reason for choosing this type of the material is that it is strong and provides clear views for flow observations across the compressed gasket and the leakage propagation. Unfortunately, the leakage propagations have taken place between the gasket and the flange, which cannot be seen. However, the blind flange has been made as thick as possible to avoid any deformation on the blind flange. Eight holes, which are identical with holes of the flanges have been made to insert the bolts. Initially, water jet cutter (Flow Mach 2 203Ib) has been used to make the holes but unfortunately, many cracks around the holes have been appeared. As a result, a CNC machine has been used instead of the water jet cutter to make holes for the bolts.

The blind flange for the other end, which is bonded to the HD flange, has been made of mild steel of thickness 25 mm. Eight holes have been made for the bolts. In addition, three holes have been drilled for the inlet, outlet and the pressure gauge. See Fig. 4.27 (b).

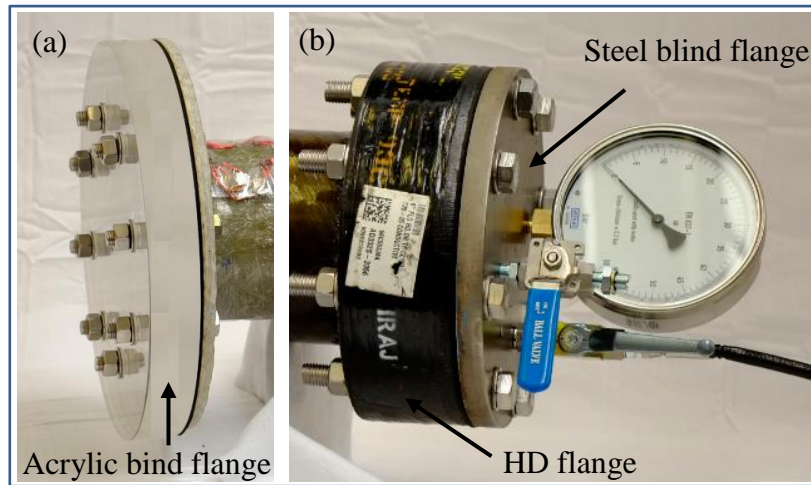


Fig. 4.27: HD and blind flanges: (a) Acrylic blind flange attached to the fabricated flange and (b) HD and steel blind flange attached to the HD flange.

#### 4.10 Assembly of the joint components

After manufacturing all the components of the pressure vessel, the final assembly has been carried out as shown in the schematic diagram in the Fig. 4.28. Other tools that have been added to the assembly for conducting the test will be described in the next chapter.

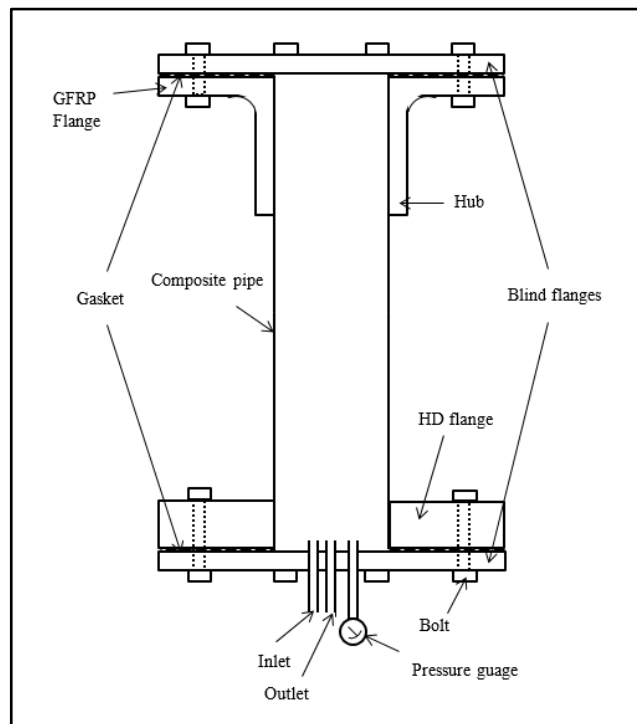


Fig. 4.28: Schematic diagram of the pressure vessel

### 4.11 Summary

A bolted composite flange made of glass fibre braid reinforced polymer provides good solutions to stop the most common types of failures found in commercially-available GFRP flanges manufactured by hand lay-up or filament winding processes. Therefore, in this chapter, the bolted GFRP flanges have been fabricated using a bespoke made mould and vacuum infusion process (bag moulding). In addition, a number of experiments have been conducted to solve the faced issues, to improve the manufacturing process and to obtain a GFRP flange with high quality and strength. Furthermore, to improve the quality of the drilled flange holes, a comparative study has been carried out using two types of drill bits. Several GFRP flanges have been manufactured to conduct the tests discussed in the next chapter where the discussion will be evolved around the experiments of the material characteristics, the fittings, the strain gauges' set up for the composite flange and the bolts and the required test rigs as well as the testing of the pressure vessel.

## CHAPTER FIVE

# EXPERIMENTAL METHODOLOGY

### 5.1 Introduction

The other main part of the experimental work carried out in this study is the testing of the manufactured pressure vessel (bolted GFRP flange joint, which has been discussed in the previous chapter). Experimental testing of the composite flange usually requires many tools and the accuracy of the test depends on the quality of the fabricated product, the tools used and the procedure followed as well as the skills of the persons involved in testing. The required tools can be divided into three groups. The first group includes the tools for all the experiments that lead to perform the materials characterisations of the composite joint system. The second group consists of all the equipment for measuring the required data. These equipment are the strain indicator and recorder, the required software, the strain gauges for the composite flange and the pipe. The third group contains all other rigs, which are necessary for the test, such as fittings, torque wrench, pump and pressure gauge. Therefore, all these tools should be calibrated to ensure the best performances. In addition, the procedure of the test is very important and it has significant influence on the results, therefore, it should be done based on the standards.

In this chapter, all the details of the experimental testing will be discussed including the experiments of the materials characterisations, the required tools for measuring or testing the bolted flange joint, the methods of their calibrations and the procedure of the testing.

## 5.2 Materials characterisations

To specify any composite materials theoretically or numerically, many parameters should be determined initially. These parameters are the fibre volume fraction, fibre direction, the thickness of the layers and the number of each layers. These parameters have been measured experimentally as explained in the following sections.

### 5.2.1 Fibre volume fraction ( $V_f$ )

Fibre volume fraction ( $V_f$ ) has significant effect on the characteristics of the composite materials. Increasing the  $V_f$  leads to increase the strength of the composite materials. To calculate the mechanical properties of the composite flange, the  $V_f$  should be calculated first. Therefore, during the manufacturing process, many samples have been cut from the fabricated flanges for different purposes. Generally, the composite flange has been divided into two main parts, which are flange disc and the hub. Five samples have been taken from each part (flange disc and hub) at different zones. Tangentially, one sample is taken from each zone at every  $72^\circ$ . In total 10 samples of the composite flange were obtained to measure the fibre volume fraction. In addition, five samples of the filament winding pipe have been taken to measure the  $V_f$ . The fibre volume fraction ( $V_f$ ) has been calculated using burn off method (shown in Fig. 5.1) based on the published standard mentioned in the reference [103]. The average for each group of five samples located on the same part are obtained. These average values are used in the calculations of the properties of the composite. All experimental data are shown in the Table 5.1.



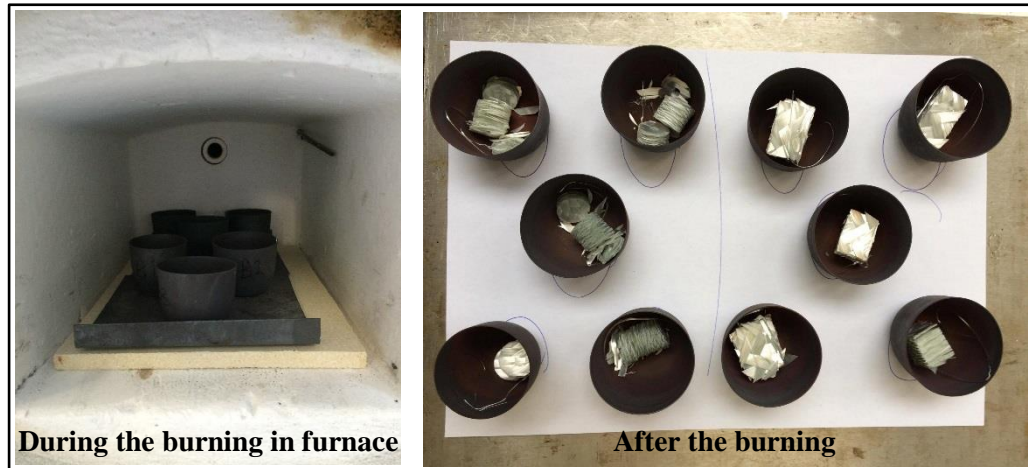
Fig. 5.1: Composite samples for calculating the  $V_f$ 

Table 5.1: Fibre volume fraction experimental data

| Parts<br>Samples | Flange<br>$V_f$ % | Hub<br>$V_f$ % | Pipe<br>$V_f$ % |
|------------------|-------------------|----------------|-----------------|
| Sample 1         | 62.65             | 60.05          | 51.56           |
| Sample 2         | 63.12             | 61.23          | 53.15           |
| Sample 3         | 59.63             | 60.48          | 51.35           |
| Sample 4         | 60.05             | 60.29          | 52.40           |
| Sample 5         | 58.18             | 58.47          | 51.52           |
| STDEVA           | 2.09              | 1.01           | 0.76            |
| Ave. $V_f$ %     | 60.70             | 60.10          | 52              |

### 5.2.2 Fibre orientation (Braiding angle)

After laying up the glass fibre braid over the mould, many images have been taken at different layers of the fabric for each part (flange disc and hub). Then, the images have been analysed using the image J software to measure the fibre angle, which is illustrated in the Fig. 5.2. The results showed that the average braid angle ( $\Theta$ ) of the fibre at the flange disc was  $65^\circ$ , whereas it was  $44.5^\circ$  at the hub region.



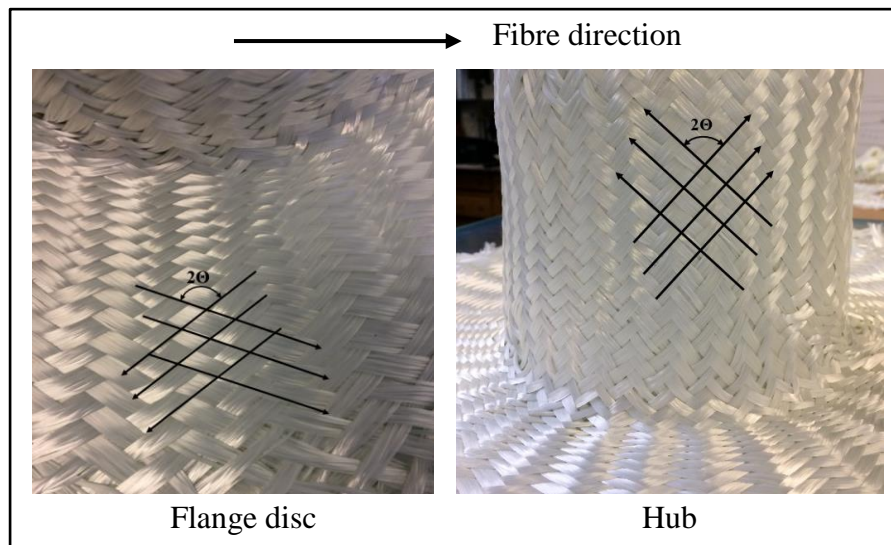


Fig. 5.2: Braiding angle of the flange disc and the hub

Furthermore, the filament-winding angle ( $\Phi$ ) of the composite pipe has been measured experimentally to obtain the accurate value. Many photos have been taken for the used composite pipe and analysed using image J as shown in the Fig. 5.3. The results showed that the average of the filament winding angle is  $\pm 55^\circ$ . This value is the same that is provided by the supplier. Also, it is the optimal angle for the composite pipe subjected to the internal pressure based on many studies [8, 72]. Therefore, it has been used for calculating the mechanical properties of the composite pipe.

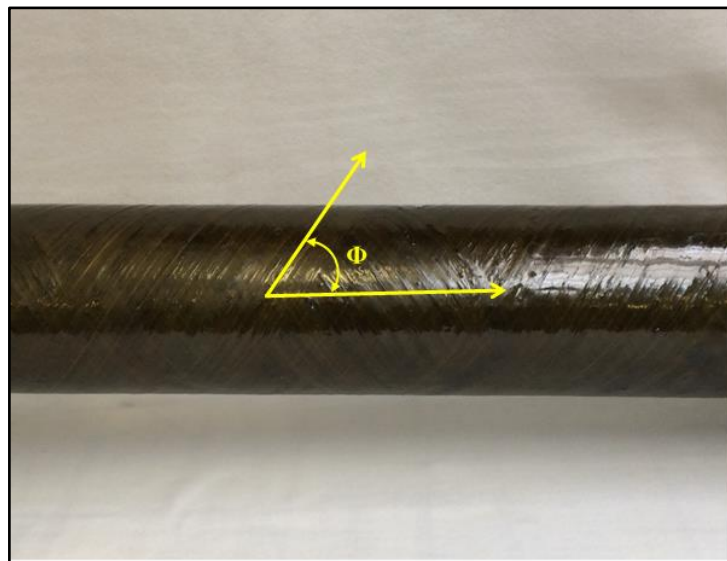


Fig. 5.3: Filament-winding angle of the composite pipe

### 5.2.3 Fibre orientation (Crimp angle)

The crimp angles of the braiding fibreglass have also been investigated in this study. Many samples, which were taken along the fibre direction at the flange disc and the hub, have been analysed using optical microscope after grinding and polishing them as shown in the Fig. 5.4. The crimp angle has been measured for the obtained images using image J software. The results have shown that the average value of the crimp angle for all the samples were less than  $5^\circ$ . Fig. 5.5 shows the influence of the orientation distribution factor on the longitudinal tensile modulus of carbon ( $60\% V_f$ ) and glass ( $50\% V_f$ ) unidirectional composites. It is observed that the crimp angle has insignificant effect on the young's modulus of the glass UD composite at the small values. When the crimp angle is  $9^\circ$ , the effect of the orientation distribution factor on the young's modulus is 5%. In addition, it is very difficult to take into account the effect of the crimp angle on the mechanical properties as there is no software that takes this effect into account. Therefore, the effect of crimp angle has been ignored in this study.

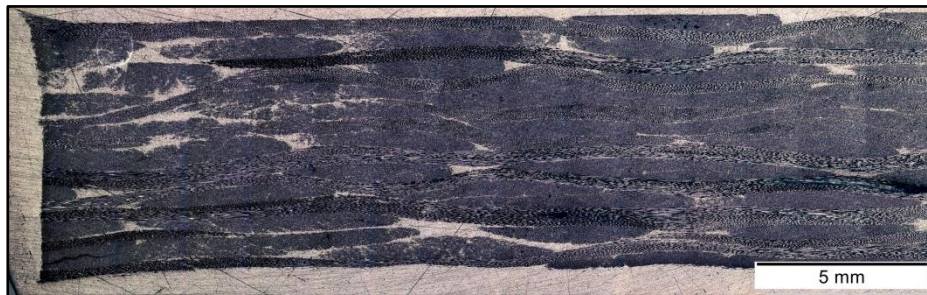


Fig. 5.4: Microscope picture of the crimp angle

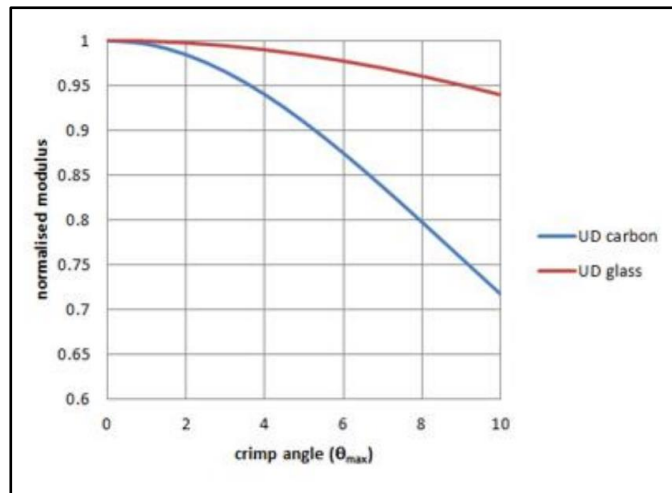


Fig. 5.5: Calculated orientation distribution factor for a plain weave tow with varying crimp angle [104]

### 5.3 Autodesk Heliuss composite validation

Autodesk Heliuss composite software has been used in the current study to calculate the mechanical properties of the composite flange and the pipe. The reason for using the software is that it is very difficult to calculate all the mechanical properties experimentally, especially, for the three dimensional composite materials. These properties are used in the FE analysis that will be discussed in the next chapter. Therefore, an experiment has been conducted to validate the results of the Heliuss composite. This has been done by manufacturing a composite laminate using glass fibre braid and polyester, which are the same as the materials of the composite flange as well as the same as the manufacturing process (VIP) as illustrated in the Fig. 5.6. The composite laminate has been made of eight layers having a thickness of 3.47 mm. The braid angle of the fabric has been measured using image J software and the average value was 28.3°. The fibre volume fraction has been measured for many samples of the laminate and the average value was 49.33%.

Young's modulus has been measured in different ways. Experimentally, six samples have been cut from the composite laminate (Fig. 5.6) and tested using flexural test (3-point bending), which is explained in the standard (BS EN ISO 14125) [105]. Fig. 5.7 illustrates a simple diagram of the 3-point bending tests. The Young's modulus has been calculated through standard calculations, Instron software, excel

calculations and Helius composite. In the Helius composite, the above characteristics (Braid angle,  $V_f$ , thickness) have been used to model the composite laminate and to calculate its mechanical properties. For more details, see appendix A.

The results show that the difference between the Helius composite and standard equation is 7.6 %, between the Helius and the Instron is 4.5 %, whereas the difference with excel calculations, which was calculated based on the obtained test data, is 7.3 %. See Table 5.2. This means there is a good agreement between all the methods. Although, the Helius composite does not take into account the effects of the crimp angle and the voids.

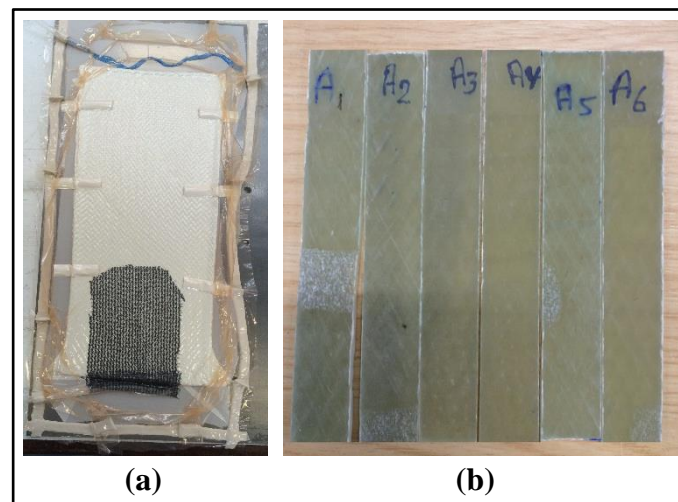


Fig. 5.6: Composite laminate (a) under the vacuum (b) samples of the test

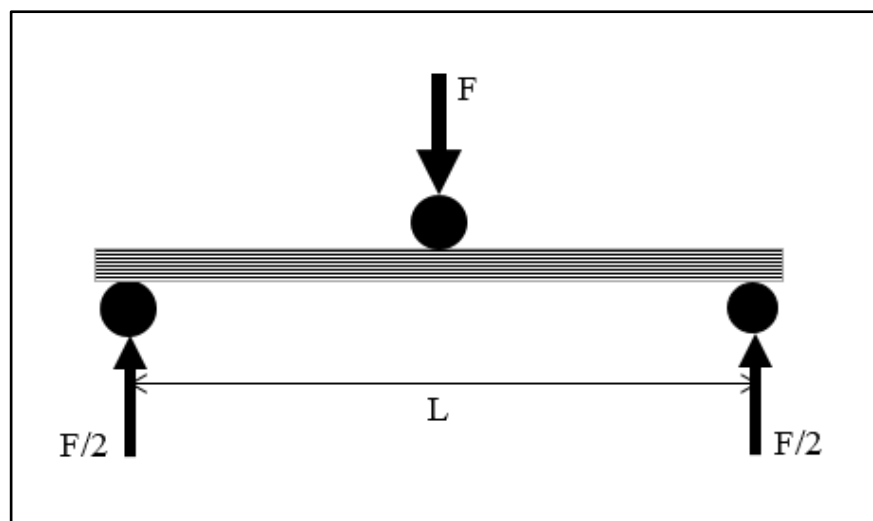


Fig. 5.7: Illustration of the 3-points bending test

Table 5.2: Comparison of the Young's modulus for a composite laminate

| Samples No.                        | Young's modulus (GPa) |                  |                    |                  |
|------------------------------------|-----------------------|------------------|--------------------|------------------|
|                                    | Standard calculations | Instron software | Excel calculations | Helius composite |
| Sample 1                           | 21.28                 | 21.73            | 21.32              | 20.72            |
| Sample 2                           | 15.21                 | 16.33            | 15.33              | 20.72            |
| Sample 3                           | 16.65                 | 17.13            | 16.78              | 20.72            |
| Sample 4                           | 17.72                 | 18.45            | 17.85              | 20.72            |
| Sample 5                           | 22.38                 | 23.06            | 22.38              | 20.72            |
| Sample 6                           | 21.58                 | 22.01            | 21.57              | 20.72            |
| Average                            | 19.14                 | 19.785           | 19.21              | 20.72            |
| % difference with Helius composite | -7.6 %                | -4.5%            | -7.3 %             | ----             |

#### 5.4 Flange-Gasket friction

During the operating condition of the joint, the friction force tries to resist the pushing out of the gasket due to the applied internal pressure. The friction between the composite flange and the rubber gasket has been taken into account in the current study. Based on the TAPPI T-815 standard method [106], the static coefficient of the friction between the composite plate and the rubber gasket has been calculated using inclined plane friction tester shown in the Fig. 5.8. The composite plate has been manufactured using the same materials as the composite flange, the same manufacturing process and the same glass plate as used for the mould. The reason of that is to obtain a composite plate with a face that has the same geometrical similarities as the flange face, which is in direct contact with rubber gasket. A piece of the rubber gasket has been attached to a metal cuboid and weighed. The composite plate was fixed on the inclined plane. The coefficient of the friction has been measured at an angle when the metal cuboid has started to slide as shown in the Fig. 5.9 using the following equations.

Many readings (10) had been taken and the average value of the static coefficient between the composite plate and the rubber gasket was determined as 1.1. This value was considered as the same for all the rubber gaskets used (e.g. Nitrile and Viton).

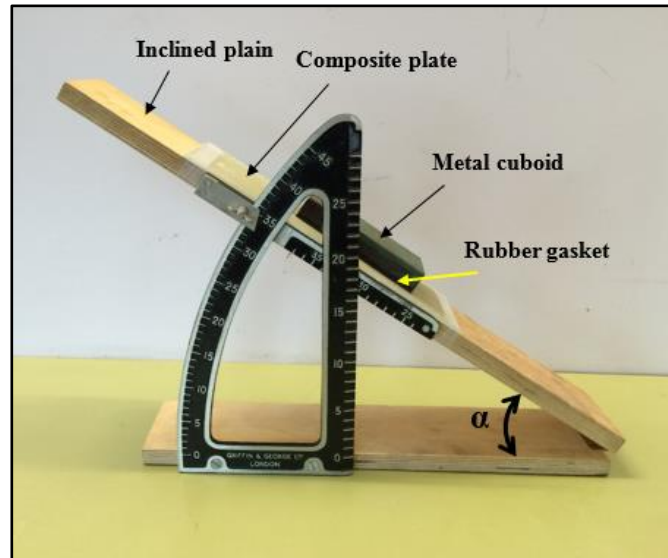


Fig. 5.8: Inclined plane friction tester

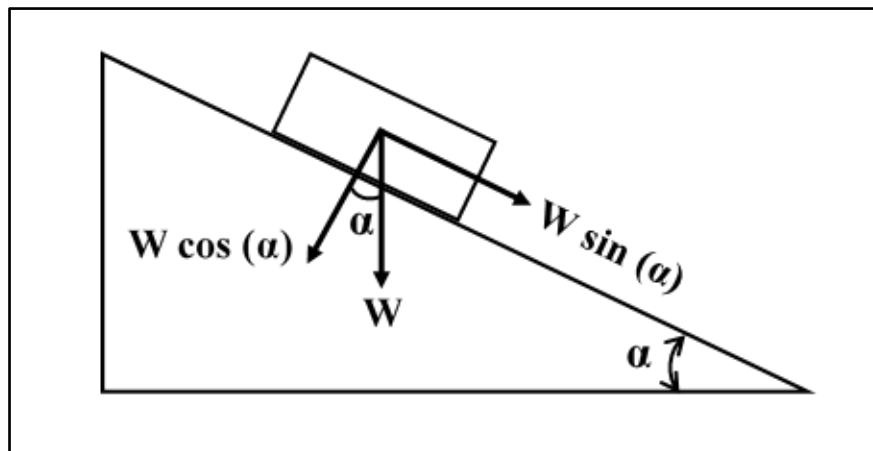


Fig. 5.9: Relationships of ramp weight components

$$F = W \sin(\alpha) \quad \dots (5.1)$$

$$N = W \cos(\alpha) \quad \dots (5.2)$$

$$\mu = \frac{F}{N} \quad \dots (5.3)$$



$$\mu = \frac{W \sin(\alpha)}{W \cos(\alpha)} \quad \dots (5.4)$$

$$\mu = \tan \alpha \quad \dots (5.5)$$

## 5.5 Data measuring equipment

When the pressure vessel are tested under the bolt load along with the internal pressure, many tools are required to collect the data, for example: data collector, strain gauges, a computer installed with a specialised software.

### 5.5.1 Strain indicators and recorders

In this study, four strain indicators have been used to collect the data from the bonded strain gauges that will be discussed in the next sections. The strain indicators used are called P3 and they have been made by Vishay Measurements Group. UK Ltd. See Fig. 5.10. Each P3 has four channels, so the total channels are 16. Before conducting the test, these P3's have been sent to the manufacturer (Vishay Measurements Group UK Ltd) for the calibration purposes. All the calibration data has been documented in the appendix B. In addition, multiple P3-D4 software has been used to record the data in the computer.



Fig. 5.10: Strain indicator and recorder

### 5.5.2 Composite flange strain gauges

For the composite flange, biaxial strain gauges (FCA-6-11) have been used. This type of strain gauges has been made by Tokyo Sokki Kenkyujo Co., Ltd. in Japan. It is also called cross strain gauges, which can measure the strain in two directions at the same point and time. They have been distributed and bonded on two lines. One of these lines passes through the centre of the bolt and the other one passes through the mid-point between the two adjacent bolts as shown in the Fig. 5.11. In addition, four of the strain gauges were located on the flange disc to measure the radial and hoop (circumferential) strains. The other four were bonded on the hub to measure the axial and hoop strains during the testing process. All the strain gauges connected to electric circles using quarter bridge method. This allowed to study the relationship between the applied load (the internal pressure and the bolt load) and the flange deformation.

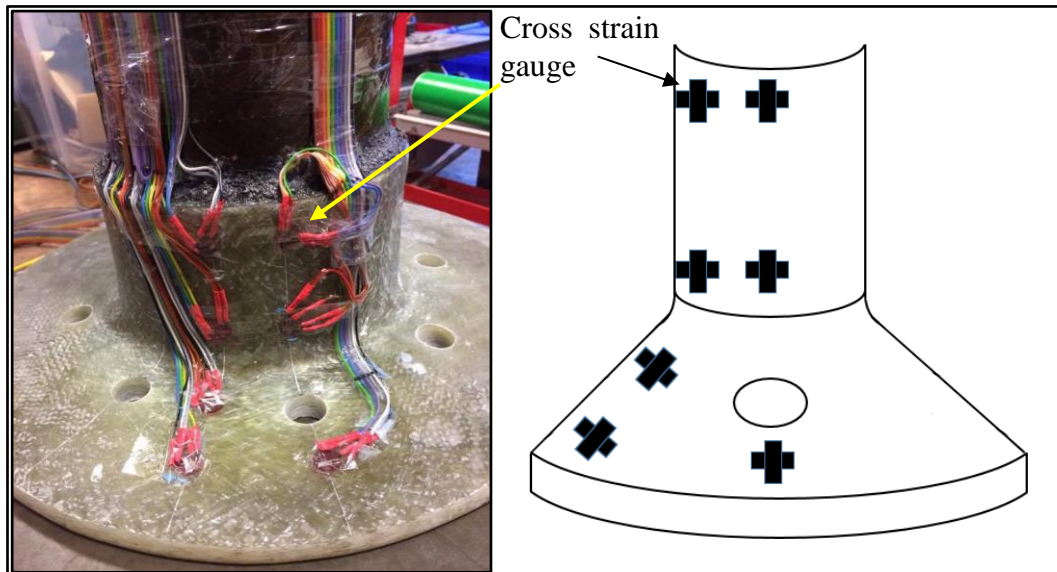


Fig. 5.11: The strain gauges set up on the composite flange body

### 5.5.3 Bolt strain gauges

The main loads in this study are the bolt load and the internal pressure. During the bolt up conditions, only the bolt load is applied whereas during the operating conditions, the internal pressure is applied in addition to the bolt load. The flange deformation and the leakage pressure both depend on the bolt load and measuring



the applied load on the bolt accurately is very important. The bolts that have been chosen for this study are M18 (304 stainless steel) and comply with standard DIN 931.

Therefore, an additional study has been conducted to find out the best method for measuring the applied load during the test. This has been done by using two types of strain gauges and tensile test machine. The types of strain gauges used for two bolts are uniaxial strain gauge and embedded strain gauge.

#### 5.5.3.1 Uniaxial strain gauge

Initially, the bolts have been machined at the shank with a depth of 2 mm as shown in the Fig. 5.12. This was done to prepare places for mounting the strain gauges at the threaded area (shank). As shown in the Fig. 5.12, two holes have been drilled for making the connections using the wires. For each of the bolts, two strain gauges have been bonded at the machined area and each one is placed on the opposite position of each other.

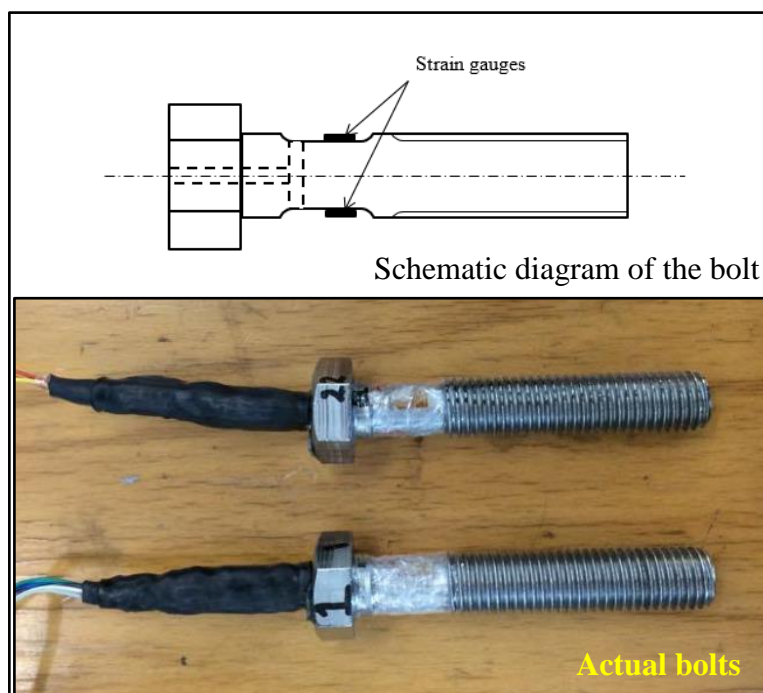


Fig. 5.12: Bolts with two strain gauges bonded on the shank

Initially, each strain gauge has been connected to the data collector using a quarter bridge and tested in the tensile machine. Unfortunately, the results of the two strain

gauges were not the same. Either one of them was positive (under tension) and the other was negative (under compression) or both of them were showing the same sign but different values. This means that the bolt is subjected to significant bending while it is loaded and the spiral thread does not evenly distribute the load to the bolt head. Ideally, both strain gauges should have the same strain values while under tension but unfortunately, this was not achieved in most of the cases.

Hence, a quarter bridge with two gauges, which are connected in series, has been used [107] to measure the pure axial bolt strain by eliminating the bending that occurs in the bolt. This method, which is illustrated in the Fig. 5.13, is also used in the cantilever beams that are subjected to the bending (tension on one face and compression on the other face). As shown in the Fig. 5.13, three resistors (240 Ohm) have been utilized. The following equations explain more details about the method.

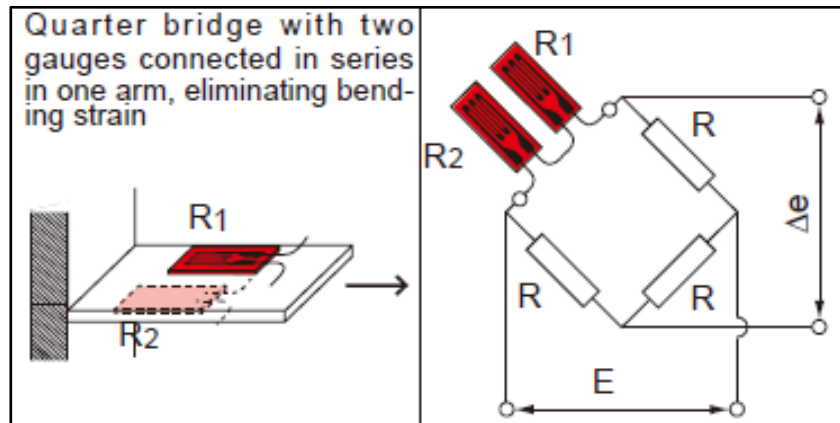


Fig. 5.13: Quarter Bridge with two gauges connected in series method [106]

$$\Delta e = \frac{E}{4} \times \frac{(\Delta R_1 + \Delta R_2)}{R} = \frac{E}{4} \cdot K \cdot \frac{(\epsilon_1 + \epsilon_2)}{2} \quad \dots (5.6)$$

$$= \frac{E}{4} \cdot K \cdot \epsilon \quad \dots (5.7)$$

$R_1$  : Strain Gauge resistance =  $R_0 + \Delta R_1$

$R_2$  : Strain Gauge resistance =  $R_0 + \Delta R_2$

$R = 2R_0$

$R_0$  : Gauge resistance before strain applied

$\Delta R_1, \Delta R_2$  : Resistance change of strain gauge  
 $R_1, R_2$

$\epsilon_1, \epsilon_2$  : Strain applied to strain gauge  $R_1, R_2$

$R$  : Fixed resistor

### 5.5.3.2 Embedded strain gauge

The other type of bolt strain gauges that have been used in this study is the embedded bolt strain gauge called BTMC-3-D20-006LE and has been made by Tokyo Sokki Kenkyujo Co., Ltd. The main characteristics of this strain include easy installation. This type of strain is also not affected by the bolt bending. The installation requires drilling a hole in the centre of the bolt head, filling the hole with appropriate adhesive and embedding the strain gauge. The installation process is very easy compare to the installation of the previous type of strain gauge. As shown in the Fig. 5.14, the position of this strain gauge is considered at the centre of the bolt to eliminate the influence of bending that creates unequal strains in all the bolt sides. Therefore, this strain gives better results of the pure axial strain for the bolt during the test.

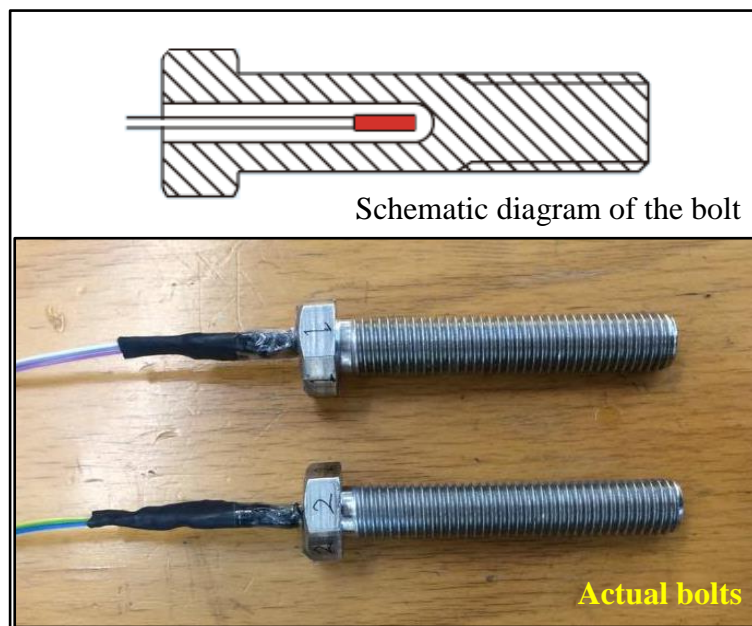


Fig. 5.14: Bolts with embedded strain gauges

### 5.5.3.3 Bolt testing results

Before testing any of the bolts mentioned earlier, a tensile test has been done for three samples that have been taken from the bolts, which were made of stainless steel 304 (A2-70). The sample has been made by machining the bolts and prepared for testing based on the standard ASTM A370-03a [108]. The purpose of this tensile test

was to calculate the Young's modulus and to compare with the standard value of the stainless steel 304, which is 193 GPa. The average obtained value from the tensile test was 194.3 GPa. Therefore, a good agreement has been obtained and the standard Young's modulus of 193 GPa will be used as the bolt property in the FEA simulations and also in the theoretical calculations.

In terms of testing the bolts with fitted strain gauges, a special holding attachment has been manufactured to hold the bolt during the tensile test. This tool is shown in the Fig. 5.15.

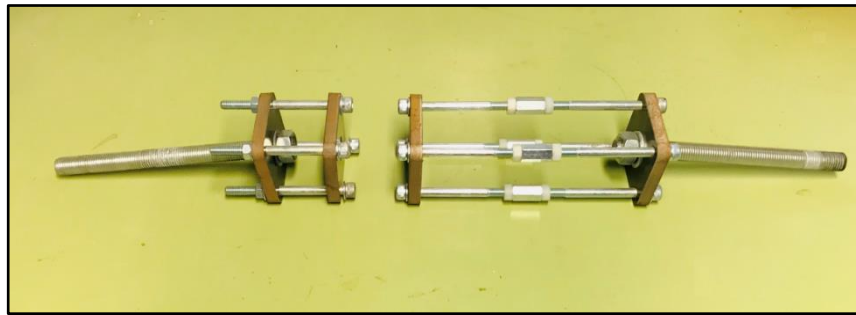


Fig. 5.15: Holding attachment for the bolt testing

For each type of the strain gauges, two bolts have been tested using the tensile test machine (Extensometer) along with the bonded strain gauge. The bolts with bonded strain gauges on the opposite sides of the shank were called SSG1 and SSG2 (**Side Strain Gauges**), whereas, the bolts with embedded strain gauges at the centre were called CSG1 and CSG 2 (**Central Strain Gauges**). In addition, all the data that were collected from the strain gauges were named with the same symbols (SSG1, SSG2, CSG1 and CSG2). The experimental results of the axial load vs axial strain have been compared with the theoretical results, which have been calculated based on the Hooke's law when the Young's modulus is considered as 193 GPa.

The variation of the axial strain with the axial load for the SSG bolt1 has been illustrated in the Fig. 5.16. The results represent the data of the strain gauge in extensometer and the data from the calculation of the theoretical axial strain. The axial strain that has been obtained from the travelling cross is ignored due to the complexity of the holding attachment, which causes errors. The results showed that when the axial load increases, the axial strain increases as well and there is a good

agreement between the values from the experiments and from the theoretical calculations. In terms of the extensometer data, it is clear that there is instability and this is because of the extensometer movement. Due to the complex geometry of the bolt (head and threaded region) as well as the holding attachment, the extensometer was always in slip and gave inaccurate data. As a result, the extensometer has been ignored for the rest of the bolts. However, it gave a good indication about the accuracy of the other data (theoretical and strain gauge).

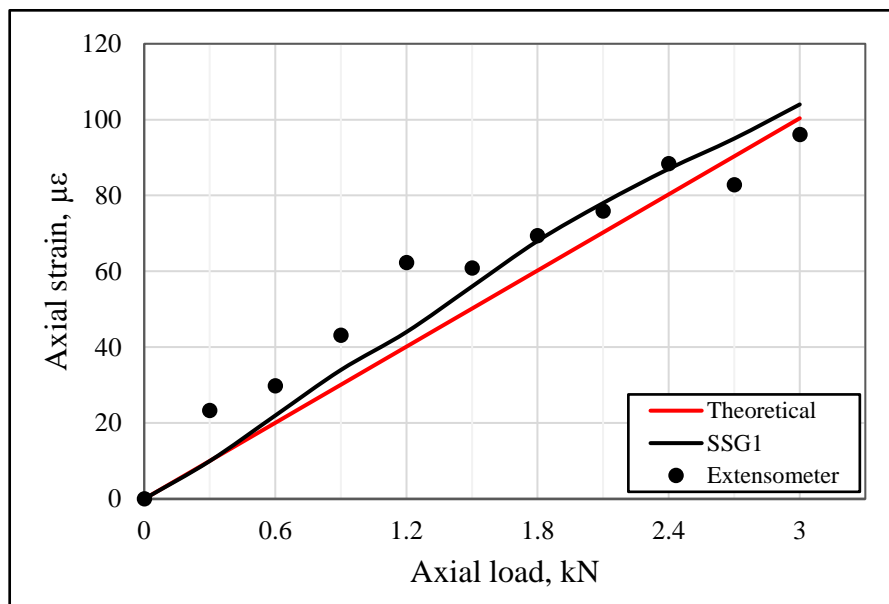


Fig. 5.16: Tensile test data of the bolt SSG1

Fig. 5.17 shows the relationship between the axial loads with the axial strain for the other bolt called SSG2 measured using the strain gauge and the theoretical calculations. As shown in the figure, the agreement between the strain gauge data and the theoretical calculation is excellent. This proves that the connection method of the strain gauges, which is discussed earlier is appropriate to be used for the bolts to measure the pure axial strain with minimal bending effect.

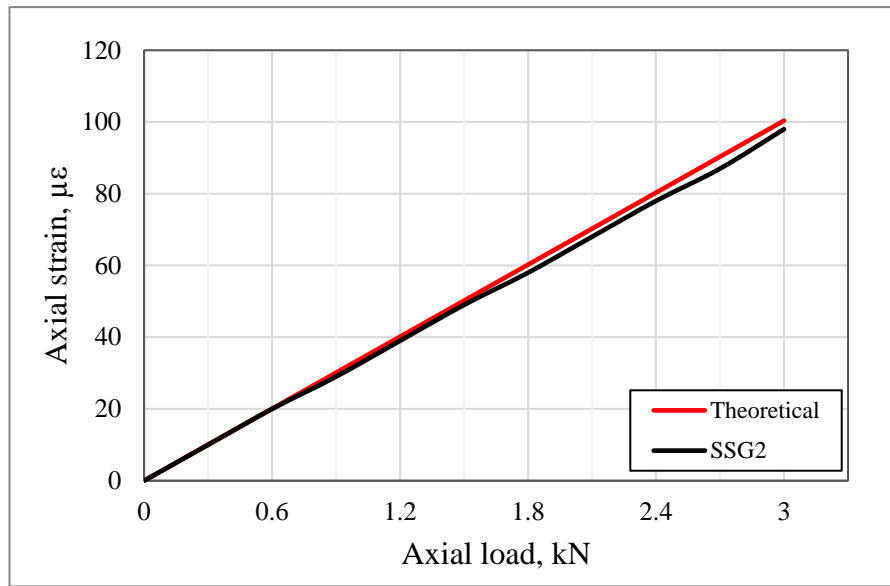


Fig. 5.17: Tensile test data of the bolt SSG2

For the other bolt type called CSG, which has embedded strain gauge at the centre of the bolt, a calibration has been done. Each bolt has been tested several times with different strain gauge factor (SGF) and all the data has been compared with the theoretical results. Fig. 5.18 shows the variation of the axial strain with the axial load for a range of SGF for the CSG bolt 1. The SGF has been varied from 1.5 to 2.5 to find the accurate value of the axial strain. An increase in the SGF leads to decrease the axial strain and thus the accurate axial strain was found at SGF 1.75 as it is very close to the theoretical axial strain.

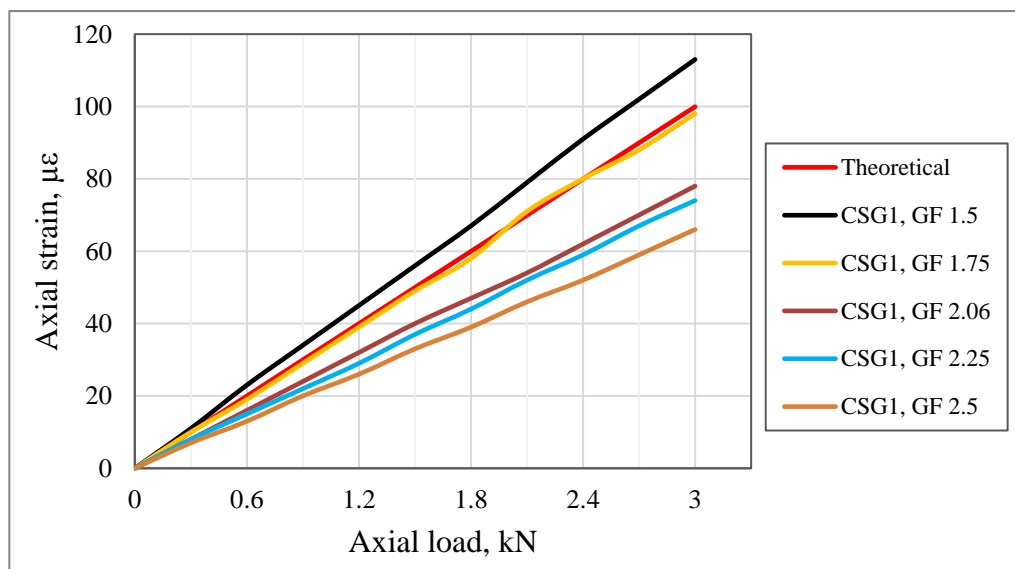


Fig. 5.18: Tensile test data of the bolt CSG1

Fig. 5.19 illustrates the calibration data of the CSG bolt 2. The axial load has been applied, SGF has been changed and the axial strain has been recorded. As with the previous bolt, the best result was obtained at SGF 1.75. Therefore, this value of the strain gauge factor will be considered whenever this type of strain gauge is used in the study.

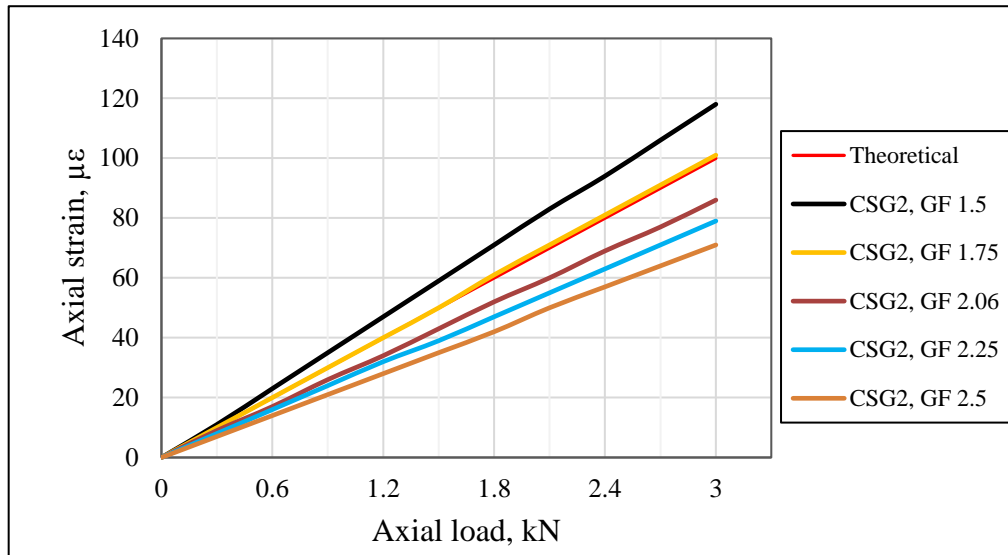


Fig. 5.19: Tensile test data of the bolt CSG2

In the Fig. 5.20, a comparison has been made between the obtained results from the theoretical calculations for the SSG and the CSG bolts using the strain gauge factor as 1.75 as well as from the extensometer. As shown in the figure, most of the results are very close to the theoretical data except for the SSG bolt1 which has slightly higher extensometer data. The extensometer data of the bolt SSG1 was not stable due to a particular reason that has been discussed earlier. Also, it is observed that the data of the CSG bolts are stable, almost the same and has a very good agreement with the theoretical data (as can be Seen in the Fig. 5.21). Practically, using a bolt with embedded strain gauge at the centre (CSG bolt) for testing the bolted flange joint is better than the bolt with bonded strain gauges on the outer surface of its shank (SSG bolt). The SSG bolts are affected by the bolt bending and thus require machining. Bonding two strain gauges with a special connection method takes long time and incurs additional costs. In addition; the SSG bolts can be damaged during the GFRP flange test as the strain gauges are bonded on the outer surface.

On the other hand, the CSG bolts are easy to set up the strain gauge, are not affected by the bolt bending, as the strain gauge is located at the bolt centre, and has less chance to be damaged as the strain gauge has been embedded inside the bolt. Furthermore, CSG bolts provide better results in comparison with SSG bolts. Therefore, the CSG bolts have been chosen for testing the bolted GFRP flange joint.

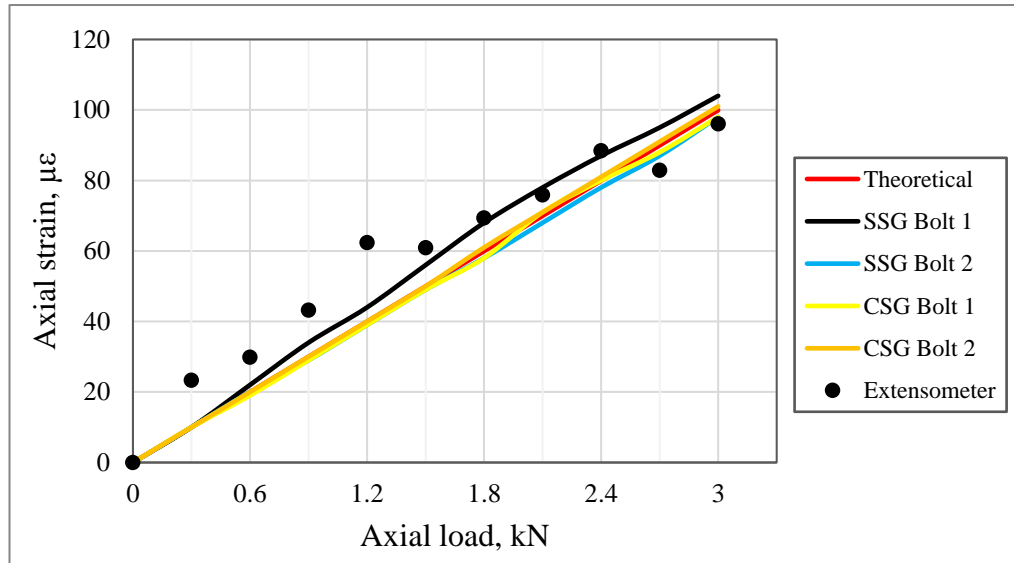


Fig. 5.20: Comparison of the tensile test data of all the bolts

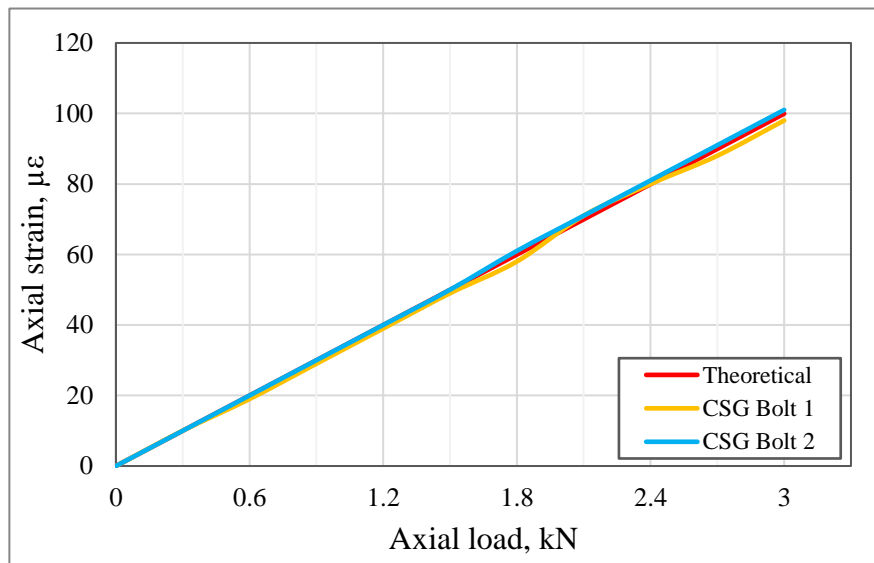


Fig. 5.21: Comparison of the tensile test data of the CSG bolts



## **5.6 Construction of the test rig**

In addition to the data measuring equipment, several test rigs have been used during testing of the pressure vessel. These rigs are comprised of digital torque wrench, fittings, pump, and pressure gauge.

### **5.6.1 Digital torque wrench**

Applying the same load on all the bolts is very important during the bolt up stage as the bolt load affects the flange deformation and the leakage pressure. To achieve a consistent bolt load, ACDelco digital torque adapter has been used to measure the applied torque. Then the same torque from the bolt that has strain gauge has been applied to the others, which have no strain gauges. This digital torque adapter has been calibrated by the manufacturer. The calibration data is shown in the appendix C. In addition, all the bolts have been lubricated by a grease to minimize the friction between the threads, which might affect the reading of the digital torque adaptor and also to keep the same conditions for all the bolts, thereby, increasing the accuracy of the applied torque.

### **5.6.2 Fittings**

Two stop valves have been used in the pressure vessel. One of them for the inlet, which is connected to the pump, and the other one is for the outlet, which is used for draining the compressed liquid after finishing the test. Furthermore, a number of other fittings have been used for the connection purposes including the connection of the gauge pressure.

### **5.6.3 Pump test**

A hand pump has been used to pump the pressure vessel through the inlet point. In addition, through this rig, the applied pressure has been controlled. This hand pump has been manufactured by TANGYE Ltd. in the England.

### **5.6.4 Pressure Gauges**

A special pressure gauge manufactured by WIKA has been used for this project. The pressure gauge has many features, which were necessary for the desired test

conditions, especially, the increments of the readings. The resolution of the increments has been selected to be every 0.2 bar, which increases the accuracy in reading the internal pressure. In addition, the pressure gauge has been calibrated by the manufacturer. The data of the calibration has been included in the appendix D.

### 5.7 Testing procedure

Initially, the tests have been divided into four groups based on the gasket type and thickness. Each group has also been divided into two stages. The first one is the bolt up stage. In this stage, the bolts have been tightened in several steps based on the bolt-tightening diagram illustrated in the Fig. 5.22, The tightening sequence for the bolts is important to distribute the bolt loading evenly to compress the gasket surface [109]. In each step, the tightening starts from the bolt number one, that has a strain gauge. The required bolt load as well as the applied torque both were read by the strain gauge and the digital torque wrench, respectively, and the measured torque was transferred to the rest of the bolts. The data has been recorded for each step. The second stage is the operating stage, in which, the pressure vessel has been pressurized in a number of steps by keeping the bolt load same as the design value. In each step, the data has been recorded up to the leakage pressure. In both stages, the entire procedure has been repeated five times and an average value has been obtained for strain or leakage pressure.

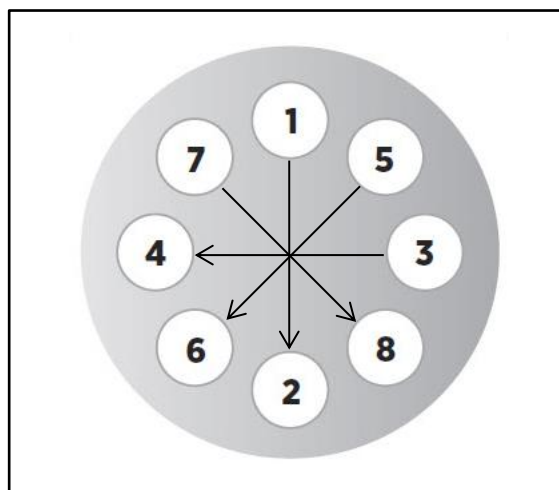


Fig. 5.22: Bolt tightening diagram [109]

## 5.8 Summary

The experimental methodology explained in this chapter can be summarised in the following points:

- The methods applied for measuring the materials characterisations (i.e. the fibre volume fraction and the fibre orientations) are appropriate and provides accurate results.
- Helius composite (Autodesk) is a useful tool to calculate the mechanical properties of the composite materials, which are very difficult to be measured in physical testing laboratory, especially, the orthotropic material properties. The validation of results has shown that there is an excellent agreement between the experimental and the Helius composite results. Therefore, the software tool is very effective in saving time and cost.
- The data measuring equipment (e.g. strain indicator, composite strain gauges and bolt strain gauges) used in this study have shown good performances during the test.
- The chosen test rig can produce very good and accurate data set once calibrated properly.
- The test procedure was selected based on the recommendations of the previous studies. It has produced good experimental results discussed in the chapter 7.

In the next chapter, FEA simulations of the GFRP flange joint system will be discussed including the method used for modelling the geometry, characterising the material properties, applying the boundary conditions and obtaining the results.

# CHAPTER SIX

## NUMERICAL SIMULATION

## METHODOLOGY

### 6.1 Introduction

FEA has become popular with fast digital computers because it is very useful and supportive practice in every design. The main features that encourage designers to use FEA for analysis complicated structures are its ability to solve a large number of simultaneous equations in a relatively short time, simulating various physical problems with arbitrary shapes. Various loads and support conditions can be applied easily. In terms of bolted flange joint, FEA can be used to simulate this system of connection with its parts such as; flange, pipe, pipe-flange adhesive bonded, rubber gasket and fastener, which includes bolt and washer. Modelling of this type of joints can be very helpful because of its flexibility and ability to calculate stress, strain, deflection and gasket contact pressure at anywhere in the structure. In contrast, experimental verification can measure only on the surfaces and at limited points, costly and time consuming. The effect of some parameters cannot be measured experimentally or too expensive, so that the FE model is a good tool to be used for studying the performance of the bolted GFRP flange connection.

In this chapter, the methodology used for finite element analysis of the bolted glass fibre reinforced polymer flange joint will be presented. The FEA model will include all the joint parts, which are flange, pipe, adhesive bonding, rubber gasket and fastener (bolt and washer). In addition, the methodologies used for fluid pressure penetration and the leakage pressure simulations will be discussed in this chapter.

## **6.2 FEA model of bolted GFRP flange joint**

A three dimensional finite element model has been developed for glass fibre reinforced plastic (GFRP) bolted flange using ANSYS version 18.1. The model includes flange, pipe, adhesive bonding, gasket and bolt with dimensions and shapes compliant with the ASME Boiler and Pressure Vessel Code, Section X [24]. Using symmetry in the geometry, a primary segment is repeated at equally spaced intervals about the axis of symmetry, so  $1/16^{\text{th}}$  portion of the total circumference of the joint has been considered for the analysis as shown in Fig. 6.1. This option has been chosen to reduce the total simulation time and computer resources. Especially, the selected diameter of the pipe for this study is 6", which is relatively large. This portion of the joint includes  $1/16^{\text{th}}$  from the flange, pipe, adhesive bonding, gasket and a half of the bolt and the washer as shown in the Fig. 6.2.

### **6.2.1 Geometry and the dimensions of the flange joint**

As mentioned earlier, the full-face gasket flange has been investigated in this project as can be seen in the Fig. 6.3. The dimensions of the fabricated flange joint have been chosen based on the ASME Boiler and Pressure Vessel Code, Section X [24], when the design internal pressure is 340 kPa. See Fig. 6.3. FEA identifies the effects of some of these dimensions on the flange strains and the leakage pressure. Therefore, some of the dimensions have been varied. These dimensions are flange diameter, flange thickness, hub length and thickness. The purpose of this variation is to find the possibility of reducing these dimensions as the preliminary experimental results showed that the strains of the flange were low under the design loads (bolt load and internal pressure).

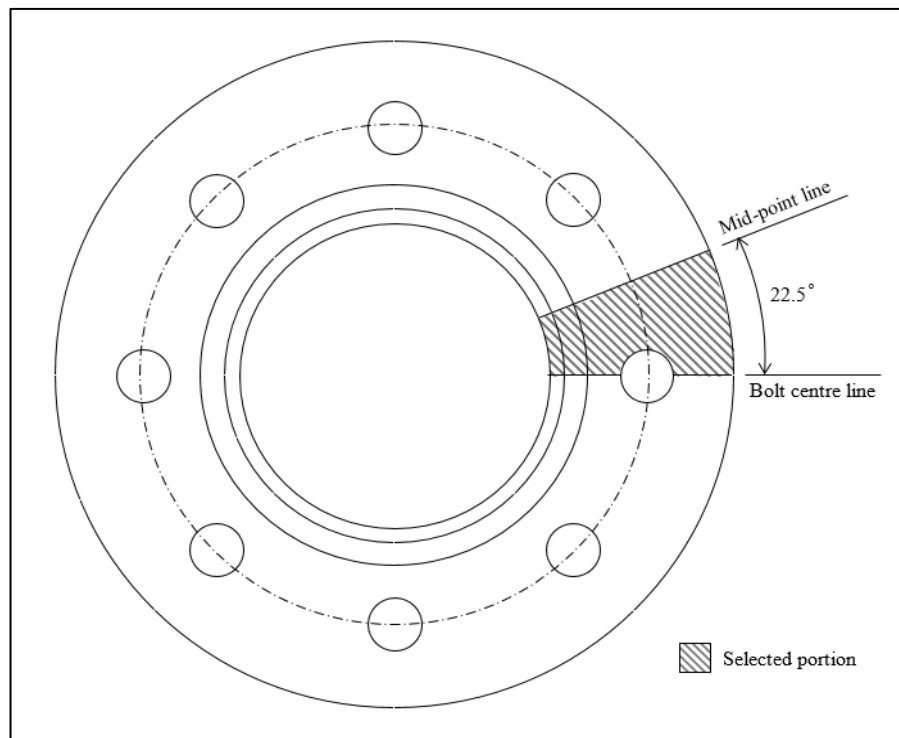


Fig. 6.1: Symmetric of the bolted flange joint

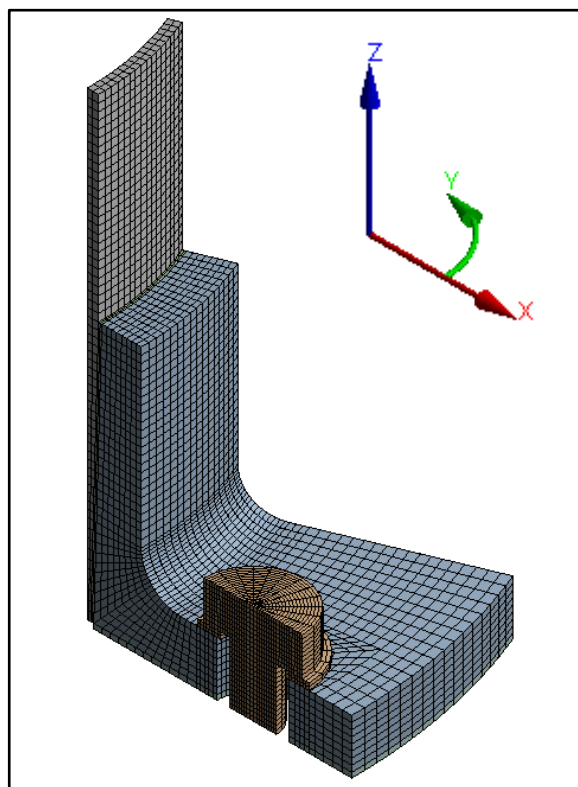


Fig. 6.2: 3D FEA model of the bolted flange joint

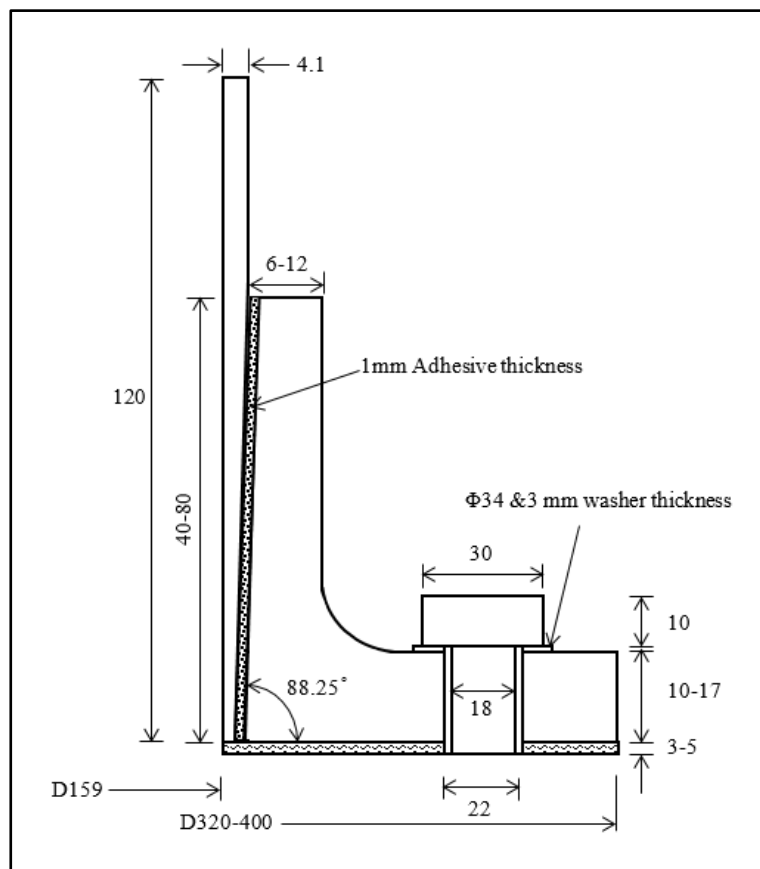


Fig. 6.3: Dimensions of the bolted flange joint (mm)

### 6.2.2 GFRP flange simulation

The bolted GFRP flange has been simulated in this FEA by taking into account its orthotropic characteristics. Since the orthotropic mechanical properties are not the same in all regions of the flange, the composite flange is divided into two main parts and are named as flange (flange disc), and the hub. As illustrated in the chapter five, the fibre volume fractions ( $V_f$ ) were measured for all the parts and they were found 60.7% for the flange and 60.1% for the hub. In addition, the braid angles of the braid fiberglass sleeves were measured for all the parts and were considered as fixed at  $\pm 65^\circ$ ,  $\pm 44.5$  for the flange and the hub, respectively.

Using the above parameters and through the Helius composite software, composite laminate were modelled for each part by using the micro mechanical properties of the fibre (glass fibre) and the resin (polyester), which are explained in the Table 6.1.

The orthotropic mechanical properties of these laminates represent the elastic properties of the composite flange, which are used in this FE model. The properties are shown in the Table 6.2.

Table 6.1: Mechanical properties of the glass fibre, polyester resin and the adhesive

|                            | Glass fibre | Polyester | Adhesive epoxy |
|----------------------------|-------------|-----------|----------------|
| $E$ (GPa)                  | 72.4        | 3.24      | 1.3            |
| $G$ (GPa)                  | 30.34       | 1.17      | 0.46           |
| $\nu$                      | 0.2         | 0.38      | 0.41           |
| Tensile strength (MPa)     |             |           | 45             |
| Compressive strength (MPa) |             |           | 80             |
| Shear strength (MPa)       |             |           | 30             |

Table 6.2: Typical orthotropic mechanical properties of the flange and the pipe

| Young's modulus              | (GPa) | Shear modulus | (GPa) | Poisson's ratio | ---- |
|------------------------------|-------|---------------|-------|-----------------|------|
| <b>Flange (disc)</b>         |       |               |       |                 |      |
| $E_x$                        | 11.90 | $xy$          | 9.45  | $xy$            | 0.25 |
| $E_y$                        | 29.53 | $yz$          | 4.22  | $yz$            | 0.12 |
| $E_z$                        | 13.77 | $xz$          | 4.34  | $xz$            | 0.35 |
| <b>Hub</b>                   |       |               |       |                 |      |
| $E_x$                        | 14.38 | $xy$          | 4.20  | $xy$            | 0.19 |
| $E_y$                        | 13.00 | $yz$          | 13.02 | $yz$            | 0.59 |
| $E_z$                        | 13.36 | $xz$          | 4.20  | $xz$            | 0.18 |
| <b>Filament winding pipe</b> |       |               |       |                 |      |
| $E_x$                        | 18.99 | $xy$          | 6.72  | $xy$            | 0.15 |
| $E_y$                        | 24.36 | $yz$          | 12.12 | $yz$            | 0.48 |
| $E_z$                        | 17.69 | $xz$          | 6.64  | $xz$            | 0.30 |



### 6.2.3 Filament winding pipe modelling

As mentioned earlier, a number of previous studies [8, 72] have indicated that the optimum winding angle of filament wound composite pipes subjected to internal pressure is  $55^\circ$ . Subsequently, in this study, an angular portion of  $1/16^{\text{th}}$  of filament wound composite pipe made of GRP materials with winding angle of  $55^\circ$  has been selected and modelled in 3D FEA model. As same the procedure of the flange, the fibre volume fraction and the winding angle both have been measured experimentally and they were 52% and  $55^\circ$ , respectively. Then, the material properties have been calculated using the Helius composite. These properties of the filament winding pipe are listed in the Table 6.2.

### 6.2.4 Bonded flange-pipe modelling

As mentioned earlier, taper-taper joint type has been chosen to connect the GFRP flange with the GFRP pipe because it is stronger than other types of joints due to the larger surface contact areas. These two bodies (flange and pipe) are bonded by using epoxy as an adhesive material. An FEA model has been developed to simulate a  $1/16^{\text{th}}$  angular portion of adhesively bonded components made of non-identical materials and properties. The mechanical properties of the adhesive (epoxy) are shown earlier in the Table 6.1. In addition, all contact surfaces are considered as smooth (in other words, the roughness does not exist).

### 6.2.5 Fasteners modelling

In this study, one-half of the upper half of the bolt has been modelled (as shown in the Fig. 6.4 because of symmetry with respect to the plane that passes through the gasket mid thickness and the bolts as well as the symmetry about the axial axis. The bolt material characteristics are assumed to be homogeneous, isotropic and linearly elastic. The bolts were chosen as stainless steel 304 (A2-70) and their mechanical properties are Young's modulus  $E=193$  GPa and poisson's ratio  $\nu=0.3$ .

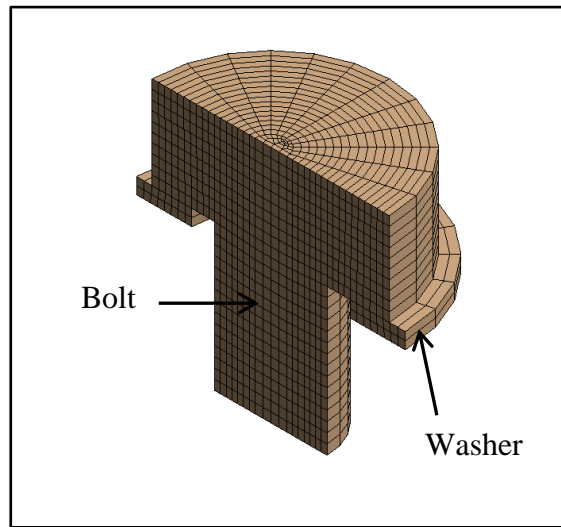


Fig. 6.4: Fastener modelling

### 6.2.6 Modelling the rubber gasket

In this study, Nitrile and Viton rubber gaskets have been chosen to seal the flange joint due to their high performances with oil and gas industries. Rubber materials are usually in compressible mode and its overall response is quite nonlinear. Therefore, it is not appropriate to use the Young's modulus and the Poisson's ratio to define a gasket in FEA as a linear material. However, it is required to apply a complete pressure-closure response which gives the actual behaviour of the rubber material exhibiting nonlinear behaviour in loading and unloading conditions. ANSYS offers a number of elements to model gaskets. These elements consider geometric and material nonlinearities. Therefore, based on the standard ASME D575-91 [110], a load compressive mechanical tests have been conducted for finding the mechanical characteristics of each gasket and during the loading and the unloading conditions. The data of both gaskets (Nitrile and Viton), which were used in the FEA model, are explained in Fig. 6.5 and Fig. 6.6 and the values are documented in Table 6.3 and Table 6.4.

In addition, the FEA model has taken into account the effect of the transverse shear stiffness  $TSS_{xy} = TSS_{xz} = G/h$ . The  $G$  is the shear modulus and the  $h$  is the thickness of the rubber gasket. The shear modulus has been measured experimentally

according to the standard BS ISO 1827 [111]. All the values are shown in the Table 6.5.

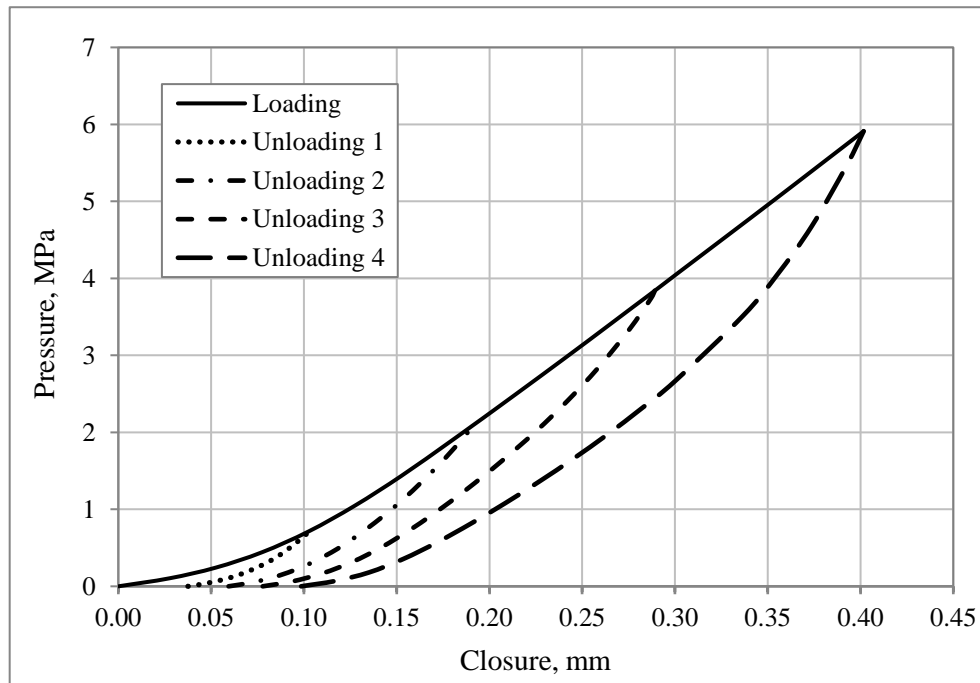


Fig. 6.5: Characteristics of the Nitrile gasket obtained experimentally

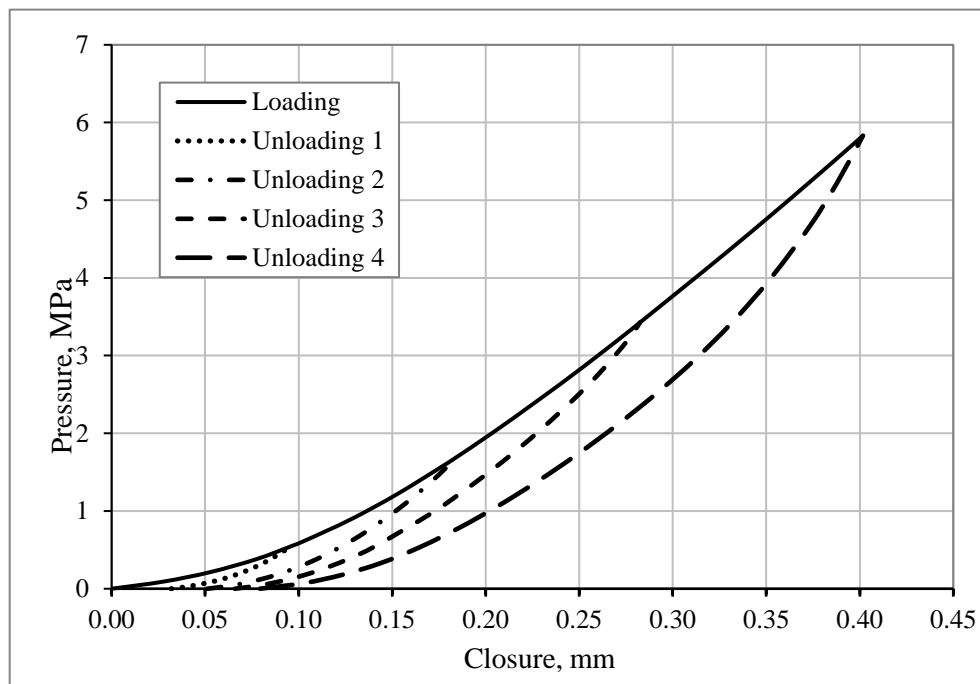


Fig. 6.6: Characteristics of the Viton gasket obtained experimentally

Table 6.3: Compressive response of the Nitrile rubber gasket

| Non-linear Loading<br>(Compression) |          | Non-linear Unloading 1 |          | Non-linear Unloading 2 |          | Non-linear Unloading 3 |          | Non-linear Unloading 4 |          |
|-------------------------------------|----------|------------------------|----------|------------------------|----------|------------------------|----------|------------------------|----------|
| Closure                             | Pressure | Closure                | Pressure | Closure                | Pressure | Closure                | Pressure | Closure                | Pressure |
| mm                                  | MPa      | mm                     | MPa      | mm                     | MPa      | mm                     | MPa      | mm                     | MPa      |
| 0                                   | 0        | 0                      | 0        | 0                      | 0        | 0                      | 0        | 0                      | 0        |
| 0.03                                | 0.14     | 0.04                   | 0.02     | 0.07                   | 0.05     | 0.09                   | 0.06     | 0.12                   | 0.07     |
| 0.05                                | 0.24     | 0.06                   | 0.09     | 0.09                   | 0.21     | 0.13                   | 0.32     | 0.15                   | 0.35     |
| 0.10                                | 0.71     | 0.06                   | 0.14     | 0.12                   | 0.48     | 0.16                   | 0.76     | 0.19                   | 0.82     |
| 0.15                                | 1.43     | 0.07                   | 0.21     | 0.13                   | 0.67     | 0.18                   | 1.03     | 0.23                   | 1.36     |
| 0.19                                | 2.09     | 0.08                   | 0.36     | 0.14                   | 0.88     | 0.19                   | 1.34     | 0.26                   | 1.97     |
| 0.23                                | 2.73     | 0.09                   | 0.48     | 0.16                   | 1.38     | 0.23                   | 2.02     | 0.30                   | 2.67     |
| 0.28                                | 3.63     | 0.10                   | 0.71     | 0.19                   | 1.99     | 0.26                   | 2.83     | 0.34                   | 3.52     |
| 0.29                                | 3.84     | -----                  | -----    | 0.19                   | 2.09     | 0.28                   | 3.74     | 0.36                   | 4.05     |
| 0.35                                | 5.00     | -----                  | -----    | -----                  | -----    | 0.29                   | 3.84     | 0.37                   | 4.67     |
| 0.40                                | 5.91     | -----                  | -----    | -----                  | -----    | -----                  | -----    | 0.40                   | 5.91     |

Table 6.4: Compressive response of the Viton rubber gasket

| Non-linear Loading<br>(Compression) |          | Non-linear Unloading 1 |          | Non-linear Unloading 2 |          | Non-linear Unloading 3 |          | Non-linear Unloading 4 |          |
|-------------------------------------|----------|------------------------|----------|------------------------|----------|------------------------|----------|------------------------|----------|
| Closure                             | Pressure | Closure                | Pressure | Closure                | Pressure | Closure                | Pressure | Closure                | Pressure |
| mm                                  | MPa      | mm                     | MPa      | mm                     | MPa      | mm                     | MPa      | mm                     | MPa      |
| 0                                   | 0        | 0                      | 0        | 0                      | 0        | 0                      | 0        | 0                      | 0        |
| 0.03                                | 0.09     | 0.04                   | 0.02     | 0.06                   | 0.04     | 0.08                   | 0.05     | 0.10                   | 0.07     |
| 0.08                                | 0.38     | 0.05                   | 0.08     | 0.09                   | 0.16     | 0.11                   | 0.24     | 0.14                   | 0.33     |
| 0.10                                | 0.55     | 0.06                   | 0.16     | 0.11                   | 0.38     | 0.14                   | 0.55     | 0.19                   | 0.78     |
| 0.15                                | 1.21     | 0.07                   | 0.22     | 0.12                   | 0.52     | 0.17                   | 0.97     | 0.21                   | 1.07     |
| 0.18                                | 1.67     | 0.08                   | 0.37     | 0.13                   | 0.68     | 0.20                   | 1.49     | 0.25                   | 1.72     |
| 0.25                                | 2.86     | 0.09                   | 0.45     | 0.16                   | 1.08     | 0.23                   | 2.08     | 0.29                   | 2.49     |
| 0.28                                | 3.43     | 0.10                   | 0.55     | 0.18                   | 1.57     | 0.25                   | 2.42     | 0.31                   | 2.93     |
| 0.33                                | 4.30     | -----                  | -----    | 0.18                   | 1.67     | 0.28                   | 3.20     | 0.35                   | 4.00     |
| 0.38                                | 5.32     | -----                  | -----    | -----                  | -----    | 0.28                   | 3.43     | 0.39                   | 5.22     |
| 0.40                                | 5.83     | -----                  | -----    | -----                  | -----    | -----                  | -----    | 0.40                   | 5.83     |

Table 6.5: Shear modulus and transfer shear stiffness of the rubber gaskets

| Gasket         | Shear modulus (G)<br>MPa | Transverse shear stiffness (TSS <sub>xy</sub> & TSS <sub>xz</sub> )<br>MN/m <sup>3</sup> |
|----------------|--------------------------|--|
| Nitrile (3 mm) | 4.3095                   | 1.4365   |
| Nitrile (5 mm) | 4.3095                   | 0.8619   |
| Viton (3 mm)   | 3.1568                   | 1.0522   |
| Viton (5 mm)   | 3.1568                   | 0.6313   |

### 6.2.7 Elements selection and contact interfaces

Several types of elements are used in this FEA model. For the flange, pipe, adhesive bonding and fastener, 3D solid structural element (SOLID185) are used [112]. This element is used for 3D modelling of solid structures and it is defined by eight nodes having three degrees of freedom. For the gasket, INTER195 element is used to simulated the rubber gasket [113]. This element also has eight nodes having three degrees of freedom and compatible with element SOLID185. At the contact zones, CONTA174 and TARGE170 elements are used to simulate the contact surfaces. The CONTA174 is used for the softer face whereas the TARGE107 is used for the stiffer face for each contact [114] .

In terms of the flange, adhesive and pipe contact surfaces, they are treated as a flexible-to-flexible category and the contact surfaces between them are modelled with bonded option. The friction between the bolt, washer and flange has been ignored due to its very small effect. For the flange-gasket contact surfaces, since the behaviour of the flange and the rubber gasket are different in terms of the load-deformation characteristics and both of these are deformable, they are treated as a flexible-to-gasket category and the contact surfaces between them are modelled with frictional option. As the gasket is softer than the flange, it is simulated as a contact surface and the flange is modelled as a target surface [114]. Finally, the coefficient of static friction between them is 1.1, which was measured experimentally in chapter 5.

### 6.2.8 Boundary and loading conditions

As mentioned earlier, due to the rotational symmetry and also due to the symmetry about the plane that passes through the gasket mid thickness, the boundary conditions and the loads are applied to an upper single segment in the analysis. For the model created in the cylindrical coordinate system, the circumferential displacements in the normal direction on the surface of the cyclic symmetry are assumed as fixed, i.e.  $U_\theta=0$ . Also, the displacements of elements that located at the bottom surface of the gasket are considered as fixed, i.e.  $U_z=0$ . See Fig. 6.7. These boundary conditions are assigned for both bolt up and pressure loading stages, which will be discussed in the next sections. These boundary conditions have been applied as suggested in previous studies [39, 40, 45].

#### 6.2.8.1 Bolt up loading conditions

Initially, a bolted flange connection system is analysed to obtain the initial stress and deformation during the seating condition in all its parts when the initial clamping force is applied during assembly. In this stage, the rubber gasket is subjected to compressive pressure that deforms the gasket to fill the irregularities on the flange face ensuring full contact over the surfaces. For achieving this initial stress value in this FE model, only the bolt pre-load force is applied to the lower bolt surface.

#### 6.2.8.2 Pressure loading conditions

This research work includes modelling the bolted flange system under combined bolt pre-load and internal pressure to study the strain, stress and the deformation of the joint and to investigate the sealing performance. Hydrostatic end force and pressure induced on the joint system as well as the bolt load have been applied in the initial clamping phase. The hydrostatic end force is calculated based on the inner diameter of a pipe as shown in the Eq. (6.1)

$$P_k = \frac{A_i}{A_k} P \quad . . . (6.1)$$

This force has been converted to equivalent pressure load and applied uniformly in the axial direction at the end of the pipe. The working pressure load is applied over all elements of the internal surfaces of the pipe and the gasket.

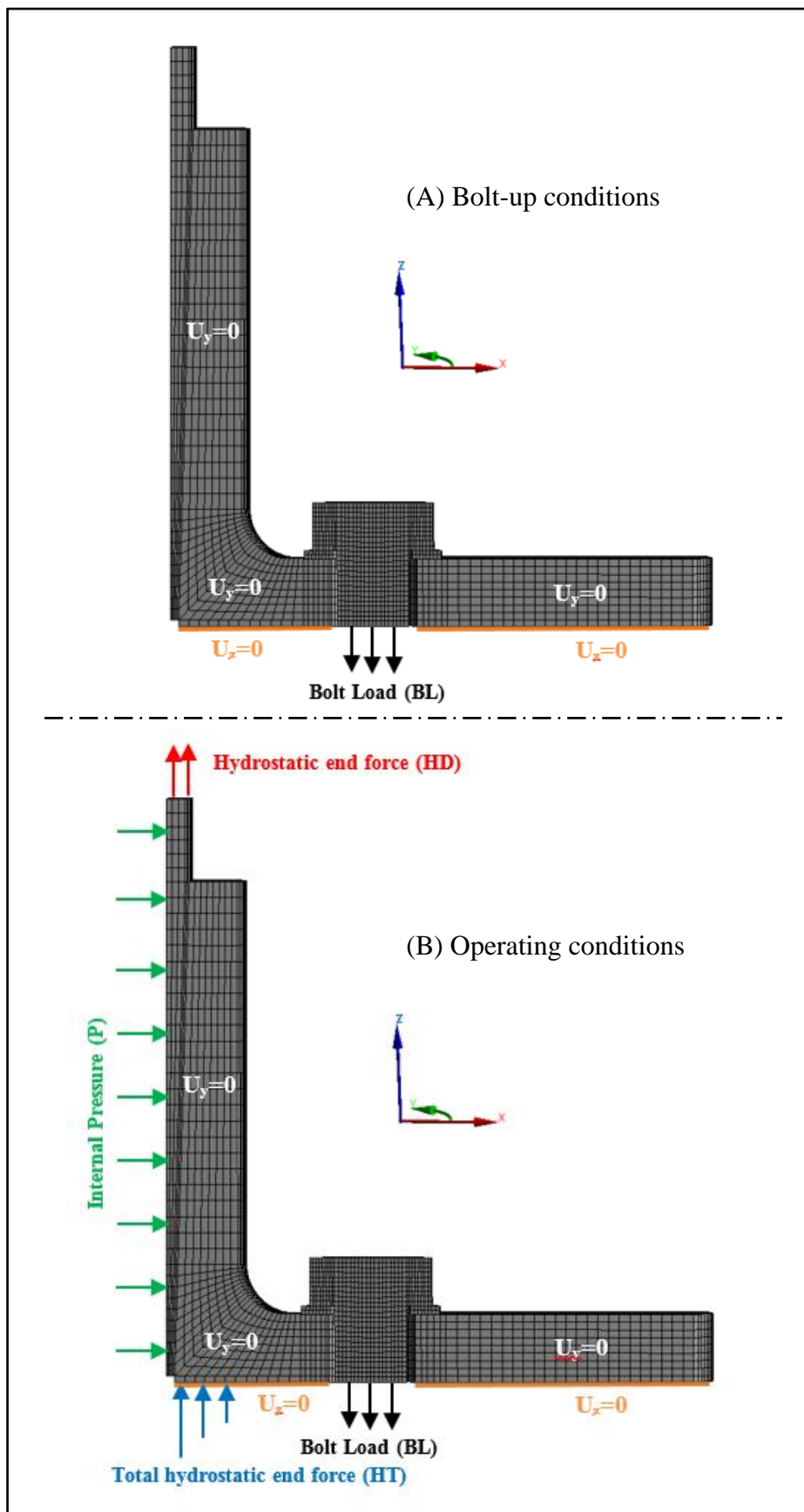


Fig. 6.7: Boundary conditions during the bolt-up and the operating conditions

### 6.2.8.3 Modelling leakage pressure

The fluid pressure penetration (FPP) between the flange and the gasket is modelled in ANSYS by a pressure-penetration criterion using the contact element real constant (PPCN). Based on the comparison between the internal pressure and the contact pressure, the fluid can penetrate new areas between the contact surfaces. For example, when the contact pressure is less than the fluid pressure, the fluid starts to penetrate from the starting points. In contrast, when the contact pressure is greater than the fluid pressure, the penetrating point returns to the starting point; that is, fluid penetration cut off point [115]. Since the contact pressure between the flange and the gasket decreases and the separation progresses as a result of the boundary conditions, the internal pressure is applied to the separated elements to induce more load on the joint system as shown in the Fig. 6.8. Due to symmetry, two edges have been specified as closed edges to prevent the fluid from entering. This simulation has been conducted by writing special commands (subroutines) in the Mechanical ANSYS. This feature of fluid pressure penetration capability has been added from version 12.0 of ANSYS [116].

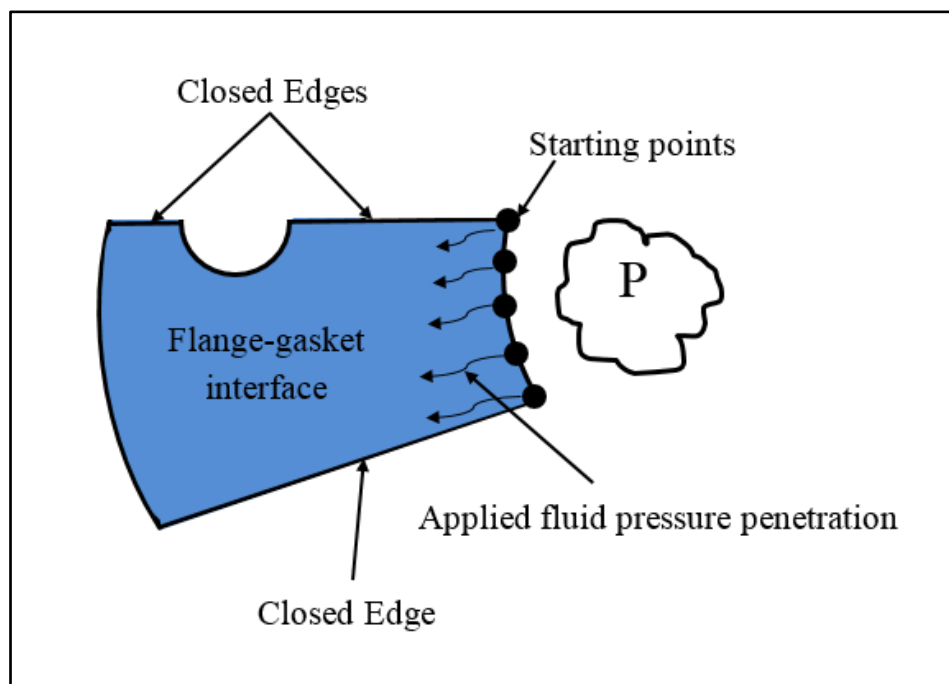


Fig. 6.8: Schematic diagram of the fluid pressure penetration modelling



### 6.3 Summary

In this chapter, the methodologies to simulate the bolted flange joint system using ANSYS FEA has been discussed. This FEA includes all components of the bolted flange joint; such as composite flange and pipe with their orthotropic mechanical properties, adhesive bonding and fastener with their isotropic properties and the rubber gaskets with their non-linear behaviour during the loading and unloading conditions. Nitrile and Viton rubber gaskets with different thicknesses have been used in this FEA. Various types of elements have been used based on the ANSYS guidelines and they have shown high performances.

Boundary conditions have been applied in two stages, bolt up and operating conditions. The symmetry boundary conditions (zero displacements) have been applied in both stages. In the bolt up condition, the bolt force has been applied whereas the internal pressure and the fluid pressure penetration along with the bolt force have been applied in the operating conditions. The fluid pressure penetration simulation has been set up using PPNC criterion and applied between the flange and the rubber gasket.

The results of this FEA will include the flange joint deformation, axial, hoop and radial strains, displacements, rotation and the leakage pressure. The effect of the applied loads, flange dimensions as well as the gasket type and thickness on all the above results will be investigated.

In the next chapter, two validations of the FE model will be conducted. The first validation will be carried out through the experimental work, which will include manufacturing of the bolted GFRP flange joint and its testing in the laboratory. The other validation will be done using an FE model, which has been investigated experimentally and numerically by a previous study. Finally, the results will be compared and discussed.

# CHAPTER SEVEN

## VALIDATION

### 7.1 Introduction

Validation is a method to verify the predictive capabilities of any mathematical or numerical model that are tested against experimental data. Validation is usually used to validate a mathematical or a numerical model of large projects, which cannot be tested at full scale, such as dams, siting of nuclear power plants [117]. In such cases, designers make a small model and test under the same conditions that are applied to the real (large) model. Then, they develop mathematical/numerical model and compare with the information collected during the test. The main reason for developing mathematical or numerical model is to eliminate the high costs of experiments that are time consuming and complex in nature [118]. Usually, the cost of experiments increases with the complexity of the test procedure. Therefore, the finite element analysis (FEA) method is considered as one of the most powerful numerical methods that are widely used for finding approximate solutions to complex methodical or physical problems.

This chapter aims to validate the numerical results obtained for an FEA model of bolted GFRP flange connection (shown in Fig. 7.1) through laboratory experiments. The numerical results will also be validated against published simulation results available elsewhere in the literature [1].

## 7.2 Experimental validation

As explained in chapter 4 and 5, the bolted GFRP flange joint (Hub flange) has been manufactured based on the ASME Boiler and Pressure Vessel Code, Section X [24] using vacuum infusion process. However, both the flange outside diameter and the hub length are considered to be more than the specified to perform a range of experiments with various dimensions. The flange has been bonded to GFRP pipe after chamfering its ends. Another type of composite flange, which is called heavy-duty (HD) flange, was bonded to the other end of the pipe. Both flanges, hubbed flange and HD flange, were sealed by using Acrylic and metallic blind flanges, respectively, along with different types of rubber gaskets such as Nitrile and Viton (both are 3 mm in thickness). For both ends, 16<sup>th</sup> bolts were used to close the system for producing a complete pressure vessel as shown in Fig. 7.2. During the test, several equipment were used such as pump, pressure gauge, digital torque wrench and various types of valves. Due to the radial symmetry, a 1/16<sup>th</sup> region of the flange joint has been chosen to collect the data from a total of 16 strain gauges that are either distributed on the flange body of the selected sector or embedded inside the bolts situated around the selected region. Four strain gauge boxes and two laptops were used during the test to construct a computerised data acquisition system. The loads were applied in two steps. These steps are categorised as (1) bolt up condition or gasket seating stage and (2) operating condition or pressurised stage. For the first stage, bolt loads from 0 up to 9.69 kN were applied at zero pressure. For the second stage, bolt loads were applied from 0 up to 9.69 kN, which is the bolt load design at the flange diameter 300 mm, with an internal pressure from 0 up to the pressure at which leak occurs.

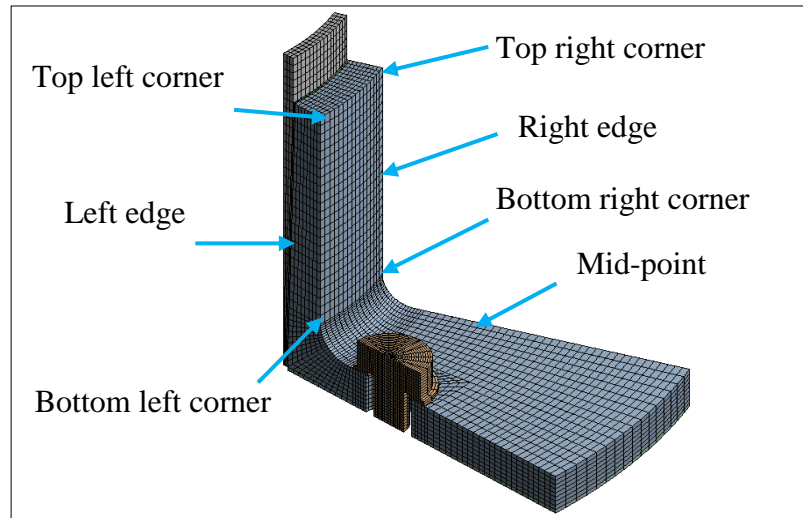


Fig. 7.1: FEA model



Fig. 7.2: Pressure vessel during the test

### 7.2.1 Bolt up condition

During this stage, various bolt preloads were applied (from 0 up to 9.69 kN) using digital torque wrench. The purpose of the digital torque wrench is to maintain the same axial loads for all the bolts. Strain gauges were attached to some of the bolts to measure the axial strain on the bolts along with the measurement of torque with the

help of torque wrench. It has been ensured that the same torque is applied to all the bolts in order to achieve required compressive pressure on the gasket. The compressive pressure deforms the gasket and fills the gaps on the flange face ensuring full contact over the entire surface. The bolt up loads and other boundary conditions explained in the chapter 6 have been applied in the numerical simulation.

#### 7.2.1.1 Hub axial strain

The interfacial region between the flange disc and the hub is one of the most important areas that are subjected to axial strain. This is due to the axial bolt loads, which are required to seat the gasket and to create a sufficient contact pressure between the flange and the gasket. The axial strain values near the bolts in the circumferential directions are higher than any other regions between the bolts. Fig. 7.3 shows the axial strain at the lower part of the hub measured at the front of the bolt centre and just above the flange-hub intersection. Fig. 7.3 clearly shows the variations in experimental and numerical values of the axial strain for different types of gasket (Flange-Nitrile (FN) gasket and Flange-Viton (FV) gasket).

It is obvious in this figure that the hub axial strain increases with the increase in the bolt loads, however, the strain values are small which indicates high performance of the proposed flange joint. The experimental data shows non-linear trend especially at the lower bolt loads whereas the FEA results are linear. This is because the lower face of the flange in the experiment was not flat. The outside diameter edge of the flange was not at the same level as it was at the edge of the inner diameter. This phenomenon is called flange spring back and it usually occurs for the hub composite flange due to the polymer shrinkage during the curing process [51]. The effect of the spring back on the axial strain is appeared clearly at the beginning of the bolt preload stage when bolt loads are low. The flange face was not in full contact with the gasket, as a result, the flange required extra bolt loads to close the gap between the flange and the gasket. This caused bending to the flange as well as reduced gasket reaction in some contact areas especially near outside the bolt circle. Therefore, higher strain values were generated. This phenomenon could not be implemented into the FEA model as a boundary condition, hence, the numerical results showed different trends

than that of the experimental observations. However, it is clear from Fig. 7.3 that the type of rubber gasket has insignificant effect on the hub axial strain.

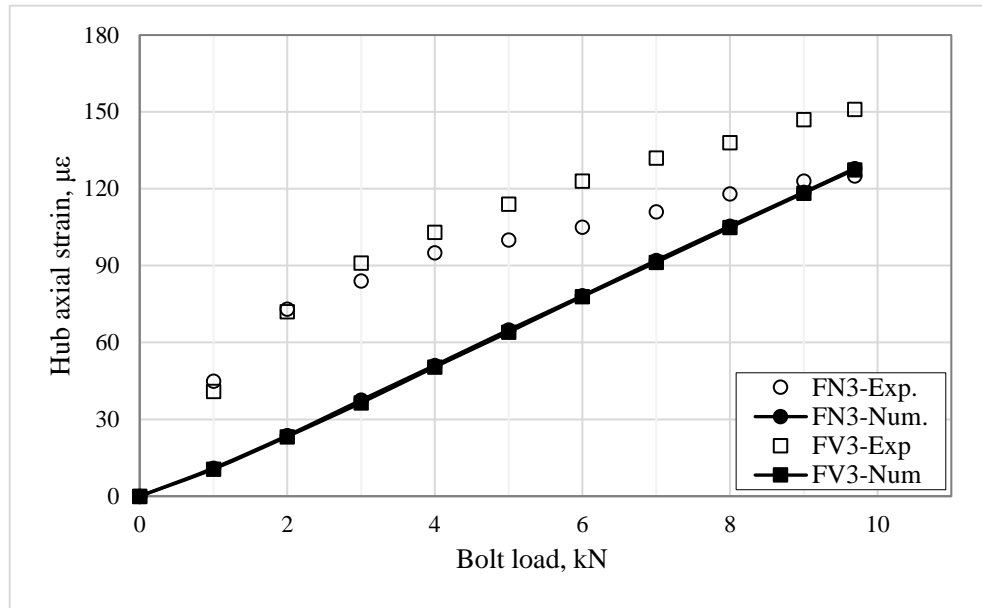
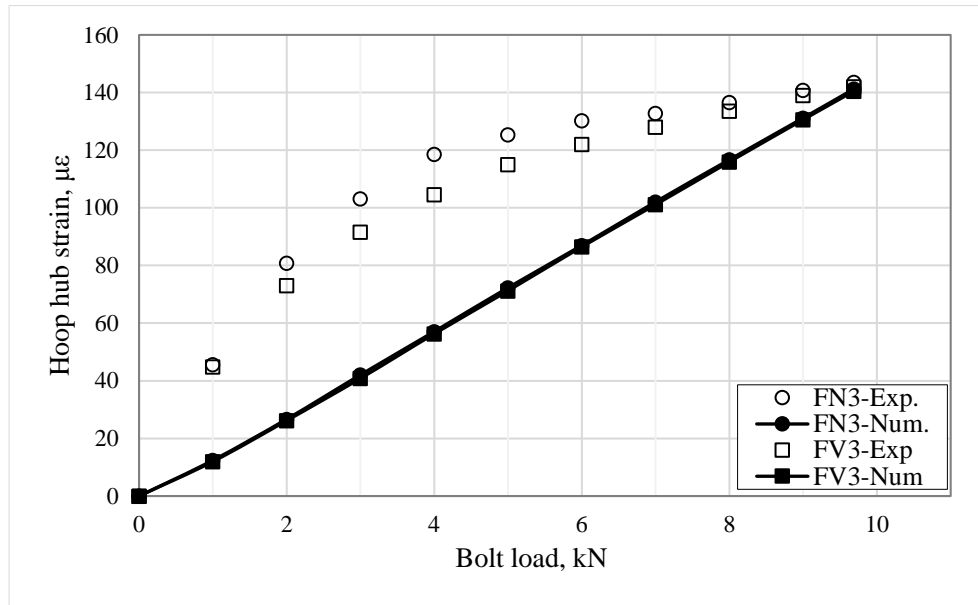


Fig. 7.3: Hub axial strain,  $\mu\epsilon$

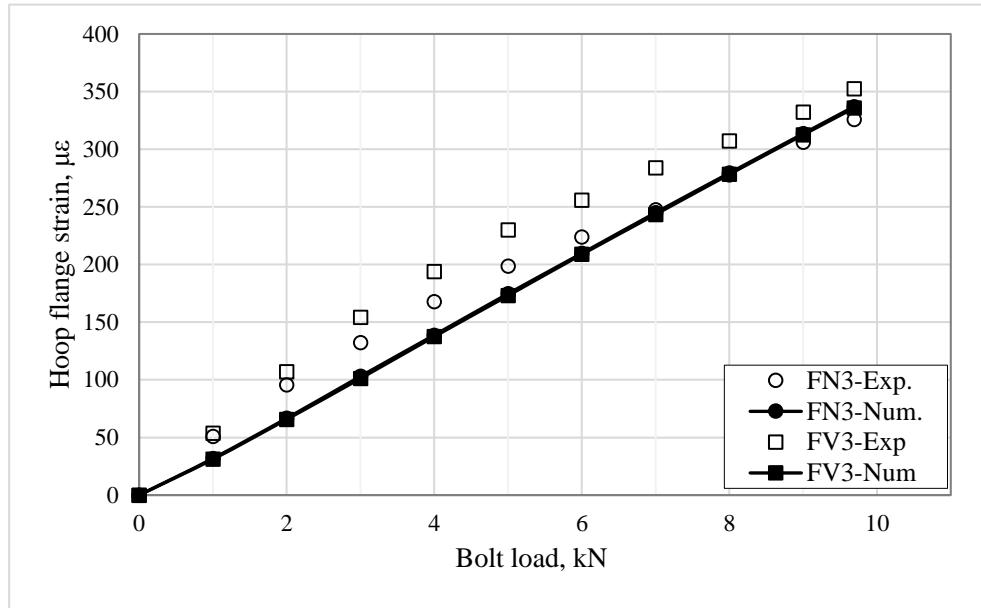
### 7.2.1.2 Hub hoop strain

The hoop strain at the hub-flange intersection region is also high compared to other regions and that is due to the unsymmetrical bolt load distribution on the flange disk. Therefore, it has been found that the hoop strain at the mid-points between the adjacent bolts is higher than that of the points near the bolts. Fig. 7.4 illustrates the relationship between the hoop strain and the bolt load at the lower part of the hub (Fig. 7.1) for Nitrile and Viton rubber gaskets of 3mm thickness. The results show that the bolt load has a significant effect on the hoop strain, which increases when the bolt load increases. Both experimental and FEA results indicate that the strain values are still low (less than  $150 \mu\epsilon$ ) even when the bolt load is increased to 9.69 kN. However, the experimental strain value is a bit higher than the numerical value and this is because of the flange spring back effect. It is observed in the experiments that the type of rubber gasket has some effects on the hoop strain but this is not found in the FEA results. However, the agreement between the experimental and the FEA results is good, especially at the design bolt load.

Fig. 7.4: Hub hoop strain,  $\mu\epsilon$ 

### 7.2.1.3 Flange hoop strain

Fig. 7.5 shows the hoop strain on the upper face of the flange at the mid-points between two adjacent bolts (Fig. 7.1). Due to the bending of flange with bolt loads and the reaction of the gasket, the upper face of the flange is subjected to hoop tension strain whereas the lower face is subjected to hoop compression strain. It can be seen in Fig. 7.5 that the hoop strain increases with the increase in the bolt load almost linearly. The experimental results showed that there was a slight difference in the hoop strain for the Nitrile gasket than that of the Viton gasket. The hoop strain with Viton rubber gasket was slightly higher than the Nitrile rubber gasket. However, the FEA results do not vary with the type of gaskets. Generally, a good agreement is achieved between the experimental and the numerical results.

Fig. 7.5: Flange hoop strain,  $\mu\epsilon$ 

## 7.2.2 Operating conditions

The internal fluid pressure of the pipe is the main load that is applied during the operating conditions (stage). This stage should always follow the bolt preload stage, which include applying the bolt load and seating the gasket to fill the irregularities of the flange faces. The stage also leads to create a contact pressure that should be able to withstand the leakage propagation of the internal pressurized fluid. The internal pressure used in this study is up to the leakage pressure including the design internal pressure (3.4 bar) at different bolt loads. Additional boundary conditions are applied in the numerical simulation, which take into account the effect of hydrostatic end force of the pipe and the symmetry of the flange. The detailed boundary conditions are explained under section 6.2.8.

### 7.2.2.1 Axial Strain

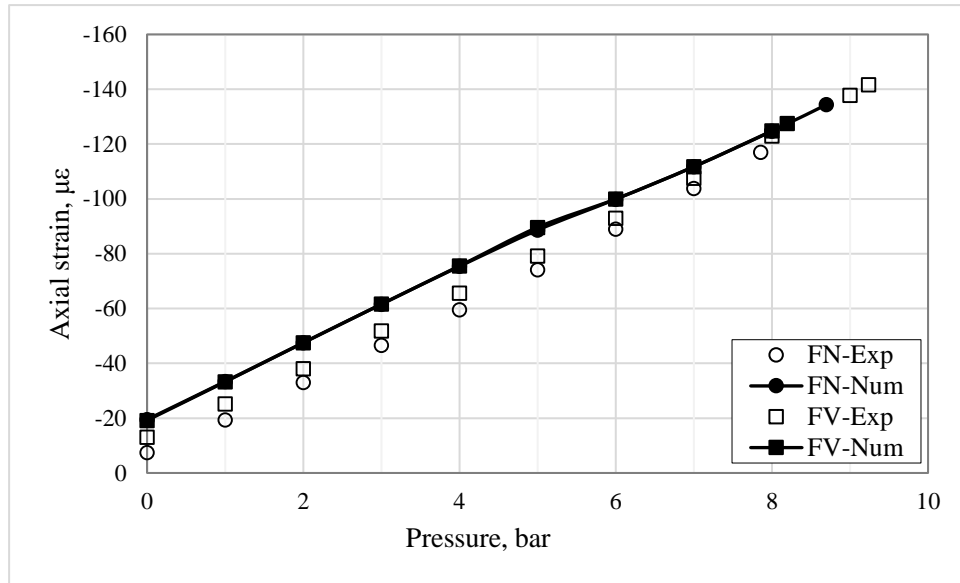
The axial strain has been measured at various places during the pressurized stage. Two strain gauges were placed at different places on a radial line that passes through the bolt centre (left edge) whereas other two strain gauges were placed on a radial line that passes through the mid-point between the contiguous bolts (right edge) as



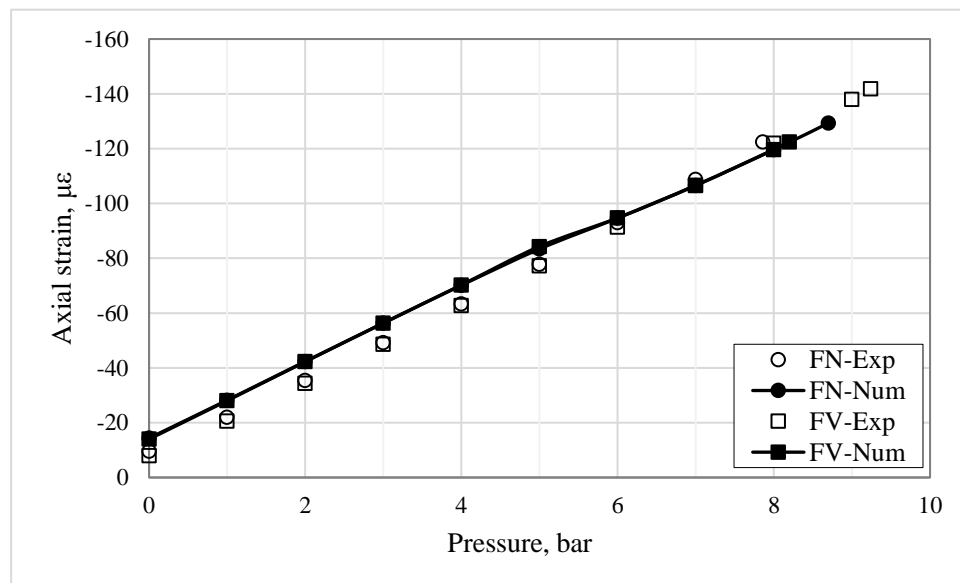
shown in the Fig. 7.1. Two of the four strain gauges (mentioned above) were placed on the top edge of the hub whereas the other two were bonded onto the bottom edge of the hub, which is just above the Flange-hub intersection that represents one of the critical points on the bolted GFRP Flange connection as shown in the Fig. 7.1.

Fig. 7.6 shows the axial strain on the top-left corner of the hub as a function of the internal pressure up to the leakage pressure for Nitrile and Viton rubber gaskets. Both the experimental and the FEA results showed that the outer face of this region was exposed to the compression axial strain. The axial compression strain increased with the increase in the internal pressure. This is due to the internal pressure that was applied on the internal face of the pipe and the force that was produced by the internal fluid of the surface contact between the flange and the rubber gasket. It is observed that the gasket type has insignificant effects on the axial strain at this region but gasket type has influenced the leakage pressure. It can be seen clearly in the figure that the leakage pressure of Flange-Nitrile gasket (FN) is 7.9 bar for the experiment and 8.7 bar for the FEA. Whereas these values are 9.2 bar and 8.2 bar respectively for the Flange-Viton gasket (FV). The variation in experimental results between the two types of gaskets is 1.3 bar whereas the difference in the FEA results is only 0.5 bar. Generally, a good agreement is obtained between the experimental and the FEA results for both the axial strain and the leakage pressure.

The variation of axial strain on the top-right corner of the hub (at a point between two adjacent bolts) with the internal pressure up to the leakage pressure at bolt load 9.69 kN is presented in the Fig. 7.7 . Similar to the axial strain in the top-left corner plotted in the Fig. 7.6, a compression axial strain was produced due to the flange bending by the internal pressure.

Fig. 7.6: Axial strain,  $\mu\epsilon$  (top-left)

The variation of the axial strain with the pressure is almost linear in both experimental and numerical cases and the agreement between them is very good. It should be noted that the results are not affected by the gasket materials. In addition, the maximum values of the axial strain in both the top corners (Fig. 7.6 & Fig. 7.7) in experiments and numerical simulations is less than  $150 \mu\epsilon$ , which is very low compared to the applied internal pressure at the point of leakage. This confirms that the proposed flange is well designed and the use of ASME code is conservative.

Fig. 7.7: Axial strain,  $\mu\epsilon$  (top-right)

As mentioned earlier, the Flange- hub intersection represents a critical region in the bolted flange joint and especially for the composite flange. This is due to the strain concentration in the region by the bolt and pressure loads. Usually, most of the commercially available hubbed composite flanges fail in the same region [33]. Fig. 7.8 represents the axial strain variation with the internal pressure at the bottom-left corner and just above the flange-hub intersection (at a height of 45 mm above the flange face). The left edge is in front of the bolt centre whereas the right edge is the edge that is allocated at the mid-point between two adjacent bolts (Fig. 7.1). This region is exposed to the tension axial strain, in contrast of the hub top edge, which is subjected to axial compression strain. When the internal pressure is increased up to the leakage pressure, both the experimental and the FEA axial strain increased.

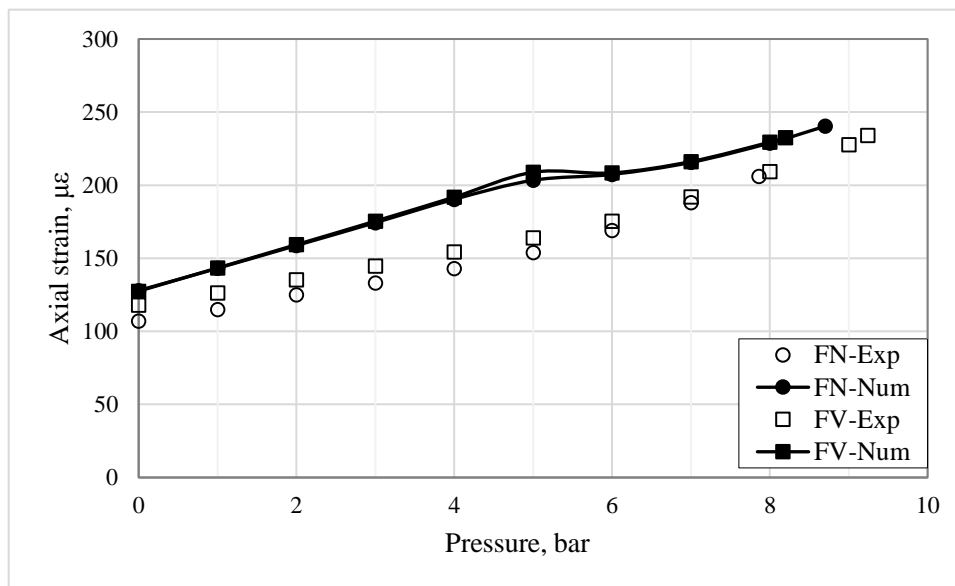


Fig. 7.8: Axial strain,  $\mu\epsilon$  (bottom-left)

However, the FEA axial strain from 5 bar to 6 bar remains almost constant. There are two reasons that could lead to this: firstly, the non-linear radial propagation of the pressurized fluid between the flange and the gasket produces extra forces on the flange face, which tries to push up the flange and minimizes the flange bending. The second reason could be the non-linear responses of the gaskets. The axial strain is not influenced by the gasket type. The agreement between the experiment and the FEA results was good as the maximum difference between the leakage pressure between them is less than 1 bar for both Flange-Nitrile (FN) and Flange-Viton (FV)

gaskets. It can be seen clearly in Fig. 7.3 and Fig. 7.8 that the bolt preload has affected the axial strain more than the internal pressure.

Fig. 7.9 presents the axial strain on the bottom of the hub at the right edge (which is in the middle of the two bolts) as a function of the internal pressure. The axial strain is affected by the internal pressure and its values at this area are less than that at the left edge near the bolt when compared with the results in the Fig. 7.8. This is because of the bolt load, which bends the flange at the bolt holes more than in any other regions. This phenomenon can be clearly explained through the calculations of the flange displacements at the inner and the outer diameters and along the flange rotation and this will be discussed extensively in the next chapter.

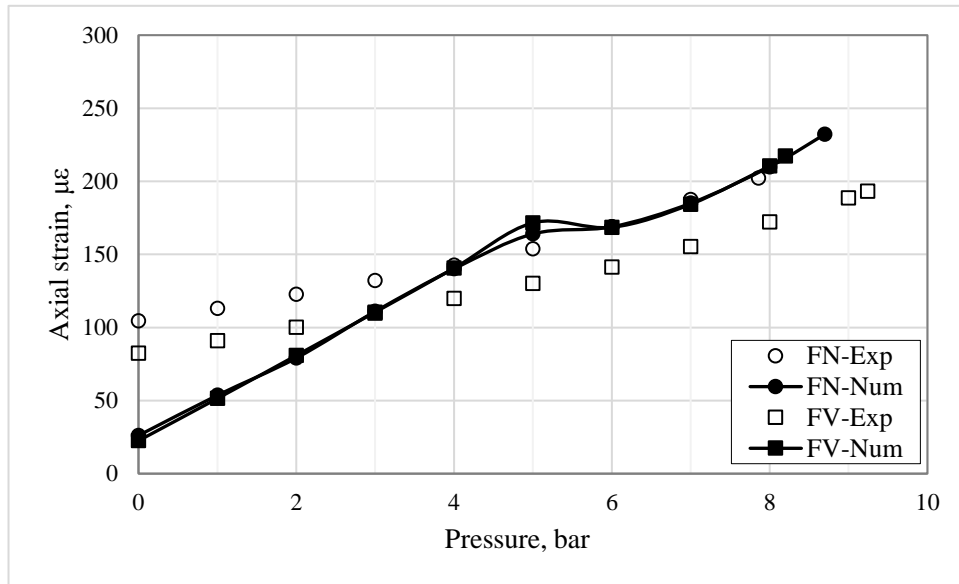


Fig. 7.9: Axial strain,  $\mu\epsilon$  (bottom-right)

#### 7.2.2.2 Hoop strain

Hoop strain is very important for the design of the bolted GFRP flange joint. At the hub, the hoop strain is measured and investigated to see the influence of the applied loads (bolt and pressure loads) on the circumferential expansion or deformation. In addition, hoop strain is a good indication to analyse the flange bending in the circumferential direction, which is produced due to the bolt preload and the internal pressure. Therefore, as with axial strain, the hoop strains were measured at different places on the flange joint body (hub and flange disc).

Fig. 7.10 shows the relationship between the hoop strain and the internal pressure, which is increased up to the leakage pressure, at the hub top-left edge of the selected portion for this study (Fig. 7.1). It is found that the internal pressure has a significant effect on the hoop strain at this area but the bolt load has very small impact. This can be seen clearly at the beginning of the plot where the pressure is zero but the bolt force is 9.69 kN. The hoop strain is increased when the internal pressure is increased and it is not affected by the gasket behaviours. The agreement between the experimental and the numerical results was excellent. This confirms that the finite elements analysis method could be considered as a good tool to simulate the bolted fibre reinforced polymer flange connection with the advantage of saving the cost for manufacturing and testing, which are also time consuming.

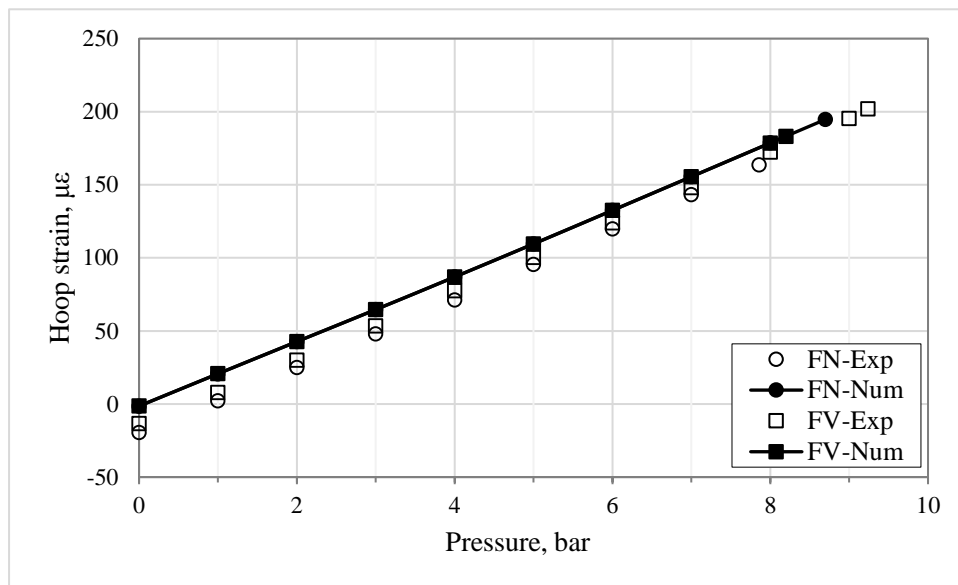


Fig. 7.10: Hoop strain,  $\mu\epsilon$  (top-left)

Fig. 7.11 demonstrates the hoop strain at the hub top right corner, which is the middle line between two adjacent bolts in the chosen part of the joint. This figure shows the hoop strain variation with the internal pressure up to the leakage for two different types of rubber gasket. Comparing with the hoop strain at the left side shown in the Fig. 7.10, the right side hoop strain is slightly less than those at the left corner, which is located at the front of the bolt corner. The gasket type has influences on the hoop strain when measured experimentally but no influence is observed when

measured numerically. The experimental data of Flange-Nitrile rubber gasket (FN) is slightly higher than that of the Flange-Viton rubber gasket (FV).

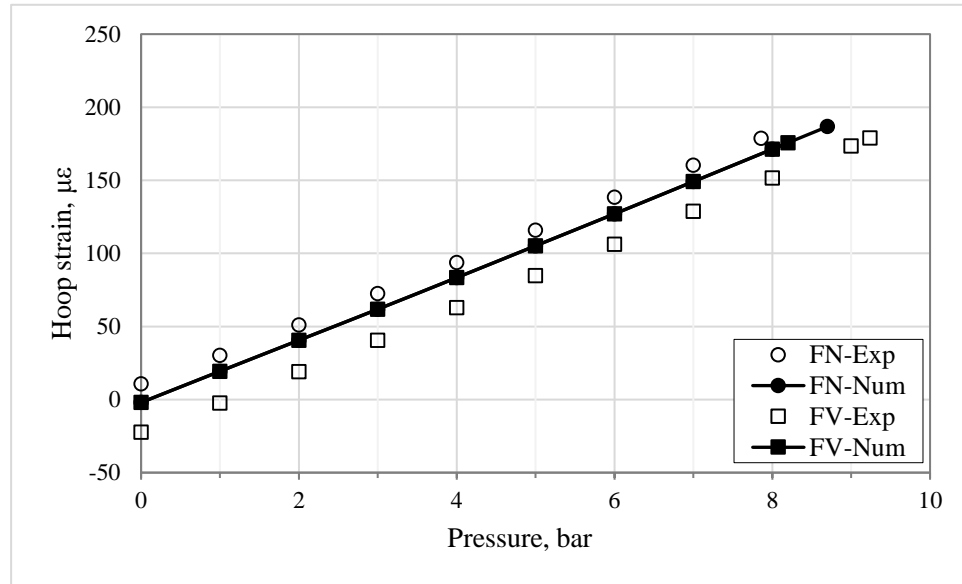
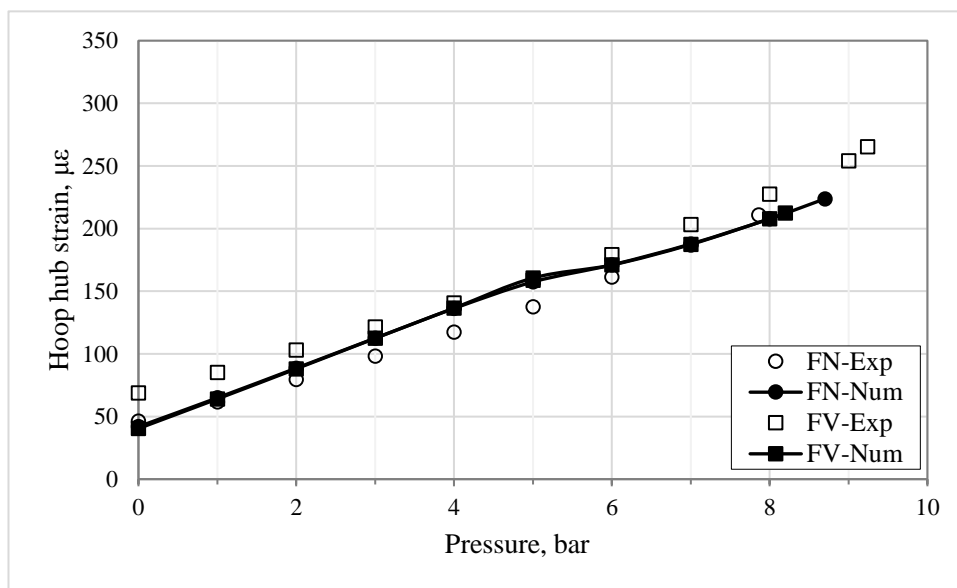


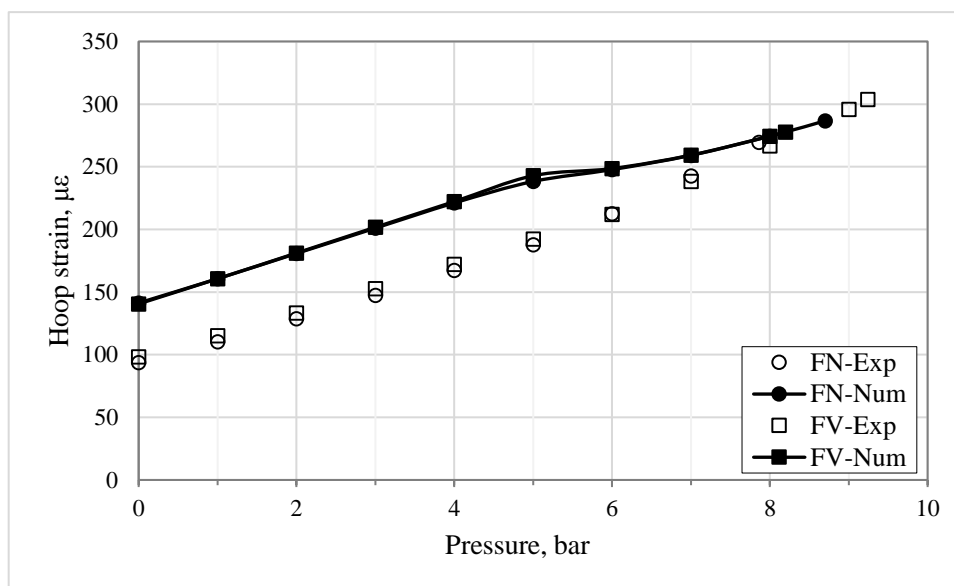
Fig. 7.11: Hoop strain,  $\mu\epsilon$  (top-right)

Fig. 7.12 denotes hoop strain as a function of the internal pressure for the hub bottom left corner of the chosen study area, which is just above the flange hub intersection. The results showed that this area is subject to the tensile hoop strain and is increased with the increase in the internal pressure up to the leakage point. The values of the hoop strain at this point are higher than those values at the hub top left shown in the Fig. 7.10. This is because the area at the bottom edge is subjected to the effects of the bolts loads in addition to the internal pressure. In other words, the influence of the bolt load at the flange-hub intersection is more than that at the top edge of the hub. This can be seen clearly when the hoop strain values at the pressure of 0 bar are compared in Fig. 7.10, Fig. 7.11, Fig. 7.12 and Fig. 7.13.

Fig. 7.12: Hoop strain,  $\mu\epsilon$  (bottom-left)

Moreover, the gasket type has insignificant impact on the hub strain and the agreement between FEA and experimental results is very good.

Fig. 7.13 illustrates the variation in the hoop strain with the internal pressure up to the leakage point for the regions at the bottom right edge of the hub. As it is observed, increasing the internal pressure has led to the increase in the hoop strain. The FEA results are slightly higher than the experimental results up to 5 bar of the pressure but it decreases after 5 bar and becomes closer to the experimental results.

Fig. 7.13: Hoop strain,  $\mu\epsilon$  (bottom-right)

This might be due to the non-linear radial propagation of the pressurized fluid between the flange and the gasket. This changes also occurred with the axial strain at the same points (as can be seen in Fig. 7.8 and Fig. 7.9). In addition, it can be noticed that the hub strain at the bottom right edge of the hub (mid-point between two adjacent bolts) is higher than that of at the bottom left edge of the hub, which is located near the bolt. In contrast, the axial strain on the hub and at the front of the bolt is higher than that at the middle point. The hub strain is not influenced by the gasket types or gasket response.

The hoop strain was also measured on the flange disc at the middle point between two adjacent bolts and along the circumferences of the holes. As shown in the Fig. 7.14, hoop strain at this point is slightly influenced by the internal pressure but it is affected significantly by the bolt. Similar effects can be seen in the results presented in Fig. 7.5 and Fig. 7.14 for zero internal pressure. Therefore, this area is already strained in the bolt preload stage.

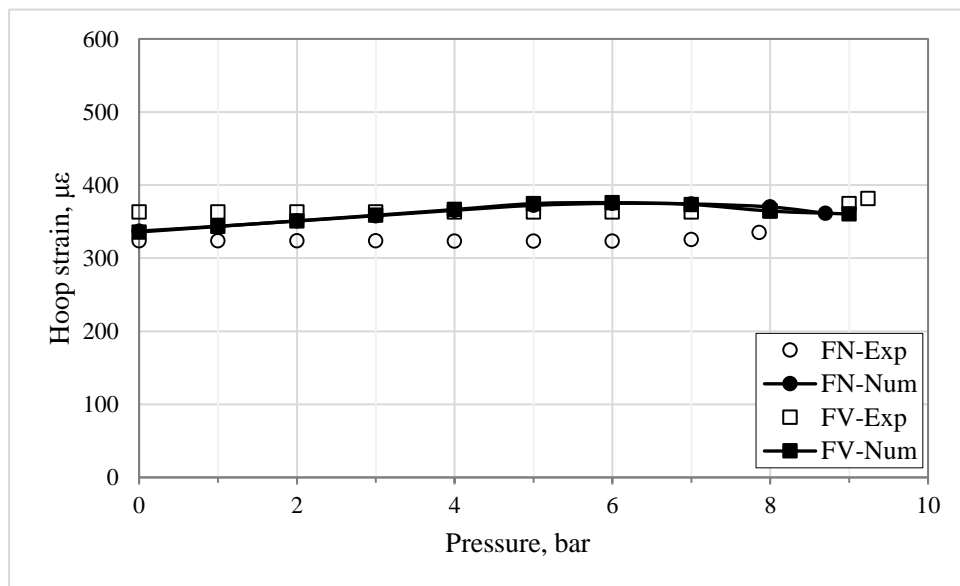


Fig. 7.14: Flange hoop strain,  $\mu\epsilon$

In addition, the FEA results show that the upper face of the flange at this point is exposed to the tensile hoop strain whereas the lower face is subjected to the compression strain. This is due to the bolt loads, which are distributed unsymmetrically around the Flange. This phenomenon will be explained and



described explicitly in the next chapter under the sections of flange displacement and rotation.

### 7.2.2.3 Radial strain

The radial strain has been measured at various places on the upper face of the flange experimentally and numerically. Most of the results showed that the radial strain values are small (less than 100  $\mu\epsilon$ ) during the bolt-up conditions as well as in the operating conditions.

The radial strain variation with the internal pressure at the bolt centre (left edge) and at the outside of the bolt circle is shown in Fig. 7.15. The experimental results illustrate that the internal pressure has negligible influence on the radial strain. The FEA results show that initially the radial strain at low or even at zero pressure is higher than the experimental data but eventually the strain becomes almost identical at higher pressures (5 bar and beyond). The difference in the radial strain values at the low pressure is the result of the flange spring back, which is not captured in the simulation.

Experimentally, the contact pressure between the flange and the gasket at the inner bolt circle is higher than that of the outer regions. The gasket reaction is also less at the outer regions thereby the radial strain is low at the beginning. In the numerical simulation, there is full contact between the flange and the gasket, so the gasket reaction is created at the same time in all of the contact areas. This has led to increase the radial strain in the numerical simulation during the bolt preload and at the low pressure. In addition, the leak propagation in the FEA simulation at the low pressure is more than that observed in the experiments thereby the pressure forces in the FEA is more than the experimental values. These forces are applied on the inner face of the pipe and on the flange-gasket interface. Increasing these forces (i.e. increasing the pressure) leads to bend the flange along with an increase in the gasket reaction at the outer area of the circumferences of the holes. This also leads to drop the radial pressure up to around 5 bar as shown in the Fig. 7.15. The gasket type has an impact and the Nitrile rubber gasket produces the radial strain more than the

Viton gasket as observed both in the experiment and in the numerical simulation. Both the experimental and the numerical results are in good agreement.

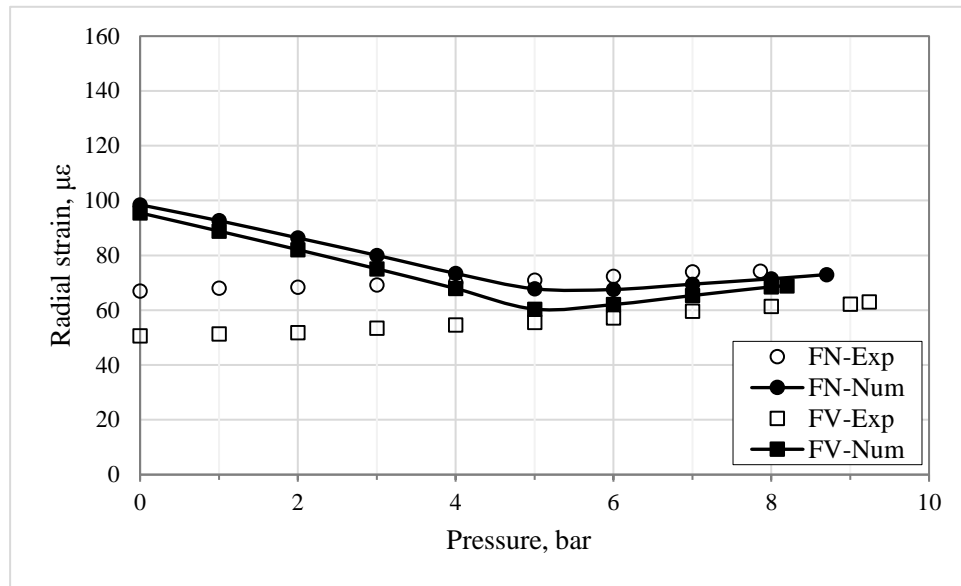


Fig. 7.15: Flange radial strain,  $\mu\epsilon$ , (bolt centre)

Fig. 7.16 shows the relationship between the radial strain and the internal pressure up to the leakage at the middle point between two adjacent bolts and at the outer bolt circle. It is observed that this point is subjected to small compression strain (less than  $40 \mu\epsilon$ ) and it is almost not influenced by the internal pressure. The FEA results was are slightly different because of the spring back of the GFRP flange. The gasket type has insignificant impact on the radial strain. Generally, the FEA and the experimental results achieved good agreement with each other.

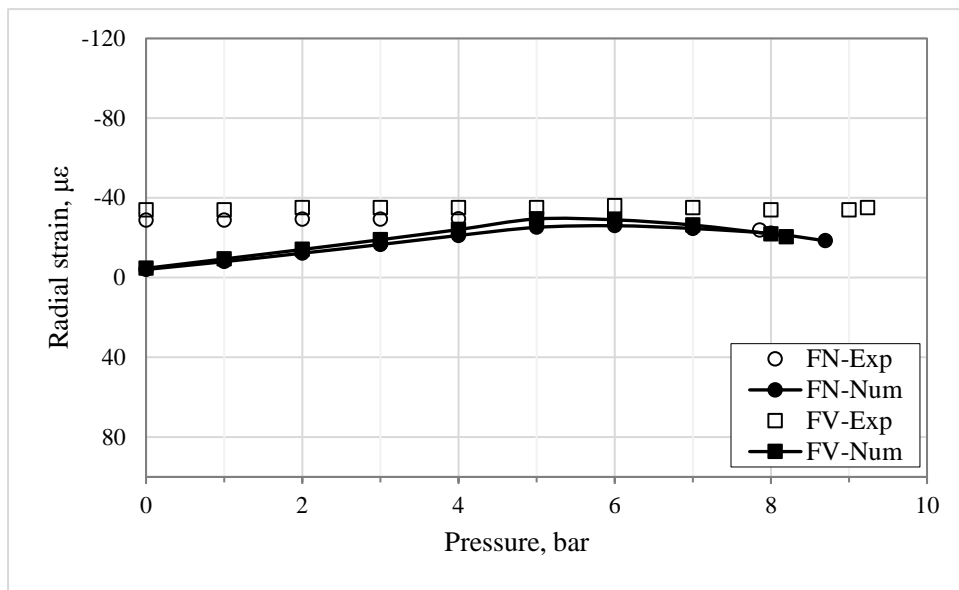


Fig. 7.16: Flange radial strain,  $\mu\epsilon$ , (mid-point)

#### 7.2.2.4 Bolt load variation

The axial bolt load is very important for the bolt flange joint to seat in the gasket, to create a sufficient contact pressure and to withstand the leakage propagation. In this study, the applied bolt load was measured using two methods: (1) using strain gauge embedded in the centre of the bolt after drilling a hole into it and (2) using a digital torque wrench.

Fig. 7.17 shows the variation of the bolt load with the internal pressure when the bolt pre load was 9.69 kN (324  $\mu\epsilon$ ). The experimental results illustrate that the internal pressure has insignificant effect on the bolt load whereas the FEA results were not affected by the internal pressure at all. However, at high pressure just before the leakage pressure, the bolt loads in the experiment showed influences due to the propagation of the pressurized fluid, which was trying to split the matched flanges. This observation is also consistent with the metallic flanges. In addition, the gasket responses have no impacts on the bolt loads but can affect the leakage pressure values. Fig. 7.18 shows the similar trend of bolt load variation with internal pressure but the results are plotted against the axial stress.

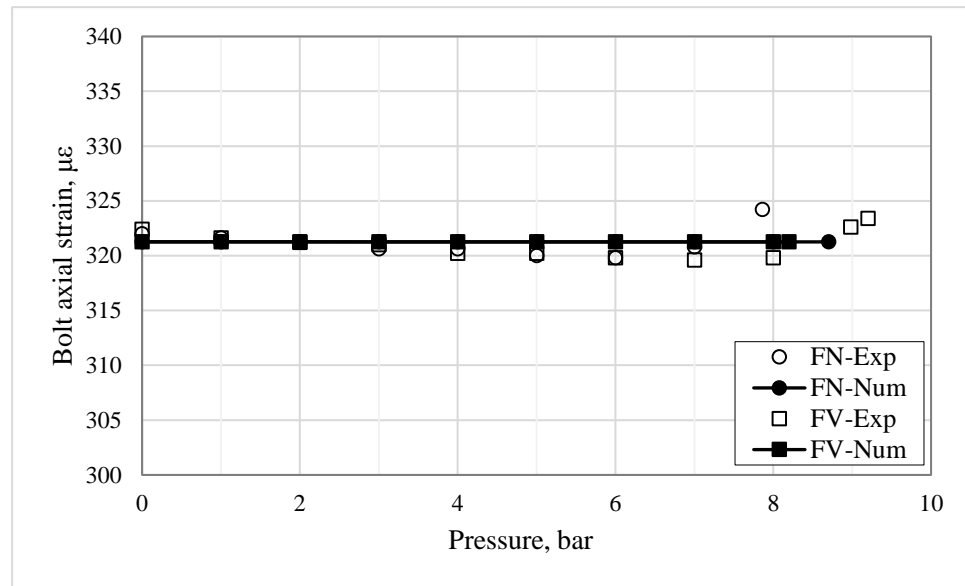
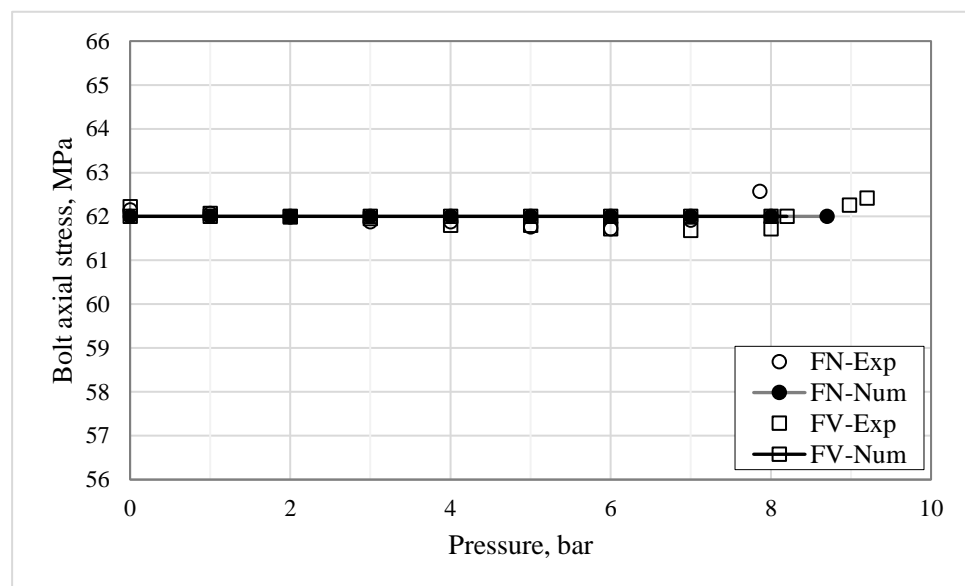
Fig. 7.17: Bolt axial strain,  $\mu\epsilon$ 

Fig. 7.18: Bolt axial stress, MPa

### 7.2.2.5 Leakage pressure and the contact pressure

Millions of tons of oil and gas are lost around the world due to the leakage that usually occurs in pipelines and in their connections. This is one of the main causes of the environmental pollutions nowadays. It is usually called an “oil spill”, which includes any spill of crude oil or distilled oil (e.g., gasoline, diesel fuels, jet fuels, kerosene, Stoddard solvent, hydraulic oils and lubricating oils). These can pollute land surfaces as well as air and water. For example, the BP oil spill incident that occurred in the Gulf of Mexico in 2010. This oil disaster led to the death millions of marine creatures. The U.S. government had estimated that the total discharge was almost 5 million barrels [119]. In this study, the leakage pressure has been measured experimentally in the laboratory using a pressure vessel manufactured in-house. The same pressure vessel has also been simulated through FEA using the PPNC criterion to understand the leakage propagation phenomena. The detailed analysis method has been discussed in the chapter six.

The distribution of the contact pressures on the top gasket surface is illustrated in Fig. 7.19 at various internal pressure values including the leakage pressure (8.8 bar). The results show that at the bolt up conditions (i.e. at 0 bar pressure), the minimum contact pressure is found at an area which is outside of the hole circumferences whereas the maximum contact pressure is concentrated around the bolt hole at the closest point to the inner diameter. When the internal pressure is increased, the contact pressure at the inner diameter of the gasket, which is in direct contact with the pressurized fluid, decreased. With the increase in the pressure, the maximum contact pressure moved away from the bolt hole to the closest point on the outer diameter of the flange where the fluid started to penetrate at the inner diameter. In addition, in the circumferential direction, the contact pressure at the bolt hole is higher than at the midpoint between the bolts. This is due to the boundary conditions, bolt loads, internal pressure, hydrostatic end force and total hydrostatic force, which produce a bending moment and hence flange rotation.

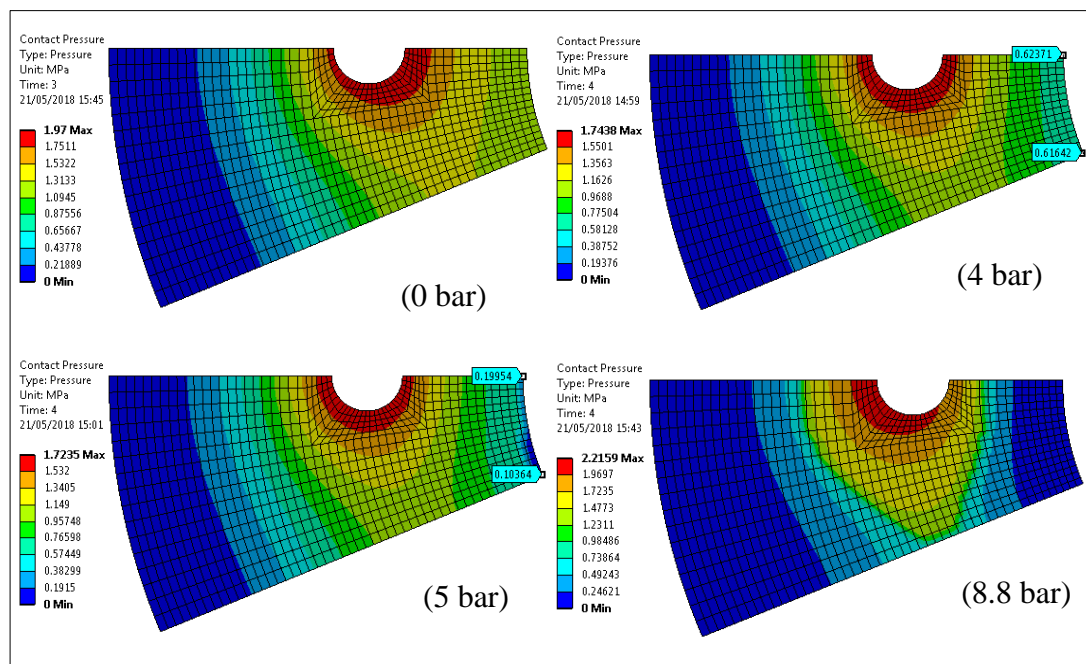


Fig. 7.19: Distribution of contact pressure on gasket

The distribution of the fluid pressure penetration (FPP) between the flange and the Nitrile rubber gasket has been illustrated in the Fig. 7.20. The results indicate that there is no leakage propagation started yet up to 4 bar and that is because of the contact pressure between the flange and the gasket at the inner diameter, which is in direct contact with the fluid and is higher than the applied fluid pressure. When the internal pressure exceeds 4 bar, the leakage starts to penetrate at the inner radius of the gasket, where the contact pressure is dropped to 0.1 MPa at the inner diameter, and propagates towards the outer radius. See Fig. 7.19.

Also, due to uneven distribution of the bolt loads in the circumferential direction, the leakage growth at the midpoint between the adjacent bolts is more than that of at the bolt centre.

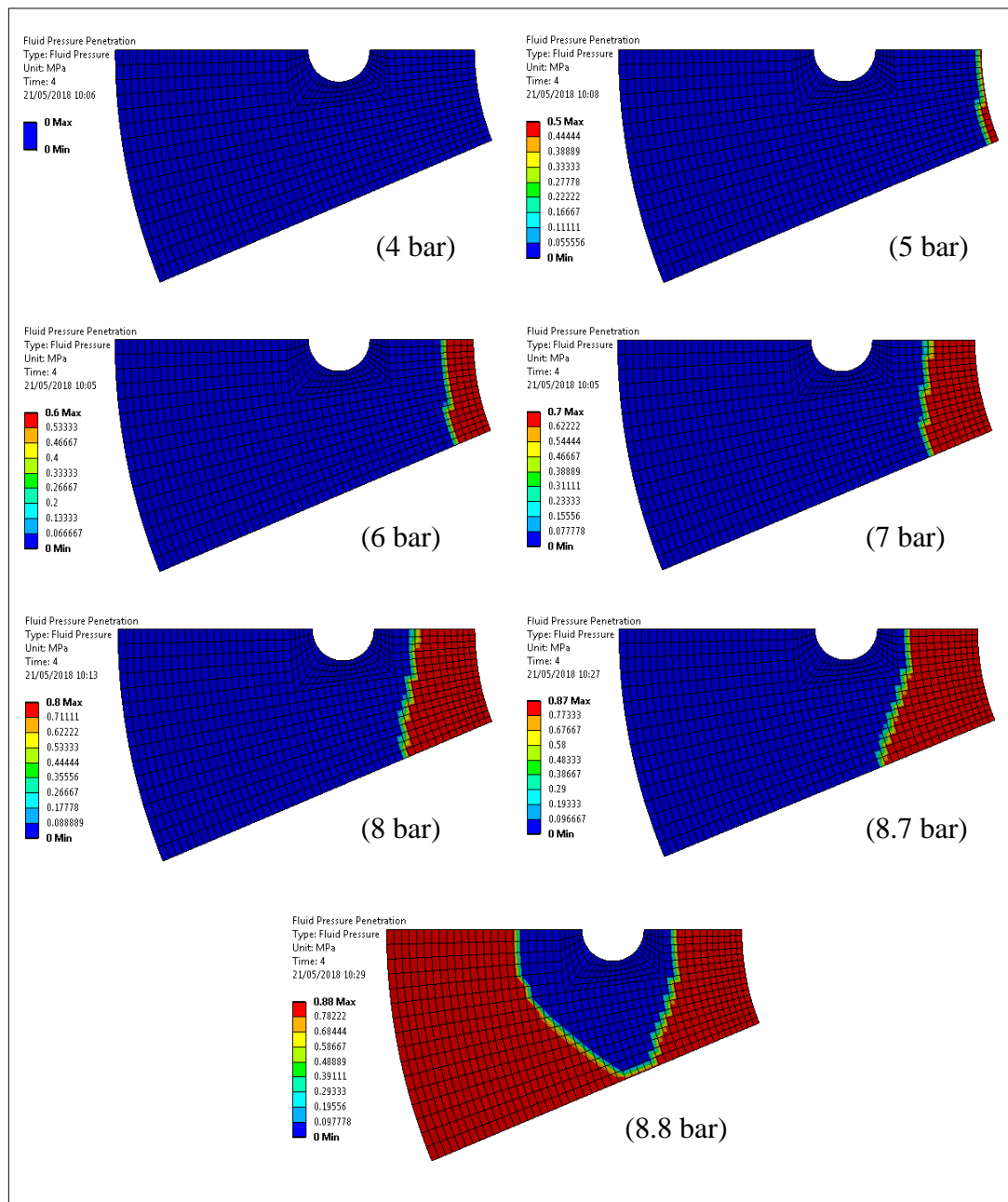


Fig. 7.20: Leakage propagation with the internal pressure up to leakage pressure

Fig. 7.21 shows the experimental and the numerical leakage pressure variations with the bolt preload of the flange and Nitrile rubber gasket. As expected, the leakage pressure increases with the increase in the axial bolt load. This occurs because of increasing the bolt load leads to increase the flange-gasket contact pressure, which is minimizing the leakage propagation. It seems that the lower bolt loads influence on the leakage pressure more than the higher bolt loads. In addition, the experimental results show that the leakage pressure at the lower bolt loads are higher than that observed in the FEA results. This is due to the spring back of the GFRP flange, which made the flange face uneven because of the shrinkage during the curing.

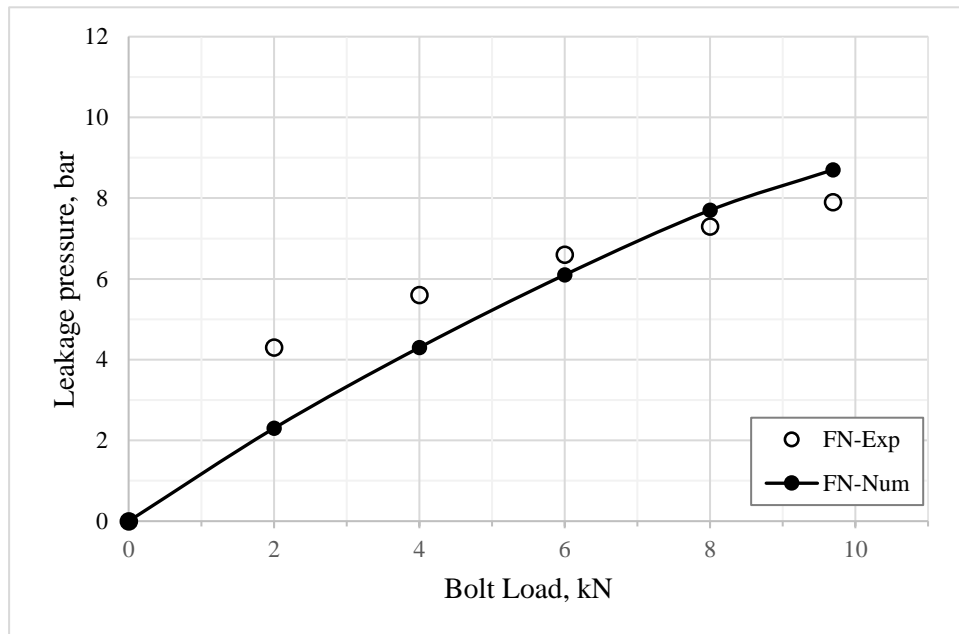


Fig. 7.21: Leakage pressure variation of Flange-Nitrile gasket with the bolt load

The contact pressure between the flange and the gasket at the inner area of the holes circle takes place before the outer area of the holes circle. Therefore, the contact pressure at the inner area is higher than that at the outer area of the holes circle at the low range of the bolt loads. This leads to increase in the leakage pressure values at the lower bolt loads during the experiments but it become closer to the FEA results at the higher bolt loads. It should be noted that the flange spring back effect is reduced at the higher bolt loads. However, an excellent agreement between the experimental and the FEA results was obtained, especially, at the design bolt load,



The FEA modelling method can be used to simulate the leakage propagation and to estimate the leakage pressure, which is expensive and also takes longer time to perform if the experimental method is used.

Fig. 7.22 explains the relationship between the leakage pressure and the bolt load of the Flange-Viton (FV) rubber gasket. Generally, the behaviour of the relationship is approximately same as the behaviour of the Flange-Nitrile (FN) rubber gasket. As with the FN, the experimental data was slightly higher than the FEA results and that is due to the flange spring back, which is discussed above. However, a good agreement has been reached between the experimental and the FEA analysis results and again it can be said that the simulation can be used to see the growth of the leakage and to estimate the leakage pressure during the design phase of GFRP flange joint.

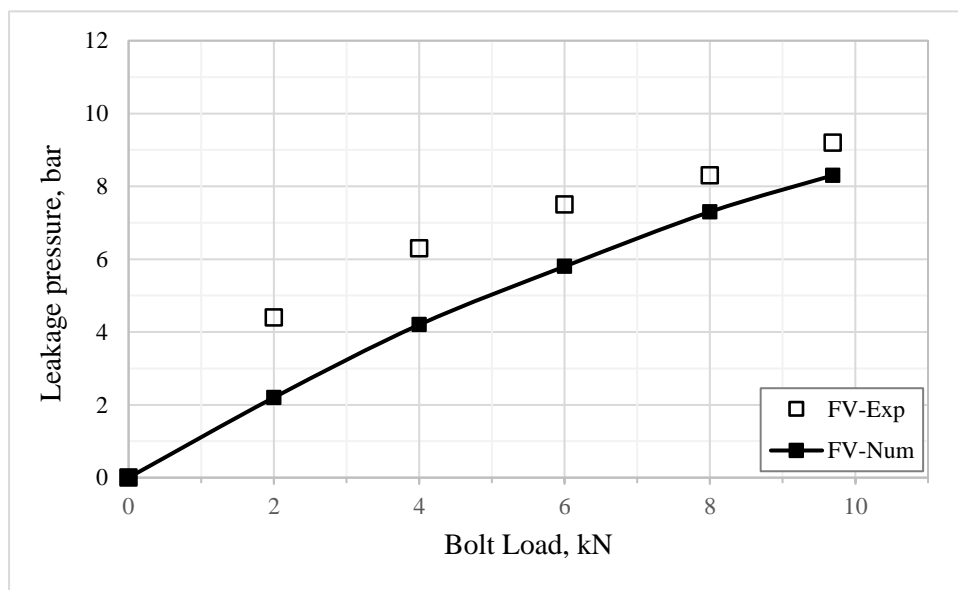


Fig. 7.22: Leakage pressure variation of Flange-Viton gasket with the bolt load

### 7.3 Numerical validation

In order to do another validation of the FEA method of the bolted GFRP flange joint, further 2D and 3D finite element analyses of a metallic bolted flange joint have been carried out. The procedure and the boundary conditions that have been applied for metallic bolted flange joint are the same as applied for the bolted GFRP flange joint. The computer model of the metallic flange joint used for the analyses consists of a raised face flange made of steel, steel bolts and an aluminium gasket. The simulation results are compared with the experimental results published by Sawa et al. [1].

#### 7.3.1 Metallic flange joint geometry and material properties

Fig. 7.23 shows the cross section of the geometry used for the finite element analysis. The dimensions of the raised face flange joint are selected from the physical model used for laboratory experiments by Sawa et. al. [41] based on standards JIS B (Japanese International standard) and ANSI B 16.5 (American standard). The joint includes two pairs of flanges, a gasket and bolts. The materials of the flange, bolt and gasket are assumed to be homogenous, isotropic and linearly elastic. The flange was made of steel (S45C, JIS), with  $E = 206 \text{ GPa}$ ,  $\nu = 0.3$ , and the bolts are chromium molybdenum steel (SCM435, JIS), with  $E = 206 \text{ GPa}$ ,  $\nu = 0.3$ . Aluminium (AI-H, JIS) was selected as the gasket material with  $E = 68.7 \text{ GPa}$ ,  $\nu = 0.3$ .

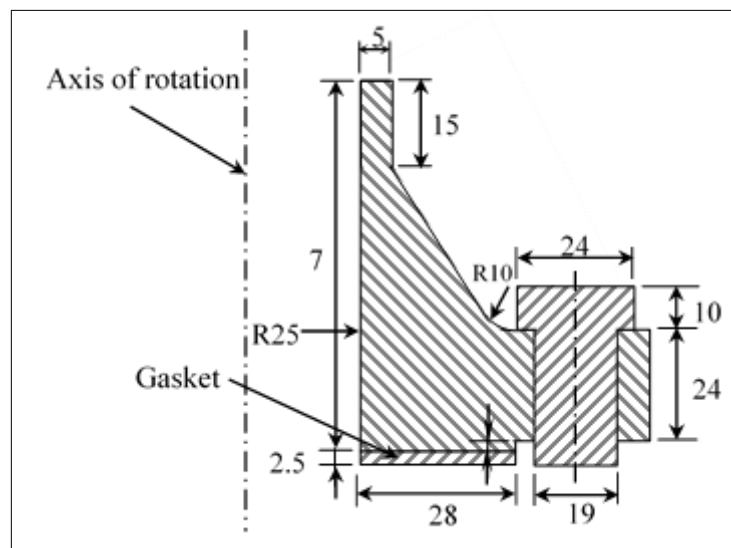


Fig. 7.23: Bolted flange joint (All dimensions in mm)

### 7.3.2 3D CAD model

A three dimensional computer model has been developed for the bolted flange joint using ANSYS Workbench v18.1. The model includes flange, gasket and bolt. Because of the symmetry, a primary segment of the geometry is repeated at equally spaced intervals about the axis of symmetry. A 1/16<sup>th</sup> portion of the total circumference of the joint as shown in Fig. 7.24 has been considered for this purpose. The axisymmetric option has been chosen to reduce the total simulation time and the computer resources.

#### 7.3.2.1 Elements selection and contact interfaces

Several different elements are used in the FEA study of the flange joint. For the flange, solid structural elements (SOLID186) are used. At the contact zones, CONTA174 and TARGE170 elements are used to simulate the contact distributions between (1) the lower face of the flange and the gasket surface and (2) the top face of the flange and the bolt head. These elements are compatible with structural element SOLID186 [115]. Since the behaviour of the flange, the gasket and the bolt are different in terms of the load-deformation characteristics, and all of them are deformable, they are treated as a ‘flexible-to-flexible’ category and the contact surfaces between them are modelled as ‘frictionless’. Because the gasket is softer than the flange, it is simulated as a contact surface and the flange is modelled as a target surface [114]. In contrast, the flange is simulated as contact and the bolt as a target in their contact interfaces.

#### 7.3.2.2 Boundary conditions

As same of GFRP flange joint modelling in chapter 6, due to the rotational symmetry and also due to the symmetry about the plane that passes through the gasket mid thickness, the boundary conditions and the loads are applied to an upper single segment in the analysis. For the model created in the cylindrical coordinate system, the circumferential displacements in the normal direction on the surface of the cycle symmetry are assumed as fixed, i.e.  $U_\theta=0$ . Also, the displacements of elements located at the bottom surface of the gasket are fixed, i.e.  $U_z=0$  (Fig. 7.24). These boundary conditions are assigned for both bolt-up and pressure loading stages, which will be discussed in the next sections.

**Bolt preload conditions**, in this stage, only the bolt load is applied in this stage to close the flange-gasket interfaces. See section 6.2.8.1 for more explanations about the boundary conditions in this stage. The design bolt load value for this joint is 15 kN and due to the symmetry, a half of this value has been applied on the lower face of the bolt.

**Pressure loading conditions**, in this stage, the internal pressure with its components have been applied in addition to the bolt load, which has been already applied in the bolt up stage. See section 6.2.8.2 for more detail about the loads in this stage.

**Modelling leakage development**, the fluid pressure penetration (FPP) between the flange and the gasket is modelled by using PPCN criterion, which has been explained in details in chapter 6 (Section 6.2.8.3).

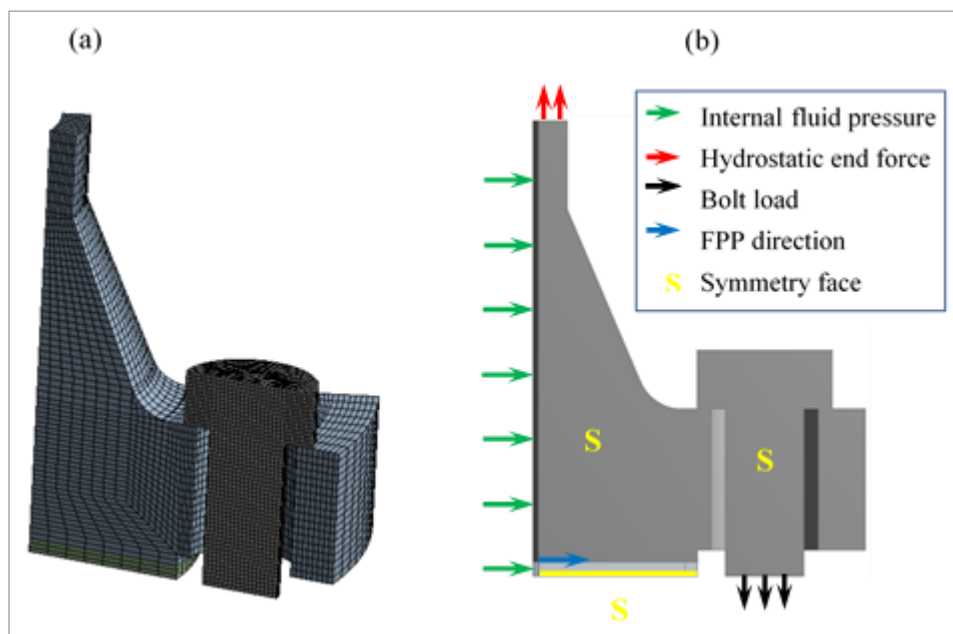


Fig. 7.24: (a) 3D model flange joint with mesh (b) Boundary conditions

### 7.3.3 2D FEA axisymmetric models

The 2D FEA of the joint has been generated using ANSYS with element PLANE183 for the flange and the gasket, and element CONTA172 for the contact region between them. The mesh of this model is shown in Fig. 7.25. As with the 3D FEA, the boundary conditions have been applied into two steps: during the first step (bolt up load stage), the axial displacement at the lower edge of the gasket has been fixed due to the axial symmetry at the mid-thickness of the gasket. The axial bolt load has been converted to the equivalent pressure force, which has been applied on the flange area under the bolt head. In the next step, the fluid pressure has been applied on the internal surface of the flange and the gasket. In addition, the axial pressure components of the hydrostatic pressure force have been applied to the top edge of the flange. The leakage propagation between the flange and the gasket has been simulated by using PPNC criterion.

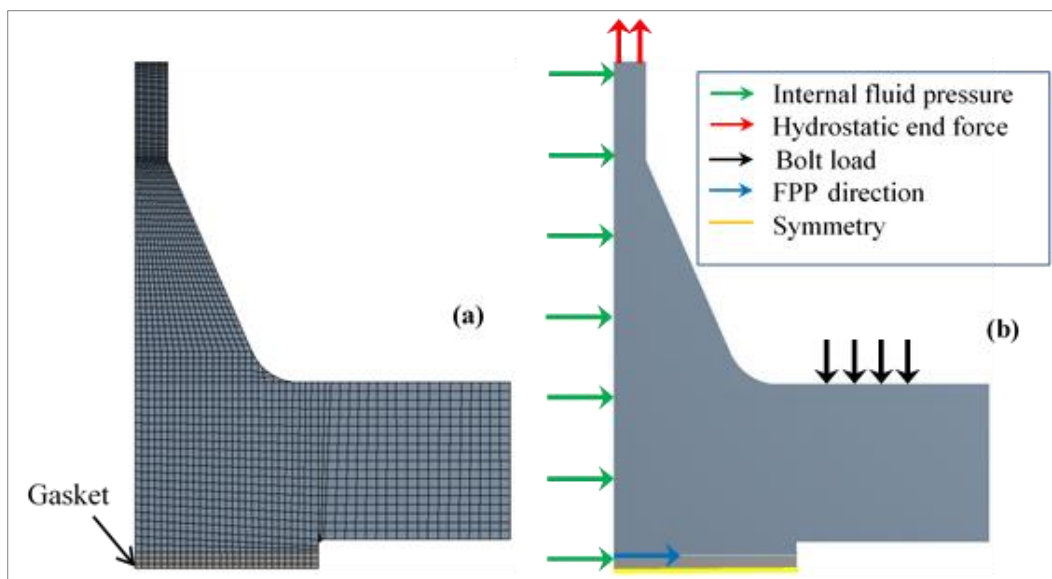


Fig. 7.25: (a) 2D FEA model flange joint with mesh (b) Boundary conditions

### 7.3.4 Simulation results

The results presented here are obtained from the finite element analyses for 3D and 2D axisymmetric models under bolt up and working conditions. The bolted flange joint is subjected to 15 kN bolt load and the internal pressure is increased up to the leakage point. At the same time, these results were compared with the results of a metallic bolted flange joint that had been investigated experimentally and numerically by Sawa et al [1].

#### 7.3.4.1 Flange hub stress

The axial flange hub stress has been calculated at the outer surface of the hub under a bolt load of 15 kN with various internal pressure values. The bolt load is high compare with the bolt load value of the composite flange. This is because of the differences in the used materials and the design pressure. The simulation results have been compared with the results presented in reference [1]. The agreement between the results is excelent as shown in Fig. 7.26.

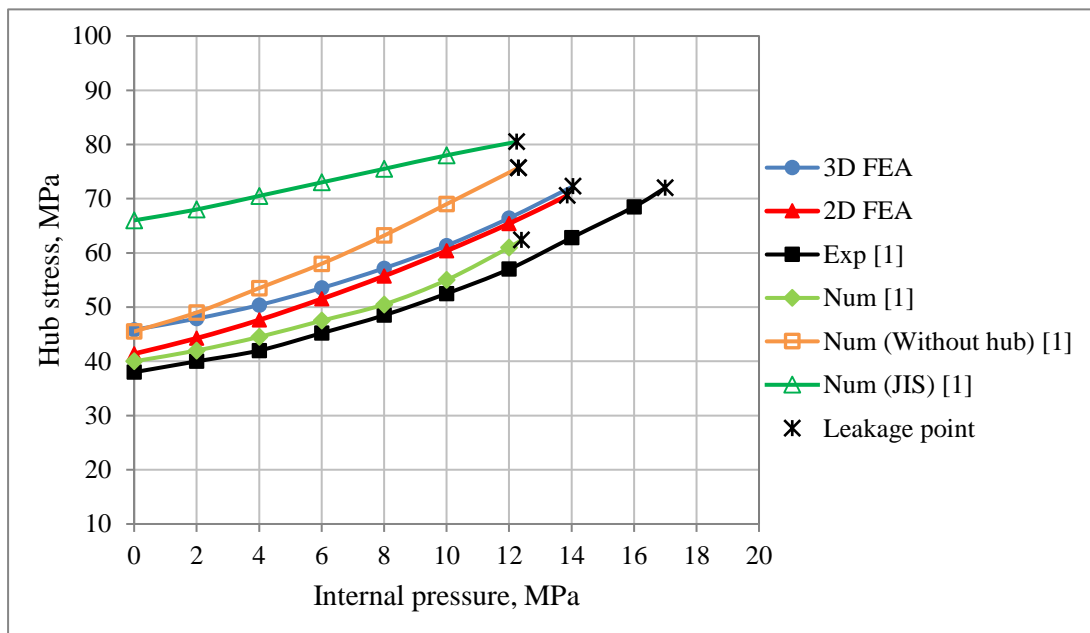


Fig. 7.26: Flange hub stress variation with the internal pressure up to leakage point

### 7.3.4.2 Leakage development

Fig. 7.27 represents the leakage propagation in the 3D model during the operating conditions under a bolt load of 15 kN. It is found that the leakage grows radially as the internal pressure increases and the leakage occurs at a pressure of 14.05 MPa. Similarly, Fig. 7.28 shows the leakage development in the 2D axisymmetric model when the flange joint is pressurized. The results reveal that the leakage has started to take place when the internal pressure has reached a value of 13.87 MPa. It is clear from this figure that the agreement between the results for 2D and 3D models is very good. The relationship between the bolt load and the internal pressure at the leakage point has been investigated using both 2D FEA and 3D FEA as shown in Fig. 7.29. It is observed in both the axisymmetric 2D and the 3D analyses that the relationship between the two variables is linear. As there is an excellent agreement between the results predicted by both types of models, the 2D axisymmetric model can be used for further extensive analyses to save computational time and efforts.

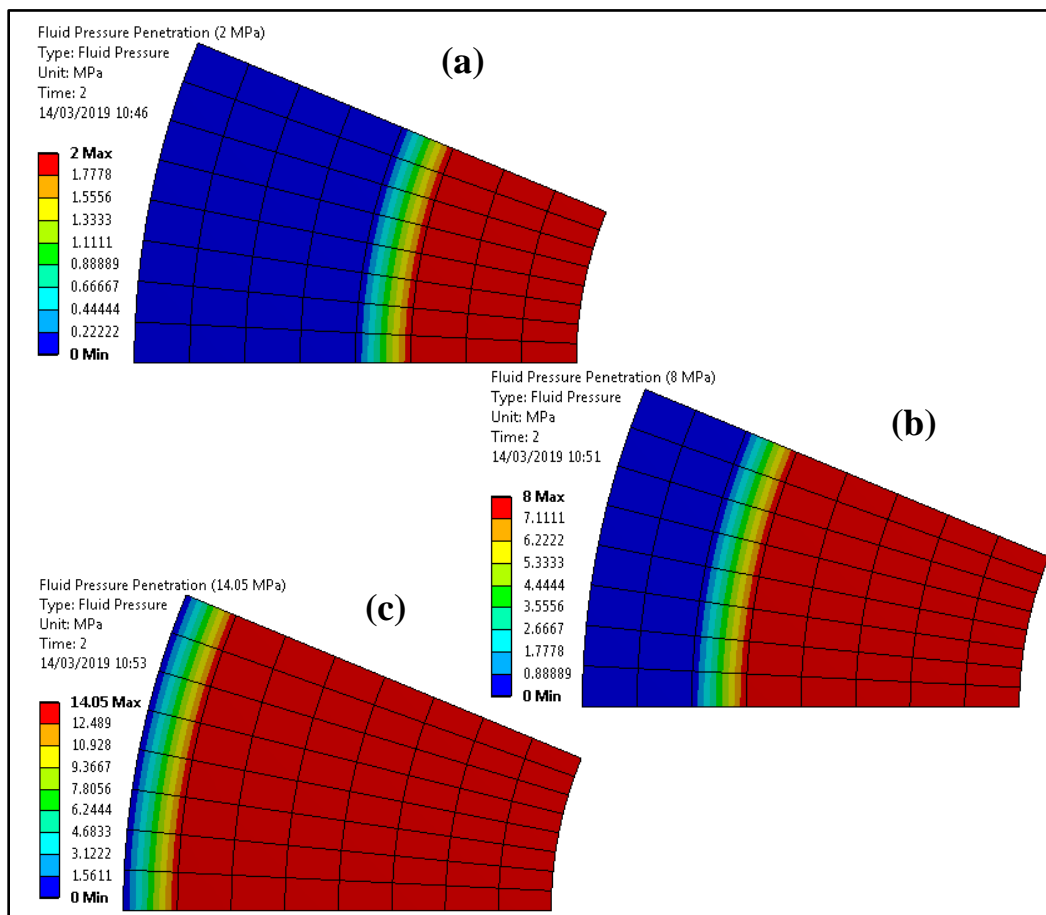


Fig. 7.27: Fluid pressure penetration of the 3D FEA (a) Internal pressure 2 MPa (b) Internal pressure 8 MPa (c) Internal pressure 14.05 MPa (Leakage point)

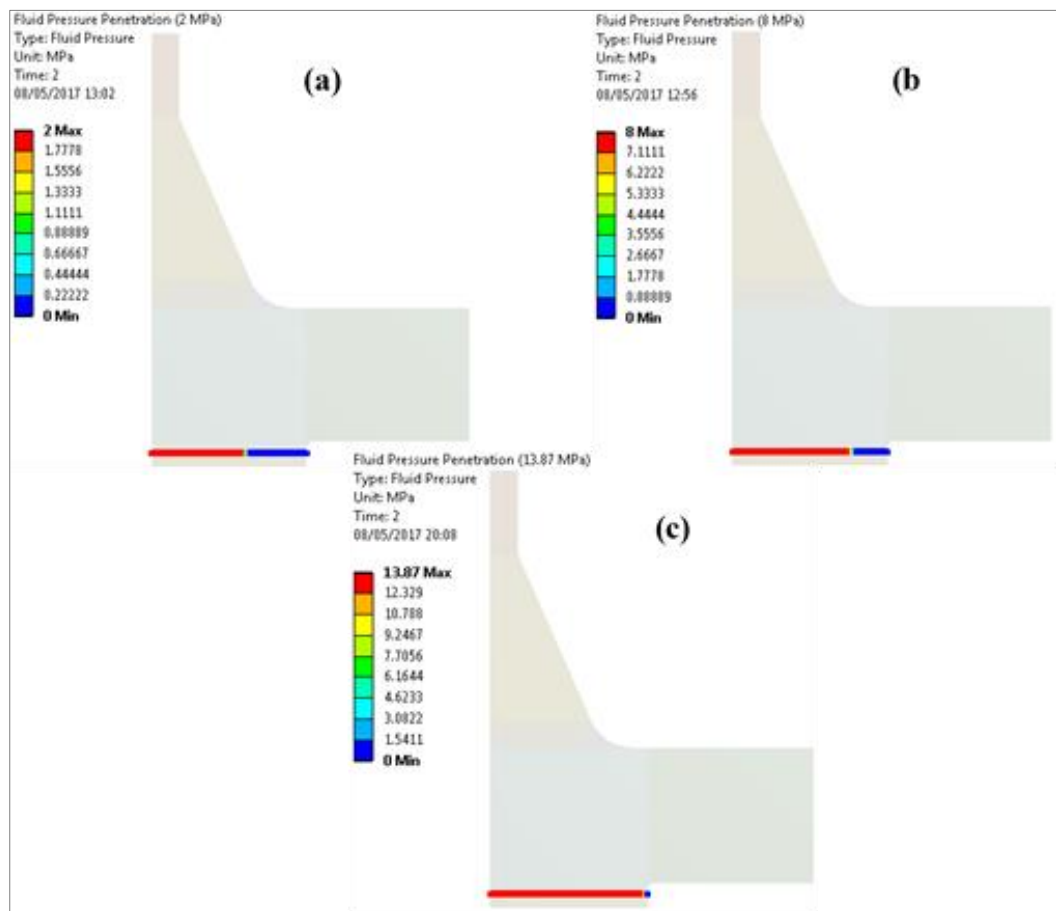


Fig. 7.28: Fluid pressure penetration of the 2D FEA (a) Internal pressure 2 MPa (b) Internal pressure 8 MPa (c) Internal pressure 13.87 MPa (Leakage point)

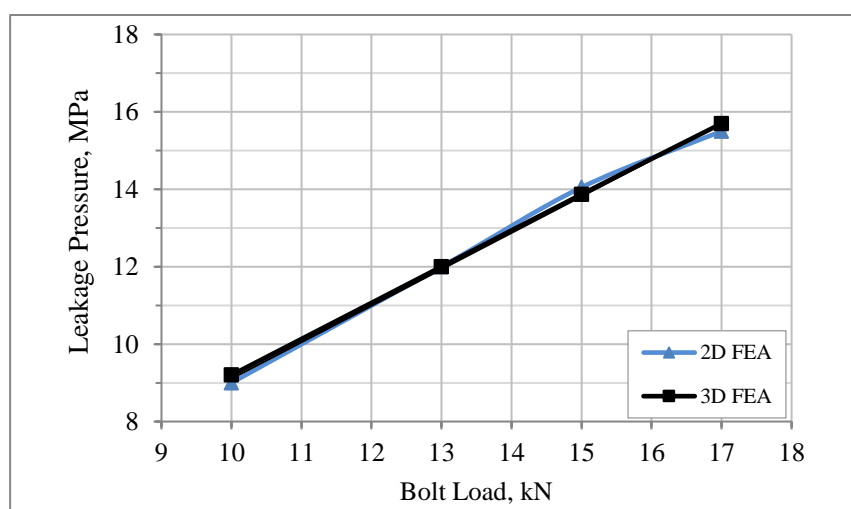


Fig. 7.29: Variation of the leakage pressure with the bolt load for the 2D and 3D FEA



## 7.4 Summary

The experimental and the numerical results of the bolted GFRP flange connection show:

- The proposed composite flange showed high quality, better performance and good strength based on the identified values of strains (axial, hoop and radial). The strain values are comparatively low even with the applied loads that are more than the recommended design conditions.
- The agreement between the experimental and the numerical results are excellent and this validates the FEA method used.
- The bolt preload has higher effect on the flange strains than that of the internal pressure load.
- The types of rubber gaskets do not influence the flange strains but affect the leakage pressure.
- The distribution of the gasket contact stress (contact pressure) is non-uniform across the gasket face. Pressure values are higher around the bolt hole and gradually decreases in the radial direction of the bolt hole.
- The leakage propagation at the midpoint between adjacent bolts is larger than those in the centres of the bolts.
- It is proved that the finite element method using PPNC in ANSYS can be considered as an efficient tool to study the leakage behaviour.

The next chapter investigates the effect of the applied loads and the flange dimensions, which are the parameters of the study, on the maximum axial, hoop and radial strains, axial displacement, flange rotation and the leakage pressure.

# CHAPTER EIGHT

## RESULTS & DISCUSSIONS

### 8.1 Introduction

To get a bolted flange joint with high performance, many parameters should be taken in to account during the design and manufacture. These parameters include sufficient strength, corrosion resistance, thermal expansion, weight, cost and dimensions, as well as the gasket material and thickness. Sufficient strength means design the flange with sufficient safety factor and its value is determined based on many conditions such as the nature of the application whether it has high risk or it costs too much were it to fail. Selecting the flange material should consider the nature of the transfer fluid and the environment of the application to achieve high corrosion resistance, which has significant impact on the service life of the pipe and flange joint. In applications that have a high range of temperature, the thermal expansion of the flange and pipe materials should be investigated carefully. Using materials of pipe and flange with different thermal expansions (composite pipe-steel or aluminium flanges) can lead to failure of the pipe-flange bonding due to the mismatch in the thermal expansions of these materials [15]. This problem can be avoided by using same material for the pipe and the flange (such as GRP pipe and flange) or different materials with the same or similar thermal expansion such as GRP pipe-GRP or CRP

flanges but not GRP pipe with steel or aluminium flange. In addition, weight of the flange is important in some applications such as in the pipelines of oil extraction from under the seabed or in the structure of airspaces.

Reducing the cost is important to market the flange. The unit cost of any product depends on many parameters as stated by Grove [104]. These parameters are: (1) the product material content; (2) the cost of the tooling and other capital equipment; (3) production cycle time (in terms of labour costs and overheads); (4) the total number of parts to be made (the batch size). Therefore, the cost of the material content can be reduced by minimizing the flange dimensions (flange materials) or by choosing cheap raw materials, which achieve the requirements of the design. Composite materials are not cheap compared to metals but they have long life service, high corrosion resistance and high strength to weight ratio, so overall the use of composite materials is cheaper and better. Therefore, composite materials have been chosen in this study to manufacture a bolted flange joint for composite pipelines, which is conducted in this can improve significantly all the influence of the above parameters. Another way to minimize the cost of the GFRP bolted flange joint is by reducing the flange dimensions and gasket thickness.

This chapter studies the influence of changing the flange dimensions, flange diameter, flange thickness, hub length and hub thickness, on the flange strains distribution, flange axial displacement, flange rotation and the leakage pressure between the flange and the gasket under various of the bolt load and internal pressure. In addition, the effect of the gasket material and thickness will be also investigated in this chapter. Finally, the objective of this chapter is to find out the possibility of reducing flange joint dimensions (flange material) and its cost.

## **8.2 ASME code predictions**

The comprehensive analytical approach of the ASME code [24] has been used to calculate the stress values in the three directions, axial, hoop and radial when the bolted flange joint is subjected to the design loads, bolt load 7.4 kN and internal pressure 3.4 bar. These values are also calculated using FEA and they are all shown

in Table 8.1. The results show that the ASME code is conservative as it predicts higher stresses when compared with the predictions from the FEA, especially, for the axial and radial stresses. There are many reasons behind this high values of ASME code, which made it conservative. For example, the ASME code analyses based on the loads and the geometries and does not take into account the material properties, which has significant effect on the flange strength and stiffness, and the leakage propagation between the flange and the gasket. On the other hand, the FEA takes into account the materials properties with their orthotropy for the composite materials and non-linear response for the rubber gasket during the loading and unloading as well as the leakage propagation. The materials properties are calculated based on many parameter such as fibre direction and fibre volume fraction of the glass fibre braid sleeve, which showed good performance during the testing. In addition, the comprehensive analytical approach of the ASME code has been modified from the codes of the metal flanges. So that many details, which are related to the composite material should be included. This problem has been pointed out by other researchers [8].

Therefore, the ASME code is general and that leads to predict high stresses, which make the flange dimensions thicker. Although, these stresses values are still low if they are compared with measured tensile strength 254.8 MPa of the composite laminate that has been described in chapter 5 (section 5.3).

Finally, this study based on the stiffness analysis no strength but the below stresses are calculated numerically for the comparison purpose against the ASME code.

Table 8.1: Stress values comparison for ASME code and FEA

|                     | ASME Code | Numerical (FEA) |
|---------------------|-----------|-----------------|
| Axial stress (MPa)  | 21.13     | 11.67           |
| Hoop stress (MPa)   | 37.91     | 33.86           |
| Radial stress (MPa) | 18.22     | 13.47           |

### 8.3 Bolted flange joint deformation

Fig. 8.1 shows the total deformation of the bolted flange joint, which includes the flange, pipe, adhesive bonding, gasket and the bolt as well as the washer. The joint has been subjected to the design loads, which are 7.4 kN bolt load (BL) and 3.4 bar internal pressure (P). The results show that the flange disc deforms more than the other parts. Also, the maximum total deformation occurs around the bolts holes due to the flange bending under the effect of the bolt force, which is required to keep the sealing tight, and the internal pressure. Furthermore, it can be seen that there is a high deformation on the bolt and the washer. In reality, this is not accurate deformation in the bolt itself but this comes from the down movement of the bolt due to the high gasket compression and high flange bending around the bolts holes.

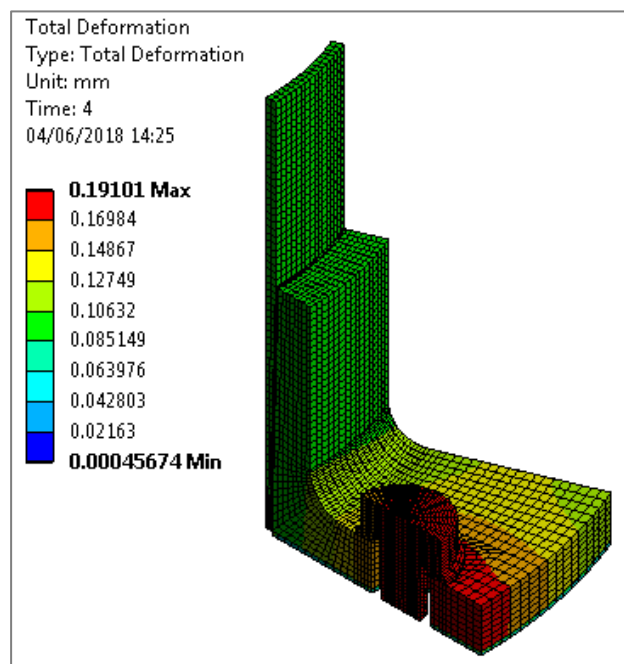


Fig. 8.1: Total deformation of the bolted flange joint

### 8.4 Flange diameter effect

This section investigates the effect of flange dimensions on the maximum axial, hoop and radial strains, axial displacement, flange rotation and leakage pressure using the FEA model, which has been validated in the previous chapter. The purpose

of this analysis is to find the possibility of reducing the dimensions that have small or insignificant influence on the flange performance. This means reducing the required materials and manufacturing process time, thereby reducing the material cost of the flange.

**Maximum axial tensile strain vs flange diameter**, the axial strain distribution of the flange connection (flange, pipe and adhesive bonding) is shown in Fig. 8.2. These results are calculated under the design conditions, which are bolt load 7.4 kN and internal pressure 3.4 bar. These results show the maximum axial tensile strain at the outer surface of the flange-hub interface due to the bending of the flange under the bolt load. In addition, the maximum axial compression strain occurs through the thickness of the flange and around the bolt holes or under the bolt head. This is because of the bolt force that compresses the flange.

Fig. 8.3 shows the maximum axial tensile strain variation with the outer flange diameter for different gasket materials and thicknesses. The maximum axial tensile strain is measured near the bolt at the outer flange-hub interface as shown in Fig. 8.2. The right ordinate represents the normalized percentage of the strain values based on the equivalent strain values of the flange diameter 320 mm and using Nitrile rubber gasket with 3 mm thickness (FN3). The results show that the maximum axial tensile strain decreases sharply with increasing the flange diameter up to 360 mm where as it becomes constant at the 360-400 mm flange.

This occurs due to the high flange bending, especially around the bolt holes, because of the applied bolt axial load, which is trying to seal the contact. The contact pressure between the flange and the gasket at the area that is outside the bolts holes circle (more than 360 mm dia.) is very small or zero. This means that the flange area, which is at the outer diameter 360 mm, is not contributing significantly to seal the contact and it is not affecting the maximum axial tensile strain. For the flange diameter range 320-360 mm, the highest value of strain was recorded at diameter 320 mm with 517  $\mu\epsilon$  and it decreases almost 10% at the diameter 360 mm. These numbers are still low and the flange outer diameter should be kept at 320 mm. In addition, the Viton rubber gasket produces axial tensile strain slightly higher than Nitrile rubber gasket. Furthermore, the results show that the gasket thickness has

small influence on the maximum axial tensile strain. Therefore, 3 mm gasket thickness can be used instead of 5 mm to save the materials and cost.

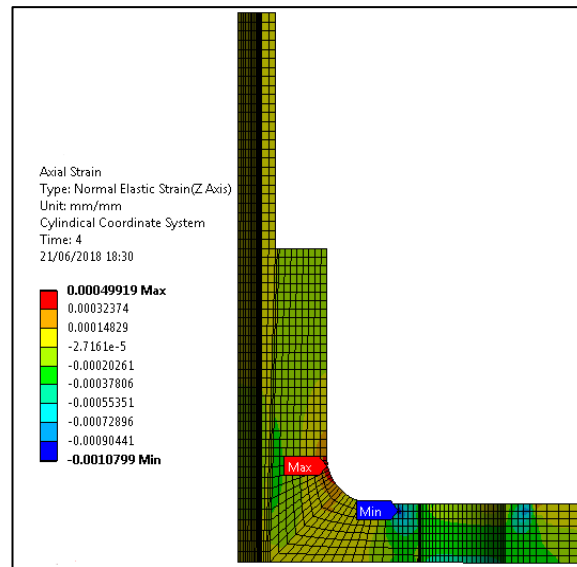


Fig. 8.2: Axial strain (mm/mm)

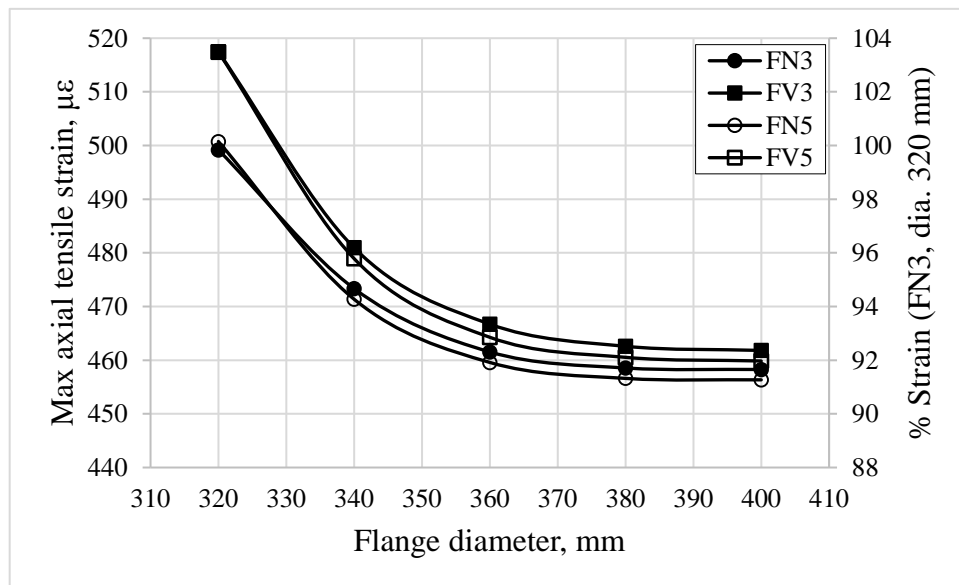


Fig. 8.3: Maximum axial tensile strain ( $\mu\epsilon$ ) variation with the flange diameter for range of gasket types and thickness

The overall history of the maximum axial tensile strain is shown in Fig. 8.4. This figure illustrates the variation of the maximum axial tensile strain with the bolt load (clamping force) and the internal pressure, which represent the bolt up and operating conditions. The ordinate of the figure represents the strain values whereas the

abscissa is divided into two stages. The first stage represents the variation of the bolt load when the internal pressure is zero. The second stage shows the variation of the internal pressure when the bolt load is 7.4 kN. The transition region between the two stages, which starts from BL 7.4 kN & P 0 bar of the first stage, and ends at pressure 0 bar & BL 7.4 kN in the second stage, has the same condition. So that the curves are horizontal at this region. This will be repeated in the next figures that have the same style. The influence of the flange diameter is also shown in this figure.

The results show that the bolt load has a higher effect on the axial strain than the internal pressure. It is clear that the maximum axial tensile strain increases significantly with increasing the bolt load whereas it increases less with the increasing of the pressure. Furthermore, it is observed that the maximum axial tensile strain is affected by the flange diameter up to 360 mm. The flange with outer diameter 320 mm produces axial strain higher than the others (360 and 400 mm). This can be clearly seen through Fig. 8.3.

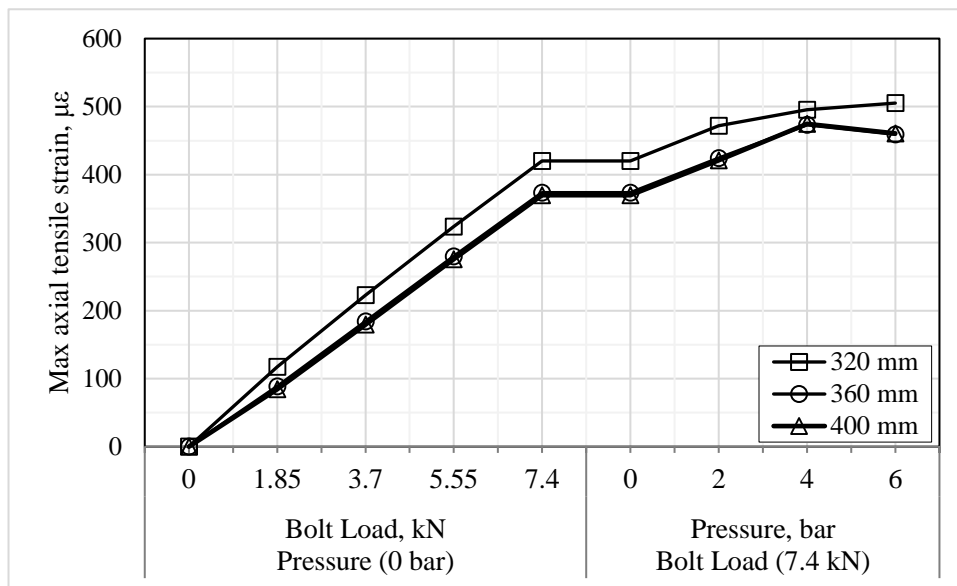


Fig. 8.4: Maximum axial tensile strain ( $\mu\epsilon$ ) variation with the bolt load and internal pressure for range of the flange diameter



**Maximum axial compression strain vs flange diameter**, the maximum axial compression strain is found near the bolt holes and under the top flange surface as illustrated in the Fig. 8.2. This occurs because of the bolted GFRP flange joint is subjected the design boundary conditions, which are 7.4 kN bolt load and 3.4 bar internal pressure. Therefore, the bolt load compresses the flange to create sufficient contact pressure between the flange and the gasket to seal the joint and stop any leakage propagation.

Fig. 8.5 explains the relationship between the maximum axial compression strain and the outer diameter of the flange for various gasket materials and thickness. It seems that the flange diameter has significant impact on the maximum compression strain, especially between the diameter range 320-360 mm. When the flange outer diameter increases, the maximum compression strain increases up to 360 mm of diameter but after that the variation becomes small or even it is not affected at the high flange diameter. In other words, the compression strain increases about 17% when the flange diameter increases from 320 mm to 360 mm, whereas it increases 2% when the diameter increases from 360 mm to 400 mm. As mentioned earlier, this is due to the applied loads and the reaction of the gasket, which bend the flange and lift up the outer edge of the flange. Furthermore, the gasket material shows small influence on the maximum compression strain but it is not affected by the gasket thickness. The Viton gasket produces strain that is slightly higher than the Nitrile gasket.

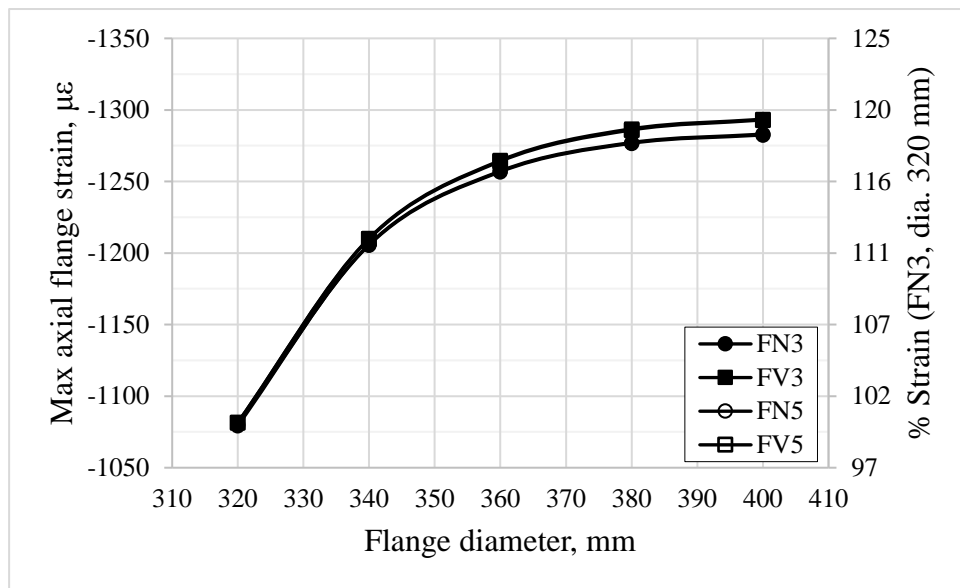


Fig. 8.5: Maximum axial compression strain ( $\mu\epsilon$ ) variation with the flange diameter for range of gasket types and thickness

**Maximum hoop strain vs flange diameter,** Fig. 8.6 illustrates the hoop strain of the flange with outer diameter 320 mm and using Nitrile rubber gasket under the design boundary conditions (bolt load 7.4 kN & internal pressure 3.4 bar). The highest hoop strain values are observed at the lower face of the flange and around the bolt holes. As shown in the figure, the maximum value of the strain is found on the line that passes through the pipe and bolt hole centres. This area of the flange is exposed to the high hoop strain due to the axial bolt, which causes the circumferential flange bending. This will be explained clearly through the calculations of the flange axial displacement and flange rotation, which will be discussed in sections 8.7 and 8.8.

The variation of the maximum hoop strain with the outer flange diameter has been shown in Fig. 8.7 for range of gasket materials and thicknesses. Generally, the results show that the outer flange diameter has small influence on the maximum hoop strain, which is less than 4% for the Flange-Nitrile gasket (FN) and 5.5% for the Flange-Viton gasket (FV). However, the high variation range occurs when the flange diameter increased from 320 mm to 360 mm whereas the high flange diameter does not affect significantly the hoop strain. Therefore, it is better to keep it at the minimum allowable outer diameter, which means reducing the required materials

and cost, to reduce the hoop strain. In addition, the gasket materials effect on the hoop strain and the Viton gasket causes hoop strain higher than Nitrile gasket. In contrast, the hoop strain is not affected by the gasket thickness, so that encourages using a thin gasket instead of the thick, which costs more.

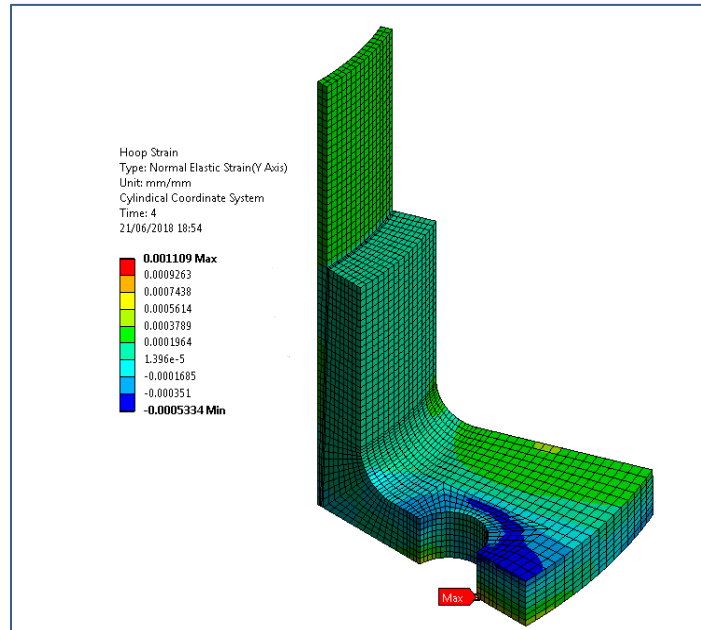


Fig. 8.6: Hoop strain (mm/mm)

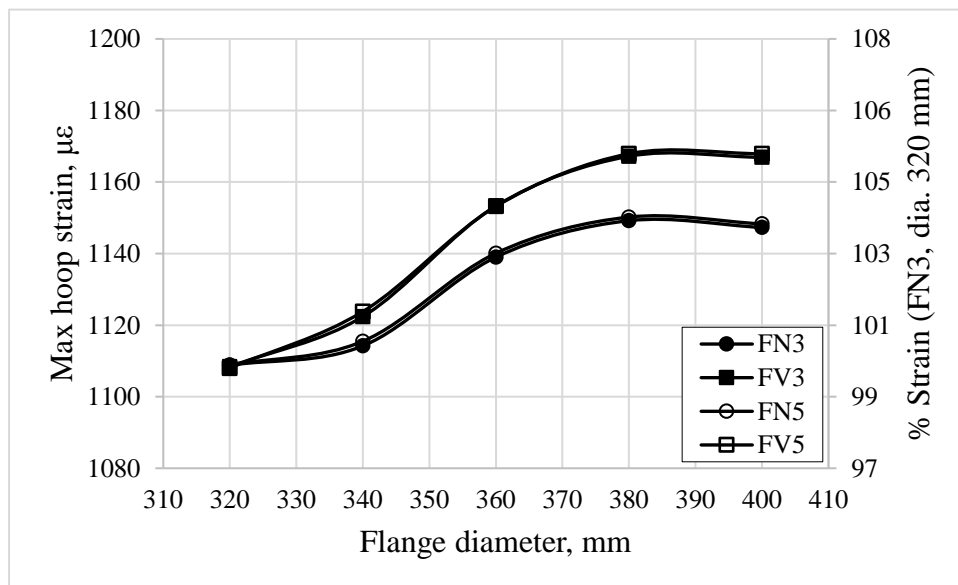


Fig. 8.7: Maximum hoop strain ( $\mu\epsilon$ ) variation with the flange diameter for range of gasket types and thickness

**Maximum radial strain vs flange diameter,** The maximum radial strain occurs around the bolt hole at the point that is allocated on the holes circle at the lower face of the flange. As shown in the Fig. 8.8, these regions of the flange are subjected to the high tensile radial strain when the flange joint is exposed to the bolt force (7.4 kN) and the internal pressure (3.4 bar). These loads are trying to bend the flange at the bolts circle diameter, thereby, producing high tensile radial strain at the lower face of the flange around the bolt holes.

Fig. 8.9 describes the maximum radial strain as a function of the flange outer diameter using the Nitrile and the Viton rubber gaskets with 3 and 5 mm thickness. The results indicate that increasing the flange outer diameter (320 to 400 mm) leads to increase the radial strain approximately 30% (1110-1450  $\mu\epsilon$ ) and most of the increment (27%) occurred at the range 320-360 mm whereas almost 3% in the range 360-400 mm . This happens due to the circle geometry of the flange disc, which is bent under the bolt load at bolts holes. This circle geometry helps the outer edge of the flange to move up, so that increasing the outer diameter leads to increase this phenomena, thereby, produce more tensile radial strain at the lower face of the flange. Regarding the gasket material and thickness influences, the Viton rubber gasket shows radial strain higher than the Nitrile at the higher flange outer diameter (360-400 mm) whereas this difference is tiny at the lower outer diameter. In addition, the results show that the gasket thickness has no impact on the radial strain. Therefore, small flange outer diameter and small gasket thickness has positive impact on the radial strain and the flange joint cost.

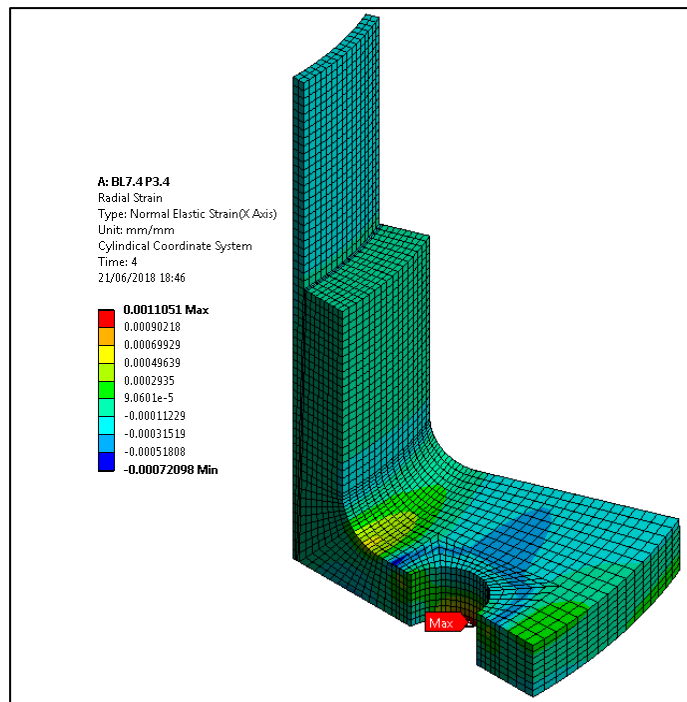
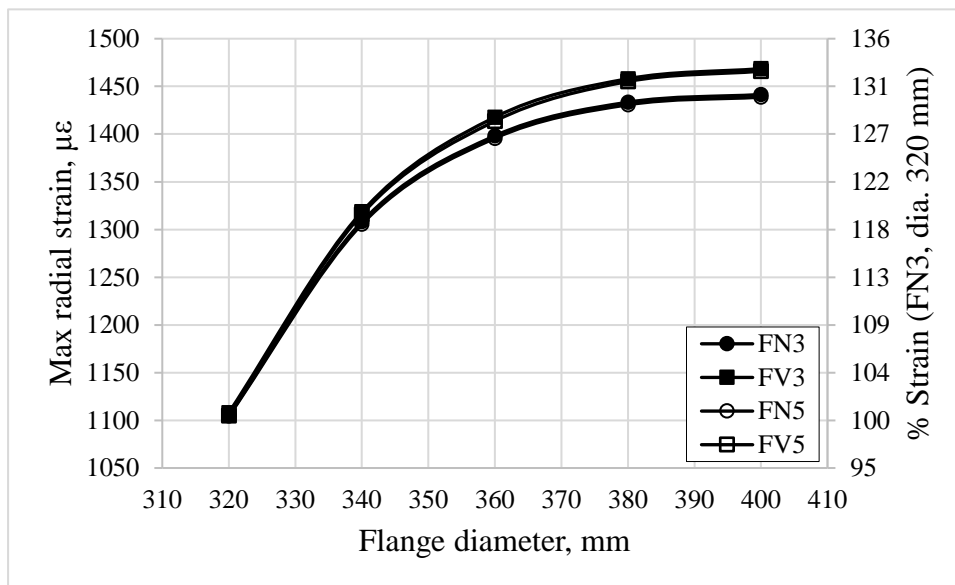


Fig. 8.8: Radial strain (mm/mm)

Fig. 8.9: Maximum radial strain ( $\mu\epsilon$ ) variation with the flange diameter for range of gasket types and thickness

**Bolt axial strain vs flange diameter,** Fig. 8.10 explains the axial strain distribution on the bolt when the bolt load (7.4 kN) and the pressure (3.4 bar) are applied. It is clear that the maximum axial bolt strain is observed at the corner at the bolt head and shank interface, where they meet. This because of the sudden change in the geometry.

Regarding the flange outer diameter and the bolt axial strain relationship, the axial strain has been measured numerically at the central axis of the bolt as shown in the Fig. 8.10. This point has been chosen to be the same point that includes the strain gauge in the experiment, which was embedded through a drilled hole from the top bolt head surface. Fig. 8.11 illustrates the bolt axial strain variation with the flange diameter for various gasket materials and thicknesses. It seems that the bolt axial strain is not influenced by the flange outer diameter, gasket materials and gasket thickness. This strain stays constant at  $245 \mu\epsilon$  over the load history.

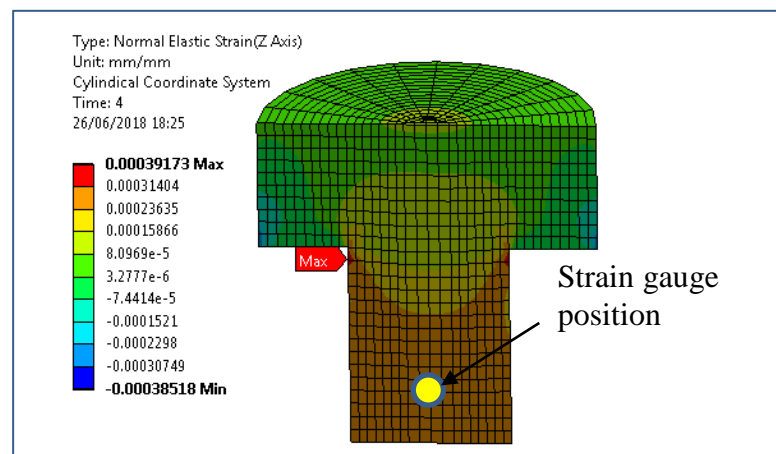


Fig. 8.10: Bolt axial strain ( $\mu\epsilon$ )

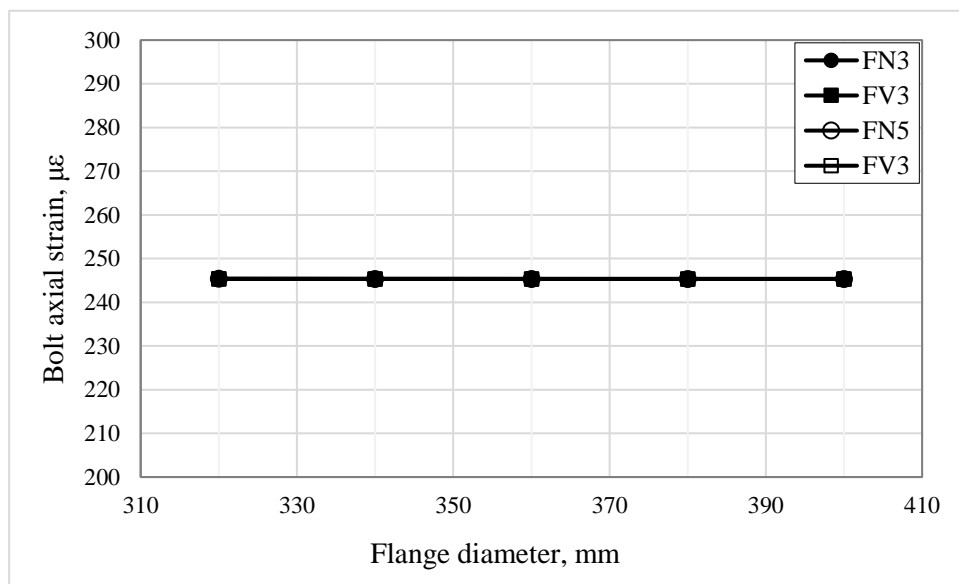


Fig. 8.11: Bolt axial strain ( $\mu\epsilon$ ) variation with the flange diameter for range of gasket types and thickness

### 8.5 Flange thickness effect

This study investigates the impact of the decreasing the flange thick from 15 mm to 10 mm. Therefore, the results will be shown in the Fig. 8.12, Fig. 8.13, Fig. 8.15 and Fig. 8.16, which have three axis. The x-axis and left y-axis represent the flange thickness and the real values of the strain, respectively, whereas the right y-axis shows the percentage normalized of the strain based on the strain value of the flange thickness 15 mm with 3 mm of Nitrile rubber gasket.

**Maximum axial tensile strain vs flange thickness**, Fig. 8.12 illustrates the maximum axial tensile strain variation with the flange thickness for different gasket materials and thicknesses. The strain has been measured at the outer face of the hub-flange intersection as shown in the Fig. 8.2. It observed that the decreasing the flange thickness (15 to 10 mm) leads to increase the maximum tensile strain almost 30% (500 to 656  $\mu\epsilon$  for the Nitrile gasket and 517 to 672  $\mu\epsilon$  for the Viton gasket). This occurs because of the decreasing in the bending resistance of the flange, which becomes more flexible. This produces more tensile strain at the flange-hub intersection because of applying the bolt axial force.

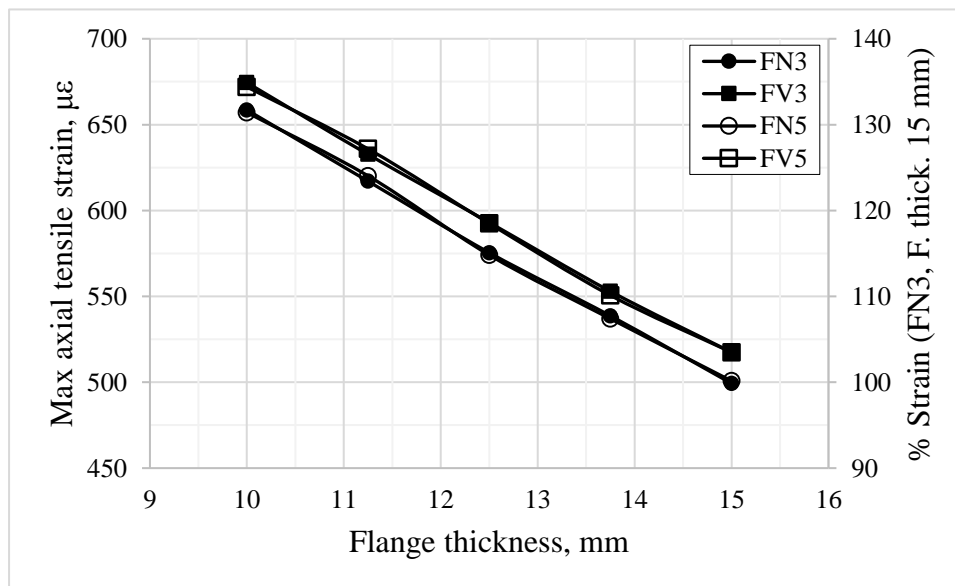


Fig. 8.12: Maximum axial tensile strain ( $\mu\epsilon$ ) variation with the flange thickness for range of gasket types and thickness

In addition, the Viton rubber gasket produces maximum tensile strain almost 3% more than the Nitrile gasket where the gasket thickness has no effect on the tensile strain.

**Maximum axial compression strain vs flange thickness**, the influence of the flange thickness on the maximum axial compression strain has been illustrated in Fig. 8.13 for range of gasket materials and thicknesses. The maximum axial compression strain has been found and measured numerically around the bolt hole and under the surface as explained in the Fig. 8.2. The results show that the maximum axial compression strain has been affected significantly by the flange thickness and it has increased when the flange thickness decreased. The increment was around 40% (1079 to 1510  $\mu\epsilon$ ) for all the gaskets and regardless their material and thickness, which has not affected the compression axial strain. Decreasing the thickness of the flange leads to decrease the flange stiffness. Therefore, more compression axial strain is produced due to the applied boundary conditions, which are bolt load and internal pressure.

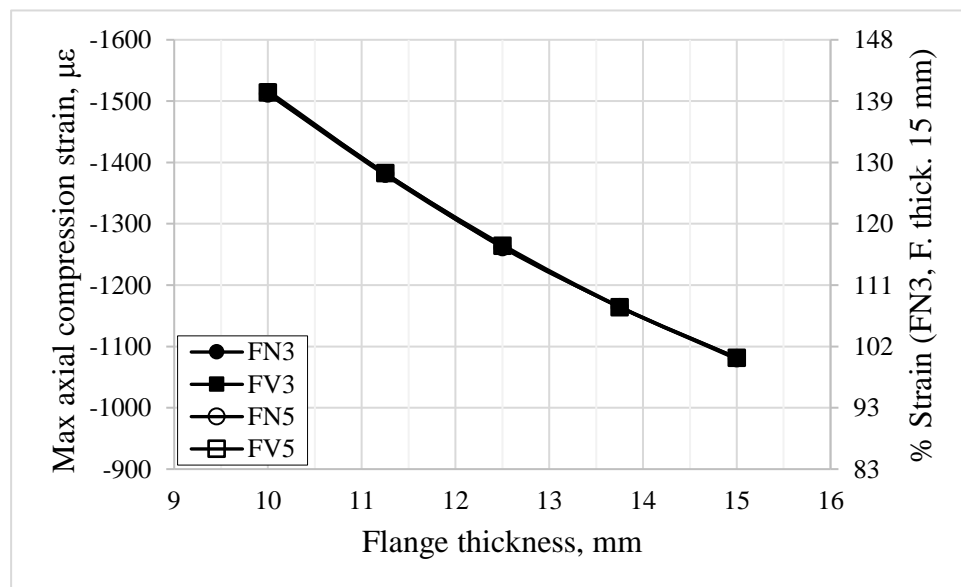


Fig. 8.13: Maximum axial compression strain ( $\mu\epsilon$ ) variation with the flange thickness for range of gasket types and thickness



Fig. 8.14 shows the overall variation of the maximum axial compression strain with the applied loads, which are the bolt load and the internal pressure for range of the flange thickness. The x-axis of the figures is divided into steps. The first step shows the gasket seating (bolt up stage) and the second step illustrates the operating stage at the bolt load 7.4 kN. It is observed that the bolt load has significant impact on the maximum axial compression strain whereas the internal pressure has very small influence. When the bolt load increases, the maximum axial compression strain increases sharply but it stay almost same when the internal pressure increases. In addition, the effect of the flange thickness can be seen clearly through the results. The flange thickness leads to increasing the maximum axial compression strain during both stages, which are bolt up and operating.

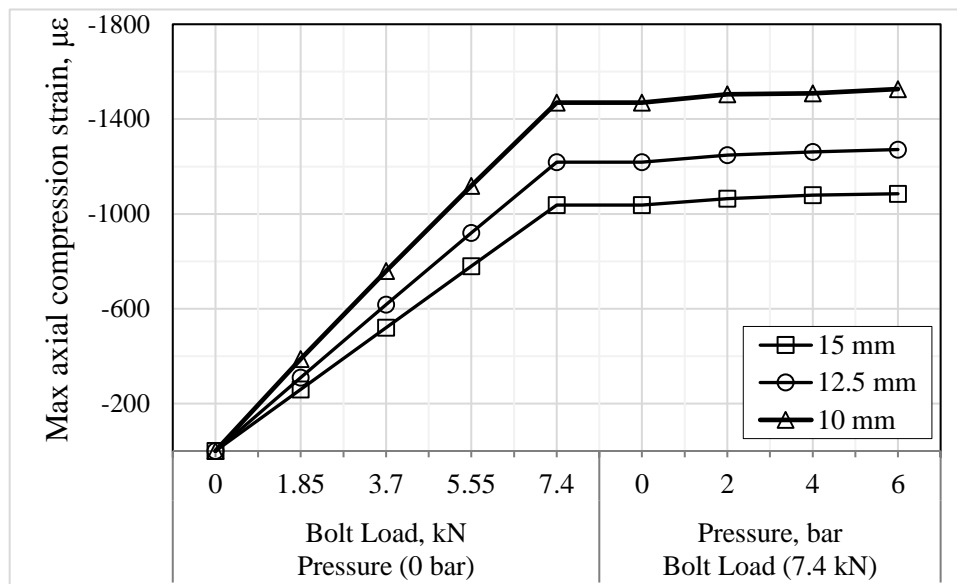


Fig. 8.14: Maximum axial compression strain ( $\mu\epsilon$ ) variation with the bolt load and the internal pressure for range of the flange thickness

**Maximum hoop strain vs flange thickness,** Fig. 8.15 describes the relationship between the maximum hoop strain with the flange thickness, gasket material and gasket thickness. The maximum hoop strain is observed and measured around the bolt hole and at the lower face of the flange as shown in Fig. 8.6. It seems that the maximum hoop strain is affected significantly by the flange thickness and the flange shows high strain at low thickness (10 mm). The maximum hoop strain has increased

almost 67% when the flange thickness decreased from 15 to 10 mm. This is because of the bolt load that has high effect on the thin flange rather than thick. In addition, this influence will be illustrated clearly in the flange axial displacement (section 8.9) and flange rotation (section 8.10). Furthermore, the maximum hoop strain is not affected by the gasket thickness and gasket material except at the lower flange thickness as there is a tiny influence between the Viton and the Nitrile rubber gaskets.

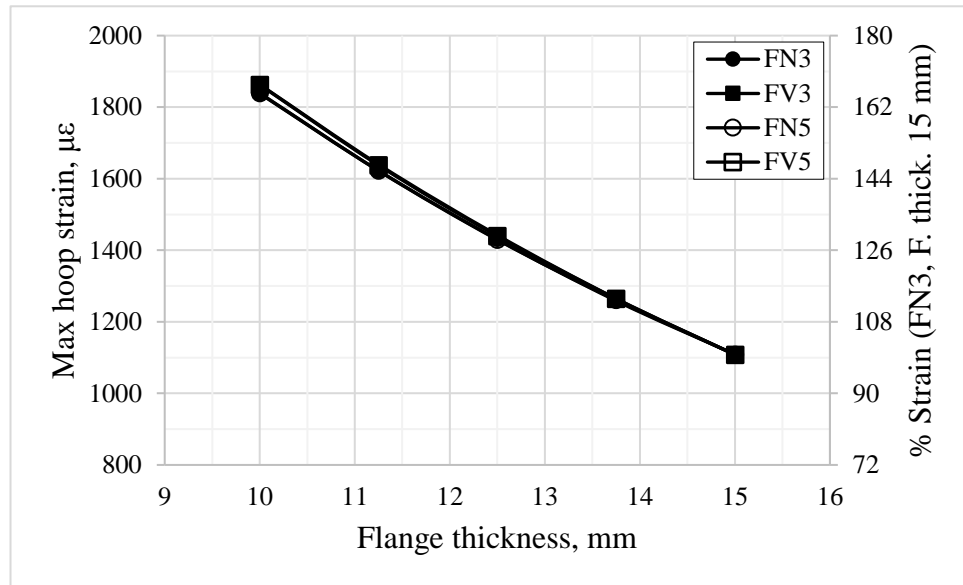


Fig. 8.15: Maximum hoop strain ( $\mu\epsilon$ ) variation with the flange thickness for range of gasket types and thickness

**Maximum radial strain vs flange thickness,** The influence of the flange thickness, gasket type and thickness on the maximum radial strain is shown in the Fig. 8.16 when the bolted GFRP flange connection is subjected to the bolt load 7.4 kN and internal pressure 3.4 bar. The maximum radial strain is observed around the bolt hole at the lower face of the flange and on the line of the holes circle diameter as explained in Fig. 8.8. The results show that the decreasing of the flange thickness leads to increase the maximum radial strain. The maximum radial strain has increased 59% when the flange thickness decreased from 15 to 10 mm. This occurs due to the high bending of the thin flange because of the reduction in the flange stiffness and applying the bolt load. In addition, it seems that the gasket material (gasket behaviour) and thickness does not affect the maximum radial strain values.

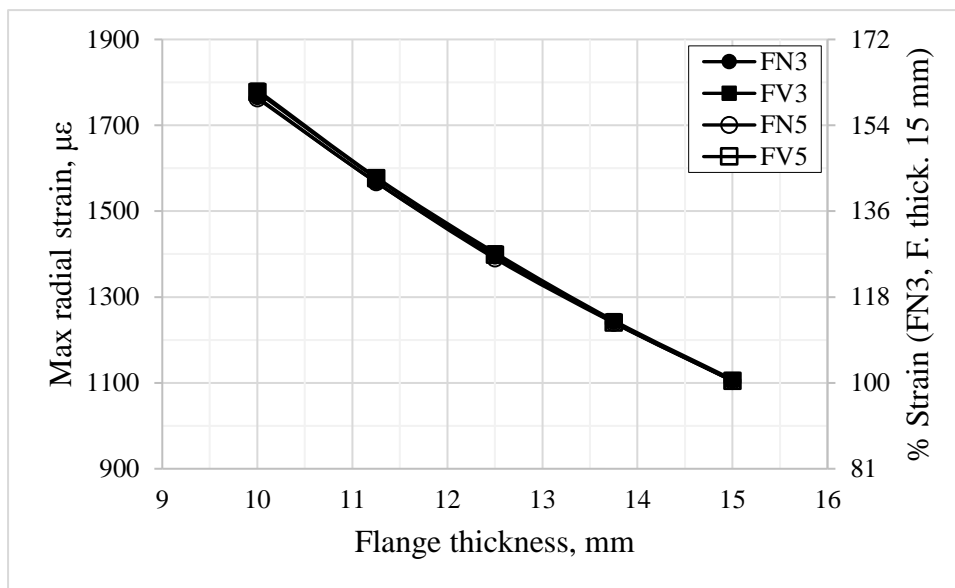


Fig. 8.16: Maximum radial strain ( $\mu\epsilon$ ) variation with the flange thickness for range of gasket types and thickness

**Bolt axial strain vs flange thickness**, Fig. 8.17 shows the variation of the bolt axial strain with the flange thickness and gasket material and thickness. The strain is calculated at the point where the strain gauge has been fitted as explained in Fig. 8.10. It is clear that the axial strain is slightly affected by the flange thickness but not influenced by the gasket type and thickness. When the flange thickness decreases, the bolt axial strain increases. This is because of the reduction in the flange strength when the flange is thin, it deforms easily and the fluid pressure penetration grows more between the flange and the gasket. Therefore, more axial forces are produced and these forces are trying to split the matched flanges and gasket. These forces lead to increase axial bolt strain.

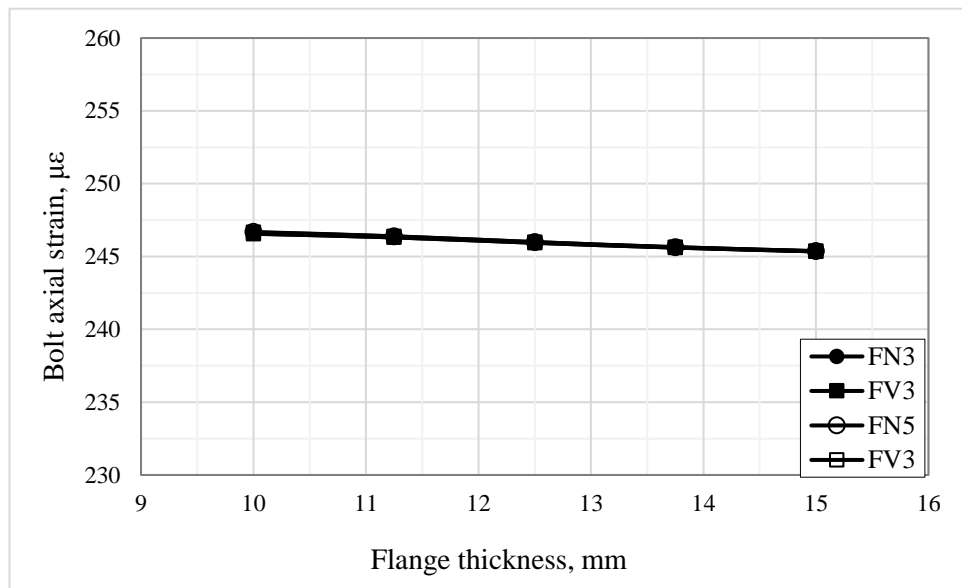


Fig. 8.17: Bolt axial strain ( $\mu\epsilon$ ) variation with the flange thickness for range of gasket types and thickness

## 8.6 Hub length effect

This section studies the effect of the hub length on maximum axial, hoop and radial strains of the flange using different gasket materials and thicknesses. The hub length is decreased from 80 mm to 40 mm as shown in Fig. 8.18, Fig. 8.19, Fig. 8.20, Fig. 8.21, Fig. 8.22 and Fig. 8.23. In addition, the strains have been shown as real values on the left ordinate and as normalized percentage in the right ordinate. The normalized percentage has been calculated based on strain of the hub length 80 mm and 3 mm Nitrile rubber gasket.

**Maximum axial tensile strain vs hub length,** Fig. 8.2 showed the axial strain distribution and the maximum value is indicated at the outer surface and bottom of the hub. The variation of the maximum axial tensile strain with the hub length, gasket type and thickness is illustrated in Fig. 8.18.

The results show that decreasing the hub length decreases the maximum axial strain. The axial strain decreases by 10% when the hub length is reduced from 80 to 60 mm and sharply (50%) when the length is reduced more from 60 to 40 mm. Therefore, it is better to reduce the hub length strain and the flange material cost.

In addition, the gasket material has a small influence on the axial strain and the Viton gasket produces more strain than the Nitrile gasket. Furthermore, the maximum axial strain is not impacted by the gasket thicknesses, so that encourage using the thin gasket which is cheaper than the thick.

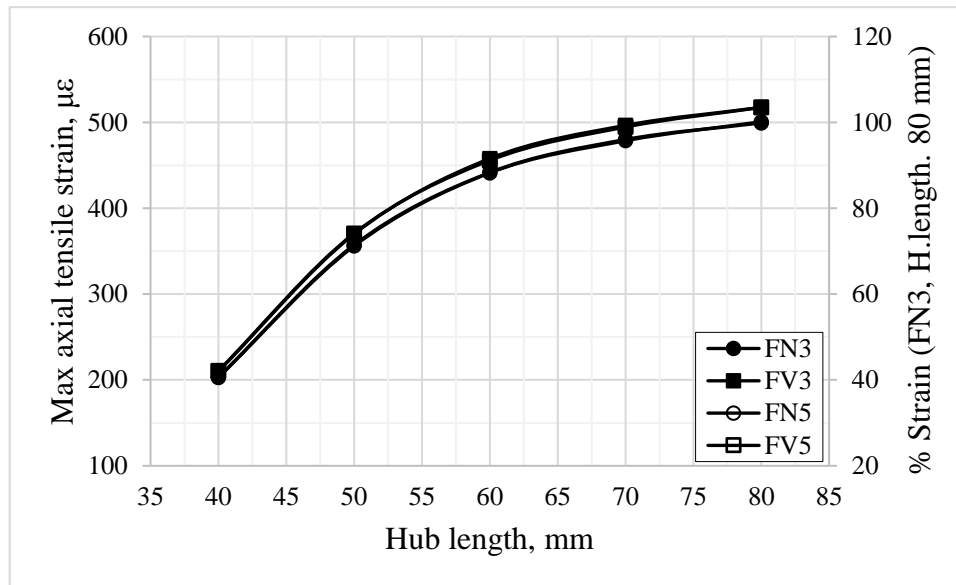


Fig. 8.18: Maximum axial tensile strain ( $\mu\epsilon$ ) variation with the hub length for range of gasket types and thickness

**Maximum axial compression strain vs hub length,** The influence of the hub length on the maximum axial compression strain is illustrated in Fig. 8.19. The maximum axial compression strain occurs at the bolt hole and under the bolt head as shown in the Fig. 8.2. It is observed that the hub length has no effect on the compression strain when the hub length decreases from 80 to 50 mm. When the hub length decreases more from 50 to 40 mm, the maximum compression strain increases about 2%, which is still small. Therefore, the hub length can be decreased to reduce the flange materials. In addition, the gasket thickness has tiny effect on the strain values, especially, with Viton gasket and at hub length range 60-80 mm. Regarding the gasket material, the Nitrile gasket produces axial compression strain less than the Viton and because of the non-linear behaviour of the rubber.

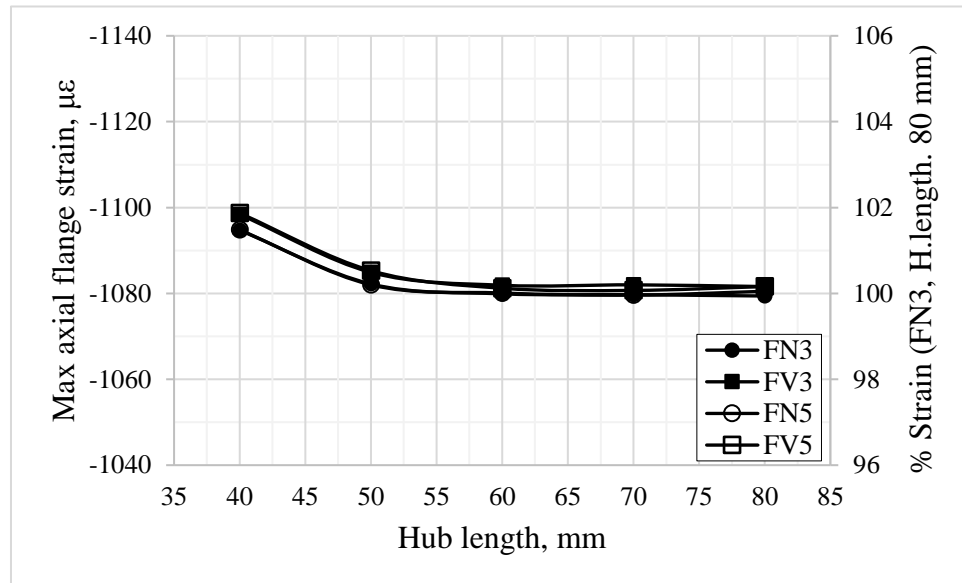


Fig. 8.19: Maximum axial compression strain ( $\mu\epsilon$ ) variation with the hub length for range of gasket types and thickness

**Maximum hoop strain vs hub length,** Fig. 8.20 shows the variation of the maximum hoop strain with the hub length and the gasket parameters (material and thickness). The maximum hoop strain is found at the lower face of the flange and around the bolt hole as explained in Fig. 8.6. As shown in the results, the hub length has very small impact on the maximum hoop strain, which is about 1%. When the hub length reduces from 80 to 40 mm, the hoop strain increases from 1109  $\mu\epsilon$  to 1118  $\mu\epsilon$ . In addition, the gasket thickness has small influence on the maximum hoop strain but the gasket material type has no effect.

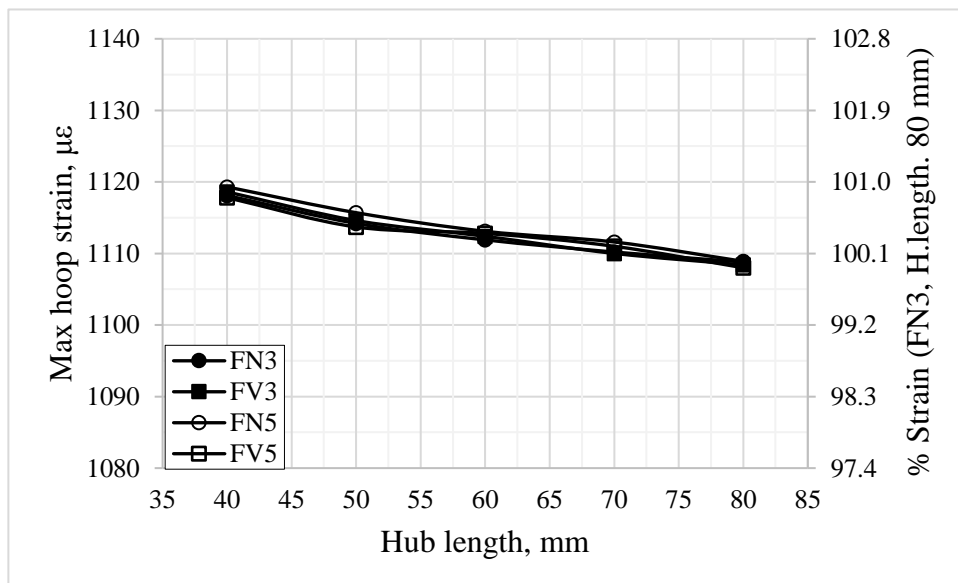


Fig. 8.20: Maximum hoop strain ( $\mu\epsilon$ ) variation with the hub length for range of gasket types and thickness

The overall variation of the maximum hoop strain with the bolt load (clamping stage) and internal pressure (pressurized stage) has been explained in Fig. 8.21 for different hub length. The style of this figure is almost same the style of Fig. 8.4. Based on the obtained results, the maximum hoop strain is affected completely by the bolt load and very small by the internal pressure. Approximately, 98% of the maximum hoop strain is produced due to the bolt load whereas 2% produced by the internal pressure when it increases up to 6 bar. Furthermore, the maximum hoop strain is not affected by the hub length and that can be seen clearly in Fig. 8.20.

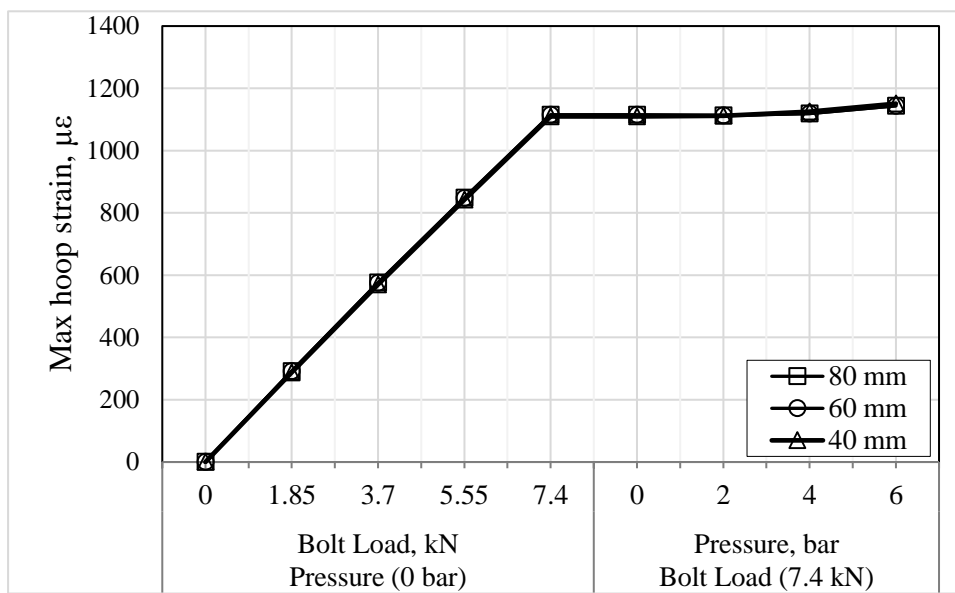


Fig. 8.21: Maximum hoop strain ( $\mu\epsilon$ ) variation with bolt load and internal pressure for range of the hub length

**Maximum radial strain vs hub length,** The relationship between the maximum radial strain and the hub length as well as the gasket type and thickness has been illustrated in Fig. 8.22. As shown in Fig. 8.8, the maximum radial strain is observed at the lower face of the flange and around the bolt hole. It is that the hub length has a small effect on the maximum radial strain. It increases approximately 5.5% when the hub length decreases from 80 mm to 40 mm. In addition, the maximum radial strain is affected by the hub length at the short hub length more than the long. Furthermore, the gasket thickness and material have a small influence on the maximum radial

strain. Finally, it can be stated that the hub length can be reduced to reduce the flange cost and material.

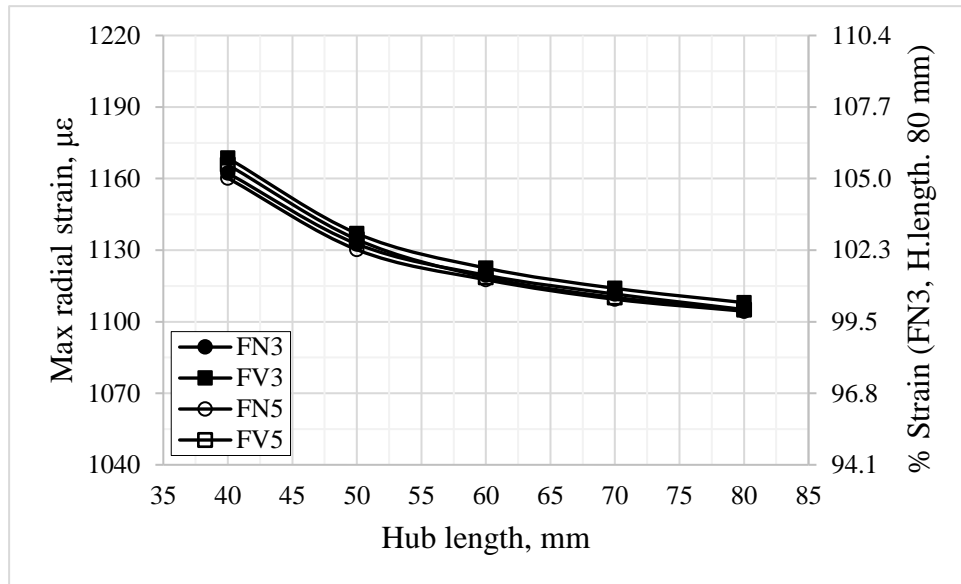


Fig. 8.22: Maximum radial strain ( $\mu\epsilon$ ) variation with the hub length for range of gasket types and thickness

**Bolt axial strain vs hub length,** Fig. 8.23 shows the bolt axial strain as a function of the hub length, gasket thickness and material. The strain values have been calculated at the point where the strain gauge has been embedded as shown in Fig. 8.10. The findings show that the axial bolt strain function is constant for all gasket thickness and materials. This means that there no relationship between the axial bolt strain and the hub length regardless of the gasket behaviour and thickness.



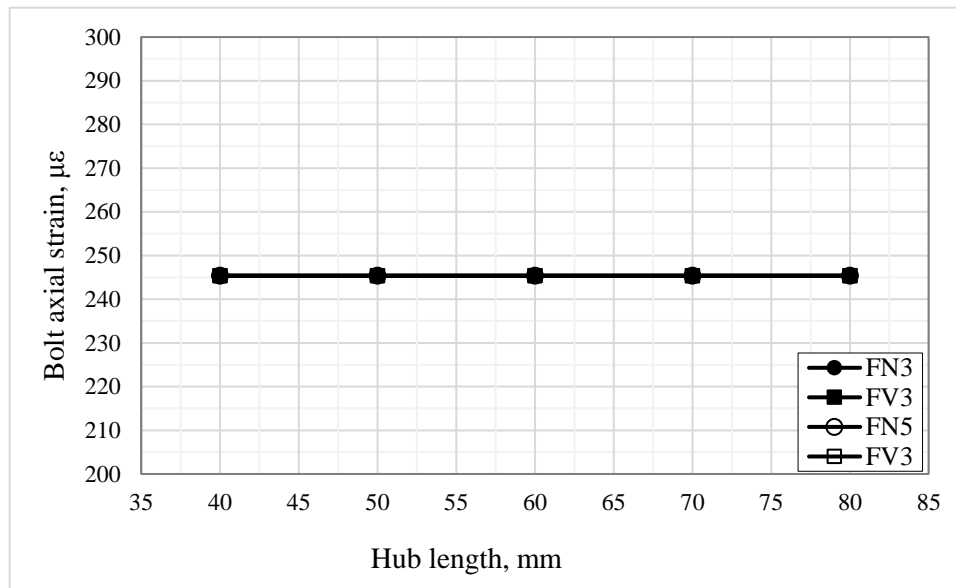


Fig. 8.23: Bolt axial strain ( $\mu\epsilon$ ) variation with the hub length for range of gasket types and thickness

### 8.7 Hub thickness effect

This section investigates the influence of the hub thickness on the strain distribution in three directions (axial, hoop, and radial) for range of gasket material and thickness. The hub thickness has been varied from 12 mm, which is the recommended value, to 6 mm. This range has been selected to study the effect of the hub thickness, and the possibility of reducing the thickness, which means reducing the flange materials. The figures, which show the axial, hoop and radial strains variation with hub thickness, have been drawn with three axes. The abscissa represents the hub thickness the left y- axis shows the real values of the strain. The right y-axis explains the normalized percentage of the strain with reference hub thickness 12 mm and using 3 mm Nitrile rubber gasket.

**Maximum axial tensile strain vs hub thickness**, The variation of the maximum axial tensile strain with the hub thickness has been shown in Fig. 8.24 for range of gasket thickness and material. The maximum strain has been measured at the outer surface of the flange-hub interface as illustrated in Fig. 8.2. The findings indicate that the

hub thickness has insignificant effect on the maximum axial strain, which is increase with less than 6%. The maximum axial strain is almost constant when the hub thickness decreases from 12 mm to 9 mm but increases approximately  $15 \mu\epsilon$  when the hub thickness decreases from 9 mm to 6 mm. In addition, the Viton rubber gasket produce axial strain higher than the Nitrile. Furthermore, the gasket thickness has very small effect on the axial strain and thick gasket shows less maximum axial strain. Based on the results, the hub thickness can be reduced to save the flange materials.

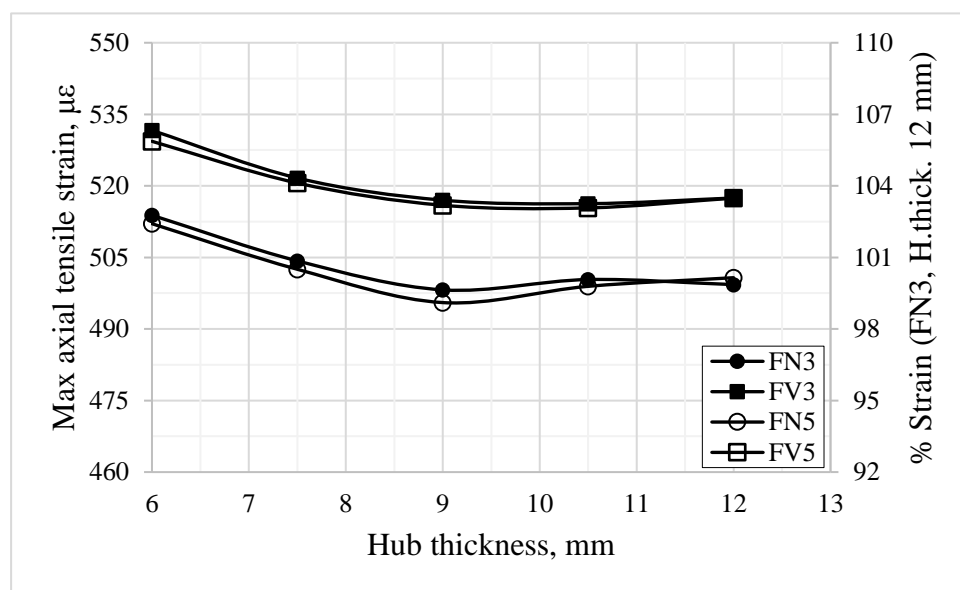


Fig. 8.24: Maximum axial tensile strain ( $\mu\epsilon$ ) variation with the hub thickness for range of gasket types and thickness

**Maximum axial compression strain vs hub thickness,** Fig. 8.25 shows the relationship between the maximum axial compression strain and the hub thickness for different gaskets and thicknesses. The maximum axial compression strain has been found and measured on the flange and around the bolt hole as explained in Fig. 8.2. The findings show that the variation of the axial compression strain with the hub thickness is very small, which is less than the 2% when the hub thickness reduces to the half (12 to 6 mm). However, the maximum compression strain increases when the hub thickness decreases. In addition, the gasket material has a small effect on the compression strain and the Viton gasket shows compression strain that is slightly

higher than the Nitrile gasket. Furthermore, the results are not influence by the gasket thickness.

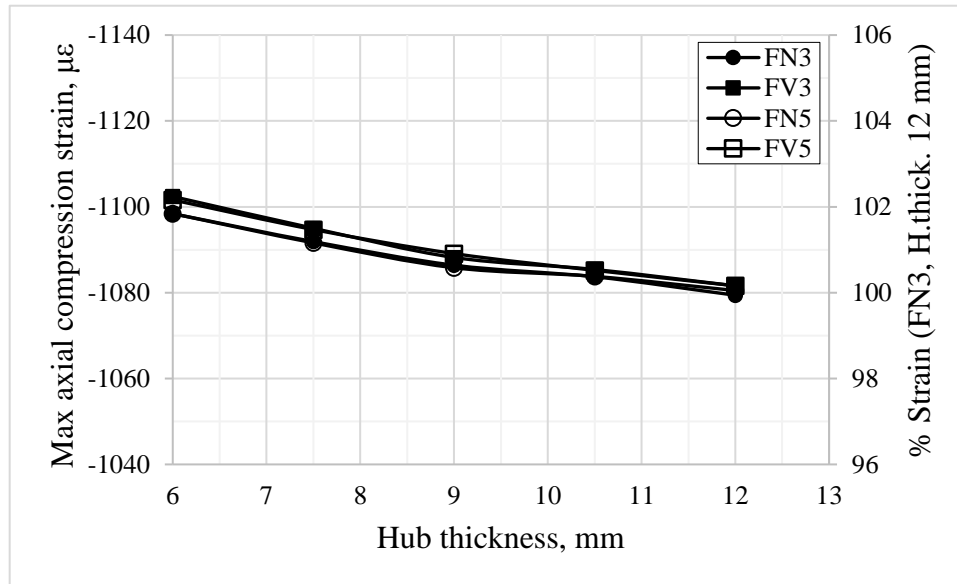


Fig. 8.25: Maximum axial compression strain ( $\mu\epsilon$ ) variation with the hub thickness for range of gasket types and thickness

**Maximum hoop strain vs hub thickness,** The influence of the hub thickness on the maximum hoop strain is shown in Fig. 8.26 for different gasket materials and thicknesses. As shown in the Fig. 8.6, the maximum hoop strain is found at the lower face and around the bolt hole, it is observed that the hub thickness has very small effect on the hoop strain when it reduces from 12 to 6 mm. The total increasing of the maximum hoop strain is less than 3% when the hub thickness is reduced to the half, which is 6 mm. The behaviour of the variation is linear. In addition, the results also show that the gasket material and thickness almost do not affect on the maximum hoop thickness. Based on the above findings, it can also stated that the hub thickness can be decreased to reduce the flange materials and cost.

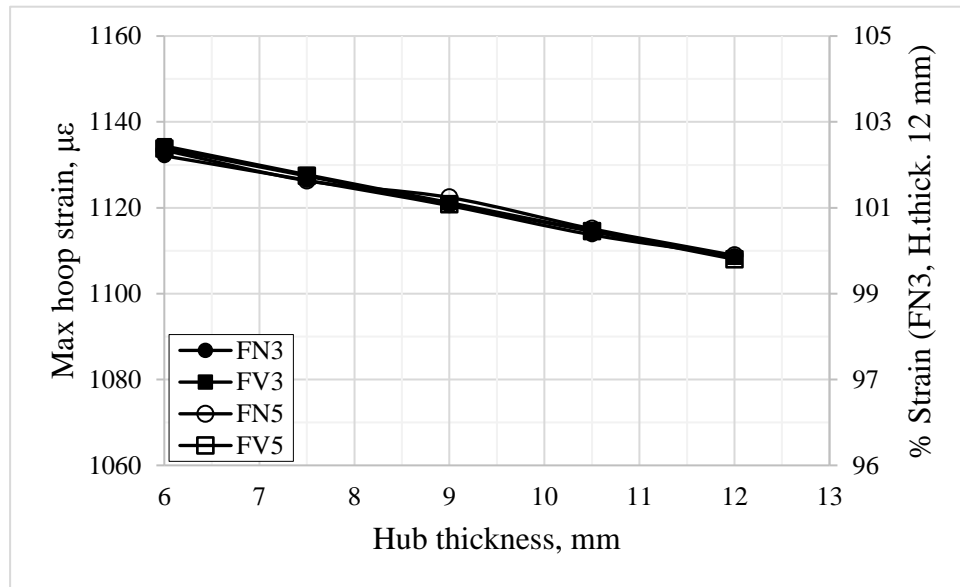


Fig. 8.26: Maximum hoop strain ( $\mu\epsilon$ ) variation with the hub thickness for range of gasket types and thickness

**Maximum radial strain vs hub thickness,** The variation of the maximum radial strain with the hub thickness has been illustrated in Fig. 8.27 using 3 and 5 mm of Nitrile and Viton rubber gaskets. The maximum radial strain is found at the lower face of the flange and around the bolt holes as shown in the Fig. 8.8. The results show that the hub thickness has insignificant impact on the maximum radial strain. The maximum radial strain increases from  $1112 \mu\epsilon$  to  $1180 \mu\epsilon$ , which is almost 7%, when the hub thickness increases from 12 to 6 mm. This is because of the increasing of the flange bending due to the bolt load. In addition, the Viton gasket produces radial strain slightly higher than the Nitrile rubber gasket. Furthermore, increasing the gasket thickness from 3 to 5mm has very small influence on the maximum radial strain.

Fig. 8.28 shows the history of the maximum radial strain when the flange joint is subjected to the bolt load and the internal pressure for range of the hub thickness. The style of this figure is same Fig. 8.4. The results show that the maximum radial strain is influenced significantly by the bolt force whereas very little by the internal pressure. The maximum radial strain increases sharply when the bolt load increases but this increment becomes very small in the operating stage when the pressure

increased up to 6 bar. In addition, decreasing the hub thickness leads to slightly increase the maximum radial strain.

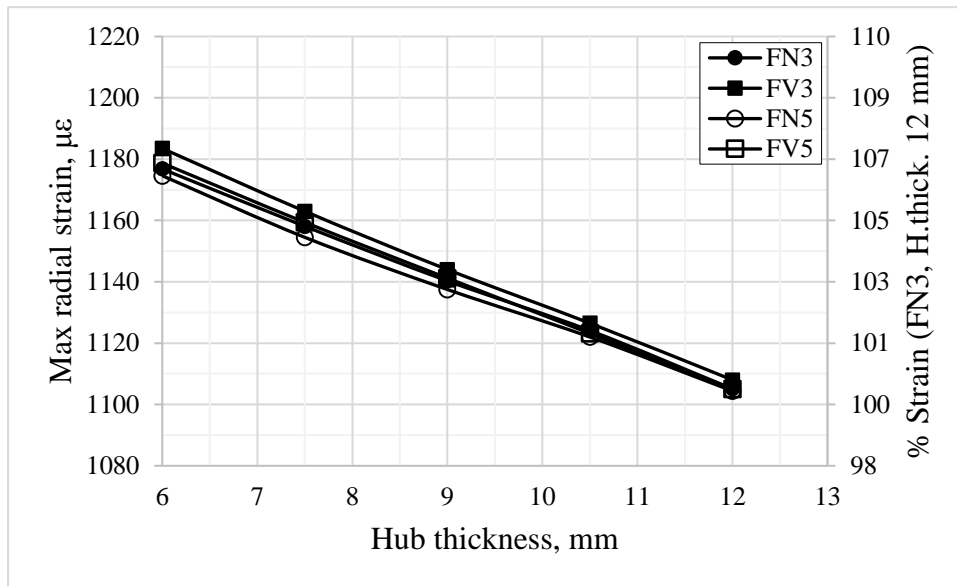


Fig. 8.27: Maximum radial strain ( $\mu\epsilon$ ) variation with the hub thickness for range of gasket types and thickness

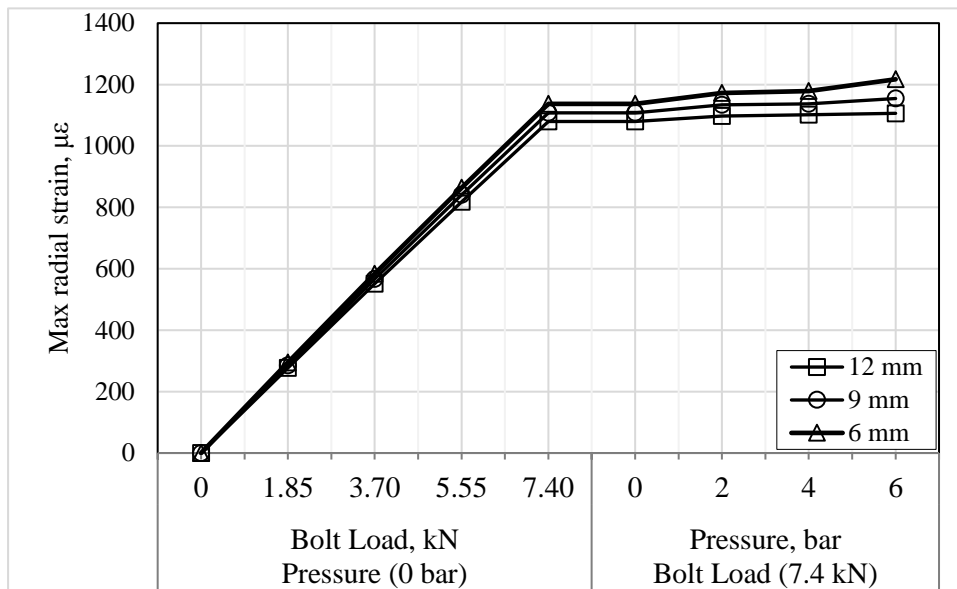


Fig. 8.28: Maximum radial strain ( $\mu\epsilon$ ) variation with the bolt load and internal pressure for range of the hub thickness

**Bolt axial strain vs hub thickness,** Fig. 8.29 shows the relationship between the bolt axial strain and the hub thickness using different gasket types and thicknesses. The axial strain of the bolt has been measured at the axial axis of the bolt where the strain gauge has been embedded. See Fig. 8.10. The findings show that there is no relationship between the bolt axial strain and the hub thickness regardless the gasket behaviour and thickness.

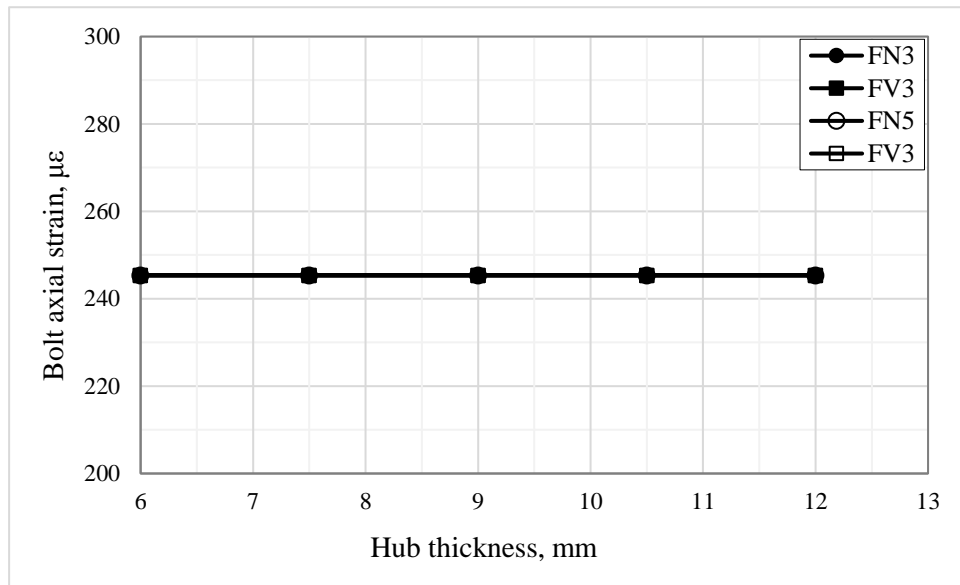


Fig. 8.29: Bolt axial strain ( $\mu\epsilon$ ) variation with the hub thickness for range of gasket types and thickness

## 8.8 Comparison of design variables effect

Table 8.2 shows summary of design variables and their effect on the maximum axial, hoop and radial strains using the 3 mm Nitrile rubber gasket as a reference. The results show that when the flange diameter, hub length, hub thickness and gasket thickness (Nitrile and Viton) are changed (decreased), the variations of the maximum strains increase up to less than 10% or even decrease up to 60%. For the flange thickness, decreasing the flange thickness leads to increase the maximum axial strain up to 40%, the maximum hoop strain 70%, the maximum radial strain 60% and the bolt axial strain 10%. However, the maximum axial tensile and compression strains are 658 and 1512  $\mu\epsilon$  and the maximum hoop and radial strains are 1838 and 1765  $\mu\epsilon$ . The overall of this comparison is that some or all the flange dimensions can be changed to reduce the flange material cost.

Table 8.2: Summary of design variables and their effect on the maximum strains

|                               | Max. axial<br>tensile<br>strain | Max. axial<br>compressi<br>on strain | Max.<br>hoop<br>strain | Max.<br>radial<br>strain | Bolt axial<br>strain |
|-------------------------------|---------------------------------|--------------------------------------|------------------------|--------------------------|----------------------|
| Flange diameter<br>320-400 mm | <b>+1</b>                       | <b>-2</b>                            | <b>-1</b>              | <b>-3</b>                | <b>+1</b>            |
| Flange thickness<br>10-15 mm  | <b>+4</b>                       | <b>+4</b>                            | <b>+7</b>              | <b>+6</b>                | <b>+1</b>            |
| Hub length<br>40-80 mm        | <b>-6</b>                       | <b>+1</b>                            | <b>+1</b>              | <b>+1</b>                | <b>+1</b>            |
| Hub thickness<br>6-12 mm      | <b>+1</b>                       | <b>+1</b>                            | <b>+1</b>              | <b>+1</b>                | <b>+1</b>            |
| Nitrile gasket<br>3-5 mm      | <b>+1</b>                       | <b>+1</b>                            | <b>+1</b>              | <b>+1</b>                | <b>+1</b>            |
| Viton gasket<br>3-5 mm        | <b>+1</b>                       | <b>+1</b>                            | <b>+1</b>              | <b>+1</b>                | <b>+1</b>            |

**Where:**

- 1 : The variation is up to 10%      ;      2 : The variation is up to 20%  
3 : The variation is up to 30%      ;      4 : The variation is up to 40%  
5 : The variation is up to 50%      ;      6 : The variation is up to 60%  
7 : The variation is up to 70%      ;      8 : The variation is up to 80%

**8.9 Flange axial displacement**

Axial displacement is another way to study the deformation and the bending on the flange joint when it is subjected to the bolt load and internal pressure. In this section, the axial displacement has been measured with two directions, hoop and radial. Generally, all the obtained results values are of negative sign, which mean both the matched flanges have moved towards the gasket to create sufficient sealing.

### 8.9.1 Axial displacement vs hoop angle

In the hoop direction, the axial displacement has been measured at the inner and outer diameters. The reason behind that is to show the variation of axial displacement in the hoop direction under range of the bolt load, internal pressure and also to show the effect of the unsymmetrical bolt load around the flange.

Fig. 8.30 shows the flange axial displacement variation with the hoop distance (hoop angle) at the inner and the outer diameters when the flange joint is subjected to the design conditions (BL 7.4 kN pressure 3.4 bar). The abscissa represents the hoop angle and it starts from 0°, which is at the line that passes through the pipe and bolt centres, and ends at 22.5°, which is at the mid-point between two adjacent bolts. This will be same for the next figures.

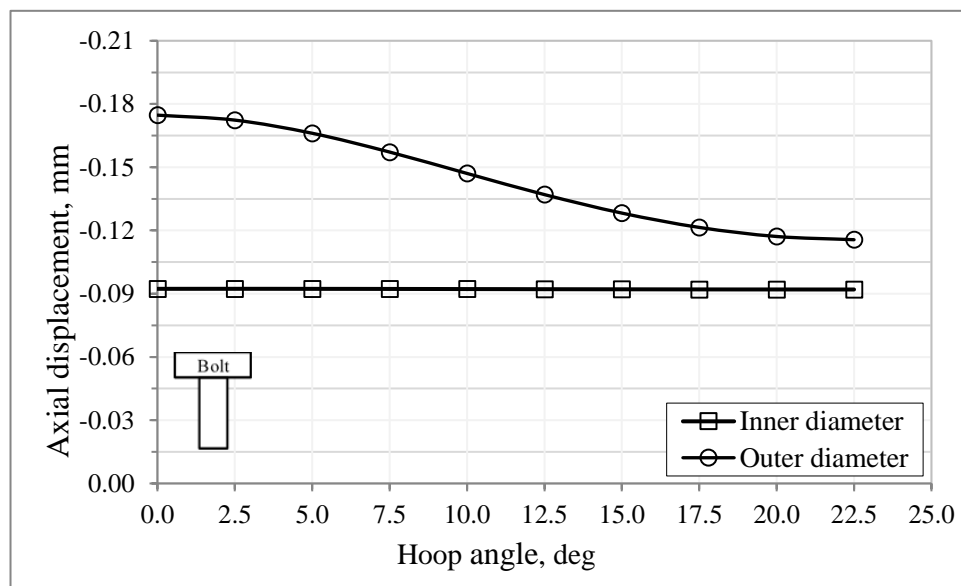


Fig. 8.30: Flange axial displacement variation with the hoop angle at the inner and outer diameters

The results illustrate that the axis displacement is constant (0.0923 mm) with the hoop angle at the inner diameter. For the outer diameter, the highest axial displacement occurs at the bolt centre and it decreases towards the mid-point between the adjacent bolts, this occurs because of the bolt load which is high at the bolt hole and decreases toward the mid-point. In addition, it is observed that the axial



displacement at the outer diameter is higher than that in the inner diameter, this is due to the flange bending, which is produced as a result of the applied loads.

Fig. 8.31 shows the relationship between the axial displacement and the hoop angle at the outer diameter under range of the bolt load. It seems that the axial displacement increases with increasing the bolt load. Increasing the bolt load leads to deform the flange and compress the gasket, thereby, increasing the axial displacement, especially at the bolts holes.

The influence of the internal pressure on the variation of the axial displacement with the hoop angle at the outer diameter is shown in Fig. 8.32. The results have been calculated when the flange joint is subjected to 0, 4 and 7.9 bar internal pressure. It seems that the internal pressure has small effect on the axial displacement. However, when the pressure increases, the axial displacement slightly increases. This is due to the applied pressure forces on the internal face of the joint and on the interface between the flange and the gasket. These forces are trying to add more moment on the flange, thereby, increasing the flange bending and axial displacement. Finally, it can be seen clearly through Fig. 8.31 and Fig. 8.32 that the effect of the bolt load on the axial displacement is higher than that of the internal pressure.

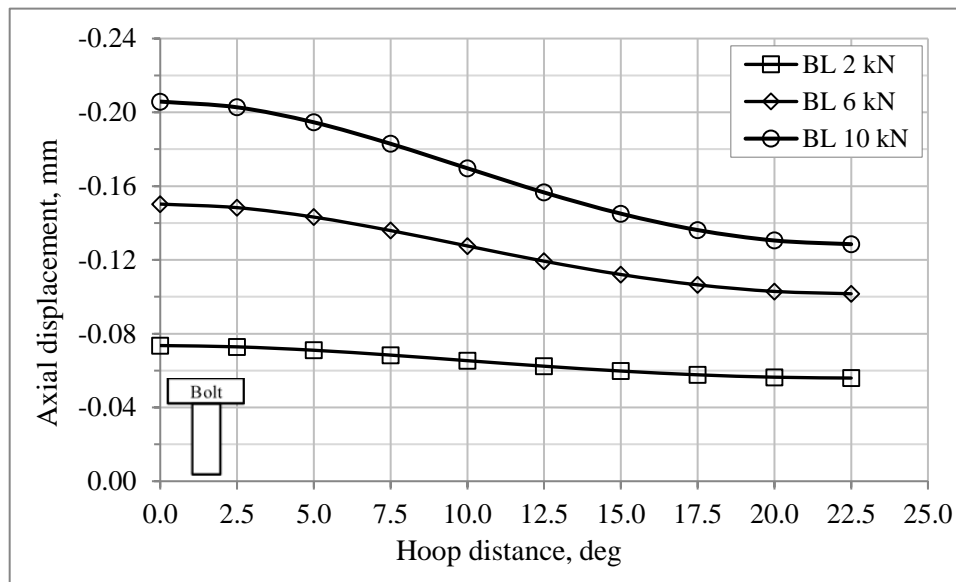


Fig. 8.31: Flange axial displacement variation with the hoop angle for range of the bolt load, P 0 bar

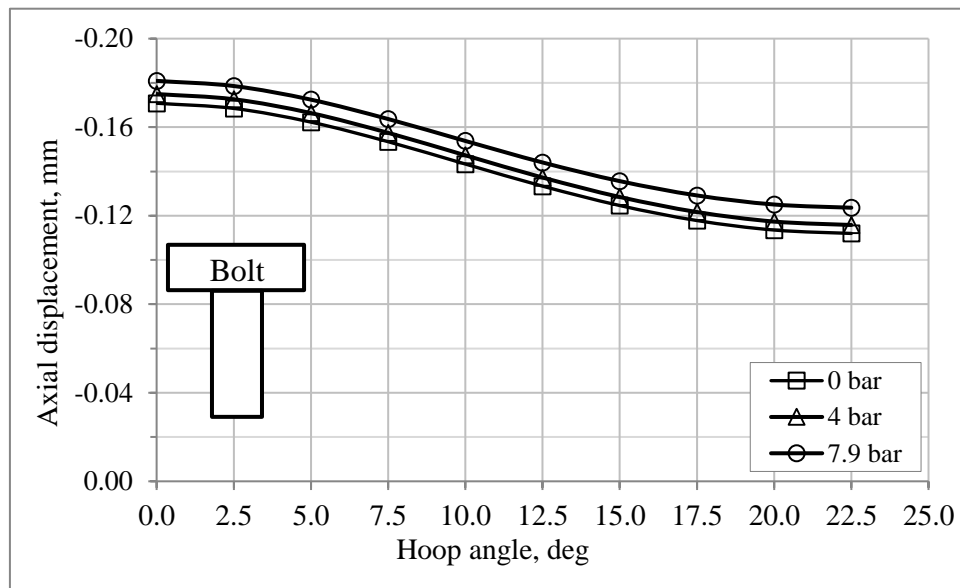


Fig. 8.32: Flange axial displacement variation with the hoop angle for range of the internal pressure, BL7.4 kN

### 8.9.2 Axial displacement vs radial distance

In the radial direction, the flange axial displacement has been measured at the right edge (located on the line that passes through the centres of the pipe and the bolt hole) and at the left edge (located on the line that passes through the centres of the pipe and the mid-point between two adjacent bolts). Fig. 8.33 shows the variation of the axial displacement with radial distance at the right and left edges when the flange is subjected to the design conditions (BL 7.4 kN, pressure 0 bar). The flange axial displacement at the right edge is higher than the left edge. This is because of the axial bolt load, which bends the flange at the holes more than any other places. In addition, the discontinuity that is shown in the curve of the axial displacement at the right edge is due to the bolt holes, which needed removing the flange material in these regions.

Fig. 8.34 explains the flange axial displacement relationship with radial distance at the right edge (bolt centre) for range of the bolt load and the pressure is zero. It seems that the flange axial displacement increases with increasing of the bolt load, especially at the holes. This is because of the applied bolt force, which deforms the

flange to seal the contact between the flange and the gasket. Furthermore, the influence of the internal pressure on the axial displacement at the same edge is shown in Fig. 8.35 when the bolt load is fixed at 7.4 kN. It is clear that the internal pressure has insignificant effect on the axial displacement as mentioned before.

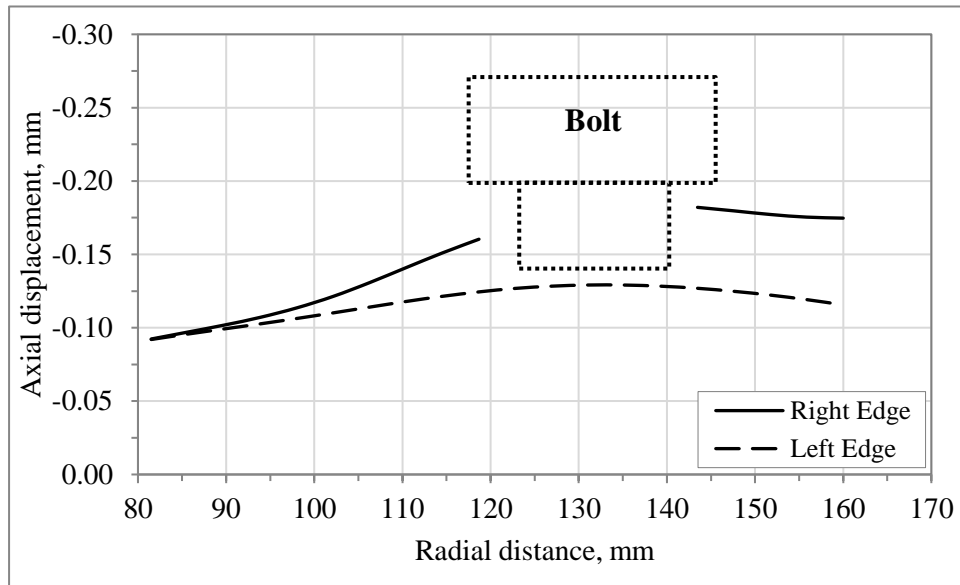


Fig. 8.33: Flange axial displacement variation with the radial distance at the right and left edges

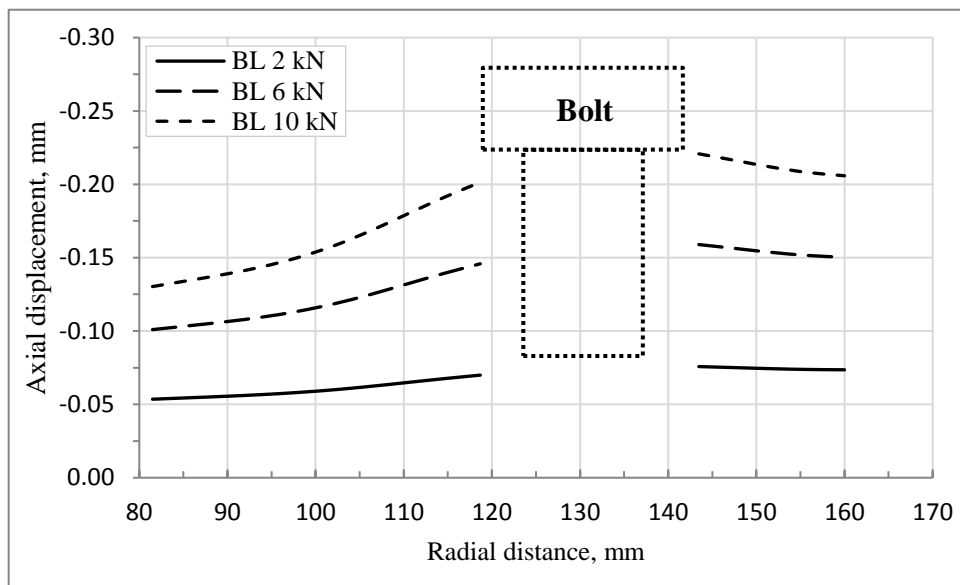


Fig. 8.34: Flange axial displacement variation with the radial distance at the right edge for range of the bolt load

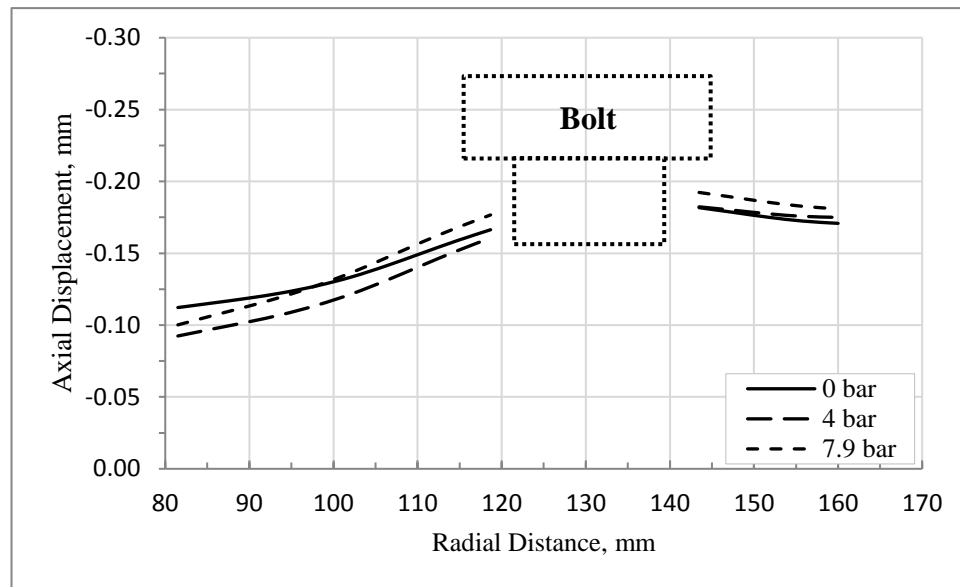


Fig. 8.35: Flange axial displacement variation with the radial distance at the right edge for range of the internal pressure

### 8.10 Flange rotation

Flange rotation is another way to get a good indication about the flange bending and performance. Flange rotation angle is calculated based on the difference in the axial displacement at the inner and the outer radiuses divided by the radial distance between of them as shown in Fig. 8.36 and the following equation:

$$\Theta = \tan^{-1} \left( \frac{S_o - S_i}{R_o - r_i} \right)$$

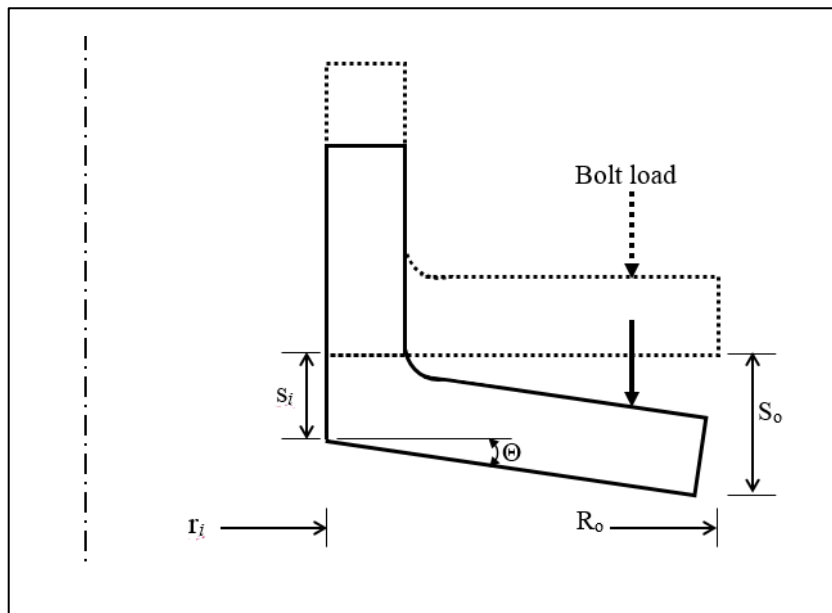


Fig. 8.36: Schematic diagram of the flange bending

In some cases, the flange displacement is measured between the inner radius and the lowest point in the flange instead of the outer radius. The reason for choosing this is that in the big flange diameters, the axial displacement around the holes is higher than that at the outer diameter so that gives accurate calculation for the flange rotation.

Fig. 8.37 describes the flange rotation angle with the hoop angle under various of the bolt loads. The 0 edge of hoop represents the bolt side and the 22.5 edge hoop angle represents the mid-point between two adjacent bolts. The findings indicate that the flange is subjected to the rotation at the bolt holes higher than any other region. This occurs due to the high concentration of the bolt load at the bolts holes. In addition,

the effect of the bolt load on the flange rotation can be seen clearly in the same figure. When the bolt load increases 2, 6 and 10 kN, the flange rotation increases due to the produced flange bending.

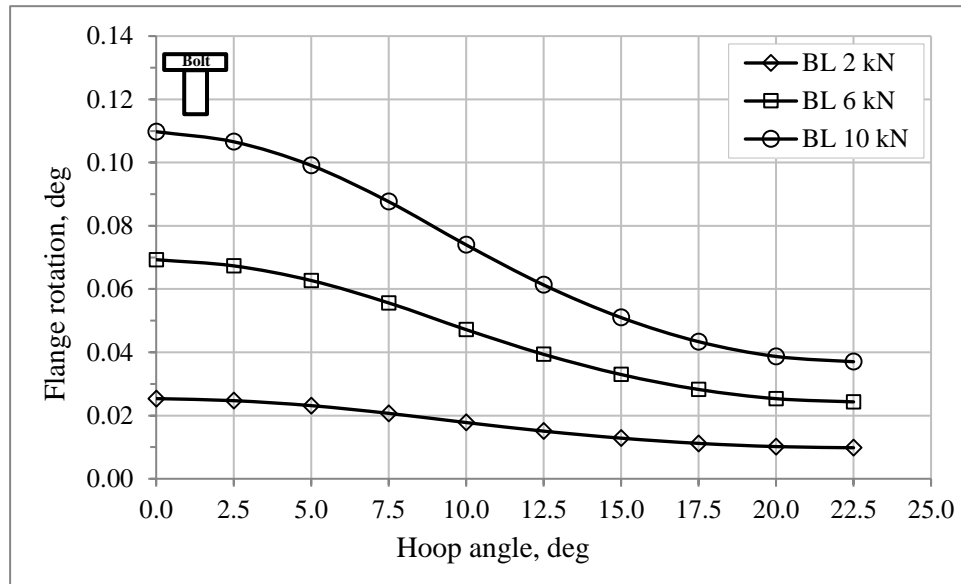


Fig. 8.37: Flange rotation variation with the hoop distance for range of the bolt load

The influence of the internal pressure on the flange rotation has been shown in Fig. 8.39 when the bolt load is 7.4 kN. It is observed that the flange rotation is increased by the internal pressure. This happens because of the pressure forces including the hydrostatic end force and penetrated pressure force between the flange and gasket are trying to lift up the inner flange diameter, which means increasing the flange rotation.

Fig. 8.38 illustrates the variation of the flange rotation with internal pressure up to the leakage pressure under different bolt loads. As mentioned earlier, the internal pressure and the bolt load are the main loads that affect on the flange rotation. When they increase, the flange rotation increases. Therefore, the GFRP flange should be designed carefully with high stiffness to withstand the applied loads, especially, at the flange neck, which represents the common failure point in the available commercial flanges. Reinforcing the neck region (hub-flange intersection) leads to reduce the flange bending, thereby, reducing the flange rotation.

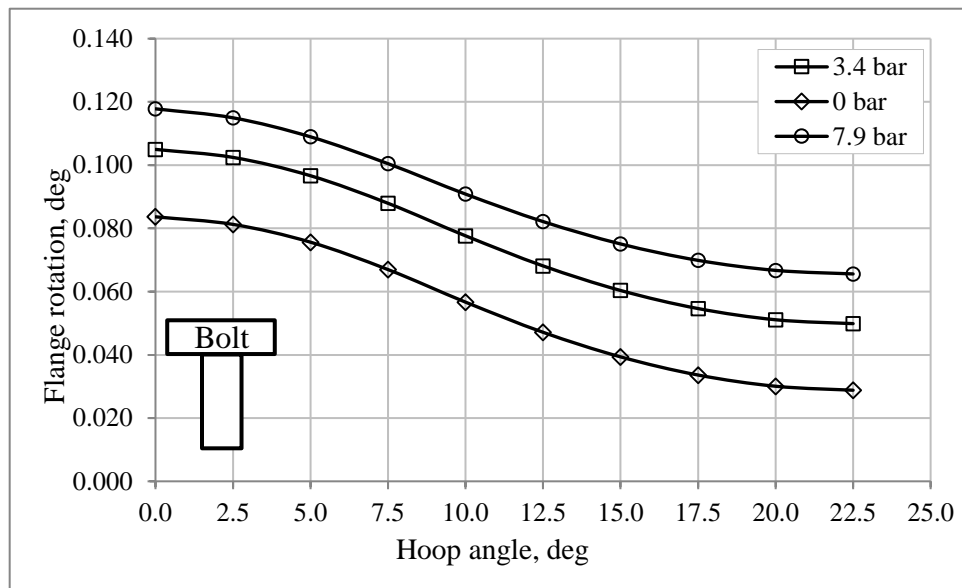


Fig. 8.39: Flange rotation variation with the hoop angle for range of the internal pressure

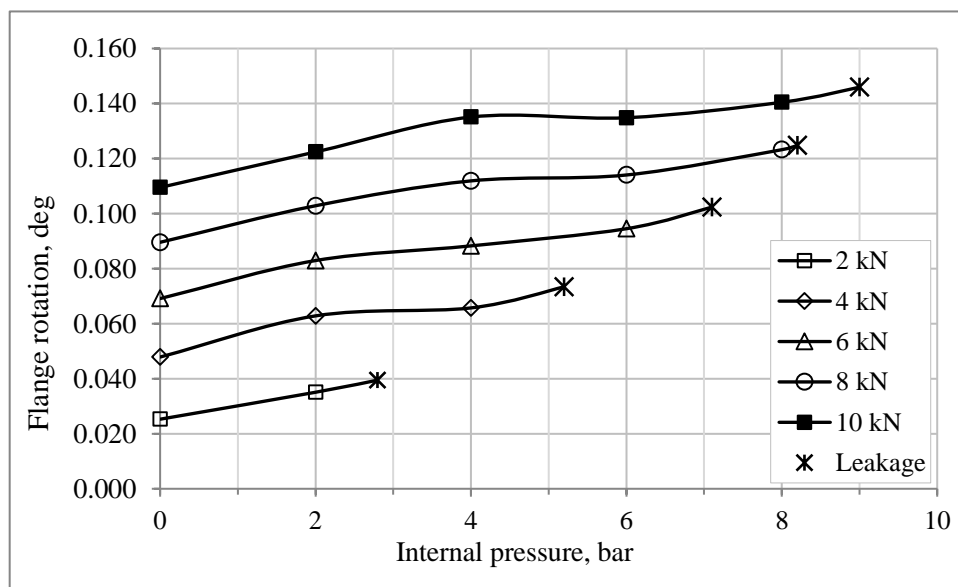


Fig. 8.38: Flange rotation variation with the internal pressure for range of the bolt load

## 8.11 Leakage pressure

Leakage pressure (LP) is one of the critical points that should be avoided in the pipelines or the pressure vessels. Catastrophic problems can be occurred if the leakage happen in many applications. In this chapter, the leakage pressure has been calculated numerically by using ANSYS with the PPNC criterion, which has been explained in details in chapter 6. This section investigates the relationship between the leakage pressure and the flange dimensions as well as the bolt load.

### 8.11.1 Leakage pressure vs flange diameter

Fig. 8.40 illustrates the leakage pressure (LP) variation with the flange diameter for different gasket materials and thicknesses when the bolt load is 7.4 kN. The findings show that the highest LP occurs at the lowest diameter (320 mm) regardless of the gasket characteristics. This is because of the high flange bending when the bolt load is applied and low gasket reaction. This creates high compression pressure on the gasket, which controls the fluid pressure penetration. When the flange outer diameter increases to 340 mm, the LP decreases almost one bar. This occurs due to the increasing in the contact area between flange and the gasket. This increment leads to increase the gasket reaction and reduce the flange bending, thereby decreasing the contact pressure, which decreases the LP.

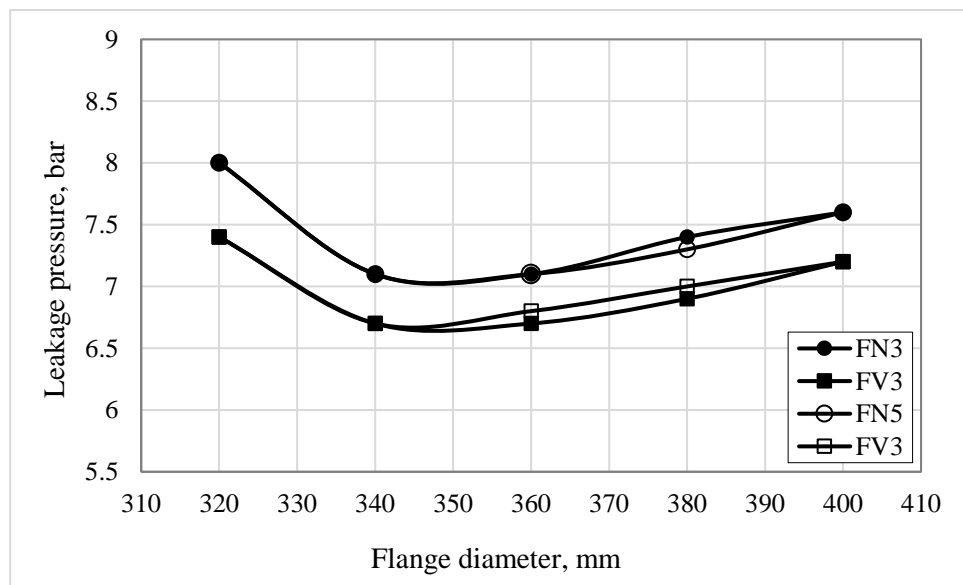


Fig. 8.40: Leakage pressure variation with the flange diameter for different gasket materials and thickness



When the flange outer diameter increases more up to 400 mm, the LP starts again to increase but slightly, which means the effect of the diameter within this range on the leakage pressure has decreased. The reason of this change is that the contact pressure at the new area (340 – 400 mm) is very low or even approximately zero. See Fig. 8.41 . This means that there is little or no contact between the flange and the gasket at the area that outside the 340 mm diameter. Therefore, increasing the outer diameter will move up more the outer edge of the flange due to bolt load, high gasket reaction and the circular geometry of the flange disc. This increases the gasket reaction at the bolt circle diameter region and leads to increase the contact pressure, which increases slightly the LP. In addition, the LP is affected by the gasket material and the Nitrile gasket increases the LP almost 0.5 bar more than the the Viton gasket for all the diameters. It seems that the gasket thickness does not influence on the LP except a small effect at the diameter range 360 – 380 mm.

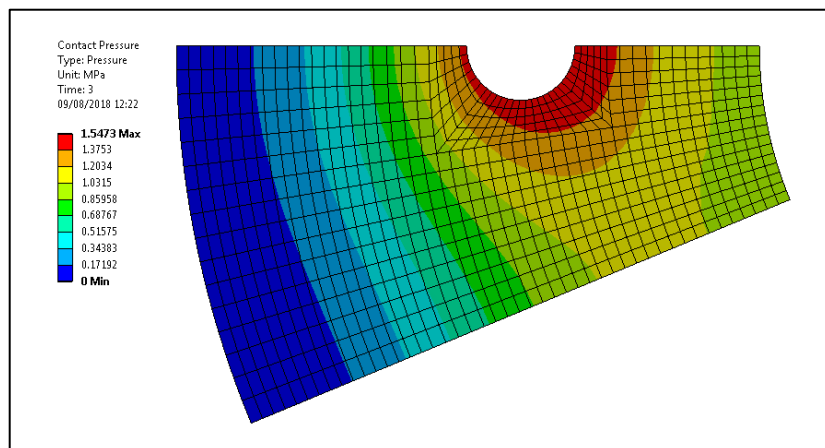


Fig. 8.41: Contact pressure between the flange and the gasket

The influence the bolt load on the LP variation for different flange outer diameter has been described in Fig. 8.42. The bolt force is 7.4 kN and 3 mm Nitrile rubber gasket has been used. The results show that there is a non-linear relationship between the LP and the bolt load. Increasing the bolt load leads to increase the LP. The lowest LP was recorded at the flange diameter 360 mm whereas the highest was with the 320 mm flange (except at the high bolt loads) and the middle LP was with 400 mm. The reasons behind those values have been explained earlier.

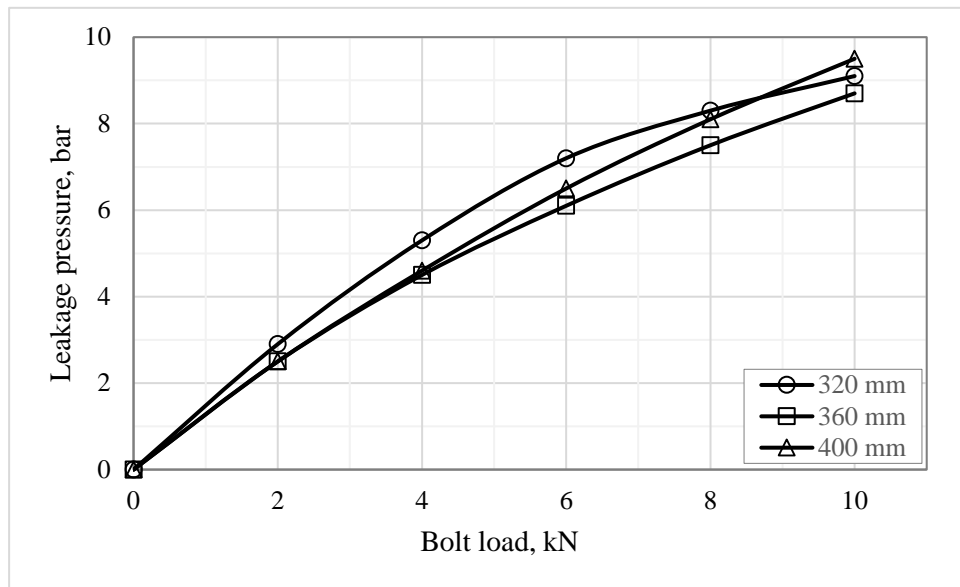


Fig. 8.42: Leakage pressure variation with the bolt load for different flange diameter

### 8.11.2 Leakage pressure vs flange thickness

The effect of the flange thickness on the leakage pressure using different gasket types and thicknesses is shown in Fig. 8.43. The bolt load is 7.4 kN. It is observed that the relationship between the LP and the flange thickness is linear. Increasing the flange thickness leads to increase the LP. This occurs due to the increasing in the flange strength, which reduces the flange deformation. Usually, the leakage occurs at the mid-point between two adjacent bolts as shown in Fig. 8.44. Therefore, increasing the flange stiffness leads to distribute the bolts loads uneven on all the flange disc, thereby, increasing the leakage pressure. In addition, the gasket thickness does not affect on the LP but the gasket material affect on the LP. The Nitrile rubber gasket produces LP higher than the Viton gasket regardless the flange thickness.

Furthermore, the impact of the bolt load on the LP is shown in Fig. 8.45 for various flange thickness using 3 mm Nitrile gasket. As mentioned earlier, the LP increases with increasing of the bolt load. However, the effect of the bolt load on the LP decreases with increasing bolt load. It is high at the low bolt load values but less at the high values. The LP increases with increasing the flange thickness except at the

low bolt load values, which less than 4 kN. At the low bolt load, the leakage pressure is not affected by the flange thickness, this is because of that, at the low bolt load, the leakage occurs at the bolts holes instead of the mid- point between two adjacent bolts.

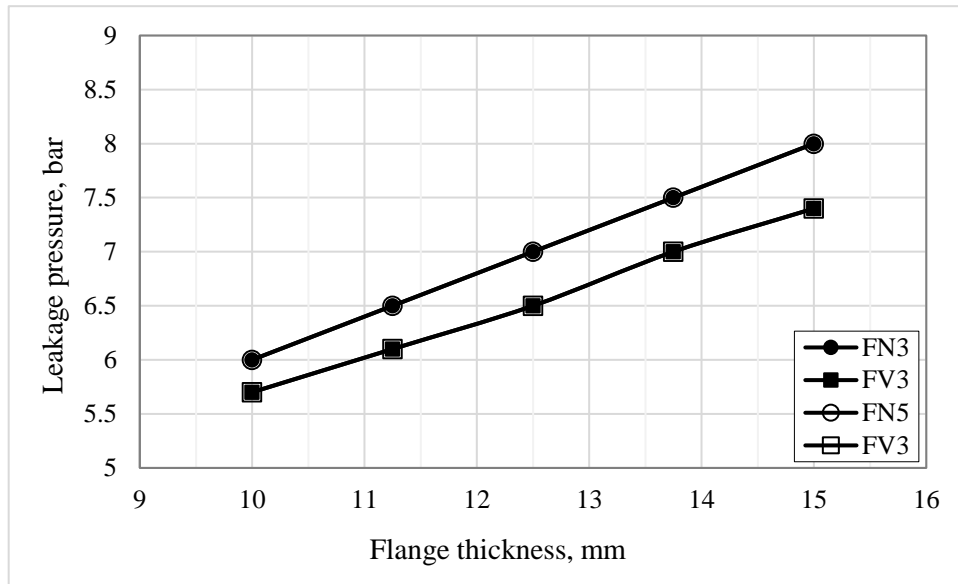


Fig. 8.43: Leakage pressure variation with the flange thickness for range

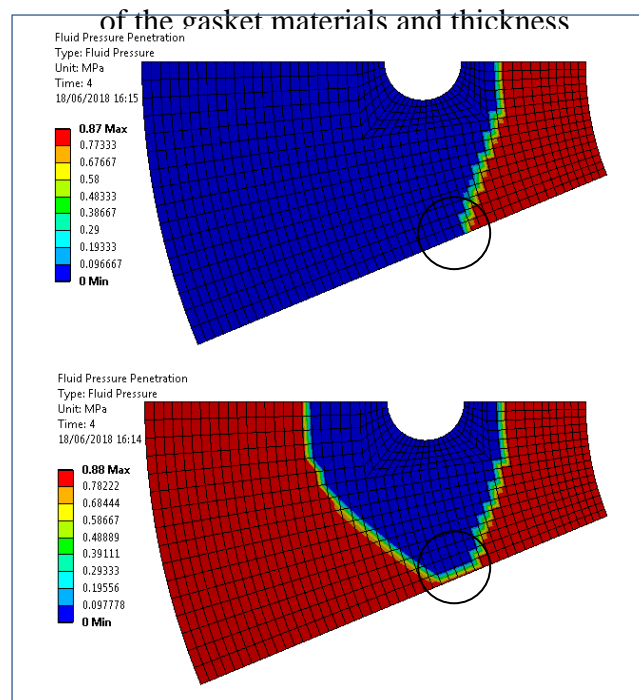


Fig. 8.44: Leakage pressure point

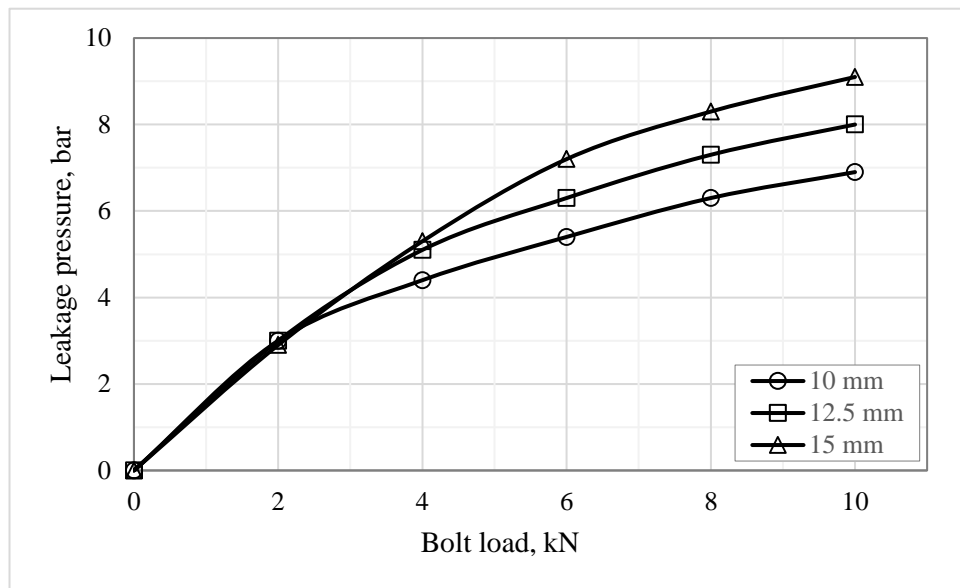


Fig. 8.45: Leakage pressure variation with the bolt load for different flange thickness

### 8.11.3 Leakage pressure vs hub length

The variation of the leakage pressure (LP) with the hub length has been shown in Fig. 8.46 for range the gasket materials and thickness under 7.4 kN bolt load. It seems that the LP decreases when the hub length increases. The reason is that when the hub length decreases the flange bending increases (due to the circular geometry of the hub), thereby, the compression stress on the gasket at the holes circle increases as well. This increment in the gasket compression stress is trying to stop the leakage propagation and increasing the LP. As the previous, the Nitrile gasket produce LP higher than the Viton gasket and this is because the natural behaviour of the rubber. The gasket thickness does not effect the LP.

In addition, Fig. 8.47 illustrates the effect of the bolt load on the LP for different hub length using 3 mm Nitrile rubber gasket. Increasing the bolt load leads to increase the leakage pressure. The relationship between of them is non-linear. The influence of the bolt load on the LP is high at the low bolt loads comparing with it at the high bolt loads. Furthermore, the hub length has small impact on the LP. The LP at the hub length 40 mm is higher than those at the hub length 60 and 80 mm.

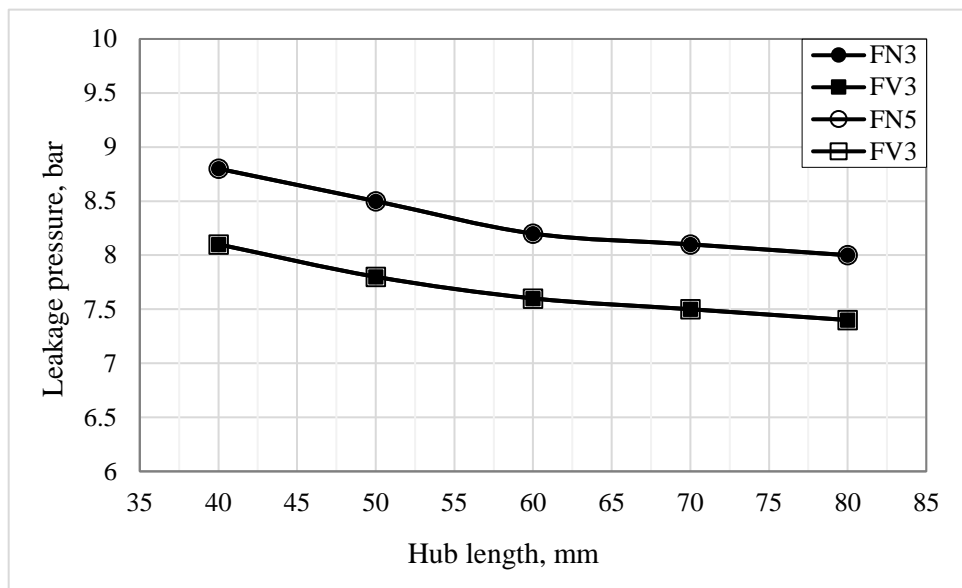


Fig. 8.46: Leakage pressure variation with the hub length for range of gasket materials and thickness

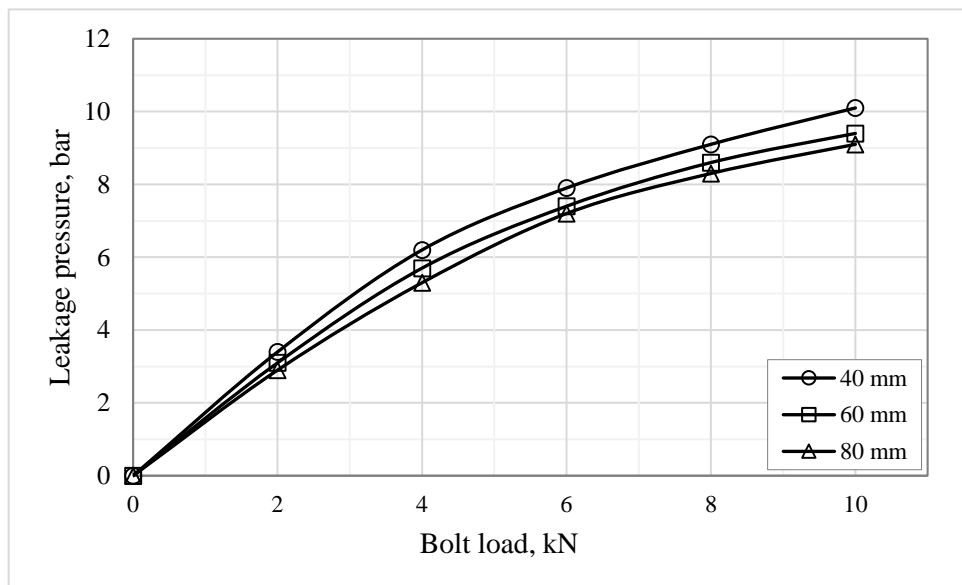


Fig. 8.47: Leakage pressure variation with bolt load for different hub length

### 8.11.4 Leakage pressure vs hub thickness

Fig. 8.48 explains the relationship between the leakage pressure (LP) and the hub thickness when the bolt load is 7.4 kN using different gasket thicknesses and materials. It is clear that the hub thickness has a small effect on the LP. The LP has decreased (less than 0.5 bar) when the hub thickness increased from 6 to 12 mm. Increasing the hub thickness means increasing the hub stiffness and the stiffness of the hub-flange interface. This increasing in the stiffness minimizes the flange bending under the applied loads. Therefore, the LP decreases. Regarding the gasket behaviour, the Viton rubber gasket gives LP less than Nitrile gasket and the gasket thickness does not affect the LP.

In addition, Fig. 8.49 describes the impact of the bolt load on the LP using Nitrile gasket with 3 mm thickness. Generally, the results are same the results of Fig. 8.47 but the hub thickness has different influence. The hub length does not effect on the LP at the low bolt loads (0-6 kN) (and after that, the bolt load starts to affect). At the beginning of the bolt preload (low bolt load values), the rubber gasket deforms firstly, because of it is soft material. The flange bending, which is affected by the hub thickness, occurs later at the high bolt load after deforming the rubber gasket. So that, the leakage pressure is affected by the high bolt load rather than the low.

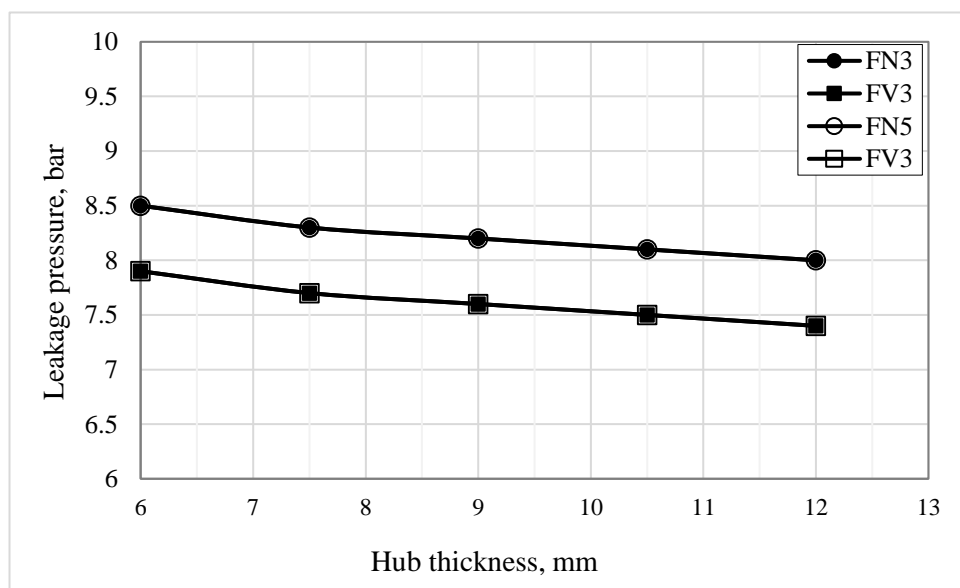


Fig. 8.48: Leakage pressure variation with the hub thickness for various gasket materials and thickness

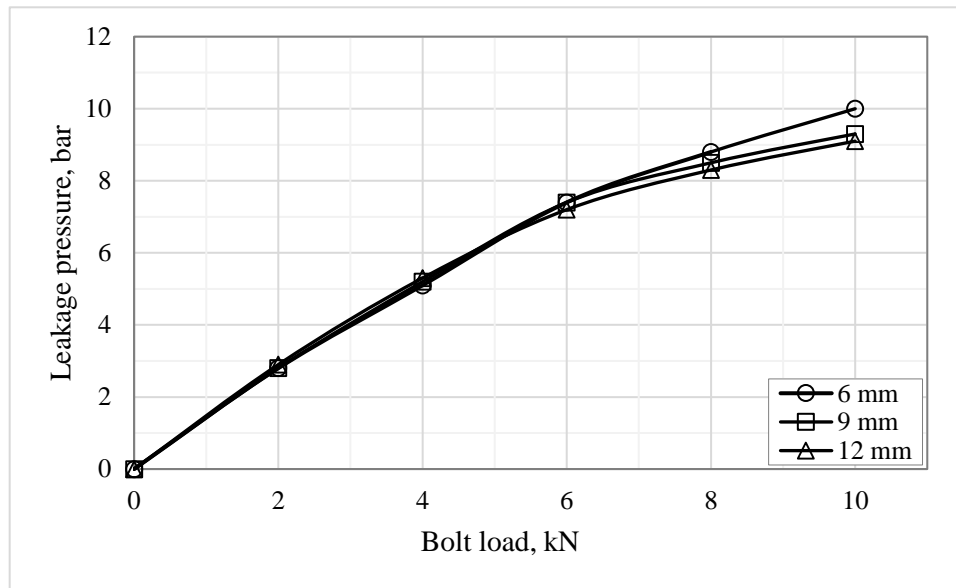


Fig. 8.49: Leakage pressure variation with the bolt load for different hub thickness

### 8.12 Results contribution

The obtained results have contributed significantly in the design and manufacturing of the composite flange. The manufacturing process and the used materials with the selected fabric structure have produced a good GFRP flange with high strength. So that it can be used as a reference for further studies. In these studies, other manufacturing methods (RTM or hand lay-up) with other material and different structure can be used to find out the best manufacturing process, materials and fabric structure, thereby obtaining a good composite flange with a high strength, quick fabrication process and low in the cost.

In terms of the flange dimensions (Flange outer diameter, flange thickness, hub thickness and hub length), most of these dimensions have small effect on the maximum axial, hoop and radial strains. Based on the obtained results, most of the dimensions can be reduced to save the materials. Therefore, an optimization study using Taguchi method or Normalized Normal Constraint Method is required to determine the amount allowable reduction in the dimensions. These reductions are important to reduce the required materials and their cost. In addition, the results

show that the ASME Code was conservative due to the good selections of the manufacturing process, materials and fabric structure. This conservative also has been found by other study for a metallic flange [36], which has been discussed in section 2.4.3.

For the gasket type and thickness, they have small influence on the flange strains distributions. Therefore, other types of rubber gaskets, which are used for different purposes such as water industry, such as EPDM or Neoprene can be tested and compare their results with the current results.

This study has been conducted under range of the bolt load and internal pressure and at zero external load. Based on obtained results, a further study is required to investigate the effect of the external loads, which can be force or pressure. This is important in the pipelines that are subjected to external loads such as extracting the oil from under the seabed. Similarly, the results of this study have been measured and calculated at the room temperature. Other investigation is required to find the effect of the thermal load (internal or external thermal load) on the flange behaviour. In the high temperature applications, the thermal deformation is a big problem and it can lead to fail the joint either mechanical failure or leakage. More details can be found in chapter 2, section 2.4.6, which includes many studies [39-42] about the influence of the thermal load on the metal flange joint.



### 8.13 Summary

This chapter analyses the effect of the flange dimensions on the maximum strains in the axial, hoop and radial directions using the FEA analysis. These dimensions are the flange outer diameter, flange thickness, hub length and hub thickness. Various gasket materials and thickness has been used. Various loads, including the designed loads, which are the bolt load 7.4 kN and the internal pressure 3.4 bar, have been applied. In addition, the flange axial displacement, flange rotation and leakage pressure has been investigated in this chapter for a range of the flange dimensions and loads.

Based on the obtained results, it can be summarized that the GFRP flange showed high performance and the values of the strains were low. The influence of the bolt load on the axial, hoop and radial strains is higher than the internal pressure load. Most of the flange dimensions (within the selected range) have a small effect on the maximum strains and that encourages reducing the flange dimensions, which means reduce the materials and cost. The axial bolt strain is not influenced by the flange dimensions. The gasket material has a small effect on the maximum strain whereas the gasket thickness has no affect. This encourages the use of thin gaskets to reduce the cost. The flange axial displacement and flange rotation are high at the bolts holes due to the bolt loads. The flange axial displacement and flange rotation are affected by the bolt load more than the internal pressure. The leakage pressure is affected by varying the flange dimensions due to the changing in the flange strength and stiffness. The relationship between the leakage pressure and the bolt load is non-linear.

# CHAPTER NINE

## CONCLUSIONS &

## RECOMMENDATIONS

### 9.1 Conclusions

This PhD work has been conducted to investigate the design and the manufacture of bolted flange joint made of glass fibre reinforced polymer for oil and gas applications using the experimental and the numerical methods. Many areas can be concluded in the following sections.

#### 9.1.1 Composite flange standards or design codes

Most of the current standardizations and the relevant design codes of the bolted GFRP flange joint have been modified from their counterpart of metallic design methods so that they neglect the composite materials behaviours, which are different from those of the metallic materials. For example, the analytical approach of ASME code, which is used in this study, does not take into account of the mechanical properties of the composite materials, which are affected significantly by the type of material, fabric structure, fibre content and directions, and the type of the manufacturing process. Therefore, there is an urgent need for a design code, which takes into account of all the details of the composite materials.

### **9.1.2 Manufacturing of the GFRP flange**

The GFRP flange has been fabricated based on the ASME code, Section X. The fabrication process are mainly divided into two steps: (1) mould manufacturing and (2) flange fabrication, which represent one of the novelties in this project. The mould has been designed and manufactured using aluminium and glass materials as well as bolts and O-ring rubber gasket. The manufactured mould has achieved all the requirements, which are flange strength or stiffness, required flange dimensions, flange surface quality and the flange removal from the mould after the curing.

In terms of the flange manufacturing, the bolted GFRP flanges have been fabricated using glass fibre braid, polyester and vacuum infusion process (bag moulding), which is one of the four methods that are recommended by the ASME code. In addition, a number of experiments have been conducted to solve the faced issues (dry regions, voids and cracks) and to improve the manufacturing process. The fabricated GFRP flange was good product with high quality and performance. Furthermore, a comparative study has been carried out using two types of drill bits (Erbauer diamond tile drill bit and Brad & Spur K10 drill) with various rotation speed. The best obtained drilled flange holes were by using Erbauer diamond tile drill bit at rotation speed 800 rpm. The flange has been bonded to composite pipe as well as another type of flange. These and other components (rubber gasket, blind flanges, fasteners and fitting) have been assembled to produce a pressure vessel.

### **9.1.3 Bolted GFRP flange testing**

After fixing all the requirements for collection the required data, the bolted flange joint has been tested under various bolt and internal pressure loads using different types of rubber gaskets (Nitrile and Viton) with 3 and 5 mm thicknesses. The required data were axial, hoop and radial strains and leakage pressure. The obtained data were very good and that confirms the high quality of the testing set up.

Another novelty in this work is that a parallel study has been conducted about the bolt strain gauges. Two types of strain gauges (bonded strain gauges and embedded strain gauges) have been used in this study to find out the best strain gauge that can measure the axial bolt load with high accuracy. The results show that both types are good but the embedded strain gauge is better as its installation is easier and quicker than the bonded strain gauge.

#### **9.1.4 FEA model of GFRP flange joint**

The bolted flange joint system has been simulated in this study using FEA with ANSYS. The FEA includes all components of the bolted flange joint; such as composite flange and pipe with their orthotropic mechanical properties, adhesive bonding and fastener with their isotropic properties and the rubber gaskets (Nitrile and Viton) with their non-linear behaviour during the loading and the unloading conditions. In the FEA of this study, the novel work was the simulating of the fluid pressure penetration. The fluid pressure penetration has been simulated using PPNC criterion and applied between the flange and the rubber gasket. The flange joint deformation, axial, hoop and radial strains and stress, axial displacements, flange rotation and the leakage pressure were measured in this FEA. All the FEA results were very good and have good agreement with the experimental results. This proves the high performance of the FEA model, which can be used for further investigations.

#### **9.1.5 Validation of results**

The experimental and the numerical results have been compared for both the boundary conditions (bolt up and operating). The relationships between these results, which are axial, hoop and radial strains, flange-gasket contact pressure and leakage pressure, and the bolt and internal pressure loads have been investigated. The results show that the proposed composite flange has high quality, good performance and good strength based on the identified values of strains (axial, hoop and radial). The strain values are comparatively low even with the applied loads that are more than the recommended design conditions. The agreement between the experimental and the numerical results are excellent and this validates the FEA method used. The distribution of the gasket contact stress (contact pressure) is non-uniform across the gasket face. Pressure values are higher around the bolt hole and gradually decreases in the radial direction of the bolt hole. It is proved that the finite element method using PPNC in ANSYS can be considered as an efficient tool to study the leakage behaviour.

In addition, another FEA model has been developed for a metal flange with the same boundary conditions of the GFRP flange FEA and the fluid pressure penetration criterion (PPNC). This flange has been investigated experimentally and numerically by [1]. The results show that there is an excellent agreement with the published results. This can be considered as another validation of the FEA method used.

### **9.1.6 Effect of the applied loads**

The effect of the bolt and internal pressure loads on the strains distributions, flange axial displacement and rotation, leakage pressure have been investigated in this study. The results show that increasing these loads lead to increase the flange strains, flange axial displacement and rotation. In addition, the leakage pressure increases with increasing the bolt load. It is observed that the effect of bolt load is higher than the internal pressure for the strain distributions, flange axial displacement and rotation.

### **9.1.7 Effect of the flange dimensions**

The relationships between the flange dimensions with the maximum axial, hoop and radial strains and the leakage pressure have been investigated in this project. These dimensions are flange outer diameter and thickness and hub length and thickness. The results indicated that the GFRP flange showed high performance and the values of the maximum strains were low. Most of the flange dimensions (within the selected range) have a small effect on the maximum strains and that encourages reducing the flange dimensions, which means reduce the materials cost. The leakage pressure is mostly affected by the flange thickness but less affected by the flange outer diameter, the hub length and the thickness. The above-mentioned points represent novel results and should be considered in the related future works.

### **9.1.8 Effect of the gasket materials and thickness**

Two types of rubber gaskets with 3 and 5 mm thicknesses have been studied. These gaskets are made of Nitrile and Viton rubber, which are commonly used in the oil and gas industry. The findings indicated that the gasket materials and thickness have very small effects on the flange strains, the axial displacement and the rotation. The leakage pressure is affected more by the gasket materials than the thickness.

## 9.2 Recommendations for future work

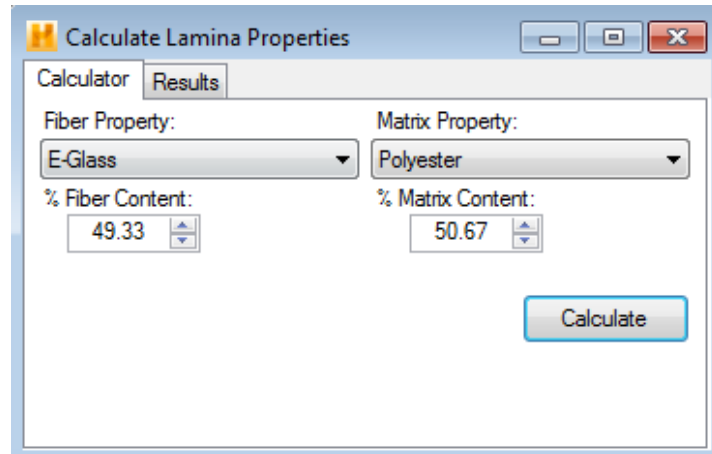
The following areas of future research are recommended:

1. More experimental studies are required to manufacture the composite flange with different manufacturing processes such as hand lay-up or resin transfer moulding. In this research, vacuum infusion process is used. So that the results can be compared with the results of this study. So far, the current fabricated flange is over-designed. Therefore, other manufacturing processes such as RTM or hand lay-up, which are probably faster and cheaper, can be used. These manufacturing processes have less fibre content than the vacuum infusion process and that will effect on the all the mechanical properties. However, the over-designed of the current flange can be compensated by changing the manufacturing process to be cheap and fast.
2. Based on the obtained results, an optimization study is required to study the reducing of the flange dimensions taking into account the cost parameter.
3. More loads can be applied on the bolted flange joints. These loads are external force, external pressure. This can extend the use of the flange in other applications.
4. Study the effect of the fluid flow and fluid thermal load on the performance of the GFRP flange joint.
5. Using different types of the rubber gaskets such as Neoprene and EPDM, which are used in the water industries and PTFE that is commonly used in the chemical applications.
6. Study the effect of the fluid viscosity on the leakage propagations between the flange and the rubber gasket. This can be done by using ANSYS fluid codes such as CFX or CFD.
7. Study the effect of corrosion and erosion on the composite flange performance. In some applications, these problems are important.

8. Study the electric conductivity of the composite flange and add some nano materials (carbon nanotubes), which help to improve mechanical properties and the electric conductivity of the composite. This can help to detect the mechanical damages (cracks) and avoid them before they becomes catastrophic. It also minimizes the effect of the static electric shock.

## APPENDICES

**Appendix (A):** Helius composite validation properties of the composite properties



Calculate Lamina Properties

Calculator Results

Fiber Property: E-Glass

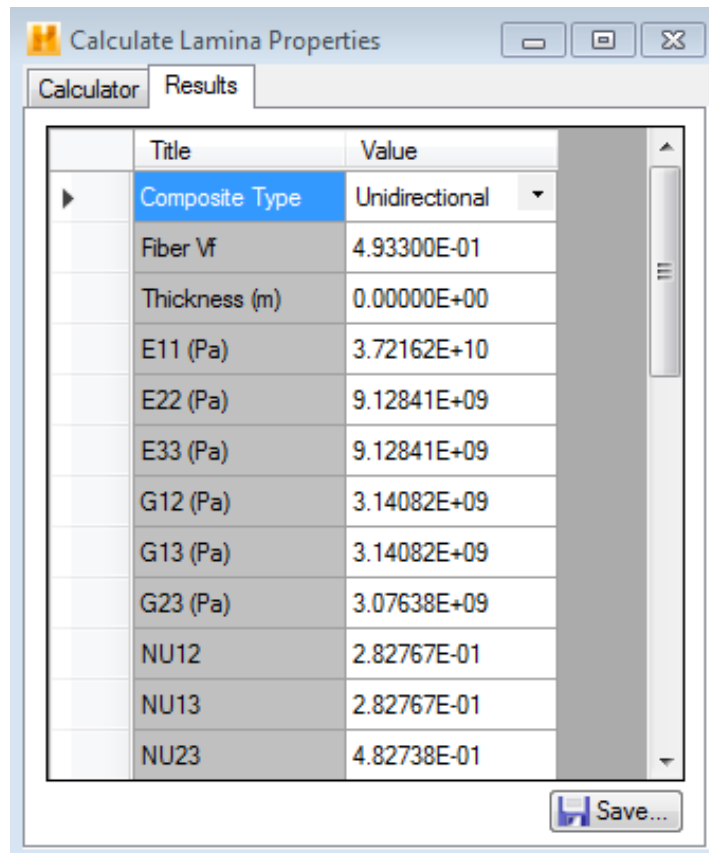
Matrix Property: Polyester

% Fiber Content: 49.33

% Matrix Content: 50.67

Calculate

Fig. A.1: Design of GFRP lamina



Calculate Lamina Properties

Calculator Results

| Title          | Value          |
|----------------|----------------|
| Composite Type | Unidirectional |
| Fiber Vf       | 4.93300E-01    |
| Thickness (m)  | 0.00000E+00    |
| E11 (Pa)       | 3.72162E+10    |
| E22 (Pa)       | 9.12841E+09    |
| E33 (Pa)       | 9.12841E+09    |
| G12 (Pa)       | 3.14082E+09    |
| G13 (Pa)       | 3.14082E+09    |
| G23 (Pa)       | 3.07638E+09    |
| NU12           | 2.82767E-01    |
| NU13           | 2.82767E-01    |
| NU23           | 4.82738E-01    |

Save...

Fig. A.2: GFRP lamina properties



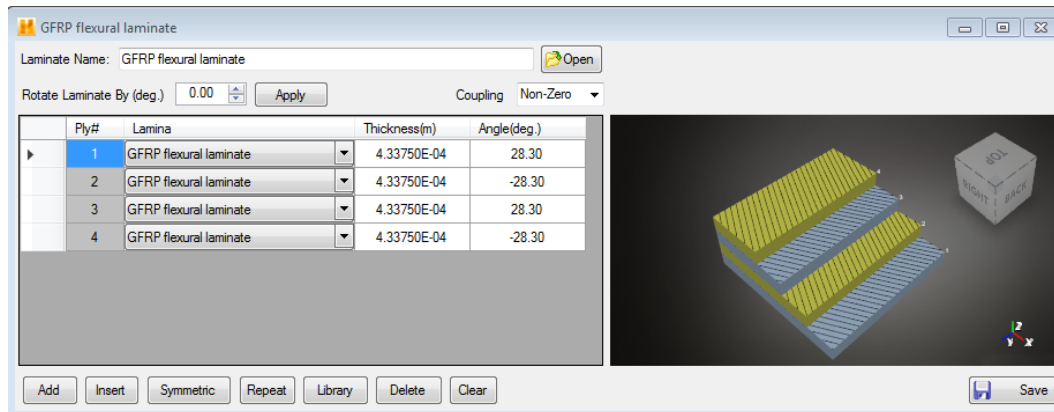


Fig. A.3: Design of GFRP laminate

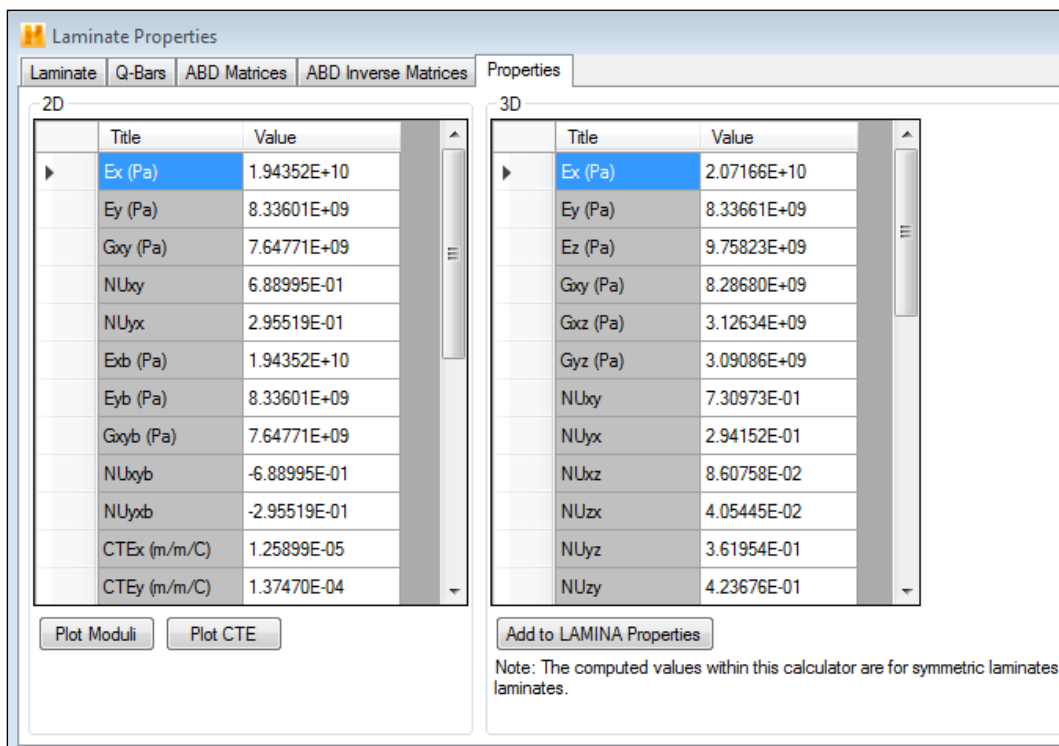



Fig. A.4: 2D and 3D mechanical properties of the GFRP laminate

**Appendix (B):** Calibration of the strain indicators and recorder (P3's)



HQ Number:

1242

Instrument:

Model P3

Serial Number:

0161615

Customer:

University of Plymouth

Customer Ref Number:

129577

Test Date:

09 May 2017


Carried Out By:

Alan Fulbrook

## Unit Calibration Details

| Model 1550A Input Setting | Expected Reading | Before Adjustment |          |           |           | After Adjustment |            |           |           |
|---------------------------|------------------|-------------------|----------|-----------|-----------|------------------|------------|-----------|-----------|
|                           |                  | Channel Number    |          |           |           | Channel Number   |            |           |           |
|                           |                  | 1                 | 2        | 3         | 4         | 1                | 2          | 3         | 4         |
| 000 Microstrain           | 0                | 0                 | 0        | 0         | 0         | 0                | 0          | 0         | 0         |
| 500 Microstrain           | 500              | 487               | 487      | 487       | 487       | 500              | 500        | 500       | 500       |
| 1000 Microstrain          | 1000             | 986               | 985      | 986       | 986       | 1000             | 1000       | 1000      | 1000      |
| 5000 Microstrain          | 5000             | 4987              | 4987     | 4987      | 4987      | 5001             | 5002       | 5001      | 5002      |
| 10000 Microstrain         | 10000            | 9988              | 9988     | 9988      | 9988      | 10002            | 10002      | 10002     | 10002     |
| 31000 Microstrain         | 31000            | 30985             | 30985    | 30984     | 30985     | 31002            | 31001      | 31001     | 31002     |
| 000 Microstrain           | 0                | 0                 | 0        | 0         | 0         | 0                | 0          | 0         | 0         |
| -500 Microstrain          | -500             | -486              | -486     | -486      | -486      | -500             | -500       | -500      | -500      |
| -1000 Microstrain         | -1000            | -986              | -986     | -986      | -986      | -1000            | -1000      | -1000     | -1000     |
| -5000 Microstrain         | -5000            | -4987             | -4986    | -4987     | -4987     | -5000            | -5000      | -5000     | -5000     |
| -10000 Microstrain        | -10000           | -9986             | -9986    | -9986     | -9985     | -10001           | -10001     | -10000    | -10001    |
| -30500 Microstrain        | -30500           | -30986            | -30986   | -30986    | -30986    | -30498           | -30498     | -30485    | -30498    |
| Gain                      |                  | 0.1208508         | 0.120844 | 0.1208493 | 0.1208449 | 0.1208167        | -0.1208114 | 0.1208153 | 0.1208128 |
| AmpZero                   |                  | -211              | -90      | -56       | -43       | -62              | -43        | -40       | -33       |

Fig. B.1: Calibration data of P3, SN 0161615



Instrument:

Serial Number:

Customer:

Customer Ref Number:

Test Date:

Carried Out By:

Model P3

0169299

University of Plymouth

129577

09 May 2017

Alan Fulbrook


HQ Number:

1242

Unit Calibration Details

|                           |                  | Before Adjustment |           |           |           | After Adjustment |           |           |           |
|---------------------------|------------------|-------------------|-----------|-----------|-----------|------------------|-----------|-----------|-----------|
|                           | Expected Reading | Channel Number    |           |           |           | Channel Number   |           |           |           |
| Model 1550A Input Setting |                  | 1                 | 2         | 3         | 4         | 1                | 2         | 3         | 4         |
| 000 Microstrain           | 0                | 0                 | 0         | 0         | 0         | 0                | 0         | 0         | 0         |
| 500 Microstrain           | 500              | 487               | 487       | 487       | 487       | 500              | 500       | 500       | 500       |
| 1000 Microstrain          | 1000             | 986               | 985       | 986       | 986       | 1000             | 1000      | 999       | 1000      |
| 5000 Microstrain          | 5000             | 4987              | 4987      | 4987      | 4987      | 5002             | 5001      | 5001      | 5001      |
| 10000 Microstrain         | 10000            | 9988              | 9988      | 9988      | 9988      | 10001            | 10001     | 10001     | 10002     |
| 31000 Microstrain         | 31000            | 30985             | 30985     | 30984     | 30985     | 31002            | 31002     | 31001     | 31002     |
| 000 Microstrain           | 0                | 0                 | 0         | 0         | 0         | 0                | 0         | 0         | 0         |
| -500 Microstrain          | -500             | -486              | -486      | -486      | -486      | -500             | -500      | -500      | -500      |
| -1000 Microstrain         | -1000            | -986              | -986      | -986      | -986      | -1000            | -1000     | -1000     | -1000     |
| -5000 Microstrain         | -5000            | -4987             | -4986     | -4987     | -4987     | -5000            | -5000     | -5000     | -5000     |
| -10000 Microstrain        | -10000           | -9986             | -9986     | -9986     | -9985     | -10001           | -10000    | -10000    | -10001    |
| -30500 Microstrain        | -30500           | -30986            | -30986    | -30986    | -30986    | -30493           | -30498    | -30498    | -30491    |
| Gain                      |                  | 0.1206976         | 0.1206879 | 0.1206962 | 0.1206938 | 0.1206632        | 0.1206598 | 0.1206632 | 0.1206617 |
| AmpZero                   |                  | -216              | -213      | -215      | -217      | -202             | -193      | -195      | -195      |

Fig. B.2: Calibration data of P3, SN 0169299



Instrument:

Serial Number:

Customer:

Customer Ref Number:

Test Date:

Carried Out By:

Model P3

0170024

University of Plymouth

129577

09 May 2017

Alan Fulbrook


HQ Number:

1242

### Unit Calibration Details

| Model 1550A Input Setting | Expected Reading | Before Adjustment |           |           |           | After Adjustment |           |           |           |
|---------------------------|------------------|-------------------|-----------|-----------|-----------|------------------|-----------|-----------|-----------|
|                           |                  | Channel Number    |           |           |           | Channel Number   |           |           |           |
|                           |                  | 1                 | 2         | 3         | 4         | 1                | 2         | 3         | 4         |
| 000 Microstrain           | 0                | 0                 | 0         | 0         | 0         | 0                | 0         | 0         | 0         |
| 500 Microstrain           | 500              | 487               | 487       | 487       | 487       | 501              | 500       | 500       | 500       |
| 1000 Microstrain          | 1000             | 986               | 985       | 986       | 986       | 1001             | 1000      | 1000      | 1000      |
| 5000 Microstrain          | 5000             | 4987              | 4987      | 4987      | 4987      | 5002             | 5002      | 5001      | 5002      |
| 10000 Microstrain         | 10000            | 9988              | 9988      | 9988      | 9988      | 10002            | 10002     | 10002     | 10002     |
| 31000 Microstrain         | 31000            | 30985             | 30985     | 30984     | 30985     | 31002            | 31001     | 31001     | 31002     |
| 000 Microstrain           | 0                | 0                 | 0         | 0         | 0         | 0                | 0         | 0         | 0         |
| -500 Microstrain          | -500             | -486              | -486      | -486      | -486      | -500             | -500      | -500      | -500      |
| -1000 Microstrain         | -1000            | -986              | -986      | -986      | -986      | -1000            | -1000     | -1000     | -1000     |
| -5000 Microstrain         | -5000            | -4987             | -4986     | -4987     | -4987     | -5000            | -5000     | -5000     | -5000     |
| -10000 Microstrain        | -10000           | -9986             | -9986     | -9986     | -9985     | -10000           | -10000    | -10000    | -10000    |
| -30500 Microstrain        | -30500           | -30986            | -30986    | -30986    | -30986    | -30497           | -30498    | -30485    | -30497    |
| Gain                      |                  | 0.1207292         | 0.1207273 | 0.1207297 | 0.1207273 | 0.1206962        | 0.1206923 | 0.1206942 | 0.1206933 |
| AmpZero                   |                  | -44               | -41       | -42       | -38       | -76              | -66       | -44       | -61       |

Fig. B.3: Calibration data of P3, SN 0170024



Instrument:

Model P3

Serial Number:

0170060

Customer:

University of Plymouth

Customer Ref Number:

129577

Test Date:

09 May 2017

Carried Out By:

Alan Fulbrook

HQ Number:

1242

Unit Calibration Details

| Model 1550A Input Setting | Expected Reading | Before Adjustment |           |           |           | After Adjustment |           |          |           |
|---------------------------|------------------|-------------------|-----------|-----------|-----------|------------------|-----------|----------|-----------|
|                           |                  | Channel Number    |           |           |           | Channel Number   |           |          |           |
|                           |                  | 1                 | 2         | 3         | 4         | 1                | 2         | 3        | 4         |
| 000 Microstrain           | 0                | 0                 | 0         | 0         | 0         | 0                | 0         | 0        | 0         |
| 500 Microstrain           | 500              | 487               | 487       | 487       | 487       | 500              | 500       | 500      | 500       |
| 1000 Microstrain          | 1000             | 986               | 985       | 986       | 986       | 1000             | 1000      | 1000     | 1000      |
| 5000 Microstrain          | 5000             | 4987              | 4987      | 4987      | 4987      | 5001             | 5001      | 5001     | 5002      |
| 10000 Microstrain         | 10000            | 9988              | 9988      | 9988      | 9988      | 10002            | 10002     | 10002    | 10002     |
| 31000 Microstrain         | 31000            | 30985             | 30985     | 30984     | 30985     | 31003            | 31002     | 31002    | 31002     |
| 000 Microstrain           | 0                | 0                 | 0         | 0         | 0         | 0                | 0         | 0        | 0         |
| -500 Microstrain          | -500             | -486              | -486      | -486      | -486      | -500             | -500      | -500     | -500      |
| -1000 Microstrain         | -1000            | -986              | -986      | -986      | -986      | -1000            | -1000     | -1000    | -1000     |
| -5000 Microstrain         | -5000            | -4987             | -4986     | -4987     | -4987     | -5000            | -5000     | -5000    | -5000     |
| -10000 Microstrain        | -10000           | -9986             | -9986     | -9986     | -9985     | -10001           | -10000    | -10000   | -10001    |
| -30500 Microstrain        | -30500           | -30986            | -30986    | -30986    | -30986    | -30498           | -30499    | -30498   | -30499    |
| Gain                      |                  | 1208771           | 0.1208751 | 0.1208771 | 0.1208747 | 0.1208445        | 0.1208396 | 0.120843 | 0.1208411 |
| AmpZero                   |                  | -372              | -372      | -374      | -415      | -396             | -349      | -382     | -381      |

Fig. B.4: Calibration data of P3, SN 0170060

**Appendix (C):** Calibration of the digital torque adaptor

|   |  |  |             |
|---|--|--|-------------|
| <b>Production Calibration Certificate</b> |  | Nr. / No.  |             |
|   |  | Vol.   | 1.1-06-2013 |
| Article                                   |  | ISO 6789; Type II; Class C<br>Digital torque adaptor |             |
| Model                                     |  | STW290   |             |
| Range                                     |  | 40-200 N-m(29.5-147.5 lb-ft)                         |             |
| Tolerance                                 |  | ± 2 % of full scale value                            |             |
| Serie No.                                 |  | 15E05641   |             |
| Method                                    |  | according to DIN ISO 6789                            |             |
| Amb.temp.                                 |  | 23° (73.4° F.)                                       |             |

| Calibration Values | Torque Reading |           |           |            |
|--------------------|----------------|-----------|-----------|------------|
| Rated Values       | Reading        | Tolerance | Deviation | Value in % |
| Nm                 | Nm             | Nm        | Nm        | %          |
| 40                 | 39.9           | 0.8       | -0.1      | -0.25%     |
|                    | 39.9           | 0.8       | -0.1      | -0.25%     |
|                    | 40.2           | 0.8       | +0.2      | +0.50%     |
|                    | 39.9           | 0.8       | -0.1      | -0.25%     |
|                    | 39.9           | 0.8       | -0.1      | -0.25%     |
| 120                | 120.1          | 2.4       | +0.1      | +0.08%     |
|                    | 119.7          | 2.4       | -0.3      | -0.25%     |
|                    | 120.3          | 2.4       | +0.3      | +0.25%     |
|                    | 119.8          | 2.4       | -0.2      | -0.17%     |
|                    | 119.8          | 2.4       | -0.2      | -0.17%     |
| 200                | 200.1          | 4.0       | +0.1      | +0.05%     |
|                    | 200.2          | 4.0       | +0.2      | +0.10%     |
|                    | 200.8          | 4.0       | +0.8      | +0.39%     |
|                    | 200.1          | 4.0       | +0.1      | +0.05%     |
|                    | 200.1          | 4.0       | +0.1      | +0.05%     |

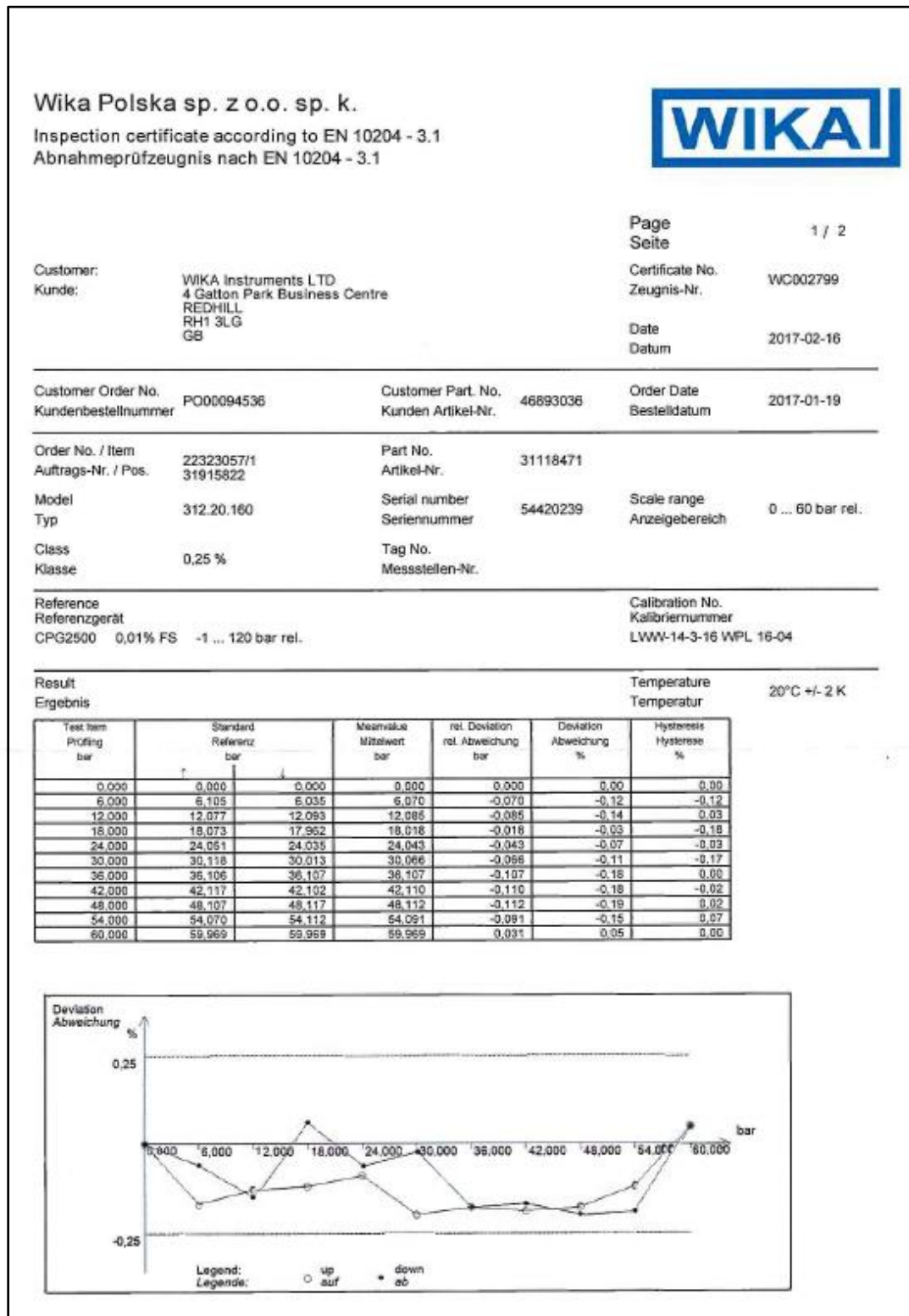
  

|           |            |
|-----------|------------|
| Result    | approved   |
| Inspector | Patty      |
| Date      | 04/01/2016 |

Rayjay Technology Co., Ltd

Fig. C.1: Calibration data of digital torque adaptor

# Appendix (D): Calibration of the pressure gauge




Legend:  
Legende: ○ up auf    ● down ab

Fig. D.1: Calibration data of pressure gauge

---

**REFERENCES**

1. Sawa, T., Higurashi, N., and Akagawa, H., *A stress analysis of pipe flange connections*. Journal of Pressure Vessel Technology, 1991, 113(4): P. 497-503.
2. Mallinson, J.H., *Corrosion-resistant plastic composites in chemical plant design*. Marcel Dekker, New York, 1988.
3. Lees, J.M., *Behaviour of GFRP adhesive pipe joints subjected to pressure and axial loadings*. Composites Part A: Applied Science and Manufacturing, 2006, 37(8): P. 1171-1179.
4. Gemi, L., Tarakçioğlu, N., Akdemir, A., Şbahin, Ö. S., *Progressive fatigue failure behavior of glass/epoxy ( $\pm 75^\circ$ )<sub>2</sub> filament-wound pipes under pure internal pressure*. Materials & Design, 2009, 30(10): P. 4293-4298.
5. Lee, C. S., Hwang, W., Park, H. C., Han, K. S., *Failure of carbon/epoxy composite tubes under combined axial and torsional loading 1. Experimental results and prediction of biaxial strength by the use of neural networks*. Composites Science and Technology, 1999, 59(12): P. 1779-1788.
6. Harvey, W.A. and Kremer, J.S., *Design, process development, and fabrication of an all IM 7/977-2 12 in. dia. pressurized fuel line required to operate at -423 F while bolted to an aluminum valve*. Evolving technologies for the competitive edge, 1997, P. 839-853.
7. Sun, L., *Bolted flanged connections made of fiber reinforced plastic materials*. Concordia University, 1995.
8. Estrada, H., *A Fiber Reinforced Plastic Joint for Filament Wound Pipes: Analysis and Design*. University of Illinois, 1997.

9. Aljuboury, M., Rizvi M.J., Grove, S. and Cullen, R., *Bolted fibre-reinforced polymer flange joints for pipelines: A review of current practice and future challenges*. Proceedings of the Institution of Mechanical Engineers, Part L: Journal of Materials: Design and Applications, 2018.
10. ASME B16.5-2003, *Pipe Flanges and Flanged Fittings*. The American Society of Mechanical Engineers, USA, 2003.
11. ASME B16.47-2011, *Large Diameter Steel Flanges*. The American Society of Mechanical Engineers, USA, 2011.
12. Brownell, L.E. and Young, E.H., *Process equipment design: vessel design*. John Wiley & Sons, 1959.
13. Lamit, L.G., *Pipe Fitting and Piping Handbook*. Prentice Hall, Inc, 1984.
14. Yang, C., *Design and analysis of composite pipe joints under tensile loading*. Journal of Composite Materials, 2000, 34(4): P. 332-349.
15. Tao, G., Liu, Z., Ly, M.Y., Chen, S., *Research on manufacture and test of advanced composite material flange*. Open Mechanical Engineering Journal, 2011, 5: P. 87-96.
16. Bickford, J., *Gaskets and gasketed joints*. CRC Press 1997.
17. Barbero, E.J., *Introduction to Composite Materials Design*. Taylor & Francis 1998, Vol. 1.
18. Gurit, *Guide to composites*. Gurit. Available at;  
[www.gurit.com/-/media/Gurit/Datasheets/guide-to-composites.pdf](http://www.gurit.com/-/media/Gurit/Datasheets/guide-to-composites.pdf)
19. Lubin, G., *Handbook of composites*. Van Nostrand Reinhold Company, 1982.
20. Adams, R. and Bogner B., *Long Term Use of Isopolyesters in Corrosion Resistance*. In *Technical Sessions of The Annual Conference-Composites Institute*. Society of the Plastics Industry, Inc, 1993.



21. Mallick, P.K., *Fiber-reinforced composites: materials, manufacturing, and design*. CRC Press, 2007.
22. Peters, S.T., *Handbook of composites*, 2<sup>nd</sup> edition. Springer Science & Business Media, 1998.
23. Bunsell, A.R. and Renard, J., *Fundamentals of fibre reinforced composite materials*. CRC Press, 2005.
24. ASME Boiler and Pressure Vessel Code, Section X, Fiber-Reinforced Plastic Pressure Vessels. The American Society of Mechanical Engineers, USA, 2010.
25. Gay, D., Hoa, S.V., and Tsai, S.W., *Composite materials: design and applications*. CRC Press, 2003.
26. Weatherhead, R., *FRP technology: fibre reinforced resin systems*. Springer Science & Business Media, 2012.
27. Hull, D. and Clyne, T.W., *An introduction to composite materials*. Cambridge University Press, 1996.
28. Potter, K., *Resin transfer moulding*. Springer Science & Business Media, 2012.
29. Tong, L., Mouritz, A.P., and Bannister M.K., *3D fibre reinforced polymer composites*. 2002: Elsevier.
30. Long, A.C., *Design and manufacture of textile composites*. Woodhead Publishing Ltd, 2005.
31. Gong, R.H., *Specialist yarn and fabric structures Developments and applications*. Woodhead Publishing Ltd, 2011.
32. Lee, S.M., *Handbook of composite reinforcements*. John Wiley & Sons, 1992.



- 
33. Dynaflow research group, *GRP Flanges design & assessment*. Rotterdam, 2011.
  34. Omiya, Y., Sawa, T., and Takagi, Y., *Stress analysis and design of bolted flange connections under internal pressure*. ASME Pressure Vessels and Piping Conference, American Society of Mechanical Engineers, 2014.
  35. Naser, K., *Bolted flanged connections with full face gaskets*. Concordia University, 1995.
  36. Nash, D.H, Spence J., Tooth, A.S., Abid, M. and Power, D.J., *A parametric study of metal-to-metal full face taper-hub flanges*. International Journal of Pressure Vessels and Piping, 2000. 77(13): P. 791-797.
  37. Shoji, Y. and Nagata, S., *Analysis of gasketed flanges with ordinary elements using apdl control*. Toyo Engineering Corporation, Narashino City, Chiba, Japan, 2002.
  38. Abid, M. and Nash D.H., *A parametric study of metal-to-metal contact flanges with optimised geometry for safe stress and no-leak conditions*. International Journal of Pressure Vessels and Piping, 2004, 81(1): P. 67-74.
  39. Abid, M., *Determination of safe operating conditions for gasketed flange joint under combined internal pressure and temperature: A finite element approach*. International Journal of Pressure Vessels and Piping, 2006. 83(6): p. 433-441.
  40. Abid, M. and Ullah, B., *Three-dimensional nonlinear finite-element analysis of gasketed flange joint under combined internal pressure and variable temperatures*. Journal of Engineering Mechanics, 2007, 133(2): P. 222-229.

- 
41. Nechache, A. and Bouzid A.-H., *The determination of load changes in bolted gasketed joints subjected to elevated temperature*. ASME Pressure Vessels and Piping Conference. American Society of Mechanical Engineers, 2003.
  42. Guruchannabasavaiah, N.G., Shanmugam, and Arun, L.R., *Effect of Temperature and associated deformations on the gasket seal compression in a pressure vessel*. International Journal of Scientific & Engineering Research, 2013, 4(8): P. 7.
  43. BS EN 1591-1 Flanges and their joints — *Design rules for gasketed circular flange connections —Part 1 Calculations*.
  44. ASME PCC-1-2013, *Guidelines for pressure boundary flanged connections*, The American Society of Mechanical Engineers, USA, 2013.
  45. Żyliński, B. and Buczkowski, R., *Analysis of bolt joint using the finite element method*. Archive of Mechanical Engineering, 2010, 57(3): P. 275-292.
  46. Zahavi, E., *A finite element analysis of flange connections*. Journal of Pressure Vessel Technology, 1993, 115(3): P. 327-330.
  47. Do, T.D., Bouzid A.-H., and My, T. , *Effect of bolt spacing on the circumferential distribution of the gasket contact stress in bolted flange joints*. Université Du Québec, 2012.
  48. Koves, W.J. *Flange Joint Bolt Spacing Requirements*. ASME Pressure Vessels and Piping Conference. American Society of Mechanical Engineers, 2007.
  49. Hwang, D.Y. and Stallings J.M., *Finite element analysis of bolted flange connections*. Computers & Structures, 1994, 51(5): P. 521-533.

- 
50. Sanjay, S.J., Sunil Kummer B.V., Kulkarni, B. and Math, V.B., *Stress analysis of a non-gasketed composite flange*. International Journal of Advancement in Engineering Technology, Mangement & Applied Science, 2014.
  51. Whitfield, G.S., Reid, R.G. and Paskaramoorthy, R., *Creep and unsymmetrical shrinkage during post-cure of GFRP pipe flanges*. 2014.
  52. Estrada, H. and Parsons, I.D., *Strength and leakage finite element analysis of a GFRP flange joint*. International Journal of Pressure Vessels and Piping, 1999, 76(8): P. 543-550.
  53. Kurz, H. and Roos, E., *Design of floating type bolted flange connections with grp flanges*. International Journal of Pressure Vessels and Piping, 2012, 89: P. 1-8.
  54. Kittel, K., Vajna, S. and Marks, L.E., *Optimisation of Grp-Flange Joints*. International Conference on Engineering Design, Paris, 2007.
  55. Fangueiro, R., Nunes, P., Soutinho, F. and Araújo M. de., *Development of fibrous preforms for FRP pipe connections*. Composites Science and Technology, 2009, 69(9): P. 1412-1416.
  56. Rod Martin, *A technology gap review of composites in the UK oil and gas industry*, Materials engineering research laboratory, UK, 2007.
  57. Bickford, J., *Handbook of bolts and bolted joints*. CRC Press 1998.
  58. Taylor Forge Inc., *Design of flanges for full-face gasket*. Engineering Department Bulletin, 1951.
  59. Krishna, M.M., Shunmugam, M.S., and Prasad, N.S., *A study on the sealing performance of bolted flange joints with gaskets using finite element analysis*. International Journal of Pressure Vessels and Piping, 2007, 84(6): p. 349-357.

- 
60. Schwaigerer, S., *Festigkeitsberechnung von Bauelementen des Dampfkessel-Behälter-und Rohrleitungsbaues*. Springer, 1961.
  61. Blach, A.E., A. Bazergui, and R. Baldur, *Bolted flanged connections with full face gaskets*. Weld. Res. Counc. Bull., 1986, (314): P. 1-13.
  62. Antaki, G.A., *Piping and pipeline engineering: design, construction, maintenance, integrity, and repair*. CRC Press, 2003.
  63. Flitney, R.K., *Seals and sealing handbook*. Elsevier, 2011.
  64. ASME B 16.20A-2000, *Metallic gaskets for pipe flanges ring-joint, spiral-wound, and jacketed*. The American Society of Mechanical Engineers, USA, 2000.
  65. Zappe, R., *Valve Selection Handbook: Engineering Fundamentals for Selecting Manual Valves, Check Valves, Pressure Relief Valves, and Rupture Discs*. Gulf Professional Publishing, 1999.
  66. Fthenakis, V.M., *Prevention and control of accidental releases of hazardous gases*. John Wiley & Sons, 1993.
  67. Bakaiyan, H., Hosseini and Ameri, E., *Analysis of multi-layered filament-wound composite pipes under combined internal pressure and thermomechanical loading with thermal variations*. Composite Structures, 2009. 88(4): p. 532-541.
  68. Tarakçıoğlu, N., Gemi, L., and Yapici, A., *Fatigue failure behavior of glass/epoxy  $\pm 55^\circ$  filament wound pipes under internal pressure*. Composites Science and Technology, 2005, 65(3): P. 703-708.
  69. Xia, M., Takayanagi, H., and Kemmochi, K., *Analysis of multi-layered filament-wound composite pipes under internal pressure*. Composite Structures, 2001. 53(4): p. 483-491.

- 
70. Mertiny, P., Ellyin, F., and Hothan, A., *An experimental investigation on the effect of multi-angle filament winding on the strength of tubular composite structures*. Composites Science and Technology, 2004, 64(1): P. 1-9.
  71. Meijer, G. and Ellyin, F., *A failure envelope for  $\pm 60^\circ$  filament wound glass fibre reinforced epoxy tubulars*. Composites Part A: Applied Science and Manufacturing, 2008, 39(3): P. 555-564.
  72. Onder, A., Sayman, O., Dogan, T. and Tarakcioglu, N., *Burst failure load of composite pressure vessels*. Composite Structures, 2009, 89(1): P. 159-166.
  73. Arikan, H., *Failure analysis of  $(\pm 55^\circ)_3$  filament wound composite pipes with an inclined surface crack under static internal pressure*. Composite Structures, 2010, 92(1): P. 182-187.
  74. Wahab, M.A., *Joining composites with adhesives*. DEStech Publications, Inc, USA, 2016.
  75. Thakare, N.B. and Dhumne, A.B., *A review on design and analysis of adhesive bonded joint by finite element analysis*, SSRG International Journal of Mechanical Engineering (SSRG-IJME), 2015, P. 6.
  76. Kim, J.H., Park, B.J. and Han Y.W., *Evaluation of fatigue characteristics for adhesively-bonded composite stepped lap joint*. Composite Structures, 2004, 66(1): P. 69-75.
  77. Matthews, F.L, Kilty, P.F. and Godwin E.W, *A review of the strength of joints in fibre-reinforced plastics. Part 2. Adhesively bonded joints*. Composites, Butterworth & Co (Publishers) Ltd, 1982, 13(1): P. 29-37.
  78. Helms, J.E., Yang, C., and Pang S.-S., *Stress-strain analysis of a taper-taper adhesive-bonded joint under cylindrical bending*. Journal of Engineering Materials and Technology, 1999, 121(3): P. 374-380.

- 
79. Erdogan, F. and Ratwani, M., *Stress Distribution in Bonded Joints*. Journal of Composite Materials, 1971, 5(3): P. 378-393.
  80. Hart-Smith, L., *Adhesive-bonded scarf and stepped-lap joints*. NASA, 1973.
  81. Reddy, M.N. and Sinha, P.K., *Stresses in adhesive-bonded joints for composites*. Fibre Science and Technology, 1975, 8(1): P. 33-47.
  82. EDO Specialty Plastics, *A comparison of two joining methods*. 2001, P. 14.
  83. Nemes, O., *Analytical model application for adhesive cylindrical assemblies made by hybrid materials*. Materiale Plastice, 2013, 50(4): P. 314-318.
  84. Cheng, J., Wu, X., Li, G. Taheri, F. and Pang, S-S., *Development of a smart composite pipe joint integrated with piezoelectric layers under tensile loading*. International Journal of Solids and Structures, 2006, 43(17): P. 5370-5385.
  85. Oh, J.H., *Strength prediction of tubular composite adhesive joints under torsion*. Composites Science and Technology, 2007, 67(7): P. 1340-1347.
  86. Oh, J.H., *Torque capacity of tubular adhesive joints with different composite adherends*. Materials Letters, 2008, 62(8): P. 1234-1237.
  87. Kumar, S., *Analysis of tubular adhesive joints with a functionally modulus graded bondline subjected to axial loads*. International Journal of Adhesion and Adhesives, 2009, 29(8): P. 785-795.
  88. Spaggiari, A. and Dragoni, E., *Regularization of torsional stresses in tubular lap bonded joints by means of functionally graded adhesives*. International Journal of Adhesion and Adhesives, 2014, 53: P. 23-28.
  89. Bahr, B. and Sudhakaran, S., *Mapping the cutting force to the hole quality using neural networks*. Artificial Neural Networks in Engineering. 1988, ASME Press.

- 
90. Tsao, C., *Experimental study of drilling composite materials with step-core drill*. Materials & Design, 2008, 29(9): P. 1740-1744.
  91. Fiddes, D.E. and Lazarou, J., *Press moulded flanges for GRP pipe systems*, Composites, 1972, 3(6): P. 254-258.
  92. Khashaba, U.A., Seif, M.A, and Elhamid M.A., *Drilling analysis of chopped composites*. Composites Part A: Applied Science and Manufacturing, 2007, 38(1): P. 61-70.
  93. Stone, R. and Krishnamurthy, K., *A neural network thrust force controller to minimize delamination during drilling of graphite-epoxy laminates*. International Journal of Machine Tools and Manufacture, 1996, 36(9): P. 985-1003.
  94. Khashaba, U.A., *Delamination in drilling GFR-thermoset composites*. Composite Structures, 2004, 63(3): P. 313-327.
  95. Persson, E., Eriksson, I., and Zackrisson, L., *Effects of hole machining defects on strength and fatigue life of composite laminates*. Composites Part A: Applied Science and Manufacturing, 1997, 28(2): P. 141-151.
  96. Durão, L.M.P., *Machining of hybrid composites.*, University of Porto, 2005.
  97. Ho-Cheng, H. and Dharan, C.K.H., *Delamination during drilling in composite laminates*. Journal of Engineering for Industry, 1990, 112(3): P. 236-239.
  98. Tagliaferri, V., Caprino, G., and Diterlizzi, A., *Effect of drilling parameters on the finish and mechanical properties of GFRP composites*. International Journal of Machine Tools and Manufacture, 1990, 30(1): P. 77-84.
  99. Khashaba, U.A., *Notched and pin bearing strengths of GFRP composite laminates*. Journal of Composite Materials, 1996, 30(18): P. 2042-2055.

- 
100. Davim, J.P., Reis, P., and Antonio C.C., *Experimental study of drilling glass fiber reinforced plastics (GFRP) manufactured by hand lay-up*. Composites Science and Technology, 2004, 64(2): P. 289-297.
  101. Abrao, A.M., Campos Rubioet, J.C., Faria, P.E. and Davim, J.P., *The effect of cutting tool geometry on thrust force and delamination when drilling glass fibre reinforced plastic composite*. Materials & Design, 2008, 29(2): P. 508-513.
  102. Taylor Forge Inc., *Modern flange design*. Engineering Department Bulletin, 1964.
  103. Curtis, P., *CRAG (Composite Research Advisory Group) Test Methods for the Measurement of the Engineering Properties of Fibre Reinforced Plastics*. 1988, DTIC Document.
  104. Grove, S., *Composite Materials and Structures for Engineering Students*. Kindle Direct Publishing, ISBN: 978-1-98-334480-0, 2018.
  105. BS EN ISO 14125:1998 +A1:2011, *Fibre-reinforced plastic composites — Determination of flexural properties*, British Standard, European Standard and International Organization for Standardization, 2011.
  106. Vosler, G., *Coefficient of static friction (slide angle) of packaging and packaging materials (including shipping sack papers, corrugated and solid fiberboard; inclined plane method)*. TAPPI. 2006; Available at: <http://www.tappi.org/content/sarg/t815.pdf>.
  107. *Strain Gauges Guide*, TML Tokyo Sokki Kenkyujo co., Ltd. Japan, 2017.
  108. ASTM A370-03a, *Standard test methods and definitions for mechanical testing of steel products*, American Society for Testing and Materials, USA, 2003.



- 
109. *Guideline Assembly Instructions*, Gee Graphite Ltd. Available at:  
<http://www.geegraphite.com/About/Technical/TabId/251/PID/2586/evl/0/CategoryID/416/CategoryName/Guideline-Assembly-Instructions/Default.aspx>.
  110. ASTM D575-91: 2012, *Standard Test Methods for Rubber Properties in Compression*. American Society for Testing and Materials, USA, 2012.
  111. BS ISO 1827: 2011, *Rubber, vulcanized or thermoplastic — Determination of shear modulus and adhesion to rigid plates — Quadruple shear methods*, British Standard and International Organization for Standardization, 2011.
  112. *ANSYS help*, ANSYS, available at:  
[https://www.sharcnet.ca/Software/Ansys/16.2.3/en-us/help/ans\\_elem/Hlp\\_E\\_SOLID185.html](https://www.sharcnet.ca/Software/Ansys/16.2.3/en-us/help/ans_elem/Hlp_E_SOLID185.html).
  113. *ANSYS help*, ANSYS, Available at:  
[https://www.sharcnet.ca/Software/Ansys/15.0.7/en-us/help/ans\\_elem/Hlp\\_E\\_INTER195.html](https://www.sharcnet.ca/Software/Ansys/15.0.7/en-us/help/ans_elem/Hlp_E_INTER195.html).
  114. ANSYS User's Manual, *Contact Technology Guide*. ANSYS Inc, USA, 2009.
  115. ANSYS User's Manual, *ANSYS Mechanical APDL Technology Demonstration Guide*. ANSYS Inc, USA, 2013.
  116. Harris, T., *Implementing Fluid Pressure Penetration*. The Focus, 2009, (71).
  117. Szab , B. and Babu ska, I., *Introduction to finite element analysis: formulation, verification and validation*. John Wiley & Sons, 2011, Vol. 35.
  118. Aljuboury, M., Rizvi M.J., Grove, S. and Cullen, R., *A numerical investigation of the sealing performance of a bolted GFRP flange joint with rubber gasket*, Eleventh International Conference on Composite Science and Technology (ICCST/11), American University of Sharjah, Sharjah, UAE, 2017.

119. McNutt, M.K., Camilli, R., Crone T.J., Guthrie, G.D., Hsieh, P.A., Ryerson, T.B., Savas, O. and Shaffer, F., *Review of flow rate estimates of the Deepwater Horizon oil spill*. Proceedings of the National Academy of Sciences, 2012, 109(50): P. 20260-20267.